2021 RETROSPECTIVE: SMART MATERIALS

EDITED BY: Weihua Li

PUBLISHED IN: Frontiers in Materials

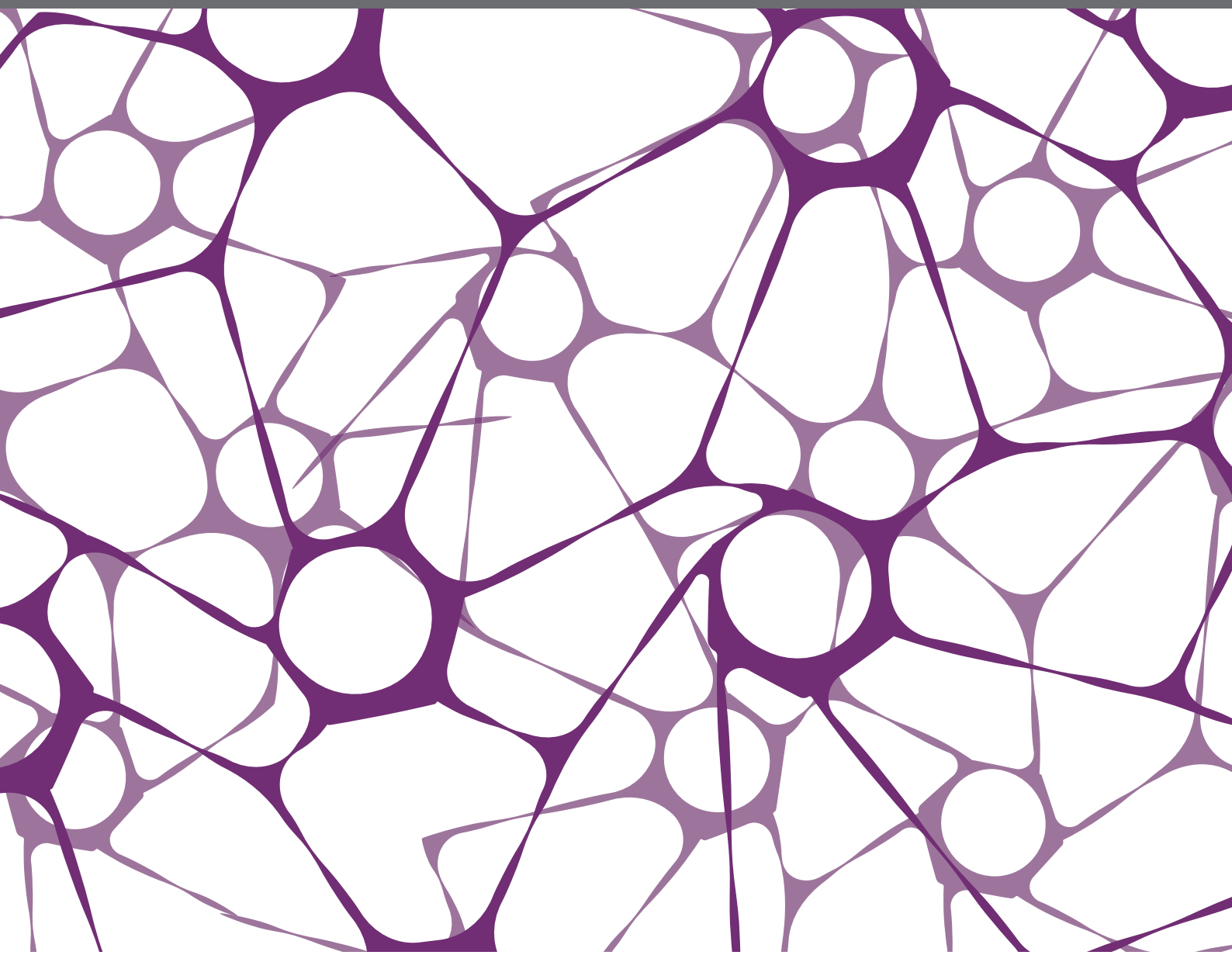

frontiers Research Topics

ISSN 1664-8714
ISBN 978-2-83250-051-4
DOI 10.3389/978-2-83250-051-4

About Frontiers

Frontiers is more than just an open-access publisher of scholarly articles: it is a pioneering approach to the world of academia, radically improving the way scholarly research is managed. The grand vision of Frontiers is a world where all people have an equal opportunity to seek, share and generate knowledge. Frontiers provides immediate and permanent online open access to all its publications, but this alone is not enough to realize our grand goals.

Frontiers Journal Series

The Frontiers Journal Series is a multi-tier and interdisciplinary set of open-access, online journals, promising a paradigm shift from the current review, selection and dissemination processes in academic publishing. All Frontiers journals are driven by researchers for researchers; therefore, they constitute a service to the scholarly community. At the same time, the Frontiers Journal Series operates on a revolutionary invention, the tiered publishing system, initially addressing specific communities of scholars, and gradually climbing up to broader public understanding, thus serving the interests of the lay society, too.

Dedication to Quality

Each Frontiers article is a landmark of the highest quality, thanks to genuinely collaborative interactions between authors and review editors, who include some of the world's best academicians. Research must be certified by peers before entering a stream of knowledge that may eventually reach the public - and shape society; therefore, Frontiers only applies the most rigorous and unbiased reviews.
Frontiers revolutionizes research publishing by freely delivering the most outstanding research, evaluated with no bias from both the academic and social point of view. By applying the most advanced information technologies, Frontiers is catapulting scholarly publishing into a new generation.

What are Frontiers Research Topics?

Frontiers Research Topics are very popular trademarks of the Frontiers Journals Series: they are collections of at least ten articles, all centered on a particular subject. With their unique mix of varied contributions from Original Research to Review Articles, Frontiers Research Topics unify the most influential researchers, the latest key findings and historical advances in a hot research area! Find out more on how to host your own Frontiers Research Topic or contribute to one as an author by contacting the Frontiers Editorial Office: frontiersin.org/about/contact

2021 RETROSPECTIVE: SMART MATERIALS

Topic Editor:
Weihua Li, University of Wollongong, Australia

Citation: Li, W., ed. (2022). 2021 Retrospective: Smart Materials. Lausanne: Frontiers Media SA. doi: 10.3389/978-2-83250-051-4

Table of Contents

frontiers in Materials

MINI REVIEW
published: 30 September 2020
doi: 10.3389/fmats.2020.588521

Application Status of Carbon Nanotubes in Fire Detection Sensors

Guoqing Xiao[1,2,3], *Hengxiang Weng*[1,2], *Liang Ge*[1,2]* *and Qi Huang*[1,2]

[1] Electrical and Mechanical Engineering Department, Southwest Petroleum University, Chengdu, China, [2] Oil and Gas Fire Protection Key Laboratory of Sichuan Province, Chengdu, China, [3] Chemistry and Chemical Engineering Department, Southwest Petroleum University, Chengdu, China

With the rapid development of the city, all kinds of high-rise buildings, large shopping malls and entertainment places have been built one after another. There are some hidden dangers of fire accidents. Effective prevention and monitoring of fire is the focus of fire prevention and control field. As the information source of fire prevention and control, the preparation of fire detection sensor with high sensitivity and short response time is of great significance for fire prevention and monitoring. At present, the commonly used fire detection sensors mainly include CO sensor, temperature sensor and flame sensor. The sensors detect the characteristic parameters in the fire environment and converts non-electric signals such as gas, temperature, and flame light into electric signals to achieve the purpose of fire warning. With the development of material technology in recent years, especially the development of Carbon Nanotube (CNT) technology, a new fire detection sensor represented by CNT materials has emerged. In this paper, the research progress of CNTs in fire detection sensors is reviewed. The applications of CNTs in CO detection, flame light detection and temperature detection are discussed in detail. Finally, the development trend of fire detection sensors based on CNTs is proposed, and the development direction of fire detection sensors in the Internet of things is prospected.

Keywords: carbon nanotubes, fire detection sensors, internet of things, application status, development trend

OPEN ACCESS

Edited by:
Wen Zeng,
Chongqing University, China

Reviewed by:
Hongfu Mi,
Chongqing University of Science and Technology, China
Jie Zhang,
Chongqing University, China
Shenghua Zou,
Hunan University of Science and Technology, China

***Correspondence:**
Liang Ge
cgroad@swpu.edu.cn

Specialty section:
This article was submitted to Smart Materials, a section of the journal Frontiers in Materials

Received: *29 July 2020*
Accepted: *03 September 2020*
Published: *30 September 2020*

Citation:
Xiao G, Weng H, Ge L and Huang Q (2020) Application Status of Carbon Nanotubes in Fire Detection Sensors. Front. Mater. 7:588521. doi: 10.3389/fmats.2020.588521

INTRODUCTION

The Internet of things was first proposed by Kevin Ashton in 1999 (Cardenas et al., 2020), then it was widely used in various fields. The core of the Internet of things is sensor, which can detect the changes of various physical and chemical quantities in the environment, convert these changes into electrical signals, and transmit them to various platforms for information sharing through wireless transmission. The essential requirement of internet of things (IoT) is that sensors and devices can operate for a long time without excessive offset or degradation (Gaur et al., 2019). Therefore, the key factor to promote the development of IoT in the future is to develop low-power and low-cost electronic sensors (Marinov, 2015). Nowadays, a variety of sensors have been developed for the Internet of things, such as temperature sensor (Chad et al., 2013), gas sensor (Sharma et al., 2014; Ge et al., 2019), pressure sensor (Takei et al., 2014), photoelectric sensor, etc. Now, with the continuous development of the Internet of things, it has been widely used in medical, public utilities, manufacturing, transportation, safety prevention and other fields (Sundmaeker et al., 2010). Especially in the safety prevention, the monitoring of the Internet of things plays a crucial role in preventing accidents. In recent years, accidents occur frequently in various places, of which fire accident is one of the disasters with the highest frequency at present. Using the Internet of Things to monitor fires has become a hot spot. The main causes of fire can be divided into smoldering fire and

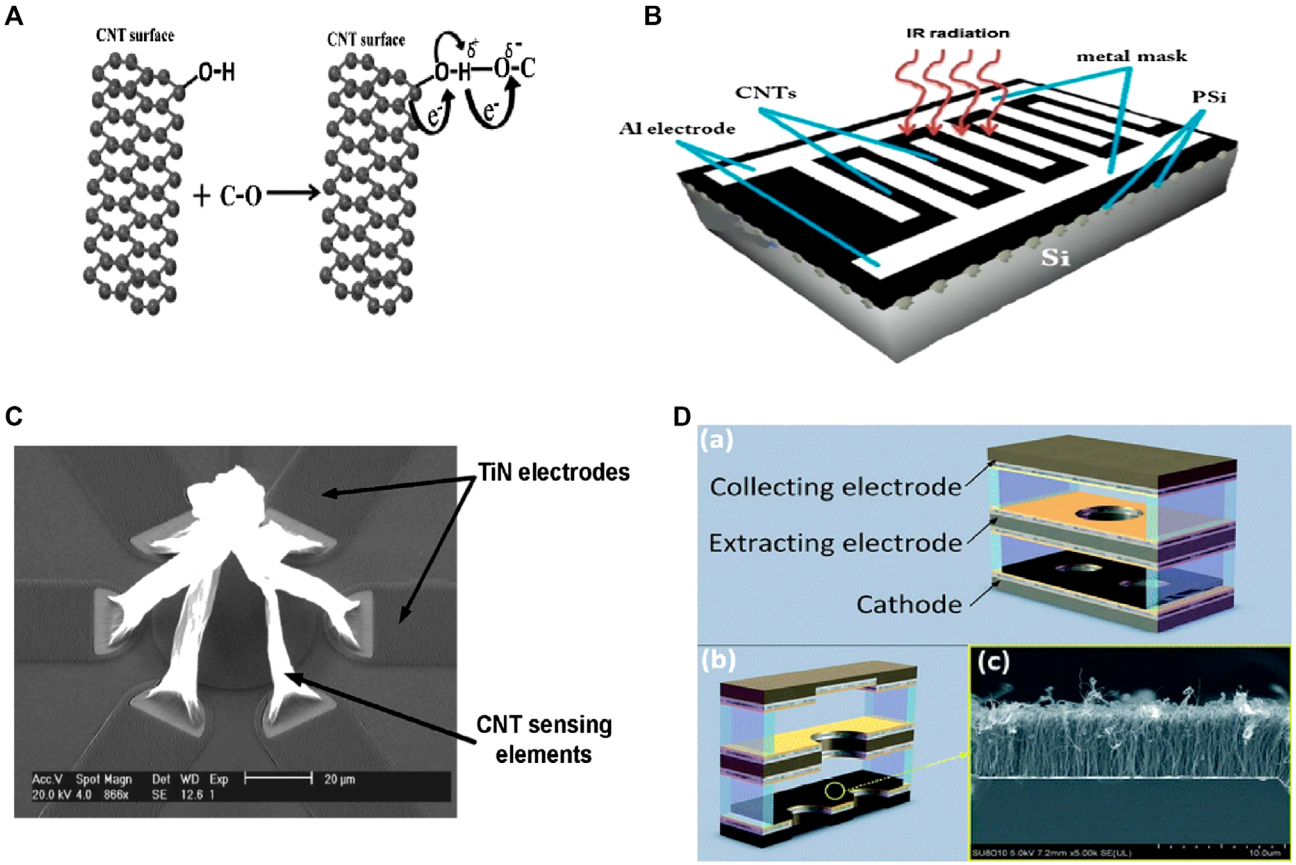

FIGURE 1 | (**A**) Adsorption of CO gas molecule on the carbon nanotubes (CNTs) functionalized with hydroxyl group. (**B**) Schematic diagram of the CNTs infrared photoconductive detector. (**C**) SEM images of the CNT based temperature sensor. (**D**) (**a**) The triple-electrode CNT-based sensor, (**b**) sectional view of the sensor, and (**c**) FE-SEM image of CNT film. Published by the Royal Society of Chemistry.

open fire. For the fire caused by smoldering fire, the concentration of smoke and co increased significantly in the early stage, and decreased significantly in the later stage; when the fire was caused by open fire, the CO concentration increased significantly in the early stage, but the smoke concentration decreased significantly, and the flame produced light radiation, and the smoke concentration increased rapidly in the later stage (Ding et al., 2018). Gas is one of the early characteristics of fire. The main gases used to detect fire include CO, CO_2, NOx, methane, H_2, H_2O, amine ($-NH_2$) (Xue et al., 2005; Wasisto et al., 2014). When a fire occurs, the temperature rises significantly, and the change of temperature can be detected by temperature sensor; the photoelectric detection for fire warning generates radiation light through flame combustion, and the sensor responds to the detection of light to detect the fire (Kwangjae et al., 2017). At present, gas sensors, temperature sensors and flame sensors are widely used in fire early warning system (Bogue, 2013; Fonollosa et al., 2018).

With the development of science and technology, more and more researchers study the preparation materials of sensors. Carbon nanotubes (CNTs) are one of the most popular electronic materials, which can improve the accuracy and response speed of sensors, thus promoting the development of IoT sensors (Chen et al., 2016). In 1991, Iijima first discovered CNTs, and then began to carry out a large number of studies on this material around the world (Iijima, 1991). It was found that CNTs have good electrical, physical, chemical and mechanical properties, for example, CNTs have good chemical stability, high carrier mobility, flexibility, etc., which greatly improve the performance of the sensor (Barcarolle et al., 2013). CNTs are hollow structures composed of graphene sheets. According to the number of graphene layers, CNTs are divided into single-walled CNTs (SWCNTs) and multi-walled CNTs (MWCNTs). MWCNTs are formed by crimping graphene (Wang et al., 2018); according to the spiral shape of graphene sheets, CNTs can be divided into two types (asymmetric type) and chiral type (symmetric type) (Tang, 2019). CNTs can be synthesized by a variety of methods, such as arc discharge (Iijima, 1991), laser ablation (Guo et al., 1995), chemical vapor deposition (Jose-Yacaman et al., 1993). At present, arc discharge has become the most widely used synthesis technology, which can produce SWCNTs and MWCNTs at the same time. Chemical vapor deposition is a common method for commercial production of CNTs. Among the three common methods, laser ablation has the highest cost, arc discharge has the lowest benefit, and chemical vapor deposition is the most effective method for commercial production of CNTs. In addition to CNT materials, CNT

composites have also become a research hotspot in sensor materials. The addition of metal oxides and polymers to CNT can change their structure and produce quantum tunneling effects, which improves the sensor materials. The electronic transportation capability of the sensor significantly improves the selectivity and sensitivity of the sensor.

This paper reviews the research progress of CNTs and their composites in three kinds of fire detection sensors: CO gas sensor, temperature sensor and flame sensor. It also introduces the improvement of the sensing characteristics of CNTs for fire detection sensors, which provides a favorable reference for the further application of CNTs in fire detection sensors.

CO GAS SENSOR BASED ON CARBON NANOTUBES

In the early stage of fire, the main products are the smoke from pyrolysis, including complete combustion products (such as CO_2 and H_2O) and incomplete combustion products, such as CO, gaseous and liquid hydrocarbons, carbon particles, alcohols, aldehydes, ketones, and other chemical substances. The main components of gas products are CO_2, CO, and water vapor. Because the humidity of air has a great influence on the water vapor content, and the content of CO_2 in the air is also high, they are generally not taken as the object of fire detection. Therefore, CO is regarded as the characteristic gas for early fire detection.

Gas Sensing Mechanism of Sensor

The traditional semiconductor CO sensor uses the principle of semiconductor conductivity change caused by the adsorption and desorption of gas molecules on the surface of semiconductor materials to detect the gas concentration. However, this kind of sensor has poor gas selectivity and poor stability, so more reliable materials are needed to prepare the sensor. It has been found that the gas sensing mechanism of SWCNTs is due to the formation of three carbon atoms on the surface of SWCNTs σ bond, one electron forms delocalized π bond between carbon and carbon. When detecting gas, the π electron cloud will change, which will lead to the change of sensor conductivity (Yuan et al., 2004). For MWCNTs, MWCNTs can form more winding structure, which makes the sensor have better conductivity (Sayago et al., 2008). The response of gas sensor based on CNTs to gas is greatly dependent on the effective active number of gas adsorbed on the sensor surface (Zhang et al., 2009). When the sensor detects the gas, the gas molecules will be adsorbed on the active sites on the surface of CNTs, and the space charge layer between the electrodes will form a new polarization (Snow, 2005). The sensor can detect the concentration change of the gas to be measured in the environment. However, due to the limitation of their own properties, the adsorption capacity of CNTs is very limited, limited to several strong reducing and oxidizing gases, such as O_2, NO_2, NH_3, SO_2, and so on. Many toxic gases and greenhouse gases cannot be adsorbed by intrinsic CNTs, such as CO and CO_2. Therefore, in order to detect more kinds of gases, it is necessary to improve the functionalization of intrinsic CNTs. The main improvement methods include nonmetallic element doping, inorganic metal doping and metal oxide doping. In 2014, Mittal reviewed the interaction between CO and hydroxyl-modified CNTs. This is due to the formation of hydrogen bonds between CNTs and the hydroxyl groups of CO molecules. The schematic diagram is shown in **Figure 1A** (Mittal and Kumar, 2014).

Research Status of Carbon Nanotube Based CO Sensors

In 2000, Kong and others found that CNT has good sensing properties for gas, so there are more and more researches on CNTs and their composites in gas sensors (Kong et al., 2000). In 2008, Wu et al. added 0.1% CNTs to the Co_3O_4–SnO_2 materials, which greatly improved the sensing characteristics of the sensor. The lowest detection limit for CO concentration was 20 ppm, the optimal working temperature was 25°C, the response value was 23 mV, and the relative signal-to-noise ratio was 2.3 (Wu et al., 2008). In 2009, Pearce prepared modified MWCNTs gas sensors by electrophoretic deposition, which improved the speed and reliability of fire gas detectors (Pearce, 2009). In 2010, Leghrib et al. synthesized SnO_2/CNTs gas sensor by precipitation of SnO_2 colloidal suspension in CNTs. The sensitivity of SnO_2/CNTs gas sensor to CO was tested at 150°C. The results show that SnO_2/CNTs composite has good sensitivity to 2 ppm CO at this temperature, and the response time is 5 min (Leghrib et al., 2010). In 2013, Iqbal et al. modified ultrasonic spray with Nano-structure ZnO by ultrasonic spray pyrolysis method, and conducted gas sensitivity test. The experimental results showed that the sensitivity of the composite to CO with volume fraction of 100 ppm at 250°C was 85%, the response time was 5 min, and

TABLE 1 | Sensing properties of carbon nanotube complexes for CO.

	Minimum detection limit (ppm)	Optimum operating temperature (°C)	Response time	Literature
SnO_2/CNT	—	150	5 min	Leghrib et al. (2010)
Pd^{2+}/SnO_2/CNT	5	100	2 s	Hu et al. (2014)
SWCNT surface with Au NPs	1	25	125 s	Choi et al. (2016)
Polyaniline-MWCNT	500	25	76 s	Roy et al. (2018)
Pt-CNT	—	100	30 s	Han et al. (2019)
CNT/Co_3O_4–SnO_2	20	25	—	Wu et al. (2008)

CNT, carbon nanotube.

the recovery time was 20 min (Iqbal et al., 2013). In 2014, Hu et al. prepared Pd^{2+} doped SnO_2 nanoparticle coated CNTs by sol-gel method. The minimum detection limit of the sensor for CO is 5 ppm, the best working temperature is 100°C, and the response time is 2 s (Hu et al., 2014). In 2016, Choi et al. synthesized a network of Au nanoparticles functionalized SWCNT by impregnation method and self-agglomeration of Au film. The sensor made of this material has high sensitivity and selectivity to low ppm CO at room temperature, and the detection limit for CO is as low as 1 ppm, achieving good selectivity for 2 ppm CO for the first time (Choi et al., 2016). In 2018, Loghin et al. used a handwriting technique to create a gas sensor based on CNTs. The sensor has a sensitivity of 0.06% ppm for CO and a measurement range of 5–45 ppm (Loghin et al., 2018). In 2019, Kim et al. fabricated a Pt CNTs flake CO gas sensor by depositing Pt nanoparticles on CNTs. The maximum response time of the sensor is 30 s and it has good sensitivity to 80 ppm CO (Han et al., 2019). In 2018, Roy et al. synthesized polyaniline coated MWCNTs and spin coated them on the interdigital electrode of the sensor. The experimental study found that the sensor has good response and repeatability for 500–1,000 ppm CO at room temperature, with a response time of 76 s and a recovery time of 210 s (Roy et al., 2018). **Table 1** is the sensing properties of carbon nanotube complexes for CO. CNTs gas sensors have attracted much attention due to their low operating temperature and minimum detection limit. Semiconductor CNTs gas sensors doped with oxides have the advantages of both oxide semiconductor gas sensors and CNTs gas sensors, and have the characteristics of high sensitivity, minimum detection limit and low working temperature (Zhang et al., 2013).

FLAME SENSOR BASED ON CARBON NANOTUBES

In addition to gas and smoke, light will also be produced when the fire happens. The flame has both radiation characteristics and chromaticity characteristics. The flame can radiate in the three parts of the spectrum, namely, ultraviolet, infrared and visible light. Ten percentage of the flame radiates in the ultraviolet light region, and the remaining 90% of the flame radiates in the infrared and visible light regions (Shekhar et al., 2012; Liu Y. et al., 2017; Gaur et al., 2019), most visible light areas are red and yellow caused by carbon in fire, so infrared and ultraviolet light are generally detected. According to research, CNTs react to radiation, which means that this response can be used to detect various radiation sources, such as those from flames.

Sensing Mechanism of Flame Sensor

The basic light response mechanism of general photodetectors is to convert the absorbed photons into electrical signals. The light response mechanisms include photoelectric effect, photoconductivity effect, optical gating effect and thermometric effect (Liu P. et al., 2020). CNTs infrared photodetectors are developed on the basis of thermal effect and optical effect. The sensing principle based on thermal effect is that the temperature change caused by light irradiation produces electrical signals (resistance, current or voltage). For the principle of optical effect, excitons are generated through the photon absorption of CNTs, and the electron hole pairs are generated by excitons. It is released by dissociation, thus producing photocurrent or photovoltage in the device (Avouris et al., 2008). **Figure 1B** is the schematic diagram of the CNT infrared detector (Saleh and Wasan, 2015). When ultraviolet light appears, oxygen molecules on the surface of CNTs are desorbed by the energy of photoinduced plasma polaritons, resulting in a significant decrease in hole concentration, which correspondingly increases the resistance of CNTs. The change of resistance of CNTs under ultraviolet light makes them able to be used for ultraviolet light monitoring (Pyo et al., 2018).

Research Status of Flame Sensors Based on Carbon Nanotubes

When a fire occurs, the radiation light produced by flame combustion includes ultraviolet light and infrared light. The flame sensor responds to the flame light immediately to judge whether the fire occurs. CNTs are promising materials for the fabrication of high-performance nanooptoelectronic devices due to their unique one-dimensional structure. In 2012, Shao et al. developed a kind of ultraviolet electric detector. The sensor uses CNTs film as coating material. The response of the detector to light frequency of 14 Hz and wavelength of 365 nm is about 0.123 A/W (Shao et al., 2012). In 2020, Pathak et al. prepared a kind of nanocomposite material based on CNTs and zinc oxide for ultraviolet sensor. The sensitivity of the device to ultraviolet light at 365 nm is 0.011 A/W (Pathak et al., 2020). In 2012, Zeng et al. designed a high-performance infrared detector based on SWCNT array, and its responsivity was 9.87×10^{-5} A/W (Zeng et al., 2012). In 2013, Lu et al. self-assembled a heterojunction at the graphene/MWCNT interface. This nanocomposite material made the detection rate of the infrared detector as high as 1.5×10^7 cm $Hz^{1/2}$ W^{-1} (Lu et al., 2013). In 2017, Huang et al. transferred the CNTs/SiO_2 structure to the PMMA substrate and designed an infrared detector that has the advantages of fast response speed and high sensitivity (Huang et al., 2017). In 2018, Pavelyev et al. proposed an infrared radiation photodetector based on MWCNT grown on silicon substrate by chemical vapor deposition. The response speed and resistance recovery time of the detector are 3 min and have obvious hysteresis characteristics (Pavelyev et al., 2018). The traditional flame sensor mainly uses ultraviolet detection and ultraviolet/infrared joint detection. In 2014, Mohanty et al. prepared MWCNTs by chemical vapor deposition method, and designed a functional flame sensor. The response characteristics and sensitivity of the sensor in the transverse and longitudinal direction of the flame were experimentally studied. It has a good working range, and this kind of flame sensor can also be used. Estimation of working distance from flame (Mohanty and Misra, 2014).

TEMPERATURE SENSOR BASED ON CARBON NANOTUBES

Temperature is one of the most obvious characteristics of a fire. When a fire occurs, a lot of heat is generated by material

combustion, which makes the surrounding temperature change. The temperature sensor responds to the change of the temperature in the environment immediately to achieve the purpose of fire warning. This section mainly summarizes the research status and sensing principle of temperature sensor based on CNTs.

Sensing Mechanism of Temperature Sensor

CNTs have the characteristics of low power consumption, high sensitivity, high stability, and wide operating temperature range, which can improve the performance of temperature sensors. The temperature measurement of the sensor is not directly expressed, but based on the characteristics of a series of physical phenomena, such as volume expansion, gas pressure change, magnetic susceptibility change, diode junction voltage and resistance exchange, thermocouple generation, and so on. CNTs based sensors use these physical phenomena to detect environmental temperature changes. For example, thermometers can be realized by measuring the thermal expansion of CNTs, because the height of one-dimensional column of continuous liquid in CNTs varies from 50 to 500°C. In addition, the temperature sensor based on CNTs can also measure the temperature of CNTs caused by thermal interaction. Temperature measurement is realized by changing the conductivity (Pan et al., 2017). **Figure 1C** shows the SEM image of a temperature sensor based on CNT (Monea et al., 2019).

Research Status of Temperature Sensors Based on Crabon Nanotubes

CNTs have become an important candidate material for temperature sensors because of their excellent electrical response to temperature changes. In 2011, Karimov et al. designed a thin-film temperature sensor. By depositing a layer of glue and CNTs powder on the paper substrate, the temperature measurement range of the sensor is 20–75°C, and its sensitivity reaches −0.24%/°C (Karimov et al., 2011). In 2013, Ali et al. synthesized the yttrium iron catalyst film on silicon substrate by wet chemical method, and prepared CNTs by chemical deposition method, and made it into a temperature sensor. Its temperature measurement range is 20–150°C, and the sensitivity is 4.21×10^{-4}/°C (Ali and Hafez, 2013). In 2015, Karimov et al. proposed a temperature sensor based on VO_2 (3-fL) and CNT composite film. The silver electrode was deposited on the glass substrate, and the VO_2 (3-fL) and CNTs composite film materials were wrapped on the top of the silver electrode. The temperature measurement range of the sensor was 25–80°C, and the sensitivity was −(0.9–1.3)% (Karimov et al., 2015). In 2017, Pan et al. successfully developed an ionization temperature sensor based on CNTs. The sensor has a temperature range of 20–100°C and a sensitivity of 4×10^{-2} (Pan et al., 2017). In 2017, Song et al. used chemical vapor deposition method to grow vertically aligned CNT arrays on SiO_2/Si substrates to prepare a temperature sensor with a temperature measurement range of 20–110°C and a sensitivity of 4.74 μA/°C (Song et al., 2017). The structure of the sensor is shown in **Figure 1D**. In the same year, Zuo et al. prepared a CNT-carbon fiber cement-based material, when 0.5% CNTs were added, the temperature measurement range was 30–60°C, and the sensitivity was 5.35×10^{-4}/°C (Zuo et al., 2017). In 2018, Sarma et al. studied the method of preparing high-efficiency thin-film temperature sensor using layered MWCNT. He prepared a thin-film temperature sensor on Si substrate by chemical vapor deposition of CNTs film with Ni as catalyst. The temperature measurement range of the sensor was 22–200°C, and the sensitivity was 1.03×10^{-3}/°C (Sarma and Lee, 2018).

DEVELOPMENT PROSPECT OF CARBON NANOTUBE FIRE DETECTION SENSOR

With the development of fire detection technology, novel sensing materials have always been an important research field of fire detection sensors, which have an extremely important impact on CO sensors, temperature sensors and flame sensors. The huge aspect ratio and specific surface area of CNTs make them become highly sensitive sensing material layer and efficient sensing channel, but the sensors based on CNTs are still in the primary stage, there are still some problems to be solved: 1) Further research on synthesis methods is needed to improve the uniformity of noble metals and semiconductor metal oxides on the wall of CNTs, so as to improve the response time and sensitivity of the sensor. 2) How to reduce the recovery time of the sensor to achieve the purpose of repeated use. 3) The sensing mechanism of the sensor is not clear, for example, whether the adsorption and desorption model of CO occurs on the surface of CNTs or metal oxides or on the interface between CNTs and metal oxides, so it is necessary to further study the sensor mechanism of the sensor. 4) Improving the sensor's anti-interference ability is of great significance to the improvement of sensor performance. In order to solve these problems, we should optimize the preparation process in the future, make metal oxides and other dopants more evenly distributed on the wall of CNTs; clarify the sensing mechanism of the sensor, explore the electrochemical reaction between CO gas molecules and which dopants, and use these dopants as the recognition layer of CNTs, which can greatly improve the selectivity of the sensor. Appropriate addition of CNTs, for example, metal oxides, inorganic metals, non-metallic elements, etc., can reduce the recovery time of the sensor. In the future, CNTs can be covered with materials that do not interact with interference sources to reduce interference and enhance the stability of the sensor.

CONCLUSION

In this paper, the fire detection sensors based on CNTs are reviewed. Firstly, the important role of sensors in the Internet of things is briefly described. The basic structure and preparation methods of CNTs are introduced. The three most commonly used fire detection sensors (CO sensor, temperature sensor and flame sensor) in the fire monitoring system of the Internet of things are analyzed. The current researches of the three kinds of sensors based on CNTs and CNT composites is briefly reviewed. Finally, the problems such as the uniform distribution of dopants, the

long recovery time and the unclear sensing mechanism of CNT sensors are prospected, improving the anti-interference ability of the sensor, which provide a favorable reference for the further application of CNTs fire detection sensors.

AUTHOR CONTRIBUTIONS

All authors listed have made a substantial, direct and intellectual contribution to the work, and approved it for publication.

FUNDING

This work was supported by the National Natural Science Foundation (51874255), Downhole Intelligent Measurement and Control Science and Technology Innovation Team of Southwest Petroleum University (2018CXTD04), the International Science and Technology Cooperation and Exchange Research Project of Sichuan Province (18GJHZ0195), and the International Science and Technology Cooperation Project of Chengdu (2020-GH02-00016-HZ).

REFERENCES

Ali, K., and Hafez, M. (2013). Growth and structure of carbon nanotubes based novel catalyst for ultrafast nano-temperature sensor application. *Superlattice. Microst.* 54, 1–6. doi:10.1016/j.spmi.2012.10.007

Avouris, P., Freitag, M., and Perebeinos, V. (2008). Carbon-nanotube photonics and optoelectronics. *Nat. Photonics* 2 (6), 341–350. doi:10.1038/nphoton.2008.94

Barcarolle, R., Orecchini, G., Alimenti, F., and Roselli, L. (2013). "Feasibility study of a fully organic, CNT based, harmonic RFID gas sensor," in IEEE international conference on RFID-technologies and applications, November 2012, Nice, France. doi:10.1109/RFID-TA.2012.6404559

Bogue, R. (2013). Sensors for fire detection. *Sens. Rev.* 33 (2), 99–103. doi:10.1108/02602281311299635

Cardenas, J. A., Andrews, J. B., Noyce, S. G., and Franklin, A. D. (2020). Carbon nanotube electronics for IoT sensors. *Nano Futures* 4, 012001. doi:10.1088/2399-1984/ab5f20

Chad, W. R., Bonifas, A. P., Behnaz, A., Zhang, Y. H., Yu, K. J., Cheng, H., et al. (2013). Ultrathin conformal devices for precise and continuous thermal characterization of human skin. *Nat. Mater.* 12 (10), 938–944. doi:10.1038/NMAT3755

Chen, K., Gao, W., Emaminejad, S., Kiriya, D., Ota, H., Nyein, H. Y. Y., et al. (2016). Printed carbon nanotube electronics and sensor systems. *Adv. Mater.* 28 (22), 4397–4414. doi:10.1002/adma.201504958

Choi, S.-W., Kim, J., Lee, J.-H., and Byun, Y. T. (2016). Remarkable improvement of CO-sensing performances in single-walled carbon nanotubes due to modification of the conducting channel by functionalization of Au nanoparticles. *Sensor. Actuator. B Chem.* 232, 625–632. doi:10.1016/j.snb.2016.04.035

Ding, C.-J., Zhao, Z.-Y., Xue-hong, Z. H. U., and Yu-bo, F. E. N. G. (2018). Application of neural network in intelligent fire alarm system. *Transducer Microsyst. Technol.* 37 (1), 154–156. doi:10.13873/J.1000-9787(2018)01-0154-03

Fonollosa, J., Solórzano, A., and Marco, S. (2018). Chemical sensor systems and associated algorithms for fire detection: a review. *Sensors* 18 (2), 553. doi:10.3390/s18020553

Gaur, A., Singh, A., Kumar, A., Kulkarni, K. S., Lala, S., Kapoor, K., et al. (2019). Fire sensing technologies: a review. *IEEE Sens. J.* 19, 3191–3202. doi:10.1109/JSEN.2019.2894665

Ge, L., Mu, X., Tian, G., Huang, Q., Ahmed, J., and Hu, Z. (2019). Current applications of gas sensor based on 2-D nanomaterial: a mini review. *Front. Chem.* 7, 839. doi:10.3389/fchem.2019.00839

Guo, T., Nikolaev, P., Rinzler, A. G., Tomanek, D., Colbert, D. T., and Smalley, R. E. (1995). Self-assembly of tubular fullerenes. *J. Phys. Chem.* 99 (27), 10694–10697. doi:10.1021/j100027a002

Han, M., Kim, J.-K., Lee, G. S., Kang, S.-W., and Jung, D. (2019). A CO gas sensor based on Pt-loaded carbon nanotube sheets. *Jpn. J. Appl. Phys.* 58 (SD), SDDE03.1–SDDE03.6. doi:10.7567/1347-4065/ab0497

Hu, Q., Liu, S., and Lian, Y. (2014). Sensors for carbon monoxide based on Pd/SnO_2/CNT nanocomposites. *Phys. Status Solidi A* 211 (12), 2729–2734. doi:10.1002/pssa.201431392

Huang, Z., Gao, M., Pan, T., Wei, X., Chen, C., and Lin, Y. (2017). Interface engineered carbon nanotubes with SiO_2 for flexible infrared detectors. *Appl. Surf. Sci.* 413, 308–316. doi:10.1016/j.apsusc.2017.04.059

Iijima, S. (1991). Helical microtubules of graphitic carbon. *Nature* 354, 56–58. doi:10.1038/354056a0

Iqbal, M., Yuliarto, B., and Nugraha, N. (2013). Modifications of multi-walled carbon nanotubes on zinc oxide nanostructures for carbon monoxide (CO) gas sensitive layer. *Adv. Mater. Res.* 789, 12–15. doi:10.4028/www.scientific.net/AMR.789.12

Jose-Yacaman, M., Miki-Yoshida, M., Rendon, L., and Santiesteban, J. G. (1993). Catalytic growth of carbon microtubules with fullerene structure. *Appl. Phys. Lett.* 62 (6), 202–204. doi:10.1063/1.109315

Karimov, K. S., Chani, M. T. S., and Khalid, F. A. (2011). Carbon nanotubes film based temperature sensors. *Phys. E Low Dimens. Syst. Nanostruct.* 43 (9), 1701–1703. doi:10.1016/j.physe.2011.05.025

Karimov, K. S., Mahroof-Tahir, M., Saleem, M., Chani, M. T. S., and Niaz, A. K. (2015). Temperature sensor based on composite film of vanadium complex (VO2(3-fl)) and CNT. *J. Semicond.* 36 (07), 073004. doi:10.1088/1674-4926/36/7/073004

Kong, J., Franklin, N. R., Zhou, C., Chapline, M. G., Peng, S., Cho, K., et al. (2000). Nanotube molecular wires as chemical sensors. *Science* 287, 622–625. doi:10.1126/science.287.5453.622

Kwangjae, L., Young-Seok, S., Young, S., Soo, H., Youn-Sung, L., and Chong-Yun, K. (2017). Highly sensitive sensors based on metal-oxide nanocolumns for fire detection. *Sensors* 17 (2), 303. doi:10.3390/s17020303

Leghrib, R., Pavelko, R., Felten, A., Vasiliev, A., Cané, C., Gràcia, I., et al. (2010). Gas sensors based on multiwall carbon nanotubes decorated with tin oxide nanoclusters. *Sensor. Actuator. B Chem.* 145 (1), 411–416. doi:10.1016/j.snb.2009.12.044

Liu, P., Yang, S.-E., Chen, Y., Ma, Y., Liu, S., Fang, X., et al. (2020). Carbon nanotube-based heterostructures for high-performance photodetectors: recent progress and future prospects. *Ceram. Int.* 46, 19655–19663. doi:10.1016/j.ceramint.2020.05.067

Liu, Y., Pang, L. X., Liang, J., Cheng, M. K., Liang, J. J., Junshu, C., et al. (2017). A compact solid-state UV flame sensing system based on wide-gap ii–vi thin film materials. *IEEE Trans. Ind. Electron.* 65, 2737. doi:10.1109/TIE.2017.2740842

Loghin, F., Aniello, F., Andreas, A., Salmeron, J. F., Markus, B., Paolo, L., et al. (2018). A handwriting method for low-cost gas sensors. *ACS Appl. Mater. Interfaces* 10 (40), 34683–34689. doi:10.1021/acsami.8b08050

Lu, R., Christianson, C., Weintrub, B., and Wu, J. Z. (2013). High photoresponse in hybrid graphene-carbon nanotube infrared detectors. *ACS Appl. Mater. Interfaces* 5 (22), 11703–11707. doi:10.1021/am4033313

Marinov, V. R. (2015). Embedded flexible hybrid electronics for the internet of things. *Int. Symp. Microelectron.* 2015, 000006–000013. doi:10.4071/isom-2015-TP12

Mittal, M., and Kumar, A. (2014). Carbon nanotube (CNT) gas sensors for emissions from fossil fuel burning. *Sensor. Actuator. B Chem.* 203, 349–362. doi:10.1016/j.snb.2014.05.080

Mohantry, S., and Misra, A. (2014). Carbon nanotube based multifunctional flame sensor. *Sensor. Actuator. B Chem.* 192, 594–600. doi:10.1016/j.snb.2013.11.019

Monea, B. F., Ionete, E. I., Spiridon, S. I., Ion-Ebrasu, D., and Petre, E. (2019). Carbon nanotubes and carbon nanotube structures used for temperature measurement. *Sensors* 19 (11), 2464. doi:10.3390/s19112464

Pan, Z., Zhang, Y., Cheng, Z., Tong, J., Chen, Q., Zhang, J., et al. (2017). Sensing properties of a novel temperature sensor based on field assisted thermal emission. *Sensors* 17, 473. doi:10.3390/s17030473

Pathak, P., Park, S., and Cho, H. J. (2020). A carbon nanotube-metal oxide hybrid material for visible-Blind flexible UV-sensor. *Micromachines (Basel)* 11 (3), 368. doi:10.3390/mi11040368

Pavelyev, V. S., Tripathi, N., Mishra, P., Mezhenin, A. V., Kurenkova, Y. G., and Sovetkina, M. A. (2018). CNT-based IR-sensor. *J. Phys. Conf. Ser.* 1096, 012127. doi:10.1088/1742-6596/1096/1/012127

Pearce, E. R. (2009). Carbon nanotubes as fire gas sensors. PhD thesis. London, UK: Imperial College London. doi:10.25560/5551

Pyo, S., Choi, J., and Kim, J. (2018). A fully transparent, flexible, sensitive, and visible-blind ultraviolet sensor based on carbon nanotube-graphene hybrid. *Adv. Electron. Mater.* 5, 1800737. doi:10.1002/aelm.201800737

Roy, A., Ray, A., Sadhukhan, P., Naskar, K., Lal, G., Bhar, R., et al. (2018). Polyaniline-multiwalled carbon nanotube (PANI-MWCNT): room temperature resistive carbon monoxide (CO) sensor. *Synthetic Metals* 245, 182–189. doi:10.1016/j.synthmet.2018.08.024

Saleh, W. R., and Wasan, R. (2015). A carbon nanotubes photoconductive detector for middle and far infrared regions based on porous silicon and a polyamide nylon polymer. *Eur. Phys. J. Appl. Phys.* 70 (3), 30401. doi:10.1051/epjap/2015150121

Sarma, S., and Lee, J. (2018). Developing efficient thin film temperature sensors utilizing layered carbon nanotube films. *Sensors* 18 (10), 3182. doi:10.3390/s18103182

Sayago, I., Santos, H., Horillo, M. C., Aleixandre, M., Fernandez, M. J., Terrado, E., et al. (2008). Carbon nanotube networks as gas sensors for NO_2 detection. *Talanta* 77, 758–764. doi:10.1016/j.talanta.2008.07.025

Shao, X., Ma, X., Yu, Y., and Fang, J. (2012). The study of carbon nanotubes as coating films for electrically calibrated detectors. *Meas. Sci. Technol.* 23 (2), 025106. doi:10.1088/0957-0233/23/2/025106

Sharma, S., Hussain, S., Singh, S., and Islam, S. S. (2014). MWCNT-Conducting polymer composite based ammonia gas sensors: a new approach for complete recovery process. *Sensor. Actuator. B Chem.* 194, 213–219. doi:10.1016/j.snb.2013.12.050

Shekhar, H., Kumar, S. J., and Rajawat, P. S. (2012). Multi infrared (IR) flame detector for tangential fired boiler. *Mobile Commun. Power Eng.* 296, 545–548. doi:10.1007/978-3-642-35864-7_84

Shekhar, H., Kumar, S. J., and Rajawat, P. S. (2013). "Multi infrared (IR) flame detector for tangential fired boiler," in AIM: International conference on advances in information technology and mobile communication 2012, Bangalore, India, April 27–28, 2009. Editors V. V. Das and Y. Chaba (Berlin and Heidelberg, Germany: Springer), 545–548.

Snow, E. S. (2005). Chemical detection with a single-walled carbon nanotube capacitor. *Science* 307 (5717), 1942–1945. doi:10.1126/science.1109128

Song, H., Zhang, Y., and Cao, J. (2017). Sensing mechanism of an ionization as temperature sensor based on a carbon nanotube film. *RSC Adv.* 7 (84), 53265–53269. doi:10.1039/C7RA09551A

Sundmaeker, H., Guillemin, P., Fries, P., and Woelfflé, S. (2010). *Vision and challenges for realising the internet of things*. Europe: CERP-IoT. doi:10.2759/26127

Takei, K., Yu, Z., Zheng, M., Ota, H., Takahashi, T., and Javey, A. (2014). Highly sensitive electronic whiskers based on patterned carbon nanotube and silver nanoparticle composite films. *Proc. Natl. Acad. Sci. U.S.A.* 111 (5), 1703–1707. doi:10.1073/pnas.1317920111

Tang, W. (2019). Research progress of flexible gas sensors based on carbon nanomaterials. *Bull. Chin. Ceram. Soc.* 038 (002), 398–409. doi:CNKI: SUN: GSYT.0.2019-02-01

Wang, J., Yang, Y., Jiao, C., Liang, Y., and Zhang, W. (2018). Research progress of carbon nanotubes in the application of gas sensors. *Micronanoelectron. Technol.* 55, 239–246. doi:10.13250/j.cnki.wndz.2018.04.003

Wasisto, H. S., Steib, F., Merzsch, S., Waag, A., and Peiner, E. (2014). Vertical silicon nanowire array-patterned microcantilever resonators for enhanced detection of cigarette smoke aerosols. *Micro Nano Lett.* 9 (10), 676–679. doi:10.1049/mnl.2014.0249

Webb, R. C., Bonifas, A. P., Behnaz, A., Zhang, Y., Yu, K. J., Cheng, H., et al. (2013). Ultrathin conformal devices for precise and continuous thermal characterization of human skin. *Nat. Mater.* 12 (10), 938–944. doi:10.1038/NMAT3755

Wu, R.-J., Wu, J.-G., Yu, M.-R., Tsai, T.-K., and Yeh, C.-T. (2008). Promotive effect of CNT on Co_3O_4–SnO_2 in a semiconductor-type CO sensor working at room temperature. *Sensor. Actuator. B Chem.* 131 (1), 306–312. doi:10.1016/j.snb.2007.11.033

Xue, G., Ren-Cheng, Z., Xiang-Ying, H., and Xiao-Hua, Z. (2005). Current research and development trends of gas fire detector. *Fire Sci. Tech.*, 735–737. doi:CNKI: SUN: XFKJ.0.2005-06-025.

Yuan, Y., Liu, Z., and Li, X. (2004). Improving SWNT gas sensors by doping atoms. *Opt. Mater. Express* 000 (010), 7–9. doi:10.3969/j.issn.1002-1841.2004.10.003

Zeng, Q., Wang, S., Yang, L., Wang, Y., Pei, T., Zhang, Z., et al. (2012). Carbon nanotube arrays based high-performance infrared photodetector [invited]. *Opt. Mater. Express* 2 (6), 839–848. doi:10.1364/OME.2.000839

Zhang, L., Meng, F., Chen, Y., Liu, J., Sun, Y., Luo, T., et al. (2009). A novel ammonia sensor based on high density, small diameter polypyrrole nanowire arrays. *Sensor. Actuator. B Chem.* 142 (1), 204–209. doi:10.1016/j.snb.2009.07.042

Zhang, X.-q., Wang, Y.-y., Zhang, K., and He, D.-n. (2013). Research progress of gas sensors based on nanometer materials. *Transducer Microsyst. Technol.* 32 (5), 1–5, 8. doi:10.3969/j.issn.1000-9787.2013.05.001

Zhu, Z. (2011). Summary of carbon nanotube gas sensor. *Sci. Technol. Inf.* 000 (022), 119–121. doi:10.3969/j.issn.1001-9960.2011.22.106

Zuo, J., Zhou, H., Yao, W., Wu, D., Liu, X., and Zhang, Y. (2017). Research on the sensing properties of CNT-CF/cement-based materials. *Mater. Rev.* (22), 125–129. doi:10.11896/j.issn.1005-023X.2017.022.025

Conflict of Interest: The authors declare that the research was conducted in the absence of any commercial or financial relationships that could be construed as a potential conflict of interest.

frontiers in Materials

MINI REVIEW
published: 06 November 2020
doi: 10.3389/fmats.2020.580245

Morphological Characteristics of Molybdenum Disulfide and Current Application on Detecting SF_6 Decomposing Products

Guochao Qian, Qingjun Peng, Haozhou Wang, Shan Wang and Weiju Dai*

Electric Power Science Research Institute of Yunnan Power Grid Co., Ltd., Kunming, China

MoS_2 has been considered a potential novel material in various fields due to its large specific surface area, high carrier mobility, and tunable electronic properties. However, with the increasing demand for sensor substrates, different strategies have been made to achieve its high performance, usually by adopting the method of controlling the microstructure. SF_6 gas-insulated electrical equipment has gained considerable attention in electric systems with the advantages of small volume, high security, strong breaking performance, and high-pressure fracture tolerance. Nevertheless, in the process of equipment operation, the SF_6 gas will occur inevitably decompose due to partial discharge, resulting in the deterioration of the insulation performance of the equipment. Therefore, detecting SF_6 decomposition products is significant for the safe and stable operation of power systems. In this mini review, we start from the synthesis of various MoS_2 morphological structures. Then, the beneficial characteristics of the unique synthesized nanostructures at present are analyzed. Besides, we focus on the gas-sensing mechanisms and applications of MoS_2-based sensors for detecting SF_6 decomposition products. Finally, the future development in this field is proposed.

Keywords: molybdenum disulfide, morphological characteristics, SF_6 decomposing products, sensing application, gas insulated switchgear

OPEN ACCESS

Edited by:
Wen Zeng,
Chongqing University, China

Reviewed by:
Yanqiong Li,
Chongqing University of Arts and Sciences, China
Jianbo Yin,
Northwestern Polytechnical University, China

****Correspondence:***
Guochao Qian
164688847@qq.com

Specialty section:
This article was submitted to Smart Materials, a section of the journal Frontiers in Materials

Received: *05 July 2020*
Accepted: *02 September 2020*
Published: *06 November 2020*

Citation:
Qian G, Peng Q, Wang H, Wang S and Dai W (2020) Morphological Characteristics of Molybdenum Disulfide and Current Application on Detecting SF_6 Decomposing Products. Front. Mater. 7:580245. doi: 10.3389/fmats.2020.580245

INTRODUCTION

Sulfur hexafluoride (SF_6) is a non-color, tasteless, and non-flammable insulating gas, which is widely known for applications in gas insulated switchgear (GIS) (Lu et al., 2018; Lu et al., 2019). Although GIS has advantage of high stability, insulation faults such as partial discharge, breakdown discharge, and spark discharge inevitably occur during a long running process (Zeng et al., 2015; Liu et al., 2017), which will lead to the decomposition of the SF_6 gas into various sulfur fluorides, including H_2S, SO_2, SO_2F_2, and SOF_2 etc. (Wei et al., 2020). Previous research has indicated that these characteristic gases can accelerate the corrosion rate of facilities and increase the probability of system paralysis (Zhang X. X. et al., 2017a; Zhou et al., 2018b). Therefore, it is of great necessity to evaluate the operational status of GIS equipment by effectively detecting these typically decomposed products of SF_6 (Zhang X. X. et al., 2017b; Zhou et al., 2018d). In this respect, bidimensional nanomaterials have captured widespread attention for its multiple physical and chemical properties in the detection of SF_6 decomposed gas (Zhou et al., 2018a; Chen et al., 2018).

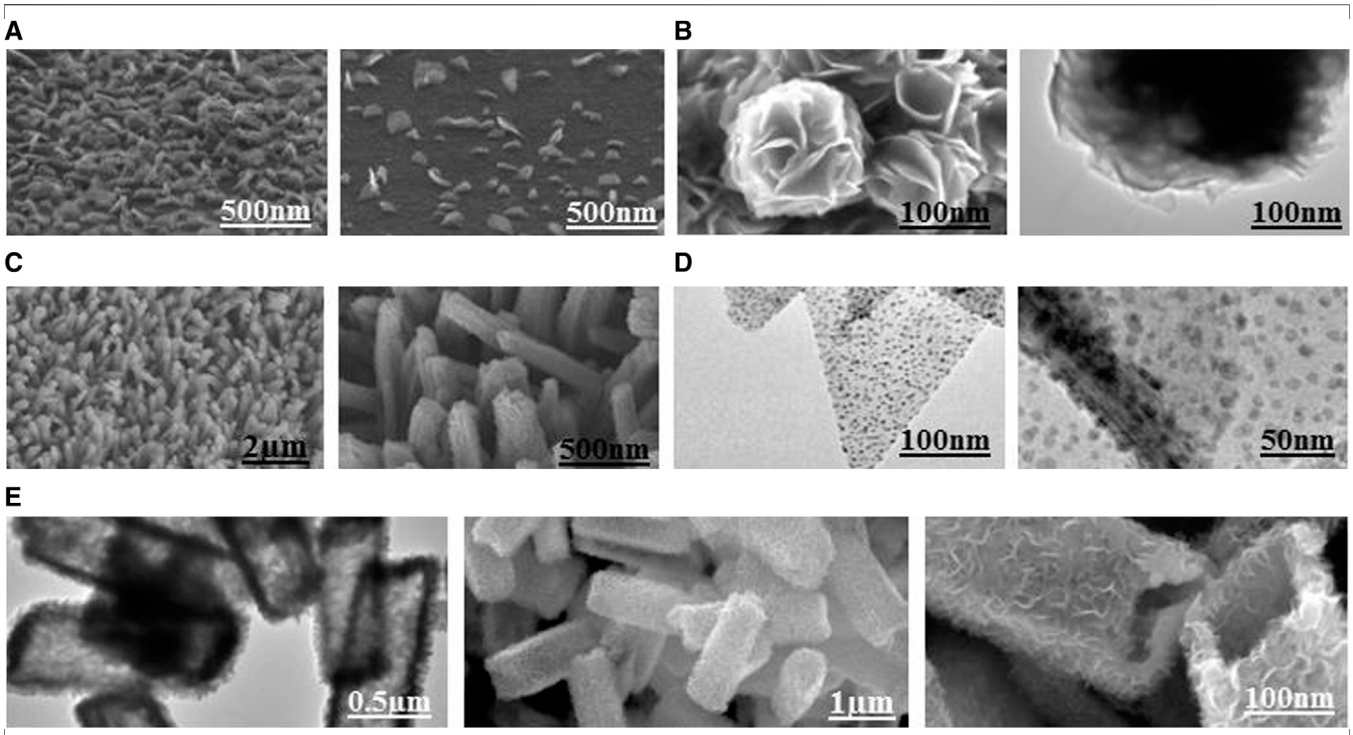

FIGURE 1 | MoS_2 with different hierarchical structures: **(A)** Vertical nanoflakes. Reprinted with permission from Kang et al. (2017). Copyright (2017) American Chemical Society. **(B)** Flower-like spheres. Reprinted with permission from Tu et al. (2019). Copyright (2019) American Chemical Society. **(C)** Nanorods. Reprinted with permission from Sun et al. (2018). Copyright (2018) American Chemical Society. **(D)** Porous film. Reprinted with permission from Li et al. (2019). Copyright (2019) American Chemical Society. **(E)** Porous hollow rhomboids. Reprinted with permission from Han et al. (2020). Copyright (2020) American Chemical Society.

Given this, various 2-D nanomaterials such as carbon nanotube (CNT), graphene, and molybdenum disulfide (MoS_2) have been synthesized by different methods (Zhou et al., 2018e; Choi et al., 2020). As an n-type semiconductor material with wide band gap, MoS_2 receives the most interest because of its high surface activity and chemical stability (Fan et al., 2017; Zhang et al., 2019). Up to now, a large number of studies have been carried out on the various nanostructures of MoS_2, including nanoflakes (Johari et al., 2020), nanotubes (Zhong et al., 2020), nanospheres (Li Y. X. et al., 2019) and other complex hierarchical nanostructures (Zhang et al., 2018b; Agrawal et al., 2020), to realize more effective methods of detecting SF_6 decomposed products. Besides, the evident correlation has been confirmed between unique structures and performances (Barzegar et al., 2019; Wang et al., 2020). Therefore, the morphology synthesis and analysis of MoS_2 nanostructures are of great significant to discuss. This mini review summarizes the morphological features and sensing applications of MoS_2, especially for detecting SF_6 decomposed products.

Morphology and analysis of MoS_2

MoS_2 is deemed as a viable and effective material owing to its stable semiconducting property and high thermal stability (Sahoo et al., 2016; Sangeetha and Madhan, 2020). Until now, the diverse morphology of MoS_2 nanostructures have been designed by investigators through various methods to achieve excellent sensing properties in the aspects of chemical, optical, and gas sensors (Zhang et al., 2018a; Bhakhar et al., 2019). Kang et al. demonstrated vertical MoS_2 nanoflakes (shown in **Figure 1A**) fabricated on SiO_2/Si substrates by the deposition and thermal evaporation. They found the vertical flakes supplied an effective surface area and sufficient oxygen vacancies for the adsorption of NO_2 gas. The minimum concentration of the NO_2 detection was 0.15 ppm at room temperature (Kang et al., 2017). Tu et al. synthesized hierarchical MoS_2 spheres with flower-like structures (shown in **Figure 1B**) presented efficient aluminum storage properties. These flower-like microstructures for aluminum storage possessed open and well-defined hierarchical structures, leading to a higher specific capacity and prominent cycling stability. The as-prepared MoS_2 electrodes delivered reversible capacities of 112.2 mAh g^{-1} at 153.6 mAh g^{-1} after 100 cycles (Tu et al., 2019).

Sun et al. developed MoS_2 nanorods (shown in **Figure 1C**) by the hydrothermal and ammonia annealing approach and found that the fabricated nanorods exhibited excellent catalytic performances due to a more specific surface area and a sufficient ion transportation channel (Sun et al., 2018). Li et al. fabricated a three-dimensional porous MoS_2 film of surface-grown Pt nanocrystals (shown in **Figure 1D**) via the CVD-TA method, and found that higher Pt loading yields improved the performances of the hydrogen evolution reaction with a smaller specific surface area. Besides, these special porous constructions could effectively solve the stacking and agglomeration problems owing to the electrochemical reaction,

guarding remarkable cycling stability (Li et al., 2019). Han et al. reported electrode material performance of hierarchically porous MoS_2-Carbon hollow rhomboids (shown in **Figure 1E**) prepared by a self-templated solvothermal reaction. The as-prepared electrodes delivered reversible capacities of 506 mAh g^{-1} at 0.1 A g^{-1} after 3,000 cycles. The authors ascribed the excellent storage energy properties of MoS_2-C rhomboids structures to the distinct internal void structure (Han et al., 2020).

MoS_2 SENSOR FOR SF_6 DECOMPOSING PRODUCTS

Theoretical calculations about MoS_2-based sensors

In order to analyze and investigate the adsorption process between SF_6 decomposed gases and MoS_2-based material, corresponding adsorbing factors containing total adsorption energies (E_{ads}), the value of charge transfer (Q_t), and projected or total density of state can be attained (Azofra et al., 2017). The calculation formula is as follows:

$$E_{ads} = E_{MoS_2/gas\ molecule} - E_{MoS_2} - E_{gas\ molecule} \quad (1)$$

$E_{MoS_2/gas\ molecule}$ is the systemic energy after reaction, $E_{gas\ molecule}$ and E_{MoS_2}, signify the energy of gas molecule and the full energies of the MoS_2 before the reaction, respectively (Wang et al., 2019c). The negative value of E_{ad} illustrates the exothermic procedure of gas adsorption and the spontaneity of reaction. Moreover, the charge transfer Q_t before and after the gas molecule adsorbed on the MoS_2 system is defined by **Eq. 2**:

$$Q_t = Q_a - Q_b \quad (2)$$

where Q_a and Q_b present the number of charge after adsorption carried by the gas and the net carried charge of isolated gas molecules, respectively (Zhao et al., 2016; Wang et al., 2019b). The negative value of Q_t presents the electrons transfer from the MoS_2-based system to gas molecules.

The adsorption procedures between gas sensing materials and SF_6 decomposing products were studied based on the density functional theory (DFT) (Singh et al., 2018; Cui et al., 2019). For instance, Abbasi et al. studied the adsorptions properties of SO_2 molecules on MoS_2 monolayers in the aspects of charge transfer, band structures, adsorption energy, and charge density differences. They found that SO_2 gas molecules were adsorbed on the surface monolayer by physisorption. The S-O bonds of the adsorption gas molecules were lengthened after the adsorbed process. Furthermore, elongation of the bond lengths was mainly owed to the transfer of charge density from the original to the new bonds between the MoS_2 monolayers and target gas molecules, and the adsorption of SO_2 changed the electronic properties of MoS_2 monolayer (Abbasi and Sardroodi 2019). Chen et al. theoretically discussed the adsorption behavior of five types of SF_6 decomposing products (H_2S, HF, SO_2, SOF_2, and SO_2F_2) on the MoS_2 monolayer by employing the NEGF combined with DFT method. Among the five types of gas molecules, MoS_2 monolayer had the best adsorption performance for SO_2 caused by the special electronegativity (Chen et al., 2019a).

TABLE 1 | Comparison of adsorption parameters for H_2S and SO_2 in different systems.

SF_6 Decomposing products	System	E_{ad} (eV)	Q_t (e)	References
H_2S	MoS_2	−0.22	0.02	Chen et al., 2019a
	Si-MoS_2	−0.68	0.16	Gui et al., 2019
	Ni-MoS_2	−1.319	0.254	Wei et al., 2018
	Pt-MoS_2	−1.465	0.302	Qian et al., 2019
SO_2	MoS_2	−0.30	−0.04	Chen et al., 2019a
	Ni-MoS_2	−1.382	−0.016	Wei et al., 2018
	Pt-MoS_2	−1.584	0.036	Qian et al., 2019
	Al-MoS_2	−2.33	−3.43	Zhang et al., 2018

In another instance, Qian et al. researched the adsorption property of H_2S and SO_2 on the Pt-decorated MoS_2 and found that Pt-MoS_2 showed a strong interaction with gas molecules due to the strong chemical activity of with Pt atom. The adsorption energy of H_2S and SO_2 molecules adsorbed on Pt-MoS_2 was −1.465 and −1.584 eV, respectively, suggesting the occurrence of strong chemisorption in the contact surfaces. The charge transfer amount between H_2S and Pt-MoS_2 was up to 0.302 e, which is much higher than that of SO_2 (0.036 e). The results indicated that Pt-MoS_2 exhibited an excellent adsorption property for H_2S gas (Qian et al., 2019). Wei et al. reported the response behavior of Ni-MoS_2 towards SF_6 typical decomposition products: SO_2 and H_2S. The different adsorption sites for the SO_2 and H_2S on Ni-MoS_2 surface were designed to find the site of optimal adsorption energy. The result of SO_2 and H_2S was −1.382 and −1.319 eV, respectively, indicating the strong chemical interaction between the Ni-doped MoS_2 monolayer and two kinds of gases (Wei et al., 2018). Gui et al. reported that Si-doped MoS_2 were used to investigate its adsorptive properties to H_2S and SOF_2, and found that the most stable doping site were above the S atom. The adsorption energy was −0.68 eV when H_2S adsorbed on Si-MoS_2, while pristine MoS_2 was only −0.17 eV. The adsorption energy of SOF_2 adsorbed on Si-MoS_2 reached −3.63 eV, which was much higher than the −0.01 eV of the pristine MoS_2 adsorption system. The results provided that the adsorption capacities of pristine MoS_2 for H_2S and SOF_2 gases could be greatly improved by doping them with a nonmetallic atom (Gui et al. 2019). Li et al. selected the Pd atom as the dopant to modify the surface of the MoS_2 monolayer in the latest study, and an adsorbent with higher properties for the adsorption of SOF_2 and SO_2F_2 gases was obtained on this basis. In addition, the double gas molecules could still be stably adsorbed on the surface of Pd-MoS_2, indicating the feasibility of the adsorbent (Li et al. 2020).

In the above, the adsorption of H_2S and SO_2 molecules in different systems have been discussed in detail. The simulation results of H_2S and SO_2 molecules adsorption are in **Table 1**. These values may be obtained by different DFT functions. Compared with the adsorption construction of a pristine MoS_2 system, the introduction of novel elements promotes the surface chemical activity of the MoS_2 system. In addition, the addition of dopants enhances the affect of orbital hybridization between the MoS_2 monolayer and gas molecules, and facilitates the electronic transfer. The

adsorption capacity of the modified materials to the goal gas will be further improved, when the dopant is suitable (Zhang et al., 2017a).

Experimental analysis about MoS_2-based sensors

At present, there are few experimental studies on the detection of SF_6 decomposed byproducts, the few that do mainly focus on the H_2S, SO_2, and CO gases (Wang et al., 2019a; Zhou et al., 2019). Park et al. prepared a MoS_2 gas sensor modified with Pt nanoparticles with a low detection limit and high sensitivity for H_2S gas. The Pt-MoS_2-based sensor reduced the minimum detection concentration of H_2S gas to 5 ppm, which was much lower than that of the pure MoS_2 sensor (30 ppm) (Park et al., 2018). The Pt-MoS_2 film structures were formed by the introduction of Pt nanoparticles with ultra-small diameters, which could distinctly improve the performance of sensors. The Ni-doped MoS_2 nanoflower synthesized by Zhang et al. displayed a faster and higher response to 5 ppm SO_2 gas (Ra/Rg = 14.75) at room temperature. The main reason was that the richer porosity in the nanoflower structures provided sufficient adsorption sites for SO_2 gas (Zhang et al., 2017b). Hierarchical MoS_2 nanospheres assembled from nanosheets fabricated by Zhou et al. exhibited high properties to CO. The response value of the gas sensor to 500 ppm CO reached 92.6 at 230°C. Besides, this sensor had almost no response to other gases when the operation temperature was higher than 200°C, indicating the outstanding selectivity toward CO gas (Zhou et al., 2018c). The experimental results show that these unique nanostructures can enhance the gas-sensing performance, which is attributed to the increase of oxygen vacancies and the promotion of gas adsorption-desorption efficiency. Although some advancements have been made in the detection of SF_6 decomposed products, more high-accuracy experiments are needed for other decomposition gases such as SOF_2 and SO_2F_2.

Gas sensing mechanism

The gas sensing mechanism of the MoS_2-based sensors to SF_6 decomposed products can be explained by the change of conductivity caused by the interaction between oxyanions (mainly O^-) on the material surface and target gas molecules. Firstly, the oxygen molecules in air will adsorb on the surface of semiconductor materials and capture electrons from the adsorption sites to form oxyanions. The formation of an electron depletion layer and the increase of resistance are caused by oxygen adsorption. Then, when sensors are placed in an environment of reductive gas, the test gas molecules react with oxyanions to release the electrons back to the surface of the material, resulting in the decrease of the electron depletion layer and the occurrence of conductivity change. The relevant reactions are depicted as follows (take H_2S gas as an example):

$$O_{2\,(g)} \rightarrow O_{2\,(ads)} \tag{3}$$

$$O_{2\,(ads)} + 2e^- \rightarrow 2O^-_{(ads)} \tag{4}$$

$$H_2S_{\,(g)} \rightarrow H_2s_{\,(ads)} \tag{5}$$

$$H_2s_{\,(ads)} + 3O^- \rightarrow SO_2 + H_2O + 3e^- \tag{6}$$

CONCLUSION

In this paper, we focused on the morphological characteristics and application of MoS_2 materials for the detection of SF_6 decomposed products in GIS. Firstly, partial reports of sensing properties of MoS_2 with various morphologies were concluded. Diverse MoS_2 structures presented relatively different sensing properties at specific operating temperatures, so it was possible to promote sensing performances of MoS_2 by simple surface morphology modification. With the increasing demand for sensor materials, simples and more convenient synthetic routes and more favorable morphology structures should be proposed. Next, it was shown that the selectivity and sensitivity of MoS_2 gas sensors could also be enhanced by the enlargement of the active surface area and the introduction of metal or non-metal elements based on formerly theoretical and experimental investigations. Then, the gas-sensing mechanism of the MoS_2 based sensors to SF_6 decomposed products was described by comparing the characteristics of material substrate and gas molecules. Although some developments have been obtained in theoretical research into SF_6 decomposed products, a large number of fundamental experiments are needed to further prepare MoS_2 sensors for practical industrial applications.

DATA AVAILABILITY STATEMENT

The raw data supporting the conclusions of this article will be made available by the authors, without undue reservation, to any qualified researcher.

AUTHOR CONTRIBUTIONS

All authors listed have made a substantial, direct, and intellectual contribution to the work, and approved it for publication.

REFERENCES

Abbasi, A., and Sardroodi, J. J. (2019). Adsorption of O_3, SO_2 and SO_3 gas molecules on MoS_2 monolayers: a computational investigation. *Appl. Surf. Sci.* 469, 781–791. doi:10.1016/j.apsusc.2018.11.039.

Agrawal, A. V., Kumar, R., Yang, G., Bao, J. M., Kumar, M., and Kumar, M. (2020). Enhanced adsorption sites in monolayer MoS_2 pyramid structures for highly sensitive and fast hydrogen sensor. *Int. J. Hydrog. Energy* 45 (15), 9268–9277. doi:10.1016/j.ijhydene.2020.01.119.

Azofra, L. M., Sun, C. H., Cavallo, L., and MacFarlane, D. R. (2017). Feasibility of N_2 binding and reduction to ammonia on Fe-deposited MoS_2 2D sheets: a DFT study. *Chem. Eur. J.* 23 (24), 8275–8279. doi:10.1002/chem.201701113.

Barzegar, M., Zad, A. I., and Tiwari, A. (2019). On the performance of vertical MoS_2 nanoflakes as a gas sensorformance of vertical MoS_2 nanoflakes as a gas sensor. *Vacuum* 167, 90–97. doi:10.1016/j.vacuum.2019.05.033.

Bhakhar, S. A., Patel, N. F., Zankat, C. K., Tannarana, M., Solanki, G. K., Patel, K. D., et al. (2019). Sonochemical exfoliation and photodetection properties of MoS_2 nanosheets. *Mater. Sci. Semicond. Process.* 98, 13–18. doi:10.1016/j.mssp.2019.03.017.

Chen, D. C., Tang, J., Zhang, X. X., Li, Y., and Liu, H. J. (2019a). Detecting decompositions of sulfur hexafluoride using MoS_2 monolayer as gas sensor. *IEEE Sens. J.* 19, 39–46. doi:10.1109/JSEN.2018.2876637.

Chen, D. C., Zhang, X. X., Tang, J., Cui, H., and Li, Y. (2018). Noble metal (Pt or Au)-doped monolayer MoS_2 as a promising adsorbent and gas-sensing material to SO_2, SOF_2, and SO_2F_2: a DFT study. *Appl. Phys. A-Mater.* 124 (2), 194. doi:10.1007/s00339-018-1629-y.

Choi, G. J., Mishra, R. K., and Gwag, J. S. (2020). 2D layered MoS_2 based gas sensor for indoor pollutant formaldehyde gas sensing applications. *Mater. Lett.* 264, 127385. doi:10.1016/j.matlet.2020.127385.

Cui, H., Zhang, X. X., Zhang, G. Z., and Tang, J. (2019). Pd-doped MoS_2 monolayer: a promising candidate for DGA in transformer oil based on DFT method. *Appl. Surf. Sci.* 470, 1035–1042. doi:10.1016/j.apsusc.2018.11.230.

Fan, C., Liu, G. Z., Zhang, Y. H., and Wang, M. J. (2017). Synthesis and gas-responsive characteristics to methanol and isopropanol of bean-sprout-like MoS_2. *Mater. Lett.* 209, 8–10. doi:10.1016/j.matlet.2017.07.092.

Gui, Y. G., Liu, D. K., Li, X. D., Tang, C., and Zhou, Q. (2019). DFT-based study on H_2S and SOF_2 adsorption on Si-MoS2 monolayer. *Results Phys.* 13, 1–8. doi:10.1016/j.rinp.2019.102225.

Han, L. F., Wu, S. D., Hu, Z., Chen, M. Z., Ding, J. W., Wang, S. W., et al. (2020). Hierarchically porous MoS_2-carbon hollow rhomboids for superior performance of the anode of sodium-ion batteries. *ACS Appl. Mater. Interfaces* 12 (9), 10402–10409. doi:10.1021/acsami.9b21365.

Johari, M. H., Sirat, M. S., Mohamed, M. A., Nasir, S. N. F. M., Teridi, M. A. M., and Mohmad, A. R. (2020). Effects of Mo vapor concentration on the morphology of vertically standing MoS_2 nanoflakes. *Nanotechnology* 31 (30), 305710. doi:10.1088/1361-6528/ab8666.

Kang, M. A., Han, J. K., Cho, S. Y., Bu, S. D., Park, C. Y., Myung, S., et al. (2017). Strain-gradient effect in gas sensors based on three-dimensional hollow molybdenum disulfide nanoflakes. *ACS Appl. Mater. Interfaces* 9 (50), 43799–43806. doi:10.1021/acsami.7b14262.

Li, S., Lee, J. K., Zhou, S., Pasta, M., and Warner, J. H. (2019). Synthesis of surface grown Pt nanoparticles on edge-enriched MoS_2 porous thin films for enhancing electrochemical performance. *Chem. Mat.* 31 (2), 387–397. doi:10.1021/acs.chemmater.8b03540.

Li, T., Gui, Y. G., Zhao, W. H., Tang, C., and Dong, X. C. (2020). Palladium modified MoS_2 monolayer for adsorption and scavenging of SF_6 decomposition products: a DFT study. *Physica E* 123, 114178. doi:10.1016/j.physe.2020.114178.

Li, Y. X., Song, Z. X., Li, Y. N., Chen, S., Li, S., Li, Y. H., et al. (2019). Hierarchical hollow MoS_2 microspheres as materials for conductometric NO_2 gas sensors. *Sens. Actuators, B-Chem.* 282, 259–267. doi:10.1016/j.snb.2018.11.069.

Liu, H. C., Zhou, Q., Zhang, Q. Y., Hong, C. X., Xu, L. N., Jin, L. F., et al. (2017). Synthesis, characterization and enhanced sensing properties of a NiO/ZnO p-n junctions sensor for the SF_6 decomposition byproducts SO_2, SO_2F_2, and SOF_2. *Sensors* 17 (4), 913. doi:10.3390/s17040913.

Lu, Z. R., Zhou, Q., Wang, C. S., Wei, Z. J., Xu, L. N., and Gui, Y. G. (2018). Electrospun ZnO-SnO_2 composite nanofibers and enhanced sensing properties to SF_6 decomposition byproduct H_2S. *Front. Chem.* 6, 540. doi:10.3389/fchem.2018.00540.

Lu, Z. R., Zhou, Q., Wei, Z. J., Xu, L. N., Peng, S. D., and Zeng, W. (2019). Synthesis of hollow nanofibers and application on detecting SF_6 decomposing products. *Front. Mater.* 6, 183. doi:10.3389/fmats.2019.00183.

Park, J., Mun, J. H., Shin, J. S., and Kang, S. W. (2018). Highly sensitive two-dimensional MoS_2 gas sensor decorated with Pt nanoparticles. *R. Soc. Open Sci.* 5 (12), 181462. doi:10.1098/rsos.181462.

Qian, H., Lu, W. H., Wei, X. X., Chen, W., and Deng, J. (2019). H_2S and SO_2 adsorption on Pt-MoS_2 adsorbent for partial discharge elimination: a DFT study. *Results Phys.* 12, 107–112. doi:10.1016/j.rinp.2018.11.035.

Sahoo, M. P. K., Wang, J., Zhang, Y. J., Shimada, T., and Kitamura, T. (2016). Modulation of gas adsorption and magnetic properties of monolayer-MoS_2 by antisite defect and strain. *J. Phys. Chem. C.* 120 (26), 14113–14121. doi:10.1021/acs.jpcc.6b03284.

Sangeetha, M., and Madhan, D. (2020). Ultra sensitive molybdenum disulfide (MoS_2)/graphene based hybrid sensor for the detection of NO_2 and formaldehyde gases by fiber optic clad modified method. *Opt. Laser Technol.* 127, 106193. doi:10.1016/j.optlastec.2020.106193.

Singh, A. K., Kumar, P., Late, D. J., Kumar, A., Patel, S., and Singh, J. (2018). 2D layered transition metal dichalcogenides (MoS_2): synthesis, applications and theoretical aspects. *Appl. Mater. Today* 13, 242–270. doi:10.1016/j.apmt.2018.09.003.

Sun, T., Wang, J., Chi, X., Lin, Y. X., Chen, Z. X., Ling, X., et al. (2018). Engineering the electronic structure of MoS_2 nanorods by N and Mn dopants for ultra-efficient hydrogen production. *ACS Catal.* 8 (8), 7585–7592. doi:10.1021/acscatal.8b00783.

Tu, J. G., Xiao, X., Wang, M. Y., and Jiao, S. Q. (2019). Hierarchical flower-like MoS_2 microspheres and their efficient Al storage properties. *J. Phys. Chem. C.* 123 (44), 26794–26802. doi:10.1021/acs.jpcc.9b07509.

Wang, J. X., Zhou, Q., Lu, Z. R., Gui, Y. G., and Zeng, W. (2019b). Adsorption of H_2O molecule on TM (Au, Ag) doped-MoS_2 monolayer: a first-principles study. *Physica E* 113, 72–78. doi:10.1016/j.physe.2019.05.006.

Wang, J. X., Zhou, Q., Lu, Z. R., Wei, Z. J., and Zeng, W. (2019c). Gas sensing performances and mechanism at atomic level of Au-MoS_2 microspheres. *Appl. Surf. Sci.* 490, 124–136. doi:10.1016/j.apsusc.2019.06.075.

Wang, J. X., Zhou, Q., Xu, L. N., Gao, X., and Zeng, W. (2020). Gas sensing mechanism of dissolved gases in transformer oil on Ag-MoS_2 monolayer: a DFT study. *Physica E* 118, 113947. doi:10.1016/j.physe.2019.113947.

Wang, J. X., Zhou, Q., and Zeng, W. (2019a). Competitive adsorption of SF_6 decompositions on Ni-doped ZnO (100) surface: computational and experimental study. *Appl. Surf. Sci.* 479, 185–197. doi:10.1016/j.apsusc.2019.01.255.

Wei, H. L., Gui, Y. G., Kang, J., Wang, W. B., and Tang, C. (2018). A DFT study on the adsorption of H_2S and SO_2 on Ni doped MoS_2 monolayer. *Nanomaterials* 8 (9), 646. doi:10.3390/nano8090646.

Wei, Z. J., Zhou, Q., and Zeng, W. (2020). Hierarchical WO_3-NiO microflower for high sensitivity detection of SF_6 decomposition byproduct H_2S. *Nanotechnology* 31 (21), 215701. doi:10.1088/1361-6528/ab73bd.

Zeng, F., Ju, T., Zhang, X., Pan, J., Qiang, Y., and Hou, X. (2015). Influence regularity of trace H_2O on SF_6 decomposition characteristics under partial discharge of needle-plate electrode. *IEEE T. Dielect. El. In.* 22 (1), 287–295. doi:10.1109/TDEI.2014.004217.

Zhang, D. Z., Jiang, C. X., Li, P., and Sun, Y. (2017a). Layer-by-layer self-assembly of Co_3O_4 nanorod-decorated MoS_2 nanosheet-based nanocomposite toward high-performance ammonia detection. *ACS Appl. Mater. Inter. Interfaces* 9 (7), 6462–6471. doi:10.1021/acsami.6b15669.

Zhang, D. Z., Wu, J. F., Li, P., and Cao, Y. H. (2017b). Room temperature SO_2 gas-sensing properties based on a metal-doped MoS_2 nanoflower: an experimental and density functional theory investigation. *J. Mater. Chem. Am.* 5 (39), 20666–20677. doi:10.1039/c7ta07001b.

Zhang, R. Y., Fu, D., Ni, J. M., Sun, C. B., and Song, S. X. (2018). Adsorption for SO_2 gas molecules on B, N, P and Al doped MoS_2: the DFT study. *Chem. Phys. Lett.* 715, 273–277. doi:10.1016/j.cplett.2018.11.054.

Zhang, S., Zhang, W., Nguyen, T. H., Jian, J., and Yang, W. (2019). Synthesis of molybdenum diselenide nanosheets and its ethanol-sensing mechanism. *Mater. Chem. Phys.* 222, 139–146. doi:10.1016/j.matchemphys.2018.08.062.

Zhang, X. X., Chen, D., Cui, H., Dong, X., Xiao, S., and Tang, J. (2017a). Understanding of SF_6 decompositions adsorbed on cobalt-doped SWCNT: A DFT study. *Appl. Surf. Sci.* 420, 371–382. doi:10.1016/j.apsusc.2017.05.163.

Zhang, X. X., Cui, H., and Gui, Y. G. (2017b). Synthesis of graphene-based sensors and application on detecting SF_6 decomposing products: a review. *Sensors* 17 (2), 363. doi:10.3390/s17020363.

Zhang, Y. J., Zeng, W., and Li, Y. Q. (2018a). Hydrothermal synthesis and controlled growth of hierarchical 3D flower-like MoS_2 nanospheres assisted with CTAB and their NO_2 gas sensing properties. *Appl. Surf. Sci.* 455, 276–282. doi:10.1016/j.apsusc.2018.05.224.

Zhang, Y. J., Zeng, W., and Li, Y. Q. (2018b). The hydrothermal synthesis of 3D hierarchical porous MoS_2 microspheres assembled by nanosheets with excellent gas sensing properties. *J. Alloys Compd.* 749, 355–362. doi:10.1016/j.jallcom.2018.03.307.

Zhao, B., Li, C. Y., Liu, L. L., Zhou, B., Zhang, Q. K., Chen, Z. Q., et al. (2016). Adsorption of gas molecules on Cu impurities embedded monolayer MoS_2: a first-principles study. *Appl. Surf. Sci.* 382, 280–287. doi:10.1016/j.apsusc.2016.04.158.

Zhong, Y. L., Liu, D., Wang, L. T., Zhu, H. G., and Hong, G. (2020). Controllable synthesis of hierarchical MoS_2 nanotubes with ultra-uniform and superior storage potassium properties. *J. Colloid Interface Sci.* 561, 593–600. doi:10.1016/j.jcis.2019.11.034.

Zhou, Q., Chen, W. G., Li, J., Peng, S. D., Lu, Z. R., Yang, Z., et al. (2018b). Highly sensitive hydrogen sulfide sensor based on titanium dioxide nanomaterials. *J. Nanoelectron. Optoelectron.* 13 (12), 1784–1788. doi:10.1166/jno.2018.2417.

Zhou, Q., Chen, W. G., Xu, L. N., Kumarc, R., Gui, Y. G., Zhao, Z. Y., et al. (2018a). Highly sensitive carbon monoxide (CO) gas sensors based on Ni and Zn doped SnO_2 nanomaterials. *Ceram. Int.* 44 (4), 4392–4399. doi:10.1016/j.ceramint.2017.12.038.

Zhou, Q., Hong, C. X., Yao, Y., Hussain, S., Xu, L. N., Zhang, Q. Y., et al. (2018c). Hierarchically MoS_2 nanospheres assembled from nanosheets for superior CO gas-sensing properties. *Mater. Res. Bull.* 101, 132–139. doi:10.1016/j.materresbull.2018.01.030.

Zhou, Q., Umar, A., Sodki, E. M., Amine, A., Xu, L. N., Gui, Y. G., et al. (2018d). Fabrication and characterization of highly sensitive and selective sensors based on porous NiO nanodisks. *Sens. Actuator B-Chem.* 259, 604–615. doi:10.1016/j.snb.2017.12.050.

Zhou, Q., Xu, L. N., Umar, A., Chen, W. G., and Kumar, R. (2018e). Pt nanoparticles decorated SnO_2 nanoneedles for efficient CO gas sensing applications. *Sens. Actuator B-Chem.* 256, 656–664. doi:10.1016/j.snb.2017.09.206.

Zhou, Q., Zeng, W., Chen, W. G., Xu, L. N., Kumarc, R., and Umar, A. (2019). High sensitive and low-concentration sulfur dioxide (SO_2) gas sensor application of heterostructure NiO-ZnO nanodisks. *Sens. Actuator B-Chem.* 298, 126870. doi:10.1016/j.snb.2019.126870.

Conflict of Interest: Authors GQ, QP, DZ, SW, and BY were employed by the Electric Power Science Research Institute of Yunnan Power Grid Co., Ltd.

frontiers in Materials

ORIGINAL RESEARCH
published: 17 February 2021
doi: 10.3389/fmats.2020.631069

The Influence of Additives on the Rheological and Sedimentary Properties of Magnetorheological Fluid

Xiangcheng Zhang[1], *Xiaotong Liu*[1], *Xiaohui Ruan*[1]*, *Jun Zhao*[1] and *Xinglong Gong*[1,2]

[1]School of Mechanics and Safety Engineering, Zhengzhou University, Zhengzhou, China, [2]CAS Key Laboratory of Mechanical Behavior and Design of Materials, Department of Modern Mechanics, University of Science and Technology of China, Hefei, China

In this research, the influence of additives on the rheological and sedimentary properties of the magnetorheological fluid (MRF) was tested and analyzed. The additives were stearic acid, sodium dodecyl sulfate (SDS), and their mixture, respectively. The MRF was composed of carbonyl iron particle, silicone oil, liquid paraffin, graphite particle, bentonite, stearic acid, and SDS. The results indicated that the rheological properties of the MRF were mainly influenced by the mass fraction of carbonyl iron particle. When the mass fractions of carbonyl iron particle and additive were the same, the shear stress of MRF with stearic acid was larger than that of MRF with SDS, and the maximum increment was 73.81%. When the mass fraction of carbonyl iron particle was 40–50%, the shear stress of MRF increased firstly and then decreased with the increase of the external magnetic flux density. When the mass fraction of carbonyl iron particle was 60–70%, the shear stress of MRF increased firstly and then was stable with the increase of the external magnetic flux density. The results indicated that the sedimentary property of MRF with the mixture was better than that of MRF with the stearic acid and SDS. The settling rate of MRF with the mixture increased 91.53% compared to other additives.

Keywords: MRF, stearic acid, sodium dodecyl sulfate, rheological properties, sedimentary properties

OPEN ACCESS

Edited by:
Miao Yu,
Chongqing University, China

Reviewed by:
Xufeng Dong,
Dalian University of Technology, China
Yingdan Liu,
Yanshan University, China

***Correspondence:**
Xiaohui Ruan
rxiaohui@zzu.edu.cn

Specialty section:
This article was submitted to Smart Materials, a section of the journal Frontiers in Materials

Received: *19 November 2020*
Accepted: *28 December 2020*
Published: *17 February 2021*

Citation:
Zhang X, Liu X, Ruan X, Zhao J and Gong X (2021) The Influence of Additives on the Rheological and Sedimentary Properties of Magnetorheological Fluid. Front. Mater. 7:631069. doi: 10.3389/fmats.2020.631069

INTRODUCTION

Magnetorheological fluid (MRF) was a kind of smart material whose rheological properties could be controlled by the external magnetic field (Tang and Conrad, 1996). MRF was a stable suspension that was mainly composed of ferromagnetic dispersed particles, liquid carrier, surfactant, and thixotropic agent (Phule, 1998). With the effect of external magnetic field, the distribution of the magnetic particles inside the MRF could be transformed from a disordered state to a chain or column structure within milliseconds. The chain or column structures were along with the direction of the external magnetic field, and the MRF would show the solid-like state at this time. When the magnetic field was removed, the magnetic particles would return to the original disordered state. The rheological properties and apparent viscosity of MRF changed significantly when the magnetic was applied or removed, and the reversible change between the fluid state and the solid-like state was called the magnetorheological effect (Felt et al., 1996; Lee and Jang, 2011). Because of the excellent rheological properties of MRF, MRF had been widely used in various devices, such as MR clutch (Demenko et al., 2009; Olszak et al., 2019), MR brake (Wang and Bi, 2019; Wu et al., 2020), MR damper (Marinică et al., 2016; Kazakov et al., 2017), and MR polishing (Levin and Khudolei, 2018; Xiu et al., 2018). MRF

had great development prospects in many fields, such as fitness equipment, automobile, polishing, and earthquake resistance.

Since the MR device was first designed and researched by Rabinow in 1948 (Rabinow, 1948), MRF had received extensive attention due to its high yield stress (Guo et al., 2014; Esmaeilnezhad et al., 2017). Researchers had carried out a large number of studies on the properties of MRF, including the shear stress, stability, safety, energy consumption, and economy. Researchers found that the properties of the MRF could be affected by many factors, such as temperature (Chooi and Oyadiji, 2005; Rabbani et al., 2015), shape of the magnetic particle (Kim and Choi, 2011; Shah and Choi, 2014), surfactant (López-López et al., 2008; Zhang et al., 2009; Fei et al., 2015; Xu et al., 2015), and magnetic flux density (Tian et al., 2014; Shan et al., 2015). Researches indicated that though the shear yield stress of MRF was large, the sedimentation stability of the MRF was poor, which seriously restricted the application of MRF. When the MRF was left for a period of time, magnetic particles and carrier liquid would be separated. Due to the interaction of various particles and the large density difference between magnetic particles and carrier liquid, MRF became a thermodynamically unstable system. The aggregation and settlement of solid particles were inevitable. Many methods had been carried out to improve the settling stability of MRF, such as changing the shape of magnetic particles (de Vicente et al., 2010; Laherisheth and Upadhyay, 2017), adding thixotropic agents (De Vicente et al., 2003; Xu et al., 2018), and adding surfactants (Lijesh et al., 2016; Wu et al., 2016; Son, 2018). At present, the researchers still cannot achieve perfect improvement of the rheological and settling properties of MRF, so further research is warranted.

In this article, stearic acid, sodium dodecyl sulfate (SDS), and their mixture were used as additives to study their effects on the rheological properties and settling stability of MRF. We hoped that the results would provide suggestions and references for improving the shear stress and settling properties of MRFs.

MATERIALS AND METHODS

We made the MRF used in this article ourselves. The materials included carbonyl iron particle (CI, Type: CN, Germany BASF, average particle size was 4 μm), SDS (Zhengzhou Alfa Chemical Co., Ltd.), mineral oil (Zhengzhou Alfa Chemical Co., Ltd.), bentonite (Zhengzhou Alfa Chemical Co., Ltd.), black lead (Zhengzhou Alfa Chemical Co., Ltd.), silicone oil (Zhengzhou Alfa Chemical Co., Ltd., 100 viscosity), and stearic acid (Zhengzhou Alfa Chemical Co., Ltd.). All the chemical reagents were used without any further treatment.

Firstly, the CI particles were thoroughly mixed with surfactant in proportion. Then, the mixture and 200 ml anhydrous ethanol were added to a beaker, which was put in the water bath at 80°C. The CI particles and the mixture were stirred continuously by a mechanical stirring stick until the anhydrous ethanol evaporated completely to make the wrapping of the surfactant better on the surface. The liquid paraffin, bentonite, black lead, and silicone oil were then added to the beaker, and the mixture was stirred for 30 min to make the mixture homogeneous. After the temperature of the mixture cooled down to room temperature, it was put into a ball mill and ground for 12 h. After that, the mixture was transferred to a sample bottle for subsequent experiments. The mass fraction of the ingredient in the MRF was shown in **Tables 1–3**. The mass fractions of bentonite, liquid paraffin, and black lead in all MRF were 1, 2, and 1%, respectively.

TABLE 1 | The constituent of MRF with SDS.

Sample number	CI	SDS	Silicone oil	Sample number	CI	SDS	Silicone oil
1	40.0	2.0	54.0	9	60.0	2.0	34.0
2		3.0	53.0	10		3.0	33.0
3		4.0	52.0	11		4.0	32.0
4		5.0	51.0	12		5.0	31.0
5	50.0	2.0	44.0	13	70.0	2.0	24.0
6		3.0	43.0	14		3.0	23.0
7		4.0	42.0	15		4.0	22.0
8		5.0	41.0	16		5.0	21.0

The instrument used for testing the rheological properties of MRF was the commercial rheometer (Anton Paar, MCR 302). During the test, 0.3 ml MRF was placed between the upper plate and the lower plate of the rheometer. The gap between the plates was 1 mm, and the temperature was kept at 25°C during the test. The shear rate and the magnetic field density applied to the MRF during the test could be controlled. The sedimentation properties of the MRF were evaluated by recording the scale of the interface between the supernatant and the MRF.

RESULTS

Rheological Properties

The Influence of the Mass Fraction of CI Particles

During the test, the range of shear rate was logarithmically increasing from 0.01 to 100 (1/s) and the magnetic flux density was linearly increasing from 0 to 1.1 T. The gap between the testing plates was 1 mm, and the temperature was 25°C. The shear stress of samples 1–48 varied with the magnetic flux density was shown in **Figure 1**. In **Figure 1**, the mass fractions of CI particles, SDS, stearic acid, and the mixture of SDS and stearic acid were 40–70%, 2–5%, 2–5%, and 0.5% + 0.5–0.8% + 0.8%, respectively. The maximum shear stress of MRF was obtained and shown in **Table 4**.

It could be seen from **Figure 1** and **Table 4** that the shear stress increased with the increasing of the mass fraction of CI particles and the magnetic flux density. This was because that more chains or columns could be formed when the mass fractions of CI increased. When the magnetic flux density increased, the interaction force between the particles became strong. The increasing numbers of chains or columns and the interaction force between the particles could make the MRF bear a larger load, which showed the increase of the shear stress.

From **Figure 1**, it could be seen that the change of shear stress with magnetic flux density could be divided into two stages. In the first stage, the shear stress increased rapidly with the increase of

TABLE 2 | The constituent of MRF with stearic acid.

Sample number	CI	Stearic acid	Silicone oil	Sample number	CI	Stearic acid	Silicone oil
17	40.0	2.0	54.0	25	60.0	2.0	34.0
18		3.0	53.0	26		3.0	33.0
19		4.0	52.0	27		4.0	32.0
20		5.0	51.0	28		5.0	31.0
21	50.0	2.0	44.0	29	70.0	2.0	24.0
22		3.0	43.0	30		3.0	23.0
23		4.0	42.0	31		4.0	22.0
24		5.0	41.0	32		5.0	21.0

TABLE 3 | The constituent of MRF with stearic acid and SDS.

Sample number	CI	Stearic acid	SDS	Silicone oil	Sample number	CI (%)	Stearic acid (%)	SDS (%)	Silicone oil (%)
33	40.0	0.5	0.5	59.0	41	60.0	0.5	0.5	59.0
34		0.6	0.6	58.8	42		0.6	0.6	58.8
35		0.7	0.7	58.6	43		0.7	0.7	58.6
36		0.8	0.8	54.4	44		0.8	0.8	54.4
37	50.0	0.5	0.5	49.0	45	70.0	0.5	0.5	49.0
38		0.6	0.6	48.8	46		0.6	0.6	48.8
39		0.7	0.7	48.6	47		0.7	0.7	48.6
40		0.8	0.8	48.4	48		0.8	0.8	48.4

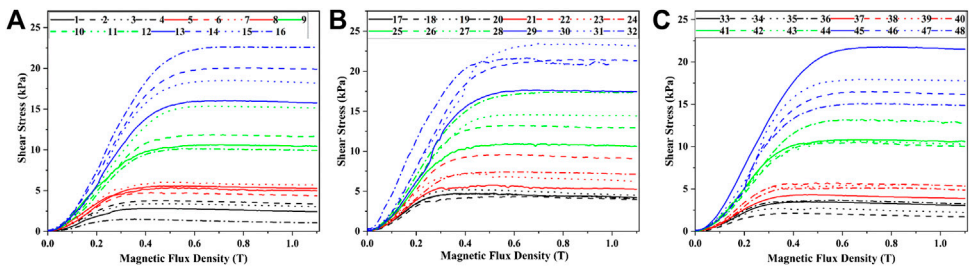

FIGURE 1 | The shear stress varies with the magnetic flux density with different surfactants.

magnetic flux density. This was because the interaction force between the particles increased rapidly at this stage. In the second stage, the shear stress gradually increased and then became stable with the increase of the magnetic flux density. This was because new particle chains were formed under the effect of the magnetic field with the increase of external magnetic flux density, so the shear stress increased gradually. The formation of new grain chains could lead to the increase of the shear stress. When the magnetic flux density increased to 0.4 T, the interaction force between the magnetic particles no longer changed after the magnetization saturation and the structures were no longer changing, which led the shear stress to a stable value.

The Influence of the Surfactant

The curves of the shear stress of MRF vs. the magnetic flux density were shown in **Figure 2**. In **Figure 2A**, the mass fractions of CI particles and additives were 40% and 2%, respectively. Those in **Figures 2B–D** were 50% and 3%, 60% and 4%, and 70% and 5%, respectively.

It could be seen that the shear stress of MRF with stearic acid was higher than that of MRF with SDS. This was because the CI particles in the MRF were gathered and arranged in a chain structure under the effect of the external magnetic field and different surfactants had different effects on the interaction force between CI particles. The stearic acid was coated on the surface of the CI particles and almost had no influence on the viscosity of the carrier liquid. The SDS was dissolved in the carrier liquid, which would make the viscosity of MRF increase. So, SDS would impede the forming of the chain or column structures inside the MRF, which would result in the decreasing of the shear stress.

The Influence of the Shear Rate

The curves of the shear stress of MRF vs. the shear rate were shown in **Figure 3**. In **Figures 3A–C**, the mass fraction of CI

TABLE 4 | Maximum shear stress of MRF.

Sample number	1	2	3	4	5	6	7	8
Maximum shear stress (kPa)	2.42	3.36	3.03	1.06	5.00	4.36	5.69	5.26
Sample number	9	10	11	12	13	14	15	16
Maximum shear stress (kPa)	10.42	11.66	15.13	9.93	15.77	19.90	18.20	22.56
Number	17	18	19	20	21	22	23	24
Maximum shear stress (kPa)	4.20	3.99	4.49	4.04	5.25	9.05	6.27	7.12
Sample number	25	26	27	28	29	30	31	32
Maximum shear stress (kPa)	10.59	12.93	14.42	17.35	17.45	21.31	23.15	21.64
Sample number	33	34	35	36	37	38	39	40
Maximum shear stress (kPa)	3.05	1.71	2.24	3.24	3.87	5.33	5.34	4.88
Sample number	41	42	43	44	45	46	47	48
Maximum shear stress (kPa)	10.62	10.03	10.27	12.85	21.50	16.16	17.77	14.86

particles was 60%. The mass fractions of SDS, stearic acid, and mixture were 2, 2, and 0.5% + 0.5%, respectively. The relationships between the shear stress and shear rate for other samples were similar, so they will not be described in this article for the sake of brevity.

It could be seen from **Figure 3** that the shear stress vs. shear rate curves can be divided into two stages. Firstly, the shear stress first decreased slightly and then increased immediately with the increase of shear rate. Then, the shear stress increases slowly or remained constant with the increase of the shear rate. This was because the magnetic particles would aggregate to form chain or column-like structures parallel to the direction of the external magnetic field when an external magnetic field was applied, which would resist the MRF to flow. In the first stage, when the shear rate was applied to the MRF, the chains between the plates were destroyed and could not be recovered timely, which would lead to the decrease of the shear stress. After that, the particle chains were rebuilt under the effect of the magnetic field, and the phenomenon was that the shear stress increased gradually. In the second stage, new particle chains were formed and, under the effect of magnetic field and chains, would connect to each other to form thick chains under the effect of the shear, so the shear stress increases gradually. At last, the fracture and rebuilt of chains would reach a balance, and the shear stress would reach a stable value. This typical phenomenon can be described by the Bingham model:

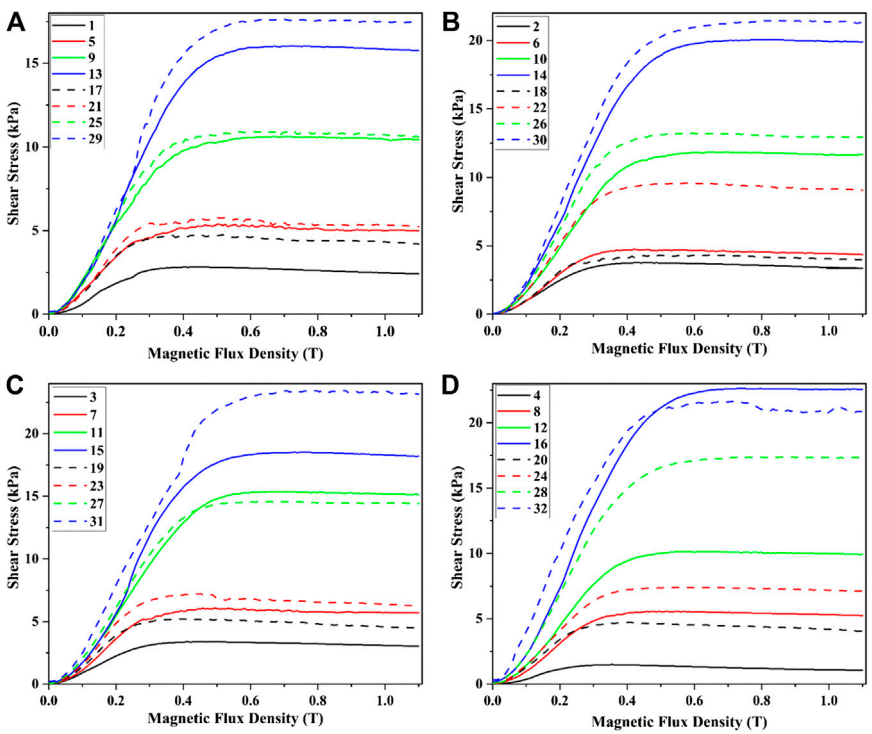

FIGURE 2 | The shear stress varies with the magnetic flux density under different content of surfactants and CI particles.

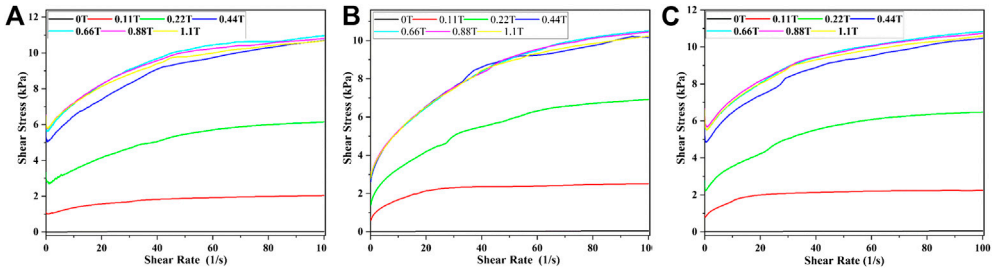

FIGURE 3 | Shear stress varies with shear rate when the mass fraction of CI was 60%, A for SDS, B for stearic acid, and C for mixture.

$$\begin{aligned} \tau &= \tau_y \cdot \mathrm{sign}\dot{\gamma} + \eta\dot{\gamma}, \quad & \tau > \tau_y, \\ \dot{\gamma} &= 0, & \tau \le \tau_y. \end{aligned} \tag{1}$$

In **Eq. 1**, τ_y was the shear yield stress of MRF, determined by the magnetic flux density H (assuming that the field strength was uniform) and the mass fraction of the CI particles, η was the viscosity of MRF, and $\dot{\gamma}$ was the shear rate.

When the mass fraction of CI particle was 40–70% and the mass fraction of SDS was 2%, the experimental and fitting curves of the shear stress *vs*. shear rate of MRF were shown in **Figure 4**. It could be seen that the experimental and fitting results matched well. The yield stress and viscosity of the samples were obtained by fitting the experimental results by **Eq. 1** and were shown in **Figure 5**. It could be seen that the yield stress increased with the increasing of the magnetic flux density and the mass fraction of CI particles. That was because the interaction between the particles increased with the increase of the magnetic flux density and the number of the chain or column structures increased with the increase of the mass fraction of the CI particles. The viscosity of the samples firstly increased and then kept almost constant with the increase of the magnetic flux density. This was because that the interaction between the particles increased with the increase of the magnetic flux density and kept almost constant after the magnetic saturation of the particles. The viscosity of the samples firstly increased and then decreased with the increasing of the mass fraction of CI particles. This was because stratified structures would be formed when the mass fraction of CI particles was very large, which would lead to the decrease of the viscosity.

Settlement Stability

During the test, 10 ml MRF was put into a small measuring cylinder, as shown in **Figure 6**. At the initial time, the liquid level of MRF was level with the scale of 10 ml. The sedimentary

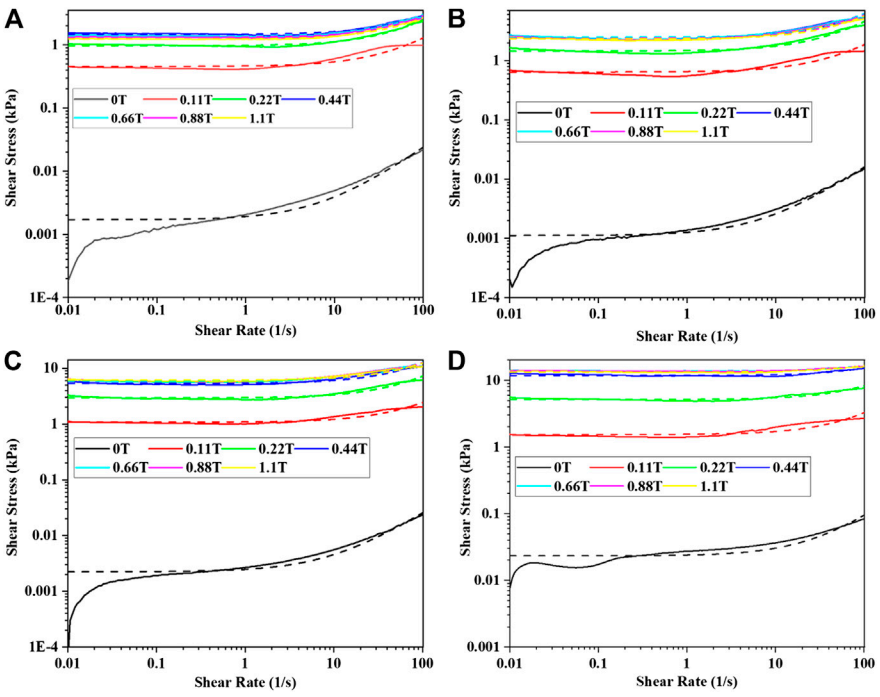

FIGURE 4 | Experimental and fitting curve of shear rate *vs*. shear stress: **(A)** 40%, **(B)** 50%, **(C)** 60%, and **(D)** 70%.

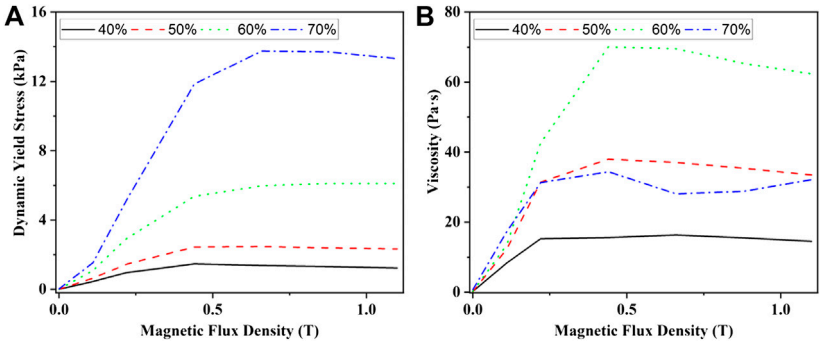

FIGURE 5 | The yield stress and viscosity of the samples.

properties of MRF were evaluated by the method of direct observation. The sedimentation rate was defined as (the height of supernatant/(the height of supernatant + the height of opaque liquid)) *100%, and the formula was as follows:

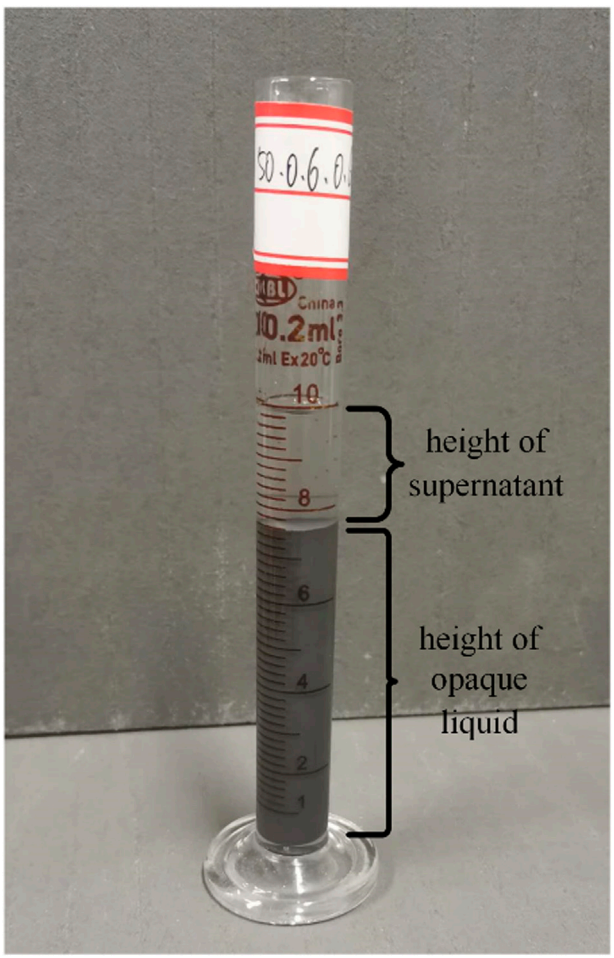

FIGURE 6 | Measuring cylinder.

$$V = \left(\frac{a}{(a+b)}\right) * 100\%. \quad (2)$$

In **Eq. 2**, a was the height of the supernatant and b was the height of the opaque liquid. It could be seen that a smaller sedimentation rate V indicated a better stability property of MRF. The calibration of the supernatant was recorded every 6 h in the first week, every 24 h in the second week, every 72 h in the third week, and every 7 days in the fourth week, until the scale of the supernatant no longer changed. The settling rates of the MRF sample were shown in **Figure 7**, when the mass fractions of CI was 40, 50, and 60% and the surfactant was SDS. Because the fluidity of the MRF was poor when the mass fraction of CI was 70%, it was not concerned here.

It could be seen from **Figure 7** that the sedimentation rate of MRF could be divided into three stages. In the first stage, the sedimentation rate of MRF increased rapidly with the increase of time. In the second stage, the sedimentation rate of MRF increased slowly with the increasr of time. In the third stage, the sedimentation rate MRF gradually tended to be stable. When the mass fraction of SDS was 2%, the increment of sedimentation rate of MRF was the largest when compared to others in the first stage. When the mass fractions of CI particle were 40, 50, and 60%, the MRF with the best settling rate was 6.8, 26.1, and 5%, respectively.

The sedimentation rates of each sample were shown in **Figure 8** when the mass fractions of CI were 40, 50, 60%, and the surfactant was stearic acid. It could be seen from **Figures 8A–C** that the increment of sedimentation rate of MRF was the largest in the first stage when the mass fraction of stearic acid was 2%. When the mass fractions of CI particle were 40, 50, and 60%, the MRF with the best sedimentation rate was 12, 24, and 12%, respectively.

The sedimentation rates of each MRF were shown in **Figure 9** when the mass fraction of CI was 40–60% and the surfactant was mixture. It could be seen from **Figure 9** that the mass fraction of mixture was 0.5%, the increment of sedimentation rate of MRF was the largest in the first stage. When the mass fractions of CI particles were 40, 50, and 60%, the MRF with the best sedimentation rate was 25.8, 0, and 0%, respectively.

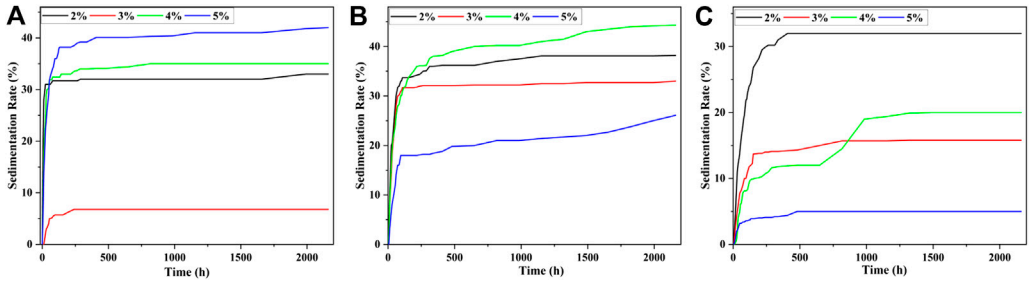

FIGURE 7 | The settling rate when the surfactant is SDS; the mass fraction of CI was **(A)** 40%, **(B)** 50%, and **(C)** 60%.

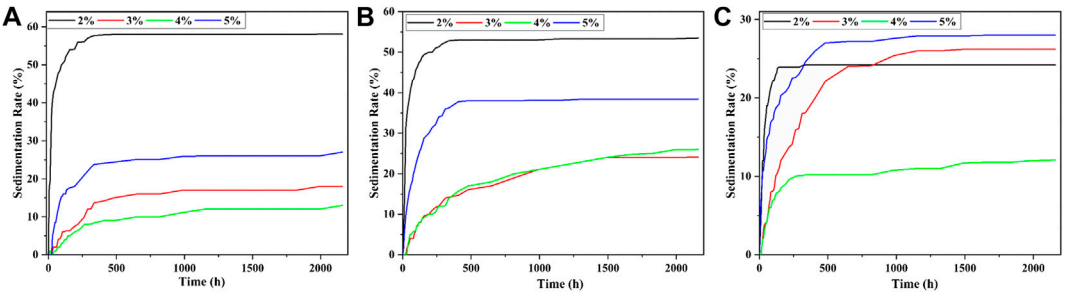

FIGURE 8 | The settling rate when the surfactant is stearic acid; the mass fraction of CI was **(A)** 40%, **(B)** 50%, and **(C)** 60%.

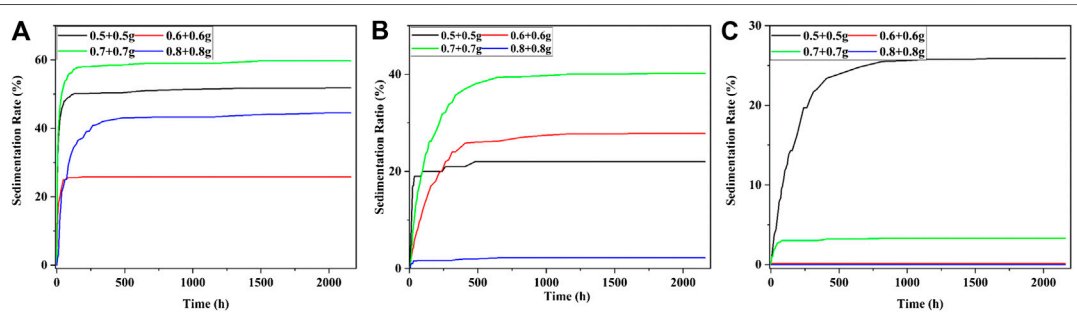

FIGURE 9 | The settling rate when the surfactant was mixture; the mass fraction of CI was **(A)** 40%, **(B)** 50%, and **(C)** 60%.

From **Figure 7** to **Figure 9**, the MRF with the best settling performance for each kind of additives was found and the result was shown in **Figure 10**.

It could be seen from **Figure 10** that the stability of MRF with the mixture was getting better and better with the increase of mass fraction of CI particles. However, when the mass fraction of CI particles was 50%, the stability of MRF decreased when the additives were stearic acid and SDS. When the mass fraction of CI was 60%, the settling stability was mixture > SDS > stearic acid. This was because surfactants had both hydrophilic and lipophilic groups. Hydrophilic groups were usually polar or ionic groups, which were adsorbed on the surface of CI particles. Hydrophobic groups were generally nonpolar groups with long carbon chains, which were dispersed outside CI particles. The long carbon chains among different surfactants were intertwined and repel each other, so they could reduce the aggregation tendency of CI particles and prevent the dispersed particles from aggregation. This kind of coating would change the surface polarity of CI particles, reducing the surface energy and thermodynamic instability and making it easier to disperse in the carrier liquid. So, the settlement problem caused by gravity and settlement stability were improved. The deposition stability of CI with a mass fraction of 50% was lower than that of CI with a mass fraction of 40% due to excess of critical equilibrium concentration. However, the mixture of the two surfactants changed the hydrophilic group and lipophilic group of the surfactant itself. The content of the surfactant never exceeded the critical equilibrium concentration, so the sedimentation

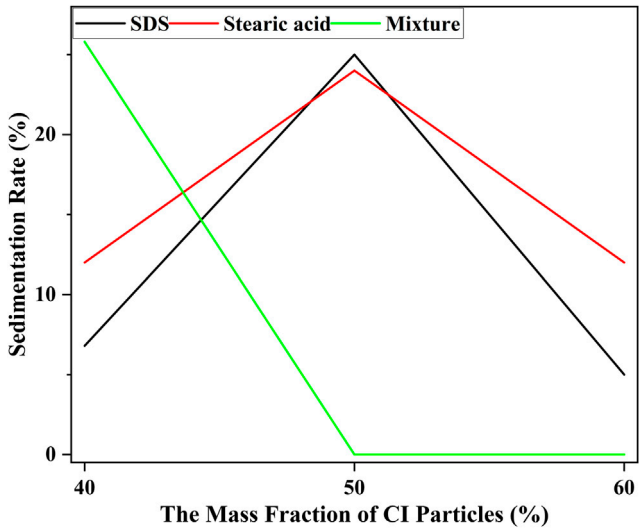

FIGURE 10 | The change of sedimentation rate with the mass fraction of CI particles.

performance would get better with the increase of the amount of surfactant.

CONCLUSION

The rheological properties and sedimentation performance of MRF with different additives had been tested and analyzed in this research. The additives used in this research were SDS, stearic acid, and their mixture. It was found that the rheological properties of MRF were mainly influenced by the mass fraction of CI particles. The shear stress of the samples increased with the increasing of the magnetic flux density and the mass fraction of CI particles. The shear stress of the samples with stearic acid was higher than that of the MRF with SDS when the mass fractions of CI particles and surfactant were equal. When the mass fraction of CI particles was 40 and 50%, the shear stress increased firstly and then decreased with the increase of magnetic flux density. When the mass fraction of CI particles was 60 and 70%, the shear stress increased firstly and then tended to be stable with the increase of magnetic flux density. The relationship between the shear stress and the shear rate could be described by the Bingham model. The yield stress increased with the increasing of the magnetic flux density and the mass fraction of CI particles. The viscosity of the samples firstly increased and then decreased with the increase of the mass fraction of CI particles. The settling stability of the MRF with the mixture of stearic acid and SDS was better than that of the MRF with other additives.

DATA AVAILABILITY STATEMENT

The original contributions presented in the study are included in the article/Supplementary Material; further inquiries can be directed to the corresponding author.

AUTHOR CONTRIBUTIONS

All authors listed have made a substantial, direct, and intellectual contribution to the work and approved it for publication.

FUNDING

Financial support for this research was provided by the National Natural Science Foundation of China (12002317 and 51408555), National Key R&D Program of China (2016YFE0125600), and Program for Changjiang Scholars and Innovative Research Team, University of Minister of Education of China (IRT_16R67); these grants are gratefully acknowledged.

REFERENCES

Chooi, W. W., and Oyadiji, S. O. (2005). Characterizing the effect of temperature and magnetic field strengths on the complex shear modulus properties of magnetorheological (MR) fluids. *Int. J. Mod. Phys. B* 19, 1318–1324. doi:10.1142/s0217979205030244

De Vicente, J., López-López, M. T., González-Caballero, F., and Durán, J. D. G. (2003). Rheological study of the stabilization of magnetizable colloidal suspensions by addition of silica nanoparticles. *J. Rheol.* 47, 1093–1109. doi:10.1122/1.1595094

de Vicente, J., Vereda, F., Segovia-Gutiérrez, J. P., del Puerto Morales, M., and Hidalgo-Álvarez, R. (2010). Effect of particle shape in magnetorheology. *J. Rheol.* 54, 1337–1362. doi:10.1122/1.3479045

Demenko, A., Jędryczka, C., Sujka, P., and Szeląg, W. (2009). The influence of magnetic hysteresis on magnetorheological fluid clutch operation. *COMPEL-Int. J. Comput. Math. Electr. Electron. Eng.* 28, 711–721. doi:10.1108/compel.2009.17428caa.001

Esmaeilnezhad, E., Choi, H. J., Schaffie, M., Gholizadeh, M., Ranjbar, M., and Kwon, S. H. (2017). Rheological analysis of magnetite added carbonyl iron based magnetorheological fluid. *J. Magn. Magn. Mater.* 444, 161–167. doi:10.1016/j.jmmm.2017.08.023

Fei, C., Zuzhi, T., and Xiangfan, W. (2015). Novel process to prepare high-performance magnetorheological fluid based on surfactants compounding. *Mater. Manuf. Process.* 30, 210–215. doi:10.1080/10426914.2014.892967

Felt, D. W., Hagenbuchle, M., Liu, J., and Richard, J. (1996). Rheology of a magnetorheological fluid. *J. Intell. Mater. Syst. Struct.* 7, 589–593. doi:10.1177/1045389x9600700522

Guo, C.-w., Chen, F., Meng, Q.-r., and Dong, Z.-x. (2014). Yield shear stress model of magnetorheological fluids based on exponential distribution. *J. Magn. Magn. Mater.* 360, 174–177. doi:10.1016/j.jmmm.2014.02.040

Kazakov, Y. B., Morozov, N. A., and Nesterov, S. A. (2017). Development of models of the magnetorheological fluid damper. *J. Magn. Magn. Mater.* 431, 269–272. doi:10.1016/j.jmmm.2016.10.006

Kim, J. E., and Choi, H. J. (2011). Magnetic carbonyl iron particle dispersed in viscoelastic fluid and its magnetorheological property. *IEEE Trans. Magn.* 47, 3173–3176. doi:10.1109/tmag.2011.2156396

Laherisheth, Z., and Upadhyay, R. V. (2017). Influence of particle shape on the magnetic and steady shear magnetorheological properties of nanoparticle based MR fluids. *Smart Mater. Struct.* 26, 054008. doi:10.1088/1361-665x/aa54a1

Lee, C. H., and Jang, M. G. (2011). Virtual surface characteristics of a tactile display using magneto-rheological fluids. *Sensors* 11, 2845–2856. doi:10.3390/s110302845

Levin, M. L., and Khudolei, A. L. (2018). Heat transfer in the course of magnetorheological polishing. *J. Eng. Phys. Thermophys.* 91, 797–805. doi:10.1007/s10891-018-1802-3

Lijesh, K. P., Muzakkir, S. M., and Hirani, H. (2016). Rheological measurement of redispersibility and settling to analyze the effect of surfactants on MR particles. *Tribol. Mater. Surface Interfac.* 10, 53–62. doi:10.1080/17515831.2015.1132133

López-López, M. T., Kuzhir, P., Bossis, G., and Mingalyov, P. (2008). Preparation of well-dispersed magnetorheological fluids and effect of dispersion on their magnetorheological properties. *Rheol. Acta.* 47, 787–796. doi:10.1007/s00397-008-0271-6

Marinică, O., Susan-Resiga, D., Bălănean, F., Vizman, D., Socoliuc, V., and Vékás, L. (2016). Nano-micro composite magnetic fluids: magnetic and magnetorheological evaluation for rotating seal and vibration damper applications. *J. Magn. Magn. Mater.* 406, 134–143. doi:10.1016/j.jmmm.2015.12.095

Olszak, A., Osowski, K., Kesy, Z., and Kesy, A. (2019). Investigation of hydrodynamic clutch with a magnetorheological fluid. *J. Intell. Mater. Syst. Struct.* 30, 155–168. doi:10.1177/1045389x18803463

Phule, P. P. (1998). Synthesis of novel magnetorheological fluids. *MRS Bull.* 23, 23–25. doi:10.1557/s0883769400030773

Rabbani, Y., Ashtiani, M., and Hashemabadi, S. H. (2015). An experimental study on the effects of temperature and magnetic field strength on the magnetorheological fluid stability and MR effect. *Soft Matter.* 11, 4453–4460. doi:10.1039/c5sm00625b

Rabinow, J. (1948). The magnetic fluid clutch. *Electr. Eng.* 67, 1167. doi:10.1109/ee.1948.6444497

Shah, K., and Choi, S.-B. (2014). The influence of particle size on the rheological properties of plate-like iron particle based magnetorheological fluids. *Smart Mater. Struct.* 24, 015004. doi:10.1088/0964-1726/24/1/015004

Shan, L., Chen, K., Zhou, M., Zhang, X., Meng, Y., and Tian, Y. (2015). Shear history effect of magnetorheological fluids. *Smart Mater. Struct.* 24, 105030. doi:10.1088/0964-1726/24/10/105030

Son, K. J. (2018). A discrete element model for the influence of surfactants on sedimentation characteristics of magnetorheological fluids. *Korea Aust. Rheol. J.* 30, 29–39. doi:10.1007/s13367-018-0004-z

Tang, X., and Conrad, H. (1996). Quasistatic measurements on a magnetorheological fluid. *J. Rheol.* 40, 1167–1178. doi:10.1122/1.550779

Tian, Y., Chen, K., Shan, L., Zhang, X., and Meng, Y. (2014). Unexpected shear strength change in magnetorheological fluids. *Apl. Mater.* 2, 096102. doi:10.1063/1.4894237

Wang, H., and Bi, C. (2019). Study of a magnetorheological brake under compression-shear mode. *Smart Mater. Struct.* 29, 017001. doi:10.1088/1361-665x/ab5162

Wu, J., Hu, H., Li, Q., Wang, S., and Liang, J. (2020). Simulation and experimental investigation of a multi-pole multi-layer magnetorheological brake with superimposed magnetic fields. *Mechatronics* 65, 102314. doi:10.1016/j.mechatronics.2019.102314

Wu, X., Xiao, X., Tian, Z., and Chen, F. (2016). Study on the preparation process and properties of magnetorheological fluid treated by compounding surfactants. *Jpn. Mag.* 21, 229–234. doi:10.4283/jmag.2016.21.2.229

Xiu, S., Wang, R., Sun, B., Ma, L., and Song, W. (2018). Preparation and experiment of magnetorheological polishing fluid in reciprocating magnetorheological polishing process. *J. Intell. Mater. Syst. Struct.* 29, 125–136. doi:10.1177/1045389x17698247

Xu, J., Li, J., and Cao, J. (2018). Effects of fumed silica weight fraction on rheological properties of magnetorheological polishing fluids. *Colloid Polym. Sci.* 296, 1145–1156. doi:10.1007/s00396-018-4332-9

Xu, Z.-D., Guo, W.-Y., and Chen, B.-B. (2015). Preparation, property tests, and limited chain model of magnetorheological fluid. *J. Mater. Civ. Eng.* 27, 04014229. doi:10.1061/(asce)mt.1943-5533.0001190

Zhang, J. Q., Zhang, J., and Jing, Q. (2009). Effect of seven different additives on the properties of MR fluids. *J. Phys.: Conf. Ser.* 149, 012086. doi:10.1088/1742-6596/149/1/012086

Conflict of Interest: The authors declare that the research was conducted in the absence of any commercial or financial relationships that could be construed as a potential conflict of interest.

frontiers in Materials

MINI REVIEW
published: 08 April 2021
doi: 10.3389/fmats.2021.637664

Research Progress of Bionic Adaptive Camouflage Materials

Yu Qiao[1,2]*, *Zihui Meng*[2], *Piaopiao Wang*[2] *and Dan Yan*[2]

[1] School of Design and Arts, Beijing Institute of Technology, Beijing, China, [2] School of Chemistry and Chemical Engineering, Beijing Institute of Technology, Beijing, China

Bionic adaptive camouflage material is a new artificial functional material, whose surface color can change adaptively according to the optical environments. Therefore, how to reduce the visual detectability of this material becomes a research hotspot of digital camouflage stealth technology. In order to clarify the limitations and opportunities of the bionic adaptive camouflage materials in the field of visual stealth, we summarize the applications of current adaptive camouflage materials and carry out a prospect of next-generation photonic crystal infrared camouflage material in this review. It is expected to provide a solution for the demand of digital camouflage adaptive materials in the modern battle field.

OPEN ACCESS

Edited by:
Brahim Aissa, MPB Technologies & Communications, Canada

Reviewed by:
Dongqing Liu, National University of Defense Technology, China
Xuan Shouhu, University of Science and Technology of China, China

***Correspondence:**
Yu Qiao
499904295@qq.com

Specialty section:
This article was submitted to Smart Materials, a section of the journal Frontiers in Materials

Received: *13 December 2020*
Accepted: *26 February 2021*
Published: *08 April 2021*

Citation:
Qiao Y, Meng Z, Wang P and Yan D (2021) Research Progress of Bionic Adaptive Camouflage Materials. Front. Mater. 8:637664. doi: 10.3389/fmats.2021.637664

Keywords: photonic crystal, adaptive, stealth, digital camouflage, color-changing

INTRODUCTION

In modern high-tech wars, military operation usually encounters quick mobility with various theater of war, frequent transformation of battlefields and different environmental backgrounds. The current camouflage painting technology cannot show self-adaptive camouflage capacity because traditional camouflage technology performs poorly in complicated optical backgrounds and battle fields with drastic change of temperature and humidity. Thus, in recent years, there has been an emerging demand on how to make camouflaged targets better adapt to the complex battlefield background. Meanwhile, bionic camouflage technology is becoming one of the vital ways to solve the focus issue (Lee et al., 2020; Xu et al., 2020). Organisms from many different phyla have evolved an impressive arsenal of light manipulation strategies that rely on the ability to generate and dynamically reconfigure hierarchically structured, complex optical material designs, often involving soft or fluid components. Optical components made fully or partially from reconfigurable, stimuliresponsive, soft solids or fluids—collectively referred to as soft photonics—are poised to form the platform for tunable optical devices with unprecedented functionality and performance characteristics (Kolle and Lee, 2018). Kolle and Lee (2018) presented the demonstration of the soft and skin-like imperceptible device that provides the instantaneous cloaking ability in the visible and IR region with the pixelized thermal operation inspired by the intriguing cloaking properties of cephalopods. They integrated the individual spectrum bands into one full-spectrum system that operates just by adjusting device temperature, thus exhibiting the active multi-spectral cloaking capability that is highly comparable to that of cephalopods. The skin-like cloaking platform not only translates fundamental camouflage features of cephalopods, but it also exhibits high practicality for the direct usage on the human skin unlike previous literature, which only examined the potential of their works in camouflage application (**Figure 1**).

In nature, millions of living beings have undergone hundreds of millions of years of evolution, with reasonable and optimized structural features and adaptability to specific environments.

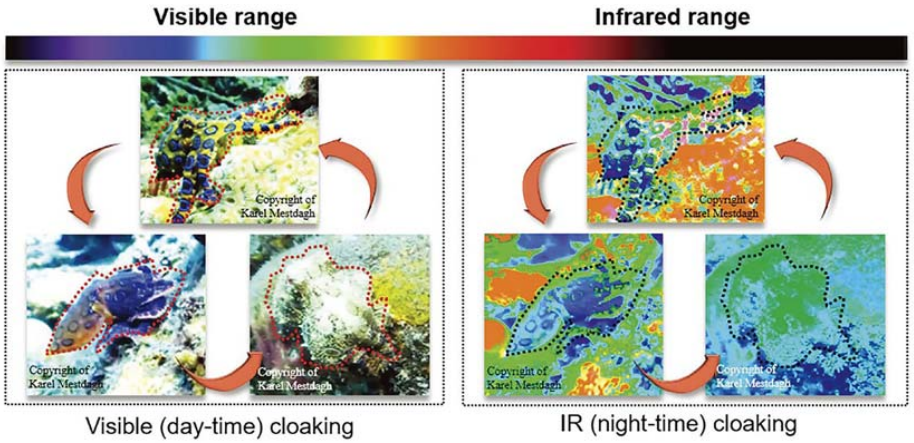

FIGURE 1 | Dynamic camouflage ability of cephalopods both in the visible and infrared spectrum (Lee et al., 2020).

They have become the knowledge treasure and inspiration source for modern technology (Xu et al., 2018). Teyssier et al. (2015) show that chameleons shift color through active tuning of a lattice of guanine nanocrystals within a superficial thick layer of dermal iridophores combining microscopy, photometric videography and photonic band-gap modeling (**Figure 2**). In addition, they show that a deeper population of iridophores with larger crystals reflects a substantial proportion of sunlight especially in the near-infrared range (Teyssier et al., 2015). In the natural world that follows the law of the jungle, the weak are the prey of the strong. In order to survive and reproduce, many creatures are born with camouflage colors suitable for their environment. Their body color can be successfully merged into the natural environment to conceal their tracks.

In general, the camouflage colors of animals can be divided into three categories: one is the same color as the background color; the other is the camouflage color that matches the background color; the third is the flower pattern and spot pattern that contrast with the background color. The first and second categories are generally suitable for animals with restricted activities in certain environments. This is the root of traditional military camouflage. Indeed, digital camouflage painting is a kind of camouflage technology in which such information as natural background color with texture can be extracted by computer and digital image processing technique and then the minor unit of color lumps can be displayed. Actually, this digital camouflage painting is a common method to deal with visual reconnaissance, and reduce the optical differences between targets and surroundings to diminish conspicuousness of targets. The four-color camouflage of US Army is sensitive to the changes in seasons and environmental conditions (**Figure 3**). It is a four-color pattern made up of tawny, brown, dark green, black, which is a group of 12 standard camouflage colors made of alkyd resin paint. The four-color camouflage technique can take effect against ultraviolet, visible light, near-infrared reconnaissance as the visibility of the target can be reduced by 30% on average. Since 1977, the four-color camouflage has been applied to all technological equipment of the US army (land force) (Wen and Feng, 2017).

However, the current digital camouflage, which belongs to "Passive Mode," can achieve anti-reconnaissance effect only in certain environment (Ye et al., 2010). When the environment changes, the existing camouflage targets are easily exposed. The visual stealth mode of military camouflage is mainly applied to the complicated battlefront environment. As the scope of military activities continues to expand, the environmental background has also undergone frequent changes. Therefore, it is of great importance to develop the visual stealth materials with the "self-adaption" function to the updated environmental background.

In fact, it is essential to learn from nature. The surface color of some living creatures can change with changes in the environment (Agez et al., 2017; Caro et al., 2017; Feller et al., 2017). For examples, oceanic cephalopods, such as sepia, their body surface colors can change in response to the surroundings' alteration, such as light stimulation or temperature changes. They can achieve camouflage through integration with various background colors (Banisadr and Chen, 2017). Therefore, the combination of military camouflage technology and bionic materials can achieve the same "adaptive" camouflage function as living creatures (Yoshida and Lahann, 2008; Singh et al., 2012; Yu et al., 2014; Ordinario et al., 2017; Li et al., 2018). In the process of evolution, the special structure of organisms is gradually optimized, which brings endless inspiration to the research of bionic materials (Phan et al., 2013; Tadepalli et al., 2013; Brzicova et al., 2014).

RESEARCH ON BIONIC CAMOUFLAGE MATERIALS IN NATURE

Self-Adaption Regulation of "Camouflage Color" in Nature

Michel Milinkovic from University of Geneva in Switzerland found that the saurian animals, such as chameleons, can

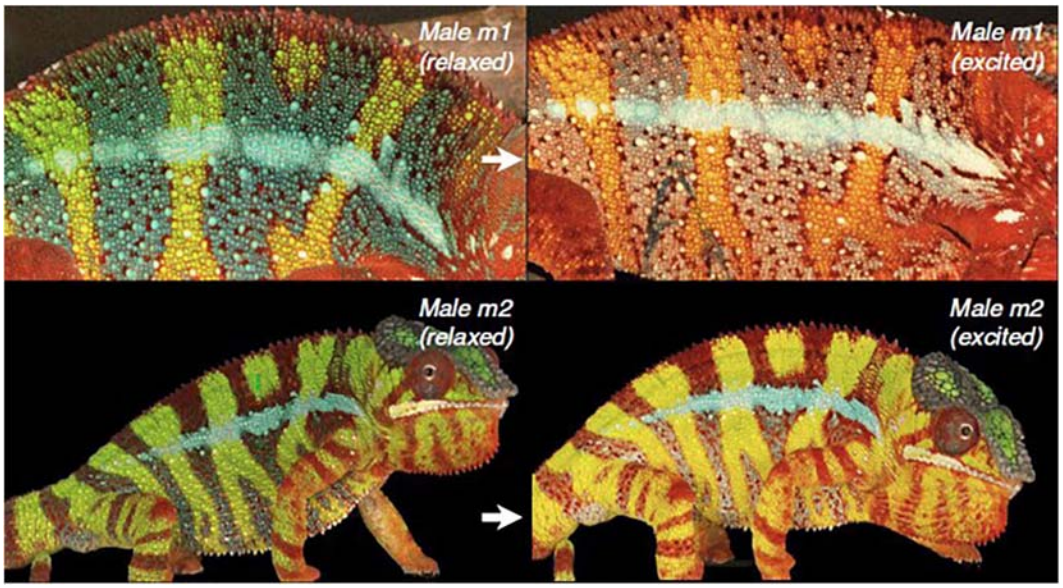

FIGURE 2 | Color change and iridophore types in panther chameleons. Reversible color change is shown for two males (m1 and m2): during excitation (white arrows), background skin shifts from the baseline state (green) to yellow/orange and both vertical bars and horizontal mid-body stripe shift from blue to whitish (m1). Some animals have their blue vertical bars covered by red pigment cells.

FIGURE 3 | Traditional four-color camouflage.

change light refraction to achieve color tuning by regulating the nanocrystals inside the skin surface. This transparent nanocrystal is located inside the iridophore layer and beneath the chromatophore of the chameleon. When the chameleon stays calmness, the nanocrystals are distributed in network and refract blue light. When the chameleon becomes excited, the nanocrystal structure becomes loose and refracts yellow or red light. In the deeper layer of the iridophore, the nanocrystal is more irregular, bigger and refracts stronger light. The two-layer structure of the iridophore is a new feature of evolution, which can make the chameleon achieve transformation between effective protective coloration and fresh bright colors, and it can also provide passive thermal protection.

As for oceanic cephalopods, there are two types of color changes: pigment color and structural color. The cells that can produce pigment molecules are pigment cells, which are located at the top of the corium layer, near the cuticle. Under the pigment cell layer, there are two kinds of cells that produce structural colors, the iridescent somatic cell and the white somatic cell (The white somatic cell usually exists in the octopus or sepia body, and the sleeve-fish does not have this cell) (**Figure 4**). In fact, the color demonstration of the cephalopod cuticle can be attributed to coefficient efforts of these three kinds of cells: the pigment cell, the iridescent somatic cell, and the white somatic cell.

The regularly arranged transparent structure in iridescent somatic cell forms the Bragg Reflector, which produces film interference to the transmitted light; meanwhile, the spherical white granule in the white somatic cell can cause broad-spectrum diffusive reflection and scattering of white light. Inside each pigment cell, there is a whippy pigment sac, whose surface has radicalized muscle fibers. Under the control of nerves, these muscle fibers can contract and relax, control the size of the pigment sac, thereby changing the density of pigment molecules in different pigment sacs.

The mode of color change of oceanic cephalopods is mainly structural color change. In the spherical white granule of the white somatic cell in the octopus and sepia, there is a protein that causes light interference. This type of protein is named "reflectin" (reflective protein) due to its high refractive index (Izumi et al., 2010; DeMartini et al., 2013; Ghoshal et al., 2013, 2014). Reflectin can accomplish self-assembly of the "Hexagon" or "Pentagon" basic units, which can be called "reflectin bricks." These basic units are just like bricks. They are fully extended on the same plane and can produce branch structures and realize various patterns. Moreover, changes in seawater temperature and pH may cause the structural change of these reflective protein, thereby changing the structural color and achieving multiple colors (Li, 2011).

The wings of coleopteran insects (such as diamond weevils) are covered with iridescent glistening scales, like a coat decorated with gems. It is found that the chitin crystal on the wings can form a diamond-type array, which reflects green, yellow, orange sunlight. Bodo Wilts from University of Groningen analyzed the diamond-type scales of the diamond weevils using Scanning Electron Microscope (SEM) and scatterometer. The crystal structure inside the weevil can be analyzed through the tiny beams reflected by the scales of the weevil. The repeating crystal structures are demonstrated that they are mostly striation patterns or the single-track wrinkle patterns. It is found that the scale is a photonic crystal similar to opal. Each type of photonic crystal can reflect a specific wavelength of light in a specific direction.

Similarly, Lepidoptera insects (such as butterflies) can tune their colors by the structural colors on their scales. When the light irradiates on their surface, some microstructures such as ridges, lines, facets, and granules generate interference, scattering, and diffraction, so that the colors change accordingly. Sometimes the structural color is called metallochrome or iridescence.

Structural color show following characteristics: one is the diversity of color levels; the second is the diversity of color types; the third is the diversity of color changes. Meanwhile, color change can be divided into three types. Firstly, the filling medium can cause color change. When the alcoholic solution with different refractive index is filled into the gaps between the scales, the optical coloring conditions of the scale structure will change, leading to the change of color. Secondly, angle alteration can make color change. For instance, the scale colors of some insects will change with the alteration of incident angle and viewing angle of light. Thirdly, under some invariant coloring circumstances, neither change of the medium's refractive index nor alteration of incident angle and viewing angle can make colors of insect scales change. Only the pigment coloring is the reason for color change.

In nature, there are many other living creatures that can change their body colors. They have attained amazing abilities of color change during continuous evolution over hundreds of millions of years. Therefore, it is of vital importance to learn from nature, make use of living creature's color-change mechanism, investigate the principles of bionic stealth and then achieve the key technology of self-adaption camouflage with color change. Based on the bionic color-change materials, it is possible to address the self-adaption issue of traditional camouflage materials and give pivotal technological support to camouflage surfaces under the military situation.

The Application of Self-Adaption Bionic Camouflage Mechanism

Researchers have simulated the bionic color-change structure for the application of the camouflage materials (Rossiter et al., 2012; Yan et al., 2016; Wang et al., 2017).

Chu Sheng and Wang Guo-ping designed a mechanized artificial chameleon, which can use the metal nanoparticles on its skin to accomplish color transformation (**Figure 5**). The color range of variation can almost cover all tones in the visible spectrum (Wang et al., 2016). Li et al. (2020) prepared adaptive thermal camouflage devices by bridging the optical and radiative properties of nanoscopic platinum (Pt) films and silver (Ag) electrodeposited Pt films (**Figure 6**). These metal-based devices have large, uniform, and consistent IR tunabilities in mid-wave IR and long-wave IR atmospheric transmission windows. Furthermore, these devices can be easily multiplexed, enlarged, applied to rough and flexible substrates, or colored,

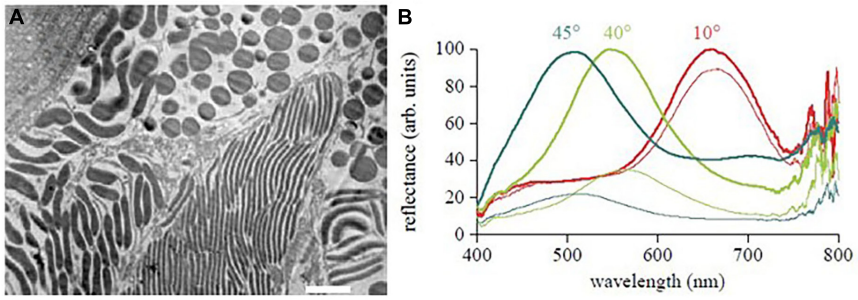

FIGURE 4 | (A) Iridophore structure of sleeve-fish and **(B)** reflection spectrum under various incident light with different angles. Adapted from Mäthger et al. (2009).

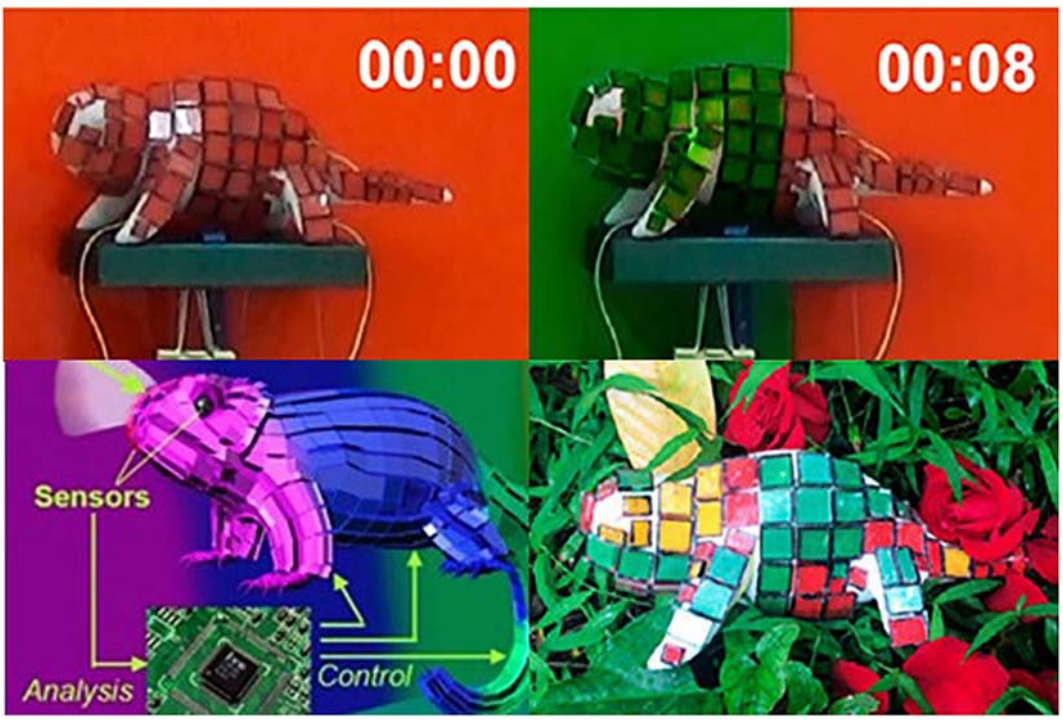

FIGURE 5 | The pictures of artificial Chameleon. Adapted from Wang et al. (2016).

demonstrating their multiple adaptive camouflaging capabilities (Li et al., 2020). Peng et al. (2018) proposed a novel approach for infrared stealth that relies on the combination of emissivity (ε) reduction in the atmospheric windows (3–5 and 8–14 μm) and radiative cooling in a non-atmospheric window (5–8 μm). The fabricated selective emitter has low emissivity ($\varepsilon_{3-5\mu m}$ = 0.18; $\varepsilon_{8-14\mu m}$ = 0.31) in the atmospheric windows for infrared "invisibility" and high emissivity ($\varepsilon_{5-8\mu m}$ = 0.82) outside the atmospheric window for radiative cooling and functions from ambient temperature to 200°C. This work shows that selective emissive materials have promising application prospects and provide a more effective solution for infrared stealth technology (Peng et al., 2018).

The neat rows of pits are etched on the silicon dioxide covering the conductive glass. Gold nanoparticles grow in these pitting layers through evaporating. And then these rows of pits were sealed by electrode plate of gelatin with silver-ion. Later the entire scale and shell were wrapped. At this moment, the "scales and shell" of the artificial chameleon can be dyed red by gold nanoparticles. In the circuit of "gelatin electrode—gold nanoparticles—conductive glass," silver-ion can be reduced to silver through an electrochemical reduction reaction and deposited onto the surface of gold nanoparticles. After the gold core surface is plated with silver, as the thickness of the silver shell increases, the color of the nanoparticles changes from red to green, and finally to blue. By adjusting the conduction time of the electrochemical reaction, the thickness of the silver shell can be controlled well.

Actually, just by several seconds of current control, the color of these scales can be repeatedly changed from

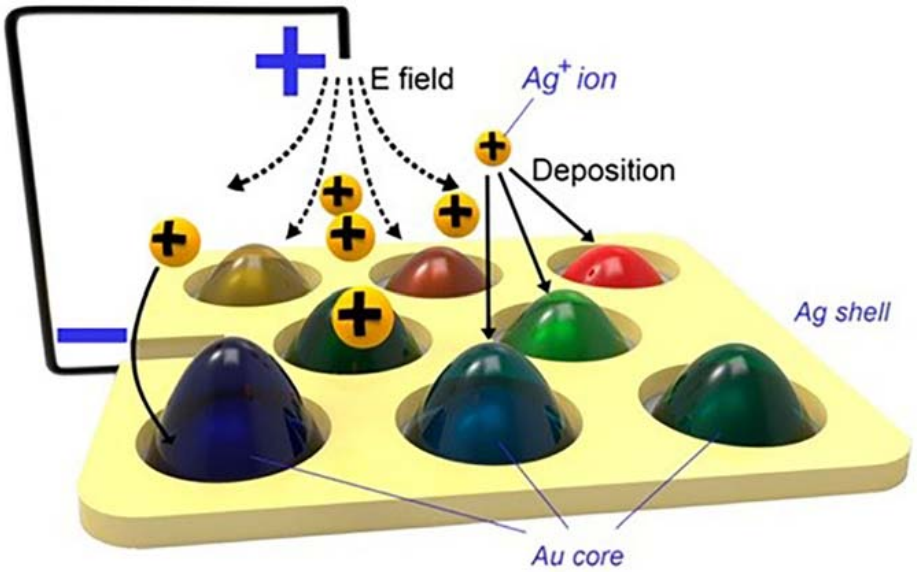

FIGURE 6 | Schematic diagram of electrochemical silver plating and the colors of nanoparticles with different silver shell thickness. Adapted from Wang et al. (2016).

red to blue. These scales can be pasted onto 3D printed chameleon model. Furthermore, eyes of chameleon are equipped with a color sensor. Through controlling the time of electro-oxidation/electro-reduction reaction, the thickness of silver shell can be controlled in real time, so that the chameleon can change its body color as the background environment changes.

Researchers from UC Irvine got inspiration from calamari and then developed a sticker material that enables soldiers against infrared camera (Teyssier et al., 2015). There are iridescence cells in the calamari's skin that have blood platelets containing reflective proteins. The calamari can regulate the thickness of these platelets and the gap between them, so that it can reflect various light. Researchers used colibacillus to cultivate the reflectin which can be packed on the hard surface layer. This film was exposed to acetic steam for heat inflation. The treated film can reflect the infrared light consistent with the infrared light reflected by the background to avoid infrared detection. The researchers integrated reflectin into a polymer sticker, which is flexible, light and thin, and available for back-stickup. By stretching the sticker, reflectin can be activated instead of acetic steam. When this sticker is pasted on the coat or equipment surfaces of the camouflage target, the camouflage target will be successfully "merged" into the background so as to avoid the "capture" of the infrared camera and achieve the purpose of camouflage.

A new "chameleon tank" are developed by the researchers in Germany and Canada. It can change its surface color at any time as the environment changes. There is a thin film on the surface of the chameleon tank, which can change the appearance characteristics of the tank according to the color of the surrounding environment, adjust the temperature of the tank in time, and make it difficult for the enemy to detect the trajectory of the tank by thermal radiation. Finally, the purpose of stealth is achieved.

It is reported that some color-changing and thermochromic coatings are currently being developed. The color-changing coatings are made of a special cloth with photosensitive substances. Therefore, their color can be automatically changed with the change of the environmental photochromism, so that the target wearing the color-changing coatings cannot be exposed in any environment. Meanwhile, the thermochromic coating is a "destined color-changing" to the alteration of environmental temperature, which can significantly reduce the detection probability of thermal imaging cameras and radar. Therefore, the successful development and application of these "Color-changing Magic" will have great potential on the battlefield in the future.

RESEARCH ON ARTIFICIAL BIO-INSPIRED PHOTONIC CRYSTALS STEALTH MATERIALS

In fact, there is a principle of survival of the fittest during the natural selection. The invisible master came into being after billions of years of evolution. For example, chameleons and marine cephalopods (such as octopus and pocket fish), their body color will change with the environmental temperature and humidity. The surface of the chameleon's skin has opal-like nanostructures, which -respond to environmental variables as the color of the specific structure changes (**Figure 7**). When the environmental temperature changes, the nanostructure will change accordingly, causing the color of the structure to change, so as to achieve the invisibility. Cephalopod skin cells contain functional protein reflectin. This spindle-shaped protein assembles into a laminar Bragg reflector. Moreover, changes

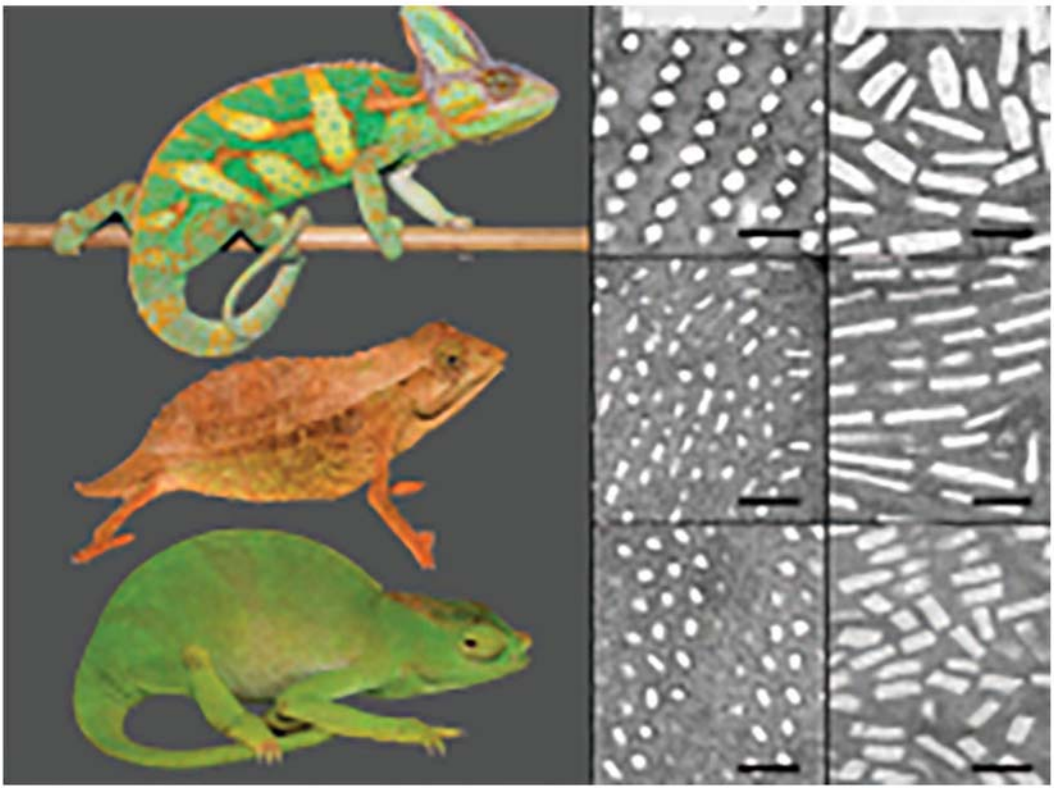

FIGURE 7 | The invisibility and skin microstructure changes of chameleons and other camouflaged animals. Adapted from Teyssier et al. (2015).

of temperature and pH in seawater can cause changes in the structure of proteins, leading to changes in the color of the structure. The above biological camouflage mechanism can be attributed to the change of the structure color of the photonic crystal (Holt et al., 2011; Wilts et al., 2012; Sun et al., 2013; Barrows and Bart, 2014; Deravi et al., 2014; Gur et al., 2016; Meng et al., 2019).

For high-temperature targets, theoretical studies have confirmed that the photonic crystal has the obvious advantages in achieving infrared suppression and stealth of multi-band or broadband. And the theory was verified by experiments. Negative refractive metamaterials, including photonic crystals, are still in the initial stages of theoretical and experimental exploration, but the realization of "invisible cloaks" in the visible band has an attractive prospect. A lot of work has been done on the design and construction of photonic crystal structures.

The stealth function of photonic crystals has been studied in the United States for many years. The United States Military Academy at West Point has established a photonic crystal research center. In recent years, DAPA has also increased its investment and sponsorship in this field. In addition, Raytheon is developing bionic adaptive optoelectronic materials and equipment. At the same time, many European companies have also received AFRL/AFOSR/IOE (EOARD) investment and sponsorship in bionic stealth technology. Biomimetic stealth technology based on photonic crystals is the key technology for intelligent stealth in future weapons and equipment (Zhou et al., 2019). Advanced and reliable stealth technology must be possessed to improve the survivability of troops and equipment. Therefore, it is very necessary to carry out independent innovation research on bionic stealth technology.

The colloidal crystals used in stealth technology are usually composed of 2D or 3D photonic crystals with long-range periodicity. The surface color of the photonic crystal is mainly determined by the width and position of the photonic band gap, which is also closely related to the lattice parameters and the refractive index of the filler (**Figure 8**). Every parameter may cause the photonic band gap to change. On the surface of colloidal crystals, the discoloration mechanism can be divided into two categories. Firstly, some gaps of the colloidal crystal can be filled with the medium material, which can change its refractive index by external stimulation, aiming to change the refractive index between the colloidal particles and the medium surroundings. Secondly, the photonic band gap position of the photonic crystal can be adjusted by changing the lattice parameters.

Color-tunable colloidal crystals have great potential in many fields. In fact, many colloidal crystals can "sense" changes in external stimuli (such as electricity, light, heat, magnetism, and chemistry) and change the structure color. These studies are based on responsive polymers. In particular, responsive polymers can be filled into the gaps of opal photonic crystals composed of

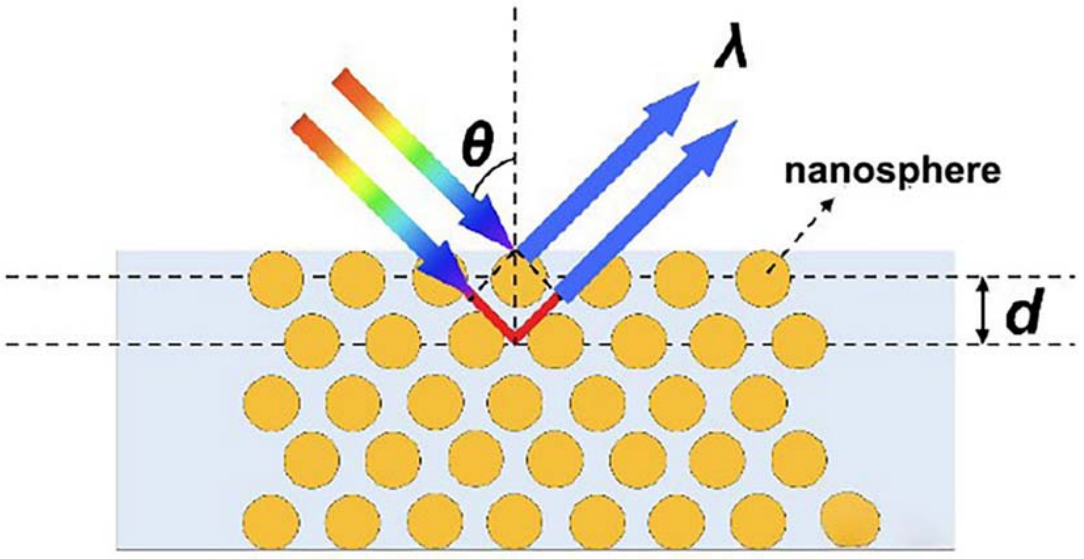

FIGURE 8 | The diffraction mechanism diagram of photonic crystal. Adapted from Qi (2020).

monodisperse polystyrene (or silica) microspheres through self-assembly. At the same time, the reactive polymer can be filled into the gaps of the inverse opal colloid. Under the stimulation of the external environment (such as temperature, electric field, magnetic field, pH), the volume of the polymer will change (swell or shrink), and its refractive index will also change, which leads to the change of the photonic band gap and the displacement of the diffraction peak. Furthermore, if the diffraction peak of the response photonic crystal is in the visible or near-infrared spectral range, the material will visually display color changes during the movement of the diffraction peak. Therefore, the performance of the responsive crystal can be evaluated by this discoloration ability. In order to obtain ideal diffraction peaks and the desired colors in the variable structure color design, it is of great significance to research the relationship between color change and colloidal crystal's refractive index and lattice spacing.

THE APPLICATION OF COLOR-CHANGING CAMOUFLAGE COATINGS FOR MILITARY OPERATION

Thermal and Photosensitive Fibers

New thermal and photosensitive fibers, which can automatically change the color, can be prepared by biomimetic materials. These fibers are sensitive to light, ambient temperature and humidity. In addition, the photosensitive chameleon fiber will change its color under ultraviolet light or visible light and display a reversible graphic pattern. The American "Chameleon" camouflage combat uniform is a successful individual equipment, which is made of photosensitive chameleon fibers. By sensing the changes in external visible light and the temperature of the heat source, it can change its color accordingly, thereby ensuring the uniform can change color with the external environment. Besides, Merck has successfully developed a thermal chameleon combat uniform based on a specific black fabric material. Microcapsules of Liquid crystal printed or dyed on black fabrics can change color in several temperature ranges, such as frigid regions, temperate regions, and tropical regions). When wearing a thermal liquid crystal chameleon combat uniform, soldiers can blend into the natural environment, even without a shield, and the enemy cannot identify them visually. In addition, this uniform also has the function of isolating the heat from the soldier, which will make infrared reconnaissance invalid.

Electrochemical Dye

Through electronic simulation technology, the camouflage coating can obtain signals from the surrounding colors and change its color accordingly, which is called electrochemical dye. In the best case, the information about the environment collected by low-light-level camera is processed by the computer and output as a signal to complete the conversion of the color system, and finally display the optical image of the soldier's background on the soldier's uniform.

Dynamic Optical Camouflage

Dynamic optical camouflage connects the visible light detector and the conductive molecule to realize the color and light conversion of the camouflage coating. When soldiers move from one background to another, dynamic optical camouflage technology can rapidly adapt to the new background, and constantly change the coat color. For example, when soldiers are in the forest, their camouflage uniforms can be the same color as the green and brown backgrounds. If soldiers move to a wheat field, the color of their coats will quickly change to orange, khaki, and brown.

Smart Camouflage Materials

The existing camouflage coating is passive. They can only achieve the effect of anti-reconnaissance in a static state. When there is wind, the enemy can easily find a "leaf" or a "bush" still in the swaying grass, causing to find the camouflage target through subtle differences. Therefore, active camouflage technology has received massive attention. The US Army has developed an electrochromic film that can be pasted or painted on camouflage uniforms. Meanwhile, this electrochromic film can be connected to micro smart processing and environmental sensor systems. During the wind, the system can change the graphic patterns on the film to achieve a swinging visual effect similar to the background and achieve the camouflage.

CONCLUSION AND PROSPECTS

The application of biomimetic adaptive color-changing materials in stealth technology is summarized in this article. For the demand of the new generation of discoloration camouflage coating, some solutions are proposed:

(A) Bionic adaptive color-changing materials suitable for battlefields not only need to select adaptive color-changing composite materials, but also need to collect environmental digital image data to establish a database of the main camouflage environment. Through image analysis software, the essential colors can be extracted from the digital environment image, thereby designing digital camouflage paintings based on different background environments. Furthermore, the color similarity and algorithm of digital camouflage painting database are analyzed. Through the structural color of the photonic crystal, traditional digital camouflage paintings can be obtained. In the optical environment, photonic crystals have the characteristics of structural discoloration, combined with the multiple matching of digital camouflage paintings, realizing the controllability of color changes, so that the bionic materials can meet the requirements of adaptive camouflage against complex environmental backgrounds.

(B) For the bionic adaptive stealth material, the priority is to set up the relationship between the color change and the optical background. In fact, the analysis of this relationship can be achieved by studying the color response of the photonic crystal to environmental variables such as temperature and humidity. Therefore, it is necessary to study the relationship between the microstructure and color of the biomimetic photonic crystal. How to adjust the microstructure of the bionic photonic crystal to meet specific color demands requires further research. In addition, how to optimize the chemical composition of the biomimetic photonic crystal to ensure the response to environmental variables is a crucial issue. Therefore, the use of suitable composite materials to construct photonic crystals is a hot spot of current research and one of the basic solutions.

(C) Although the current stealth material field is still based on traditional stealth methods, such as camouflage coating materials. Because of higher and further requirement, unceasingly updating diversity and precision of future detection methods for the stealth materials, the photonic crystals, which can be designed and dynamically adjusted due to their structure, will certainly play a greater role in the development of digital camouflage stealth in the future.

AUTHOR CONTRIBUTIONS

YQ organized and compiled this article. ZM, PW, and DY provided the ideas and references. All authors contributed to the article and approved the submitted version.

FUNDING

This work was financially supported by the 2018 Beijing Social Science Foundation project funding (Grant No. 18YTC025) and the Youth YUYOU Talent Training Program of North China University of Technology.

REFERENCES

Agez, G., Bayon, C., and Mitov, M. (2017). Multiwavelength micromirrors in the cuticle of scarab beetle *Chrysina gloriosa*. *Acta Biomater.* 48, 357–367. doi: 10.1016/j.actbio.2016.11.033

Banisadr, S., and Chen, J. (2017). Infrared actuation-induced simultaneous reconfiguration of surface color and morphology for soft robotics. *Sci. Rep.* 7, 17521–17530.

Barrows, F. P., and Bart, M. H. (2014). Photonic structures in biology: a possible blueprint for nanotechnology. *Nanomater Nanotechnol.* 4, 1–12. doi: 10.5772/58289

Brzicova, T., Feliu, N., and Fadeel, B. (2014). Biomimetic camouflage: nanoporous particles cloaked in cellular membranes. *Nanomedicine* 9, 19–20.

Caro, T., Stoddard, M. C., and Stuart-Fox, D. (2017). Animal coloration research: why it matters. *Philos. Trans. R. Soc. Lond. B Biol. Sci.* 372:20160333. doi: 10.1098/rstb.2016.0333

DeMartini, D. G., Ghoshal, A., Pandolfi, E., Weaver, A. T., Baum, M., and Morse, D. E. (2013). Dynamic biophotonics: female squid exhibit sexually dimorphic tunable leucophores and iridocytes. *J. Exp. Biol.* 216, 3733–3741. doi: 10.1242/jeb.090415

Deravi, L. F., Magyar, A. P., Sheehy, S. P., Bell, G. R. R., Mathger, L. M., Senft, S. L., et al. (2014). The structure-function relationships of a natural nanoscale photonic device in cuttlefish chromatophores. *J. R. Soc. Interface* 11:20130942. doi: 10.1098/rsif.2013.0942

Feller, K. D., Jordan, T. M., Wilby, D., and Roberts, N. W. (2017). Selection of the intrinsic polarization properties of animal optical materials creates enhanced structural reflectivity and camouflage. *Philos. Trans. R. Soc. Lond. B Biol. Sci.* 372:20160336. doi: 10.1098/rstb.2016.0336

Ghoshal, A., DeMartini, D. G., Eck, E., and Morse, D. E. (2014). Experimental determination of refractive index of condensed reflectin in squid iridocytes. *J. R. Soc. Interface* 11:20140106. doi: 10.1098/rsif.2014.0106

Ghoshal, A., Demartini, D. G., Eck, E., and Morse, D. E. (2013). Optical parameters of the tunable bragg reflectors in squid. *J. R. Soc. Interface* 10:20130386. doi: 10.1098/rsif.2013.0386

Gur, D., Leshem, B., Farstey, V., Oron, D., Addadi, L., and Weiner, S. (2016). Light-induced color change in the sapphirinid copepods: tunable photonic crystals. *Adv. Funct. Mater.* 26, 1393–1399. doi: 10.1002/adfm.201504339

Holt, A. L., Sweeney, A. M., Johnsen, S., and Morse, D. E. (2011). A highly distributed bragg stack with unique geometry provides effective camouflage for loliginid squid eyes. *J. R. Soc. Interface* 8, 1386–1399. doi: 10.1098/rsif.2010.0702

Izumi, M., Sweeney, A. M., Demartini, D., Weaver, J. C., Power, M. L., Tao, A., et al. (2010). Changes in reflectin protein phosphorylation are associated with dynamic iridescence in squid. *J. R. Soc. Interface* 7, 549–560. doi: 10.1098/rsif.2009.0299

Kolle, M., and Lee, S. (2018). Progress and opportunities in soft photonics and biologically inspired optics. *Adv. Mater.* 30:1702669. doi: 10.1002/adma.201702669

Lee, J., Sul, H., Jung, Y., Kim, H., Han, S., Choi, J. H., et al. (2020). Thermally controlled, active imperceptible artificial skin in visible-to-infrared range. *Adv. Funct. Mater.* 30:2003328. doi: 10.1002/adfm.202003328

Li, J. W. (2011). *Mechanism of Structural Color in Creatures and Bionic Design of Structural Color*. Ph.D. thesis, University of Science and Technology of China, Hefei, 31–35.

Li, J. X., Angsantikul, P., Liu, W. J., Ávila, B. E. F., Chang, X. C., Sandraz, E., et al. (2018). Biomimetic platelet-camouflaged nanorobots for binding and isolation of biological threats. *Adv. Mater.* 30:1704800. doi: 10.1002/adma.201704800

Li, M. Y., Liu, D. Q., Cheng, H. F., Peng, L., and Zu, M. (2020). Manipulating metals for adaptive thermal camouflage. *Sci. Adv.* 6:eaba3494. doi: 10.1126/sciadv.aba3494

Mäthger, L. M., Denton, E. J., Marshall, N. J., and Hanlon, R. T. (2009). Mechanisms and behavioural functions of structural coloration in cephalopods. *J. R. Soc. Interface* 6, 149–163. doi: 10.1098/rsif.2008.0366.focus

Meng, Z. P., Huang, B. T., Wu, S. L., Li, L., and Zhang, S. F. (2019). Bio-inspired transparent structural color film and its application in biomimetic camouflage. *Nanoscale* 11, 13377–13384. doi: 10.1039/c9nr04360h

Ordinario, D. D., Leung, E. M., Phan, L., Kautz, R., Lee, W. K., Naeim, M., et al. (2017). Protochromic devices from a cephalopod structural protein. *Adv. Opt. Mater.* 5:1600751. doi: 10.1002/adom.201600751

Peng, L., Liu, D. Q., Cheng, H. F., Zhou, S., and Zu, M. (2018). A multilayer film based selective thermal emitter for infrared stealth technology. *Adv. Opt. Mater.* 6:1801006. doi: 10.1002/adom.201801006

Phan, L., Walkup, W. G., and Gorodetsky, A. A. (2013). "Biomimetic camouflage inspired by cephalopods," in *Proceedings of the 245th ACS National Meeting & Exposition, Abstracts of Papers of the American Chemical Society*, New Orleans, LA, 245.

Qi, F. L. (2020). "Preparation of photonic crystals and their sensing applications to organophosphates," in *Doctoral Dissertation*. (Beijing University of technology).

Rossiter, J., Yap, B., and Conn, A. (2012). Biomimetic chromatophores for camouflage and soft active surfaces. *Bioinspir. Biomim.* 7:036009. doi: 10.1088/1748-3182/7/3/036009

Singh, A. V., Rahman, A., Sudhir Kumar, N. V. G., Aditi, A. S., Galluzzi, M., Bovio, S., et al. (2012). Bio-inspired approaches to design smart fabrics. *Mater. Des.* 36, 829–839. doi: 10.1016/j.matdes.2011.01.061

Sun, J. Y., Bhushan, B., and Tong, J. (2013). Structural coloration in nature. *RCS Adv.* 3, 14862–14889. doi: 10.1039/c3ra41096j

Tadepalli, S., Slocik, J. M., Gupta, M. K., Naik, R. R., and Singamaneni, S. (2013). Bio-optics and bio-inspired optical materials. *Chem. Rev.* 117, 12705–12763. doi: 10.1021/acs.chemrev.7b00153

Teyssier, J., Saenko, S. V., Marel, D. V., and Milinkovitch, M. C. (2015). Photonic crystals cause active colour change in chameleons. *Nat. Commun.* 6, 6368–6375.

Wang, G., Chen, X., Liu, S., Wong, C. P., and Chu, S. (2016). Mechanical chameleon through dynamic real time-plasmonic tuning. *ACS Nano* 10, 1788–1794. doi: 10.1021/acsnano.5b07472

Wang, X. Y., Deng, Y. Q., Yang, D., Xiao, Y., Zhao, H., Nian, Q. G., et al. (2017). Biomimetic inorganic camouflage circumvents antibody-dependent enhancement of infection. *Chem. Sci.* 8, 8240–8246. doi: 10.1039/c7sc03868b

Wen, Z. G., and Feng, F. P. (2017). Research progress in bionic mechanics. *Guangdong Sci. Technol.* 89–90.

Wilts, B. D., Michielsen, K., Kuipers, J., Raedt, H. D., and Stavenga, D. G. (2012). Brilliant camouflage: photonic crystals in the diamond weevil, *Entimus imperialis*. *Proc. R. Soc. B Biol. Sci.* 279, 2524–2530. doi: 10.1098/rspb.2011.2651

Xu, C. Y., Escobar, M. C., and Gorodetsky, A. A. (2020). Stretchable cephalopod-inspired multimodal camouflage systems. *Adv. Mater.* 32:1905717. doi: 10.1002/adma.201905717

Xu, C. Y., Stiubianu, G. T., and Gorodetsky, A. A. (2018). Adaptive infrared-reflecting systems inspired by cephalopods. *Science* 359, 1495–1500. doi: 10.1126/science.aar5191

Yan, Y., Liu, L., Cai, Z., Xu, J. W., Xu, Z., Zhang, D., et al. (2016). Plasmonic nanoparticles tuned thermal sensitive photonic polymer for biomimetic chameleon. *Sci. Rep.* 6, 31328–31337.

Ye, X. Q., Ji, L. H., Xie, Y. M., and Huang, L. N. (2010). Discussion on the combination of rehabilitation training robot and traditional Chinese medicine rehabilitation method. *Chin. J. Rehabil. Med.* 25, 781–784.

Yoshida, M., and Lahann, J. (2008). Smart nanomaterials. *ACS Nano* 2, 1101–1107.

Yu, C. J., Li, Y. H., Zhang, X., Huang, X., Malyarchuk, V., Wang, S. D., et al. (2014). Adaptive optoelectronic camouflage systems with designs inspired by cephalopod skins. *Proc. Natl. Acad. Sci. U.S.A.* 111, 12998–13003. doi: 10.1073/pnas.1410494111

Zhou, H., Xu, J., Liu, X. H., Zhang, H. W., Wang, D. T., Chen, Z. H., et al. (2019). Bio-inspired photonic materials: prototypes and structural effect designs for applications in solar energy manipulation. *Adv. Funct. Mater.* 28:1705309. doi: 10.1002/adfm.201705309

Conflict of Interest: The authors declare that the research was conducted in the absence of any commercial or financial relationships that could be construed as a potential conflict of interest.

frontiers in Materials

ORIGINAL RESEARCH
published: 27 April 2021
doi: 10.3389/fmats.2021.639823

Understanding the Impact of Machine Learning Models on the Performance of Different Flexible Strain Sensor Modalities

Brett C. Hannigan[1], *Tyler J. Cuthbert*[1], *Wanhaoyi Geng*[1], *Mohammad Tavassolian*[1] *and Carlo Menon*[2,1]*

[1]Menrva Research Group, Schools of Mechatronic Systems Engineering and Engineering Science, Simon Fraser University, Surrey, BC, Canada, [2]Biomedical and Mobile Health Technology Laboratory, Department of Health Sciences and Technology, ETH Zürich, Zürich, Switzerland

OPEN ACCESS

Edited by:
Miao Yu,
Chongqing University, China

Reviewed by:
Yu Wang,
University of Science and Technology of China, China
Xingzhe Wang,
Lanzhou University, China

***Correspondence:**
Carlo Menon
cmenon@sfu.ca

Specialty section:
This article was submitted to Smart Materials, a section of the journal Frontiers in Materials

Received: 09 December 2020
Accepted: 02 February 2021
Published: 27 April 2021

Citation:
Hannigan BC, Cuthbert TJ, Geng W, Tavassolian M and Menon C (2021) Understanding the Impact of Machine Learning Models on the Performance of Different Flexible Strain Sensor Modalities. Front. Mater. 8:639823. doi: 10.3389/fmats.2021.639823

Fibre strain sensors commonly use three major modalities to transduce strain—piezoresistance, capacitance, and inductance. The electrical signal in response to strain differs between these sensing technologies, having varying sensitivity, maximum measurable loading rate, and susceptibility to deleterious effects like hysteresis and drift. The wide variety of sensor materials and strain tracking applications makes it difficult to choose the best sensor modality for a wearable device when considering signal quality, cost, and difficulty of manufacture. Fibre strain sensor samples employing the three sensing mechanisms are fabricated and subjected to strain using a tensile tester. Their mechanical and electrical properties are measured in response to strain profiles designed to exhibit particular shortcomings of sensor behaviour. Using these data, the sensors are compared to identify materials and sensing technologies well suited for different textile motion tracking applications. Several regression models are trained and validated on random strain pattern data, providing guidance for pairing each sensor with a model architecture that compensates for non-ideal effects. A thermoplastic elastomer-core piezoresistive sensor had the highest sensitivity (average gauge factor: 12.6) and a piezoresistive sensor of similar construction with a polyether urethane-urea core had the largest bandwidth, capable of resolving strain rates above 300% s^{-1} with 36% signal amplitude attenuation. However, both piezoresistve sensors suffered from larger hysteresis and drift than a coaxial polymer sensor using the capacitive strain sensing mechanism. Machine learning improved the piezoresistive sensors' root-mean-squared error when tracking a random strain signal by up to 58% while maintaining their high sensitivity, bandwidth, and ease of interfacing electronically.

Keywords: wearable sensors, piezoresistive composites, capacitive strain sensors, random strain tracking, machine learning

1 INTRODUCTION

The integration of electronics into clothing to make "smart textiles" is commonly used to track motion and aid rehabilitation, improve athletic training, prevent injury, recognize gestures, and acquire bio-signals (Fleury et al., 2015). The occurrence of wearable sensor research articles has increased on average 28% yearly over the past 10 years[1] and will likely continue to grow in popularity as electronics become smaller and more integrated. Advances in soft strain sensors that enable motion tracking have progressed recently to ever higher performance. The application of different sensor materials and principles of operation can have a large effect on the signal characteristics, for better or for worse. For example, accuracy suffers when tracking running at high speeds with some resistive sensor types (Mengüç et al., 2014). Others display high sensitivity but only over a limited strain range making them best suited for tracking fine movements—such as wearable sensors using capacitance to detect strain of finger joints for gesture detection (Liu et al., 2011; Lee et al., 2015; Kim et al., 2017). Sensor properties such as strain bandwidth, dynamic range, hysteresis, and static drift affect the tracking of movements where high speeds, large strains, cyclic motion, or prolonged static periods are expected, respectively. Quite often, these deleterious effects are inherent to the materials used to create the sensor and can be overlooked when focusing on advances such as gauge factor (GF) or maximum achievable strain with new sensor compositions or fabrication methods. An alternative strategy for improving sensing performance has been to implement machine learning (ML) algorithms to predict or classify movements or estimate body segment positions (Vu and Kim, 2018). Software models have also been used to correct and improve sensor signals in the presence of detrimental sensor properties, an approach that has been limited to three reports (Kim and Kim, 2017; Miodownik et al., 2019; Oliveri et al., 2019). The ability of machine learning to extract patterns from complex, nonlinear signals in the presence of disturbances like random noise and electromagntic interference (EMI) may be used to maximize the information gained from a sensor (Miodownik et al., 2019). It is important for future developments to determine the advantageous and limiting characteristics of each sensor technology and understand the possible improvements in signal fidelity realized when each type is combined with modelling. This enables designers to gain knowledge about which sensor is best suited for a specific type of motion tracking application, or simply to push forward sensing abilities from both hardware and software approaches.

Three modalities of fiber strain sensors may be distinguished by their mode of operation: using changes in resistance, capacitance, or inductance to transduce strain. Fibre sensors using the piezoresistive effect have been fabricated with conductive polymers, polymer-conductor composites, ionic liquids, liquid metals, and carbon nanotubes (Shin et al., 2010; Seyedin et al., 2015; Wu et al., 2016; Choi et al., 2017; Keulemans et al., 2017; Zahid et al., 2017; Chen et al., 2018). Sensor arrangement for integration into textiles may incorporate monofilaments, multifilament fibres, knitted textiles, or foams (Seyedin et al., 2015; Zahid et al., 2017; Jung et al., 2019; Yin et al., 2019; Zheng et al., 2019). Polymer-conductor composite (PC) sensors are commonly used in wearable applications because of their scalable manufacturing processes, high sensitivity, and ease of interfacing with textiles and electronics (Liu et al., 2018a). Many factors (see **Supplementary Equation S1** for details) influence the piezoresistance of the polymer including mechanical polymer properties, conductive filler choice and distribution, mode of conduction, and the presence of micro-cracks between conductive regions (Stübler et al., 2011; Liu et al., 2018a).

The combination of effects that contribute to a sensor's resistance causes its signal to diverge from an ideal linear strain-resistance relationship. The most obvious of these effects is a varying GF across the working strain range (He et al., 2019). A repeatable nonlinear signal response to strain is not necessarily detrimental for strain sensing because an operating point can be chosen around which the sensor signal is approximately linear, or the nonlinearity can be compensated for in software (Oliveri et al., 2019). Even simple regression models are able to easily handle repeatable signal nonlinearities. Mechanically, thermoplastic elastomers (TPE), pristine or composite, may posses hysteresis, strain softening, and fading memory in their stress-strain relationships (Diani et al., 2009; Drozdov and Dusunceli, 2014). Analogous electrical effects are often observed in TPE conductive composites including signal hysteresis, dynamic drift, and static drift (Clemens et al., 2012). Signal hysteresis occurs when the sensor resistance is path dependent over a long number of cycles, having different resistance values for a given strain during extension and recovery (De Focatiis et al., 2012). Hysteresis modelling for composite sensors and geometrical modifications of the ionic liquid type have been used to compensate for and reduce hysteresis (Choi et al., 2017; Kim and Kim, 2017). Dynamic drift refers to a transient change in the resistance when exposed to cyclic strain that decays to a steady-state (De Focatiis et al., 2012). Static drift in resistance during constant strain is attributable to polymer stress relaxation (Kalantari et al., 2012). The readout electronics for piezoresistive sensors may be as simple as a voltage divider circuit with one analog-to-digital converter (ADC). In addition, high sensitivities (GF > 1,000) are achievable while maintaining maximum strain in excess of 100% (He et al., 2019).

Soft sensors that use capacitance to measure strain are advantageous because they greatly reduce the dependency of GF on strain when compared to the piezoresistive type. This is due to the underlying mechanism of capacitance modulation relying only on a change in geometry (see **Supplementary Equations S2, S3** for details). Capacitive sensors have been fabricated from liquid metal in tubes, polymer composites, and thin film electrodes in parallel plate, coaxial, and twisted-pair configurations (Frutiger et al., 2015; Lee et al., 2015; Wang et al.,

[1]According to the results of an *Web of Science* topic search conducted October 2020 using the keyword string "wearable sensor" restricted to date range 2009-2019.

2016; Cooper et al., 2017; Kim et al., 2017). The relative change in capacitance limits ideal capacitive sensors of this construction to unity gauge factor. A difficulty associated with capacitive sensors is the complex measurement electronics necessary to read capacitance. Whereas resistive sensors can be read with minimal electronic components, capacitive sensors require AC excitation and precise timing to measure. Conductive polymer electrodes have their own piezoresistive effect that manifests as a strain-dependent equivalent series resistance (ESR) to the measurement circuit (Michel et al., 2012; Liu et al., 2015). High ESR hinders the rate at which a capacitive sensor may be sampled and limits the strain frequencies that are measurable. Manufacturing is more complex than piezoresistive sensors because at least three layers are required—two electrode layers with electrical connections that must remain isolated by a dielectric layer—becoming difficult to manufacture at scale. Eliminating short circuits between electrodes and accessing the inner electrode in a downsized coaxial fibre are non-trivial pursuits. Coupling capacitive sensors with modelling has been limited to developing mathematical models to predict its electrical behaviour (Frutiger et al., 2015). Combining ML models with capacitive sensors has the potential to compensate for strain-depedent ESR and improve measurement at high strain rates.

Inductive strain sensors are under-represented in comparison to piezoresistive and capacitive strain sensors. The inductive sensing modality has utilized inductance of a single loop, mutual inductance between loops positioned on different body segments, or the gain between receiver and transmitter antenna coils on various segments to track relative motion (Wijesiriwardana, 2006; Laskoski et al., 2009; Sardini et al., 2012; Patron et al., 2016). The inductance of a solenoid coil is dependent on its number of turns, cross-sectional area, and total wire length. One approach to single coil sensors is to rely on the change of area of a stretchable solenoid loop to measure strain, similar to inductance plethysmography systems (Zhang et al., 2012). Like the capacitive sensor, the inductive signal is directly dependent on geometry. However, this relationship is not linear. For a sensor with a reasonable length, the logarithmic behaviour with respect to length is negligible and sensor response can be linearly approximated as the GF (Tavassolian et al., 2020). According to **Supplementary Equation S4**, the number of perimeter loops does not influence the sensitivity but rather scales the baseline inductance allowing higher signal-to-noise ratio. One challenge with inductive sensors in wearable applications is rejecting electromagnetic interference (EMI) from the environment. Furthermore, the inductive loops must enclose a larger, rectangular area on the garment as opposed to the thread-like piezoresistive and coaxial capacitive designs. The aspect ratio varies during actual use and the sensor is not specific to uniaxial strain. Competing effects (i.e., Poisson effect) of decreasing width and increasing length when stretching along only one axis causes the sensor to have lower sensitivity than expected because the inductive signal is proportional to total area.

Herein, the performance of several ML models of increasing complexity are investigated when they are paired with different sensor types. The baseline performance of the sensors are compared with and without predictive modelling to examine its effect on strain-signal accuracy and how this would translate to wearable devices. The use of ML to compensate for undesirable sensor effects is explored and future areas of research to improve sensor design and performance are proposed. The performance of the sensors and ML models is probed by utilizing a random strain pattern that can be both visualized and statistically analyzed for performance improvements. Thus, by taking advantage of the computing power available in modern low-cost microcontrollers, ML may enable the use of simpler sensors and electronics with accuracy and range not yet realized.

2 MATERIALS AND METHODS

2.1 Strain Sensor Fabrication

Two piezoresistive strain sensors, a capacitive, and an inductive sensor were used in this study. Each of these sensors are fiber-based to enable integration into textiles for quantitative motion tracking. The piezoresistive and capacitive sensors were produced using the same conductive composite of Hytrel 3078 (DuPont; Kingston, ON, Canada) and carbon black. Two different core filaments [Hytrel 3078 (H3078) monofilament and polyether urethane-urea (PEU) multifilament fiber] were used to understand the differences that mechanical supports have in affecting the piezoresistive signal. The inductive sensor was composed of an elastic fiber and coiled copper wire—it did not include any conductive composite. The sensors were fabricated as follows:

2.1.1 H3078-Core Piezoresistive Sensor (R-H3078)

A sensor with a piezoresistive sheath around a TPE core (*R-H3078*) was fabricated as described previously (Rezaei et al., 2019). A filament of H3078 TPE was extruded and dip coated once into a 50 wt% solution of H3078 and carbon black (Cabot Vulcan XC-72R; Alpharetta, GA, United States) in dichloromethane (5 wt% w.r.t. H3078) producing a fibre with 450 μm diameter, as shown in **Figure 1A**. The sensor samples were conditioned by subjecting them to 100 repeated cycles of stretching from 0–40% strain on a linear stage. The R-H3078 sensor had an unstrained specific resistance of 1.3 kΩ cm^{-1}.

2.1.2 PEU-Core Piezoresistive Sensor (R-PEU)

A second type of sensor with a piezoresistive sheath around a PEU core (*R-PEU*) was fabricated as described previously (Rezaei et al., 2019). A mixture of 50 wt% H3078 and carbon black in dichloromethane (5 wt% w.r.t. H3078) was used to dip coat a multifilament Dorlastan PEU fibre (Asahi Kasei; Düsseldorf, Germany) once, resulting in a final diameter of 600 μm (**Figure 1B**). These sensor samples were also conditioned by subjecting them to 100 repeated cycles of stretching from 0–40% strain. The R-PEU sensor had an unstrained specific resistance of 82 Ω cm^{-1}.

2.1.3 Coaxial Capacitive Sensor (C)

A capacitive sensor (*C*) was produced as previously described (Geng et al., 2020). H3078 was extruded at 190°C to a diameter of

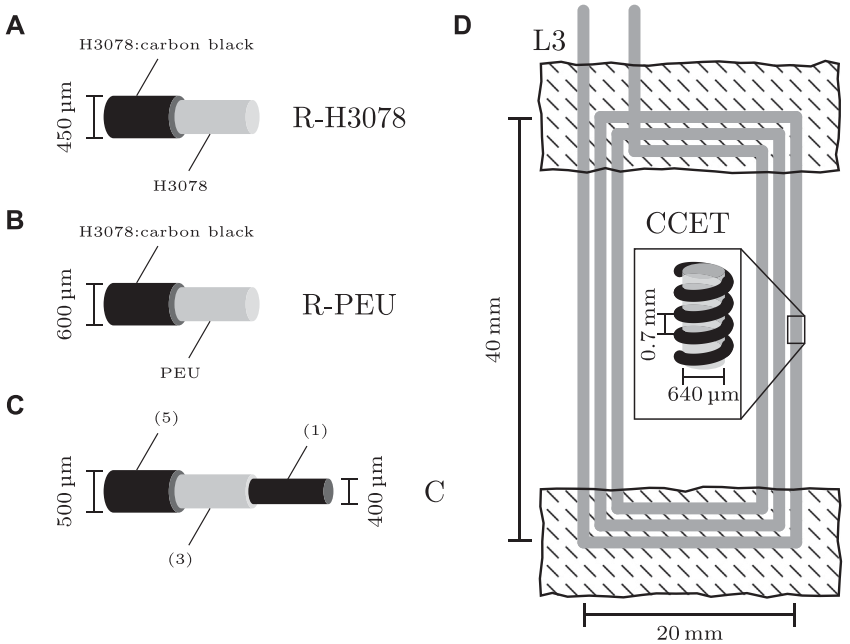

FIGURE 1 | (A) Schematic of the R-H3078 sensor, consisting of extruded TPE core (grey) and dip-coated piezoresistive sheath (black). **(B)** Schematic of the R-PEU sensor consisting of PEU core filament (grey) and dip-coated piezoresistive sheath (black). **(C)** Schematic of the C sensor consisting of conductive core electrode (referred to as (1) in text), dielectric layer (3), and outer conductive electrode (5). The intermediate layers referenced in the text as (2) and (3) are not shown. **(D)** Schematic of the L3 inductive patch sensor containing three perimeter loops (thick grey), fabric backing (hatched area), and close-up inset of the CCET with copper wire (black) coiled around an elastic thread (grey).

400 µm. The filaments were cut into 5 cm samples and dip-coated with a total of five layers: 1) 50 wt% H3078/carbon black in dicholormethane (5 wt% w.r.t. H3078); 2) polystyrene-ethylene-*co*-butylene-styrene (SEBS) in hexanes (5 wt%); 3) H3078 in dichloromethane (5 wt%); 4) SEBS in hexanes (5 wt%); 5) 50 wt% H3078/carbon black in dichloromethane (5 wt% w.r.t. H3078). Between dip-coating steps 1) and 2) the filament was inverted to ensure the inner electrode was accessible for electrical connection. Each dip-coated layer was allowed to dry before the next layer was added. After layer 5) was added, the sensors were put into a vacuum oven overnight at 60°C to ensure all volatiles were removed. The final diameter of the sensor was 500 µm (**Figure 1C**). The C sensor had an unstrained specific capacitance of 2.8 pF cm^{-1}.

2.1.4 Inductive Patch Sensor (L3)

An inductive sensor with three perimeter loops (*L3*) was fabricated as described in previous work (Tavassolian et al., 2020). Copper wire was coiled around a spandex elastic thread (diameter: 640 µm) using a custom-built machine to form a copper-coiled elastic thread (CCET). The feed rate of the thread was adjusted to obtain a helical coil with a pitch (spacing between coils) of 0.7 ± 0.1 mm. The CCET was then arranged in a rectangular pattern of three perimeter loops with approximate width of 2 cm and length of 4 cm. Rectangles of fabric backing were sewn along the width segments to provide a gripping surface for testing. The inner area of the sensor had an air gap. A schematic of this type of sensor is shown in **Figure 1D**.

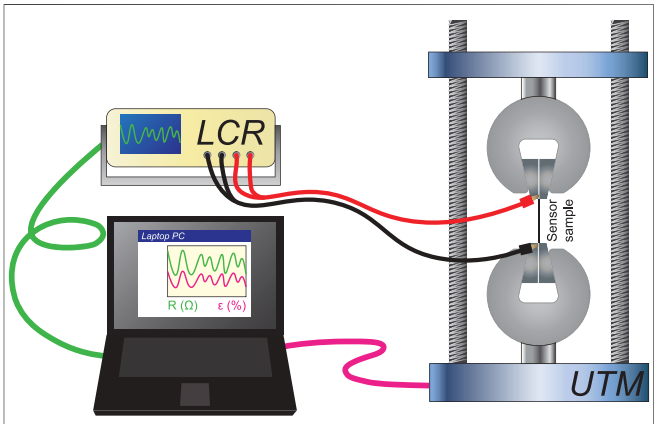

FIGURE 2 | A schematic of the experimental set-up, consisting of a universal testing machine (UTM) driven to strain a sensor sample, inductance-capacitance-resistance (LCR) meter for sensor measurement, and laptop PC to control the UTM and log the resulting strain and sensor signal data.

The L3 sensor had an unstrained specific inductance of 52 nH cm^{-1} in the length direction.

2.2 Experimental Set-Up

The experimental set-up, shown in **Figure 2**, consisted of one of the four sensor types (exposed length: 37.35 ± 5.36 mm) mounted vertically in an Instron E10000 universal testing machine (UTM)

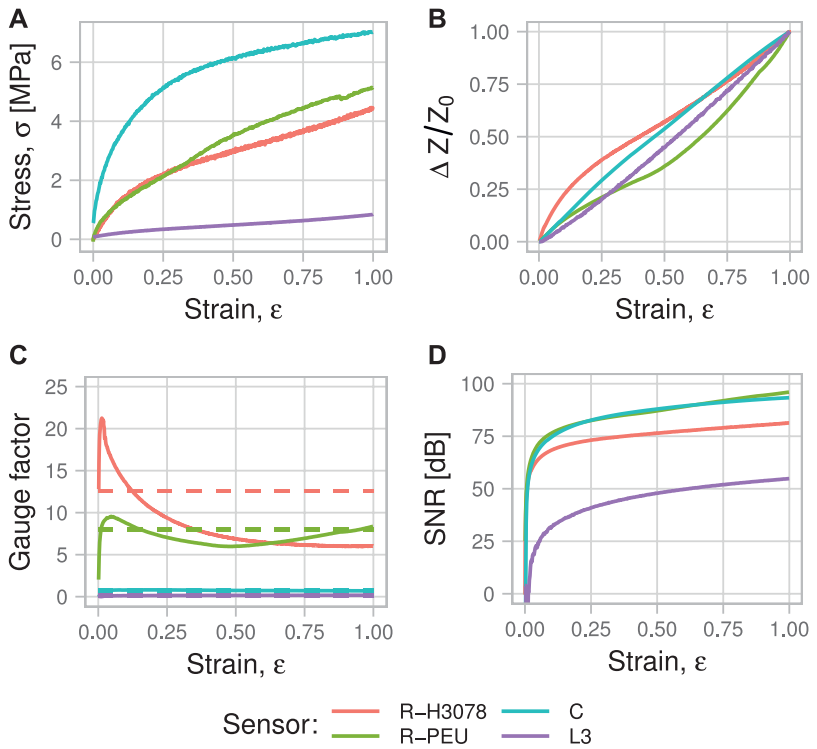

FIGURE 3 | (A) Mechanical stress-strain curves for each sensor, **(B)** sensor output signal during the elongation, **(C)** instantaneous (solid) and average (dashed) gauge factor, **(D)** signal-to-noise ratio.

(Instron; Norwood, MA, United States). A layer of electrical tape provided an even clamping force and insulated the sensors from the metal holding jaws. A strip of copper foil tape was used to connect the sensor electrodes to external electrical connections. The UTM used a 10 kN load cell sampling at 100 Hz and was subjected to linear displacement only (no torsional displacement).

Specimens were positioned in the clamps with approximate lengths of 40 mm, and the UTM cross head was retracted until the samples were just taut with minimal strain. The sensor length was manually measured and used as the reference length for 0% strain, ℓ_0. For each test, the UTM was programmed to follow preprogrammed displacement profiles. These profiles were scaled relative to ℓ_0, ensuring consistent strain among sensor samples.

The electrical response of each sensor, regardless of modality, was acquired by an Agilent E4980A precision inductance-capacitance-resistance (LCR) meter (Agilent; Santa Clara, CA, United States) with four-lead probe. The meter was configured in the mode suitable for the corresponding sensing modality and interfaced with a PC using a custom MATLAB script (The Mathworks; Natick, MA, United States). For each test, the raw impedance (resistance, capacitance, or inductance, denoted as Z) was normalized to its value at zero strain, Z_0 and expressed as the ratio $Z - Z_0/Z_0$. Mechanical data from the UTM was converted to strain $\varepsilon = \ell - \ell_0/\ell_0$ and down-sampled to match the 55 Hz LCR sampling frequency.

3 RESULTS

3.1 Tensile Stress-Strain Curve

Samples were subjected to a stress-strain test from 0–100% strain at a strain rate of 1%/s. The purpose of this test was to quantify the gauge factor, linearity, and working strain region. Plastic deformation was observed for all four specimens upon return from the strain cycle. The R-H3078 sensor elongated by 9.6%, the R-PEU sensor by 7.0%, the C sensor by 21.7%, and the L3 sensor by 1.9% compared to their pre-test length. The yield point of these thermoplastic elastomers was not abrupt and was observed as a gradual change in slope (**Figure 3A**). The elastic region, and therefore the working region, was previously found to be <30% strain for the piezoresistive fibres and this range was reasonable for use with all the sensor types (Rezaei et al., 2019). Within the working region, the Young's modulus (stiffness) for the R-H3078, R-PEU, C, and L3 sensor types was 7.4, 6.9, 13.6, and 0.94 MPa, respectively. Stress and therefore stiffness for the L3 sensor was computed per fibre, of which there were six in parallel mechanically in the three-loop configuration.

The linearity in the working strain range was measured by the coefficient of determination (R^2) between the strain and the $\Delta Z/Z_0$ signal scaled to the range $[0, 1]$. The R-H3078, R-PEU, C, and L3 sensors had R^2 values 0.962, 0.986, >0.999, and 0.997, respectively. The GF may be calculated

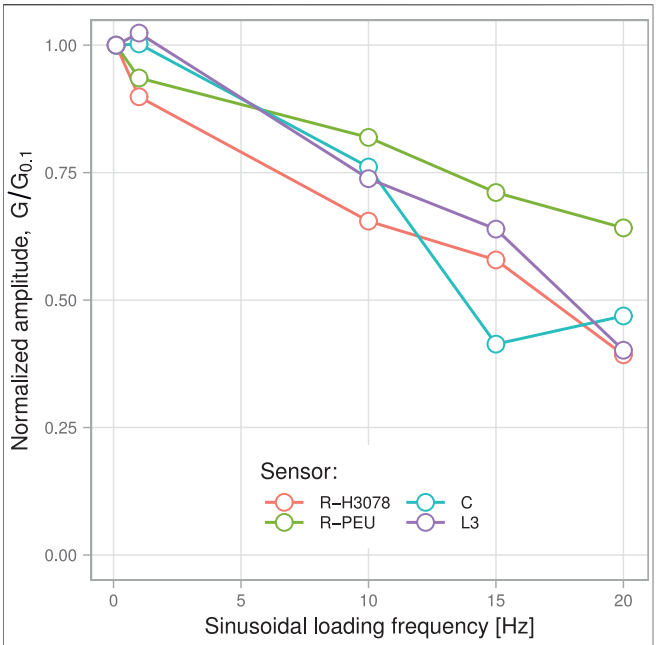

FIGURE 4 | Decreasing sensor response under sinusoidal strains of 0.1, 1, 10, 15, and 20 Hz; normalized to the 0.1 Hz trial.

conventionally, shown in **Eq. 1**, or by using the modified **Eq. 2** that reduces the influence of the signal value at zero strain (Liu et al., 2018b).

$$GF = \frac{Z - Z_0}{Z_0(\varepsilon - \varepsilon_0)} \tag{1}$$

$$GF^* = \frac{dZ}{Z \cdot d\varepsilon} \tag{2}$$

The conventional GF for the R-H3078, R-PEU, C, and L3 sensor was 12.6 ± 3.3, 8.0 ± 1.1, 0.77 ± 0.10, and 0.12 ± 0.03 [mean ± standard deviation (SD) over the working strain range]. The mean GF* was 4.2, 3.7, 0.72, and 0.14, respectively, using **Eq. 2**. Taking a 2.5 s period of zero strain just prior to the tensile test as a baseline, the signal-to-noise ratio (SNR) was defined as **Eq. 3**, where $\Delta Z = Z - Z_0$ is the change in raw sensor signal as the sample is strained and σ_b is the SD of the baseline.

$$SNR = \frac{\Delta Z}{\sigma_b} \tag{3}$$

The R-H3078, R-PEU, C, and L3 sensors showed 84, 99, 94, and 55 dB SNR, respectively. The engineering stress, signal, GF, and SNR curves are shown across the 0–100% strain range in **Figure 3**.

3.2 Sensor Bandwidth

To evaluate the loading frequency dependence of the signal, the UTM was configured to produce five sinusoidal strain patterns of increasing frequency, shown in **Supplementary Table S1**. The peak velocities (strain rates) experienced by the sensors ranged from 0.63 mm s^{-1} (1.6%/s) to 126 mm s^{-1} (314%/s).

Constrained by the LCR sample rate of 55 Hz, it is unlikely to observe a sample point at an exact maxima or minima of the sinusoidal signal during high frequency movement. This makes it difficult to reliably observe the change in signal amplitude with respect to loading frequency in the time domain. To establish whether any drop-off in sensor response occurred as loading frequency was increased, a frequency domain approach was used for greater robustness near the Nyquist rate of the LCR. Both the strain, derived from the UTM displacement, and sensor signals were fast Fourier transformed (FFT), then the FFT signal index (bin) corresponding to each loading frequency was identified. The ratio of the sensor signal FFT bin to the strain FFT bin was calculated for each frequency to produce a strain-to-signal gain metric *G*. This method should eliminate the effect of any reductions in the UTM stroke amplitude as frequency is increased. More details about the frequency-domain method are available in **Section 2** of the **Supplementary Material**. Finally, these data were normalized to the *G* obtained with the lowest loading frequency (i.e., $G_{0.1} := 1$ for each series) to show the attenuation of sensor signal with increasing strain frequencies. The results are plotted in **Figure 4**.

3.3 Signal Hysteresis

Hysteresis is a common nonlinear effect in piezoresistive strain sensors, because the re-aggregation of filler particles and thus formation of conductive pathways may be slow relative to the strain cycles (Stübler et al., 2011). Other sensor types can suffer from mechanical hysteresis of the polymer material that manifests in the signal. A test devised to measure the hysteresis of each sensor type involved straining to six levels with a symmetrical return to zero between each run at a constant strain rate (**Supplementary Table S2**).

The sensor signal recorded during individual runs are superimposed in **Figure 5A**. The two resistive sensors showed clockwise signal hysteresis loops, becoming larger in area with less positive slope as the strain maximum was increased. The sensor signal was slightly elevated upon each return to zero for the R-H3078 sensor as well as the R-PEU and C sensors, to a lesser extent. The L3 sensor showed the opposite, with considerable signal undershoot upon return to zero strain.

One way to compare hysteresis between the sensors is to measure the area encircled by each hysteresis loop (AUC), shown in **Figure 5B** (Isaia et al., 2020). Multiple loops caused by self-intersection, if present, were summed in absolute area. For a meaningful comparison despite large differences in signal level between sensors, the signal was min-max normalized following **Eq. 4**.

$$\overline{Z} = \frac{Z - Z_0}{Z_{30} - Z_0} \tag{4}$$

The C sensor had approximately one seventh the hysteresis area of the R-H3078, R-PEU, or L3 types. Both piezoresistive sensors had similar hysteresis that increased linearly with strain maximum. The R-PEU sensor had greater consistency between runs, especially at higher maximum strains. The L3 sensor showed a linear increase in hysteresis area with strain while the C sensor hysteresis are appeared exponential with respect

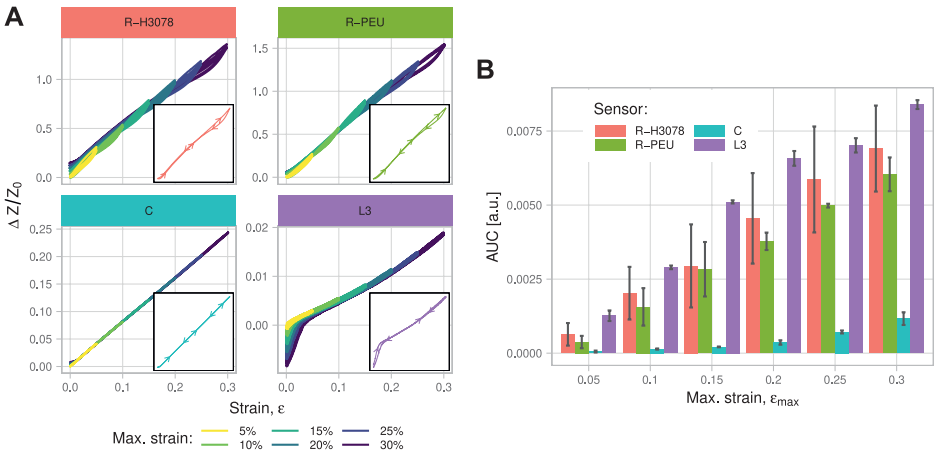

FIGURE 5 | Results of the hysteresis test. **(A)** The overlaid sensor responses to a triangular strain pattern with the directionality of the hysteresis loop at 30% strain shown (inset). **(B)** Hysteretic loss by sensor type and maximum strain level. Error bars indicate the standard deviation of 3 sequential trials.

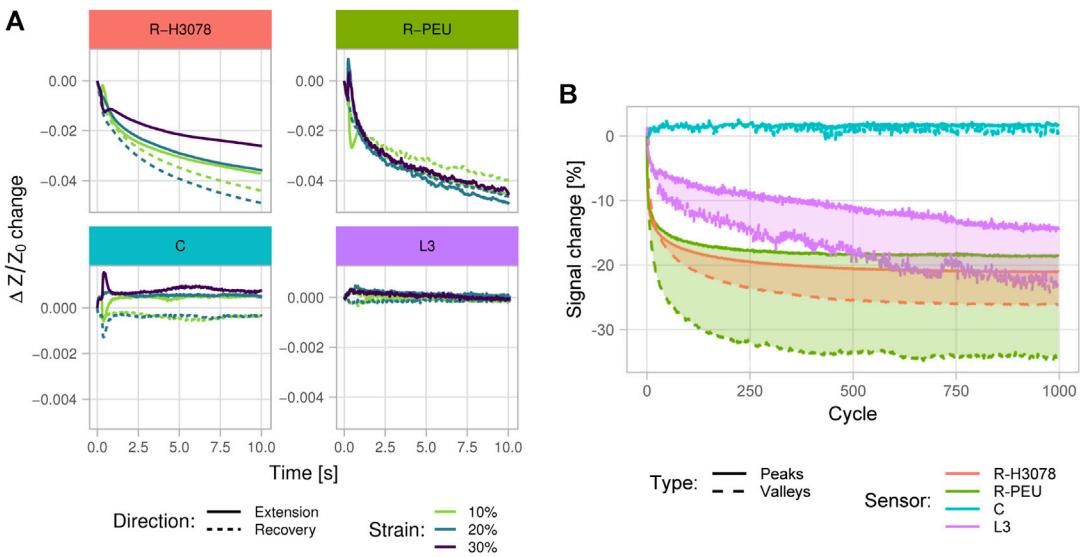

FIGURE 6 | Static **(A)** and dynamic **(B)** drift in the sensors. **(A)** Change in sensor signal reading from baseline over a 10 s hold at three strain magnitudes. For increased detail despite a lower sensitivity, the vertical scale of the non-resistive sensors (bottom) is enhanced by a factor of 10. Note that the small transient spike seen around 0.5 s is an artifact that was due to a correction from the UTM positioning algorithm. **(B)** Sensor signal drift over 1,000 sinusoidal strain cycles. Solid lines indicate the percentage change in signal peaks and dashed lines indicate the percentage change in signal valleys relative to the first cycle.

to strain, albeit having a much lower magnitude. The undershoot at low strains observed with the L3 sensor was the primary contributor to its AUC, with 54% of its total hysteresis AUC attributable to strains below 5%.

3.4 Signal Drift

3.4.1 Static Drift

Rate-dependent hysteresis, material stress relaxation, and temperature changes may contribute to drift of the sensor signal under a constant strain. The test profile (**Supplementary Table S3**) drove the UTM following a round-trip staircase displacement pattern of up to 30% strain with a hold of 30 s between each step to capture any signal drift. The step profile further allowed the analysis of static drift by comparing the signal drift at different strain levels and approaching those strain levels from lower (extension direction) or higher (recovery direction) preceding strain values.

Static signal drift shown in **Figure 6A** was found to be influenced by strain magnitude, hold duration—and sometimes—direction of the preceding strain step. The R-H3078 sensor showed monotonic decreases in resistance over time for all cases with the extension direction having less

drift than the recovery, although this could be confounded by the ordering of the strain pattern where all extension steps were done prior to all relaxation steps. For the resistive sensors, the $\Delta R/R_0$ drift was mostly independent of strain amount. The drift observed from the R-PEU sensor was similar in magnitude to that of the R-H3078, although with less directionality dependence. The C and L3 sensors showed opposite drifts in signal depending on the directionality of the preceding strain step. Aside from the small change within the first 1 s, the C sensor was very stable and quickly reached steady-state. The L3 sensor had large initial drift, but all trials converged to with 1% of the initial value after 10 s.

3.4.2 Dynamic Drift

For reliable tracking over many sessions, a wearable sensor must give a repeatable signal in response to a given strain. The dynamic drift test (**Supplementary Table S4**) was designed to evaluate sensor resilience and signal drift under cyclic strain. The sensors underwent 1,000 sinusoidal loading cycles from which the initial and final sections may be compared to observe changes in signal amplitude.

As shown in **Figure 6B**, the piezoresistive sensors had large decreases in response that mostly stabilized within 100 cycles. The L3 sensor had a lower rate of decrease in response but the drift persisted to 1,000 cycles. The C sensor was relatively unaffected by drift, having a small increase in capacitance throughout the first 10 cycles before steady-state response. For all sensor types, the drift behaviour at high and low strains were found to be consistent since the signal peaks and valleys drifted by similar amounts.

3.5 Machine Learning

Regression algorithms were used to predict strain from sensor signals in the presence of nonlinearities. A random UTM displacement signal was produced by generating a random time series normalized such that the points lie in a $[0, 1]$ range, then scaling and biasing this reference signal for each sensor so that the sample is strained between 5–15%. The reference signal was spline interpolated and low-pass filtered so that the final maximum velocity (strain rate) was 10 mm s^{-1} (25%/s). The data collected during the random strain test served as training and test sets for the regression algorithms.

Four regression models plus one model-free scaling approach were compared using 5-fold time series splitting of the random strain data. Training data consisted of the first 10, 20, 30, 40, and 50 s of the data for each fold, respectively, and testing data consisted of the 10 s immediately following the training set. This procedure was chosen over conventional 5-fold cross validation because the SVR, RF, and RNN models (described below) require contiguous past data for training.

A baseline for comparing regression models was a min-max scaling of the sensor signal. Scaling was done so that the signal minimum and maximum were equal to the strain minimum ($\varepsilon = 5\%$) and maximum ($\varepsilon = 15\%$), respectively. The scaling was performed once on the last 50 s of the data set because the dynamic drift effect led to high errors in the initial strain spikes. Fit metrics were computed per fold. The first model considered was a linear regression (LR) completed on each fold. The LR model is essentially the optimal linear scaling that minimizes the mean squared error (MSE) on that fold.

The random forest (RF) and support vector regression (SVR) models are capable of nonlinear regression and were trained over a sliding window of the past 32 sample points or 0.6 s. Parameters were tuned using a coarse grid search followed by *ad-hoc* fine tuning and were kept the same for all sensors. The RF algorithm had 30 decision trees and the SVR used radial basis functions with $\gamma = 0.005$ and $C = 0.1$.

The last model of interest was a recurrent neural network (RNN) with 32 recurrent units followed by one fully connected layer, a total of 2,113 parameters. The recurrent units used the rectified linear unit (ReLU) activation function and the dense layer used linear activation. An MSE loss function was used for backpropagation and the recurrent layer had ℓ_2 regularization with a penalty factor of 0.01. The RNN model was also trained with the 32-element sliding window, however, 30% of test data were reserved for validation. The stopping condition for training was a non-decreasing validation MSE over 200 consecutive iterations, typically terminating after 300–700 iterations for the largest fold.

The output of each sensor split by model is shown in **Figure 7A**. The quality of the regression model fit on the test data for each fold was measured by the R^2 and root mean squared error (RMSE) with results shown in **Figures 7B,C**. The results on the first two folds were typically poor because they had a smaller fraction of training data. Average R^2 and RMSE across the last three folds under the best model for each sensor type compared to that of the scaling model are shown in **Table 1**, with more detail provided in **Supplementary Table S6**.

3.5.1 Effect of the Model on Regression Fit

A Tukey multiple comparison test was run using the results of the last three folds to compare the R^2 to discriminate models using a given sensor type. For the R-H3078 and R-PEU sensors, only the baseline scaling model had significantly worse R^2 than all others ($p < 0.001$). For just the R-H3078 sensor, the SVR model had significantly better R^2 than LR ($p < 0.05$), as did the RNN model vs. LR and RF ($p < 0.05$). For the C sensor, no statistically significant difference between any models was observed. The L3 sensor showed significantly better R^2 with the SVR model versus scaling, LR, and RF ($p < 0.05$). A similar pattern of results was produced with respect to RMSE, except with the SVR model no longer having significantly better RMSE over the LR model with the R-H3078 sensor nor over RF with the L3 sensor.

3.5.2 Effect of the Sensor Type on Regression Fit

The same test was run using the R^2 and RMSE values but using sensors rather than models as factors. The R-H3078 sensor had significantly worse R^2 than the other sensors across all regression models ($p < 0.05$), with its best R^2 and RMSE of 0.8947 and 0.0068, respectively, under the RNN model. The R-PEU sensor had significantly better R^2 versus the L3 sensor using LR and RF models ($p < 0.05$). With the RNN model, the R-PEU sensor achieved a best R^2 value of 0.9576 and RMSE of 0.0042. Regarding RMSE, the R-H3078 sensor again had significantly

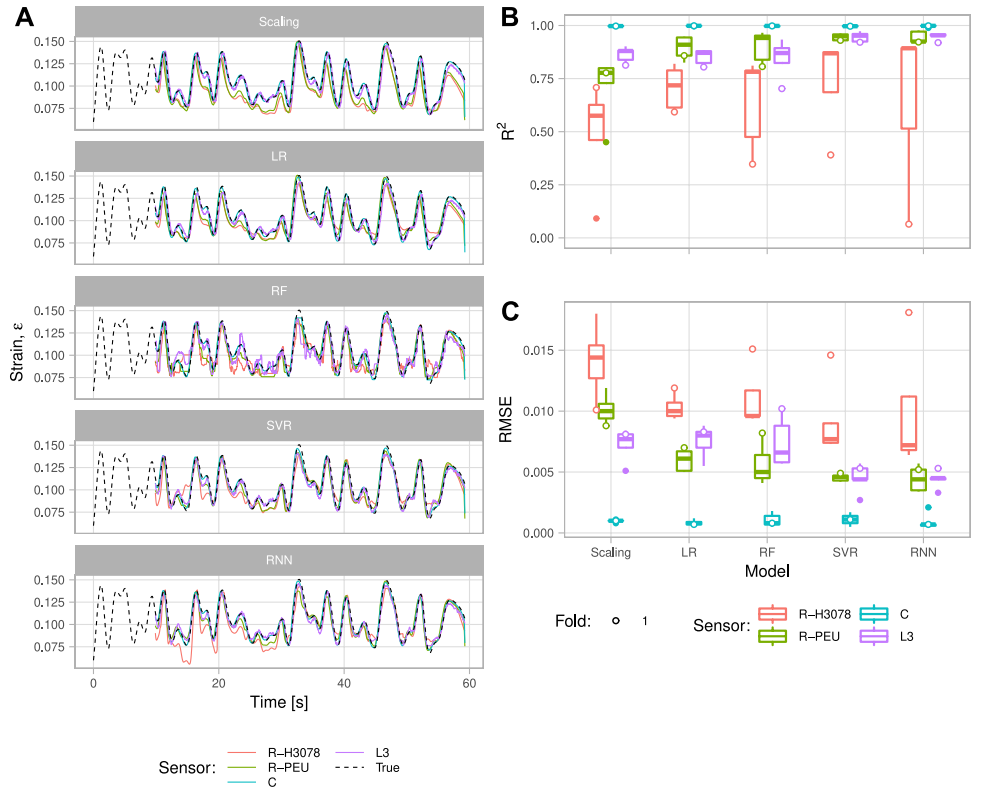

FIGURE 7 | Output traces **(A)** and performance **(B)**, **(C)** of the regression models trained on random strain data for each sensor type. **(A)** Strain estimated by each model for each sensor type (solid) and the actual strain (dashed) during the random strain test. **(B)** Box plots of the coefficient of determination for the four sensors and five regression models. Boxes indicate interquartile range (IQR) and whiskers extend to the smallest and largest observations that are up to 1.5 IQR from the boxes. Outliers are denoted with filled circles while goodness of fit values for the first fold, which often had poor results, are shown with open circles regardless of whether or not they are an outlier. **(C)** Box plots of the root mean squared error for the four sensors and five regression models.

TABLE 1 | Improvement in average R^2 and RMSE across the last three folds by the best performing model for each sensor type.

Sensor		R-H3078		R-PEU		C		L	
		R^2	RMSE	R^2	RMSE	R^2	RMSE	R^2	RMSE
Baseline		0.5541	0.0150	0.7759	0.0100	0.9977	0.0010	0.8668	0.0077
Best	Value	0.8947	0.0068	0.9576	0.0042	0.9979	0.0010	0.9548	0.0045
	Model	RNN	RNN	RNN	RNN	LR	LR	RNN	RNN
	% Change	+61.4%	−54.7%	+23.4%	−58.0%	0.0%	0.0%	+10.2%	−41.6%

worse RMSE than the other sensor types under all models ($p < 0.025$) while the C sensor had significantly better than all the other types ($p < 0.005$). Like in the R^2 case, the R-PEU sensor had significantly better RMSE than the L3 sensor using LR and RF ($p < 0.025$).

4 DISCUSSION

Three fundamentally different fiber strain sensor technologies have been reported previously—piezoresistive, capacitive, and inductive. Each sensor type has characteristics of differing importance when considering the application requirements. The majority of material science research on fiber strain sensors has focused on the increase of sensing range (% strain) and sensitivity (gauge factor). Both of these characteristics are dependent on the composition of the sensor and fabrication methods, important for widening the applications for flexible sensors in motion tracking. In theory, once a flexible sensor is incorporated into a device, the actual performance of the sensor is focused less on the accessible strain range and gauge factor, and more on the signal consistency and the characteristics that are unique to a type of sensor and motion of interest. These characteristics include strain rate and history dependence (hysteresis), gauge factor, linearity, and baseline drift, listed in **Table 2** for the sensors tested here. These factors are less prominently explored and can have a large impact on the

TABLE 2 | Summary table for the properties of each sensor studied with any test conditions noted in the comments column.

Parameter	R-H3078	R-PEU	C	L3	Comments
Young's Modulus	7.4 MPa	6.9 MPa	13.6 MPa	0.9 MPa	Per fibre
Plastic deformation	9.6%	7.0%	21.7%	1.9%	After 0–100% strain
Static linearity, R^2	0.962	0.986	>0.999	0.997	Signal-strain linear fit
Bulk impedance	1.3 kΩ cm^{-1}	82 Ω cm^{-1}	2.8 pF cm^{-1}	52 nH cm^{-1}	
Sensitivity, GF	12.6	8.00	0.77	0.12	Averaged over 0.01–30% strain range
Signal-to-noise ratio	74 dB	84 dB	84 dB	43 dB	At 30% strain
Strain bandwidth	39%	64%	48%	40%	Signal amplitude at 20 vs. 0.1 Hz
Hysteresis area	6.91 × 10^{-3}	6.04 × 10^{-3}	1.17 × 10^{-3}	8.39 × 10^{-3}	0–30–0% triangular strain profile
Static drift over 10 s	−2.2%	−2.9%	+0.3%	−0.1%[a]	After extension and hold at 30% strain
Drift over 1,000 cycles	−26%	−34%	+6.7%	−23%	Change in signal peaks

[a]*As seen in **Figure 6A**, the maximum drift for the L3 sensor is much higher than that of the C sensor, however, it stabilizes to within 0.1% after the 10 s hold period.*

performance of the sensor in a device beyond the proof-of-concept testing that is typically included in strain sensor reports. If the change of sensor characteristics is predictable, even if not initially obvious, the application of ML prediction models could rectify any perceived limitations and result in a higher tracking accuracy. To begin, three different types of sensors were tested to understand the baseline mechanical properties and identify each characteristic that could be improved with the application of ML. Additionally, two piezoresistive-type sensors (R-H3078 and R-PEU) with different structural core materials were tested to understand the effect of different mechanical properties using this popular type of sensor.

When tracking mechanical properties during extension, the stress-strain relationship of the polymer sensors (R-H3078, R-PEU, and C) in **Figure 3A** resembles the gradual decrease in slope with increasing strain reported for TPE-carbon black composites (Drozdov and Dusunceli, 2014). All sensors tested could withstand straining to 100%, indicating that they could tolerate large non-sensing strains which they might be exposed to when donning a garment, for example. The C sensor showed the largest amount of plastic deformation when straining to 100%, although it did not undergo pre-test conditioning which was standard for the other sensors. The L3 sensor was exposed to a lower engineering stress (per-fibre) because the three-loop design had six fibers running in parallel. The mechanical data collected during tensile testing established the elastic region of the sensors which can be useful to limit the amount of irreversible change to the sensors mechanical and electrical characteristics throughout the tests. Using a sensor beyond this region without a highly elastic support can result in a change in signal characteristics, such as gauge factor, by having an irreversible reduction in conductive pathways within the material—which was observed in both piezoresistive sensors. If this irreversible phenomenon occurs in a device that is attempting to track an output, the accuracy of the device post-strain would be impacted. Alternatively, if the irreversible reduction of the conductive pathways is predictable, then machine learning could enable the immediate improvement of device accuracy with enough training data.

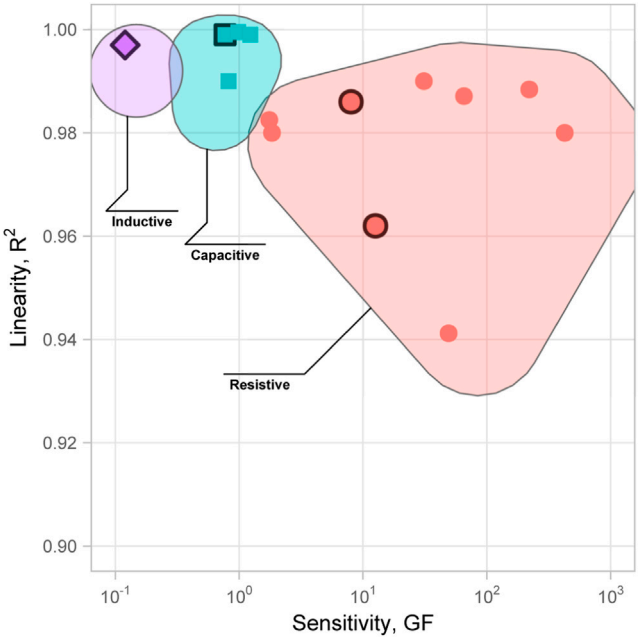

FIGURE 8 | The general trade-off between sensitivity, as measured by gauge factor, and linearity, as measured by R^2 of the linear fit between signal and strain. Clustering between sensor types is suggested by bounding polygons. Examples from literature were chosen that had published GF and R^2 data (see **Supplementary Table S9** for details) and the sensors fabricated in this research are highlighted with a black border.

Gauge factor is the primary sensor characteristic that relates signal response to strain. A constant, large GF is desirable since it enables linear correlations of signal to strain and increases resolution of small strains across a variety of pre-strains. High resolution is important for tracking fine movements such as facial expressions, where the range of strains is small (Yin et al., 2017). Gauge factors of piezoresistive sensors can vary over three orders of magnitude (**Supplementary Table S9**); ultimately, most piezoresistive sensors do not possess linear strain-to-resistance changes across both small and large strains. To compare the non-linear response of each sensor, a slow strain rate of 1%/s was used to reduce the possibility of other rate-dependent characteristics

impacting the gauge factor results. The increase in GF observed in the R-PEU sensor above 50% strain indicates that the disconnection of conductive pathways becomes the dominant piezoresistive mechanism and may be non-reversible upon release—entrance into this destructive mechanism of piezoresistive sensing is ideally avoided because it results in further negative sensor characteristics for accurate strain tracking such as unrecoverable drift. This motivated the choice to limit further testing to strains below 30% for all sensors. The gauge factor of the R-H3078 sensor peaked at low strain enabling high resolution for small signals. It displays a larger, although more variable, GF across the strain range decreasing from 5–100% strain. The R-PEU shows a more linear working region that persists to a strain of 50%. The nonlinear GF behaviour of both resistive sensors could pose significant negative effects to accuracy tracking. Linearity versus sensitivity is typically an area of trade-off between sensor mechanisms, as shown in **Figure 8**. The use of ML models to adapt to GF changes in response to certain strain magnitudes or strain rates could then improve the strain tracking accuracy.

C and L3 sensors have a lower GF equating to a reduced sensitivity. However, their GF is more constant across the strain range, bringing an increase in accuracy. These types of sensors have a sensing mechanism less dependent on the change of the conductive pathways that may undergo irreversible changes such as in a piezoresistive sensor (Busfield et al., 2003). Increased sensitivity allows the measurement of smaller strain signals using the same readout hardware. While machine learning algorithms may improve sensor accuracy, they offer no improvement to sensitivity. ML models operate after the signal has been digitized and thus are limited by the sensor GF, readout circuit, and ADC in resolving small strains. The reliance on a geometrical change for C and L3 sensors eliminates the negative effects observed in both the piezoresistive sensors and undoubtedly improved the accuracy of C and L3 sensors.

Motion tracking is not always focused on measuring fast, dynamic movements. Some motion tracking devices focus on slight changes in posture over long, nearly static periods. In these situations, signal stability at a static strain over time or between device uses may be more important than sensitivity. Inductive (L3) and piezoresistive (R-PEU/R-H3078) sensors all had signal drift of 3% or greater for 10 s holds at 30% strain, similar to what others have observed for composite sensors (Melnykowycz et al. (2014)). The L3 sensor stabilized during periods of static strain that lasted greater than 10 s, converging to within 1% of its initial value. Its repeatable drift, relatively independent of strain, is a characteristic where ML could impact the signal accuracy. Drift was not observed during the random motion testing for the C and L3 sensors whereas both piezoresistive sensors can be seen to drift following a strain maxima (**Figure 7A**, Scaling model). Machine learning was able to correct for this drift quite effectively and was observed in the last 5 s of the random motion plots in **Figure 7A** under the SVR and RNN models. However, the random strain testing patterns were quite short and lacked long static periods that could be used to quantitatively determine how much drift the machine learning compensated for.

Large numbers of repetitive cycles are likely in a lot of applications such as tracking gait parameters. Unsurprising, the C sensor was quite stable, with its reliance on the geometrical change of the fibre, as shown in **Figure 6A**. Both piezoresistive sensors stabilized after 250 cycles, indicating that sensors required for wearable devices need robust conditioning prior to use. Conditioning could reduce dynamic drift which would decrease the size of the ML training dataset required to predict this type of behaviour. The L3 sensor drifted over the 1,000 cycles at a nearly constant rate, which could allow a simpler ML model to extrapolate the baseline change more easily. The use of simpler models trained with limited data is highly useful for using these devices with ML in actual settings and will be a focus of future research.

The last sensor characteristic that can hinder performance is related to the loading frequency and rate of change of strain. Some applications require the measurement of high frequency strains, such as detecting physiological finger tremors around 6–30 Hz or shank impact shock around 4–40 Hz (Winslow and Shorten, 1989; Raethjen et al., 2000). As loading frequencies are increased, signals can be attenuated by hysteresis (Oliveri et al., 2019; Geng et al., 2020). The effect of high frequency strain on the accuracy and performance of wearable devices using strain sensors has not been extensively explored. A comparison by Shintake et al. that reported a stable signal for both resistive and capacitive sensor types at a maximum tested velocity (strain rate) of 25 mm s^{-1} (50%/s) (Shintake et al., 2018). A reduction in the accuracy of the signal could be from either mechanical lag directly correlated to the materials that comprise the sensor, or an effect from the mechanism of sensing (Costa et al., 2015). The comparison of the C and R-H3078 sensors demonstrates that the piezoresistive signal hysteresis is dominant at low loading frequencies because both sensors are comprised of the same materials, but the sensing mechanism of the C sensor eliminates the hysteresis associated with the piezoresistive material by relying on geometrical changes rather than electrode resistivity. As loading frequency increases (**Figure 4**, the C sensor performance starts to attenuate at a similar rate to the R-H3078 sensor indicating that the mechanical hysteresis phenomenon reduces the tracking performance of both sensors. In contrast, the R-PEU sensor was capable of resolving strain rates up to 126 mm s^{-1} with an attenuation of 36%—the best of the sensors tested and can be attributed to the highly elastic and resilient PEU-core (Reza et al., 2019). The R-H3078, C, and L3 sensors had 61%, 52%, and 60% attenuation, respectively. Piezoresistive rubber composites have been shown to measure in excess of 350 mm s^{-1} (7000%/s) (Boland et al., 2014). While hysteresis is dependent on the history of the material, ML training with a broad variety of strain patterns and rates could enable the ML to efficiently predict when this phenomenon is causing a reduction in accuracy. Hysteresis was observed in the random strain testing predominantly immediately after large strains followed by faster and smaller strains in **Figure 7A**. This would be compounded at higher frequencies and could saturate the strain signal leading to a loss of tracking accuracy. Development of high strain bandwidth sensors likely requires more elastic and resilient polymers to reduce any mechanical

hysteresis, while ML could be implemented to extend the range of strain frequencies that current sensors can track efficiently.

Each of the characteristics that have been discussed thus far are responsible for the performance of a strain tracking sensor. To gauge the performance of different ML models between different sensing mechanisms, a random strain pattern was generated that had a range representative of what a wearable device for running or walking might produce (Rezaei et al., 2019; Geng et al., 2020; Tavassolian et al., 2020). Different models attempt to predict the applied strain with the resulting signal change—the simplest model being a linear correlation. It was hypothesized that certain combinations of sensors and models may be more accurate when predicting strain by recognizing certain characteristics more efficiently. For instance, sensors with higher degrees of nonlinearity may require a nonlinear regression model (RF, SVR, RNN) to sufficiently correct their signal. The capacitive sensor had an inherently linear response and therefore did not benefit from any ML models. In comparison, the piezoresistive sensors have many characteristics that decrease the accuracy of the strain-signal tracking. The R-PEU linearity was improved by 23% and error reduced by 58% with the RNN model compared to the baseline (scaling) model. Similarly, the same model improved the R-PEU linearity by 61% and reduced fit error by 55% over scaling. The RNN model performed the best, in general, having the highest average R^2 and lowest average RMSE the context of the random strain experiment. While choosing the best material for the application was shown to be important for applications that require high strain frequencies (specifically elastic and resilient materials such as PEU), ML models have the capability of improving the performance of the devices in the range acceptable similar to optical motion capture devices without the spatial limitations. The advantage of using a combination of R-PEU with a ML model over the C sensor is that the sensor retains its high GF and bandwidth not currently attainable with the capacitive technology. For practical purposes, the simpler analog circuitry needed for resistive sensors and the availability of inexpensive digital computing power to run a model further create scenarios where a piezoresistive sensor would be preferred over the highest performing C sensor. Given the fact that the training dataset used was small and the ability for neural network models to improve with a large amount of data, RNN is a promising model architecture to explore further. The RF model would likely also benefit from a more diverse training dataset because its decision trees were unable to extrapolate accurate predictions outside the training set.

All sensors studied here consist of a single fiber and may be easily incorporated into a garment in areas subject to strain as a linear segment or rectangular patch. Sensors may be anchored to the base textile by means of cross-stitching or encapsulation between layers of fabric. Resistive sensors have the advantage of being read with a simple voltage divider rather than the LC-tank, bridge, or impedance measurement circuit required for the other types. Especially for multichannel systems, resistive sensor arrays with simple interfacing may lead to a significantly reduced number of components and therefore circuit cost. Multichannel systems are common approaches to motion tracking using wearable sensors and the large amount of data collected make such systems a good target for ML improvements. The susceptibility of inductive sensors to noise was observed with the inductive sensor having the lowest SNR in **Table 2** and a higher noise floor in **Figure 6A**. The issue of noise susceptibility with inductive and even un-shielded capacitive sensors have been reported (Yang et al., 2017; Patiño et al., 2020). A summary of qualitative factors relating to the practicality of using each sensor type is shown in **Table 3**. The acquisition hardware used in this study was limited to a sample rate of 55 Hz making measurements at high strain frequencies unreliable. The method used in *Sensor Bandwidth* attempts to quantify sensor response to strain rates near the LCR Nyquist frequency, but it would be useful to run a similar experiment with a faster sample rate to confirm the responses to strain rates above 20 Hz. The inclusion of tests to expose the limitations of sensor types that are often not reported combined with the machine learning model results gives insight into which types of limitations may be corrected with modelling, and to what degree, aiding future sensor development.

TABLE 3 | Ranking of sensors by their relative performance on several qualitative factors.

Factor	R-H3078	R-PEU	C	L
Cost	Low	Low	Low	Moderate
Susceptibility to EMI	Low	Low	Moderate	High
Intrusiveness	Low	Low	Low	Moderate
Readout circuit complexity	Low	Low	High	High
Manufacture difficulty	Moderate	Moderate	High	Low

5 CONCLUSION

Simpler to manufacture piezoresistive sensors may approach the high degree of strain tracking displayed by capacitive fiber sensors, when combined with machine learning. A piezoresistive sensor is a good candidate for situations with many channels or where high sensitivity is required for tracking fine movements. Piezoresistive sensors also show promise for use with high frequency strain signals, an area that has had relatively little research. Trained nonlinear regression models, such as the SVR and RNN architectures explored here, allow the designer to take advantage of the high sensitivity, bandwidth, ease of manufacturing, and simpler interfacing of piezoresistive sensors by compensating for most of the signal non-idealities. More research is needed into signal conditioning for the inductive sensor types to reduce noise and address the undershoot at low strains, although this technology also benefits from the incorporation of machine learning in its signal processing. Areas of future work may include exploring the direct prediction of joint angle from sensor data with machine learning and expanding the scope of the study to other sensor variants.

DATA AVAILABILITY STATEMENT

The raw data supporting the conclusions of this article will be made available by the authors, without undue reservation.

AUTHOR CONTRIBUTIONS

CM, TC, and BH contributed to conception and design of the study. BH wrote the first draft of the manuscript. BH and TC wrote sections of the manuscript. All authors contributed to fabrication of the samples, running of the experiments, manuscript revisions, and approval of the submitted manuscript version.

SUPPLEMENTARY MATERIAL

The Supplementary Material for this article can be found online at: https://www.frontiersin.org/articles/10.3389/fmats.2021.639823/full#supplementary-material.

REFERENCES

Boland, C. S., Khan, U., Backes, C., O'Neill, A., McCauley, J., Duane, S., et al. (2014). Sensitive, high-strain, high-rate bodily motion sensors based on graphene-rubber composites. *ACS Nano* 8, 8819–8830. doi:10.1021/nn503454h

Busfield, J. J., Thomas, A. G., and Yamaguchi, K. (2003). Electrical and mechanical behavior of filled elastomers. I: The effect of strain. *J. Polym. Sci. Part B Polym. Phys.* 41, 2079–2089. doi:10.1002/polb.20085

Chen, S., Liu, H., Liu, S., Wang, P., Zeng, S., Sun, L., et al. (2018). Transparent and waterproof ionic liquid-based fibers for highly durable multifunctional sensors and strain-insensitive stretchable conductors. *ACS Appl. Mater. Interfaces* 10, 4305–4314. doi:10.1021/acsami.7b17790

Choi, D. Y., Kim, M. H., Oh, Y. S., Jung, S.-H., Jung, J. H., Sung, H. J., et al. (2017). Highly stretchable, hysteresis-free ionic liquid-based strain sensor for precise human motion monitoring. *ACS Appl. Mater. Interfaces* 9, 1770–1780. doi:10.1021/acsami.6b12415

Clemens, F., Koll, B., Graule, T., Watras, T., Binkowski, M., Mattmann, C., et al. (2012). Development of piezoresistive fiber sensors, based on carbon black filled thermoplastic elastomer compounds, for textile application. *Adv. Sci. Technol.* 80, 7–13. doi:10.4028/www.scientific.net/ast.80.7

Cooper, C. B., Arutselvan, K., Liu, Y., Armstrong, D., Lin, Y., Khan, M. R., et al. (2017). Stretchable capacitive sensors of torsion, strain, and touch using double helix liquid metal fibers. *Adv. Funct. Mater.* 27, 1605630. doi:10.1002/adfm.201605630

Costa, P., Ribeiro, S., and Lanceros-Mendez, S. (2015). Mechanical vs. electrical hysteresis of carbon nanotube/styrene-butadiene-styrene composites and their influence in the electromechanical response. *Compos. Sci. Technol.* 109, 1–5. doi:10.1016/j.compscitech.2015.01.006

De Focatiis, D. S. A., Hull, D., and Sánchez-Valencia, A. (2012). Roles of prestrain and hysteresis on piezoresistance in conductive elastomers for strain sensor applications. *Plast. Rubber Compos.* 41, 301–309. doi:10.1179/1743289812Y.0000000022

Diani, J., Fayolle, B., and Gilormini, P. (2009). A review on the Mullins effect. *Eur. Polym. J.* 45, 601–612. doi:10.1016/j.eurpolymj.2008.11.017

Drozdov, A. D., and Dusunceli, N. (2014). Unusual mechanical response of carbon black-filled thermoplastic elastomers. *Mech. Mater.* 69, 116–131. doi:10.1016/j.mechmat.2013.09.019

Fleury, A., Sugar, M., and Chau, T. (2015). E-textiles in clinical rehabilitation: a scoping review. *Electronics* 4, 173–203. doi:10.3390/electronics4010173

Frutiger, A., Muth, J. T., Vogt, D. M., Mengüç, Y., Campo, A., Valentine, A. D., et al. (2015). Capacitive soft strain sensors via multicore-shell fiber printing. *Adv. Mater.* 27, 2440–2446. doi:10.1002/adma.201500072

Geng, W., Cuthbert, T. J., and Menon, C. (2020). Conductive thermoplastic elastomer composite capacitive strain sensors and their application in a wearable device for quantitative joint angle prediction. *ACS Appl. Polym. Mater.* 3, 122–129. doi:10.1021/acsapm.0c00708

He, Z., Zhou, G., Byun, J-H., Lee, S-K., Um, M-K., Park, B., et al. (2019). Highly stretchable multi-walled carbon nanotube/thermoplastic polyurethane composite fibers for ultrasensitive, wearable strain sensors. *Nanoscale* 11, 5884–5890. doi:10.1039/C9NR01005J

Isaia, C., McMaster, S. A., and McNally, D. (2020). "Study of performance of knitted conductive sleeves as wearable textile strain sensors for joint motion tracking," in 42nd annual international conference of the IEEE engineering in medicine & biology society (EMBC), Montreal, QC, July 20–24, 2020 (IEEE), 4555–4558.

Jung, Y., Jung, K., Park, B., Choi, J., Kim, D., Park, J., et al. (2019). Wearable piezoresistive strain sensor based on graphene-coated three-dimensional micro-porous PDMS sponge. *Micro Nano Syst. Lett.* 7, 1–9. doi:10.1186/s40486-019-0097-2

Kalantari, M., Dargahi, J., Kövecses, J., Mardasi, M. G., and Nouri, S. (2012). A new approach for modeling piezoresistive force sensors based on semiconductive polymer composites. *IEEE/ASME Trans. Mechatron.* 17, 572–581. doi:10.1109/TMECH.2011.2108664

Keulemans, G., Ceyssens, F., and Puers, R. (2017). An ionic liquid based strain sensor for large displacement measurement. *Biomed. Microdevices* 19, 1123–1126. doi:10.1007/s10544-016-0141-4

Kim, J-S., and Kim, G-W. (2017). Hysteresis compensation of piezoresistive carbon nanotube/polydimethylsiloxane composite-based force sensors. *Sensors* 17, 229–241. doi:10.3390/s17020229

Kim, S-R., Kim, J-H., and Park, J-W. (2017). Wearable and transparent capacitive strain sensor with high sensitivity based on patterned Ag nanowire networks. *ACS Appl. Mater. Interfaces* 9, 26407–26416. doi:10.1021/acsami.7b06474

Laskoski, G. T., Martins, L. D. L., Pichorim, S. F., and Abatti, P. J. (2009). "Development of a telemetric goniometer," in World congress on medical physics and biomedical engineering, Munich, Germany, September 7–12, 2009 (Berlin, Germany: Springer), 227–230.

Lee, J., Kwon, H., Seo, J., Shin, S., Koo, J. H., Pang, C., et al. (2015). Conductive fiber-based ultrasensitive textile pressure sensor for wearable electronics. *Adv. Mater.* 27, 2433–2439. doi:10.1002/adma.201500009

Liu, N., Fang, G., Wan, J., Zhou, H., Long, H., and Zhao, X. (2011). Electrospun PEDOT:PSS-PVA nanofiber based ultrahigh-strain sensors with controllable electrical conductivity. *J. Mater. Chem.* 21, 18962–18966. doi:10.1039/c1jm14491j

Liu, Z. F., Fang, S., Moura, F. A., Ding, J. N., Jiang, N., Di, J., et al. (2015). Hierarchically buckled sheath-core fibers for superelastic electronics, sensors, and muscles. *Science* 349, 400–404. doi:10.1126/science.aaa7952

Liu, Y., Wang, H., Zhao, W., Zhang, M., Qin, H., and Xie, Y. (2018a). Flexible, stretchable sensors for wearable health monitoring: sensing mechanisms, materials, fabrication strategies and features. *Sensors* 18, 645–680. doi:10.3390/s18020645

Liu, Y. F., Li, Y. Q., Huang, P., Hu, N., and Fu, S. Y. (2018b). On the evaluation of the sensitivity coefficient of strain sensors. *Adv. Electron. Mater.* 4, 1800353. doi:10.1002/aelm.201800353

Mengüç, Y., Park, Y.-L., Pei, H., Vogt, D., Aubin, P. M., Winchell, E., et al. (2014). Wearable soft sensing suit for human gait measurement. *Int. J. Rob. Res.* 33, 1748–1764. doi:10.1177/0278364914543793

Michel, S., Chu, B. T. T., Grimm, S., Nüesch, F. A., Borgschulte, A., and Opris, D. M. (2012). Self-healing electrodes for dielectric elastomer actuators. *J. Mater. Chem.* 22, 20736–20741. doi:10.1039/c2jm32228e

Miodownik, M., Oldfrey, B., Jackson, R., and Smitham, P. (2019). A deep learning approach to non-linearity in wearable stretch sensors. *Front. Robot. AI* 6, 27. doi:10.3389/frobt.2019.00027

Oliveri, A., Maselli, M., Lodi, M., Storace, M., and Cianchetti, M. (2019). Model-based compensation of rate-dependent hysteresis in a piezoresistive strain sensor. *IEEE Trans. Ind. Electron.* 66, 8205–8213. doi:10.1109/TIE.2018.2884204

Patiño, A. G., Khoshnam, M., and Menon, C. (2020). Wearable device to monitor back movements using an inductive textile sensor. *Sensors* 20, 905–922. doi:10.3390/s20030905

Patron, D., Mongan, W., Kurzweg, T. P., Fontecchio, A., Dion, G., Anday, E. K., et al. (2016). On the use of knitted antennas and inductively coupled RFID tags for wearable applications. *IEEE Trans. Biomed. Circuits Syst.* 10, 1047–1057. doi:10.1109/TBCAS.2016.2518871

Raethjen, J., Pawlas, F., Lindemann, M., Wenzelburger, R., and Deuschl, G. (2000). Determinants of physiologic tremor in a large normal population. *Clin. Neurophysiol.* 111, 1825–1837. doi:10.1016/S1388-2457(00)00384-9

Reza, M. S., Ayag, K. R., Yoo, M. K., Kim, K. J., and Kim, H. (2019). Electrospun spandex nanofiber webs with ionic liquid for highly sensitive, low hysteresis piezocapacitive sensor. *Fibers Polym.* 20, 337–347. doi:10.1007/s12221-019-8778-2

Rezaei, A., Cuthbert, T. J., Gholami, M., and Menon, C. (2019). Application-based production and testing of a core-sheath fiber strain sensor for wearable electronics: feasibility study of using the sensors in measuring tri-axial trunk motion angles. *Sensors* 19, 4288–4313. doi:10.3390/s19194288

Sardini, E., Serpelloni, M., and Ometto, M. (2012). "Smart vest for posture monitoring in rehabilitation exercises," in Proceedings of 2012 IEEE sensors applications symposium, SAS 2012 - proceedings, Brescia, Italy, February 7–9, 2012 (IEEE), 161–165.

Seyedin, S., Razal, J. M., Innis, P. C., Jeiranikhameneh, A., Beirne, S., and Wallace, G. G. (2015). Knitted strain sensor textiles of highly conductive all-polymeric fibers. *ACS Appl. Mater. Interfaces* 7, 21150–21158. doi:10.1021/acsami.5b04892

Shin, M. K., Oh, J., Lima, M., Kozlov, M. E., Kim, S. J., and Baughman, R. H. (2010). Elastomeric conductive composites based on carbon nanotube forests. *Adv. Mater.* 22, 2663–2667. doi:10.1002/adma.200904270

Shintake, J., Piskarev, E., Jeong, S. H., and Floreano, D. (2018). Ultrastretchable strain sensors using carbon black-filled elastomer composites and comparison of capacitive versus resistive sensors. *Adv. Mater. Technol.* 3, 1700284. doi:10.1002/admt.201700284

Stübler, N., Fritzsche, J., and Klüppel, M. (2011). Mechanical and electrical analysis of carbon black networking in elastomers under strain. *Polym. Eng. Sci.* 51, 1206–1217. doi:10.1002/pen.21888

Tavassolian, M., Cuthbert, T. J., Napier, C., Peng, J., and Menon, C. (2020). Textile-based inductive soft strain sensors for fast frequency movement and their application in wearable devices measuring multiaxial hip joint angles during running. *Adv. Intell. Syst.* 2, 1900165. doi:10.1002/aisy.201900165

Vu, C. C., and Kim, J. (2018). Human motion recognition by textile sensors based on machine learning algorithms. *Sensors* 18, 3109–3125. doi:10.3390/s18093109

Wang, H., Liu, Z., Ding, J., Lepró, X., Fang, S., Jiang, N., et al. (2016). Downsized sheath-core conducting fibers for weavable superelastic wires, biosensors, supercapacitors, and strain sensors. *Adv. Mater.* 28, 4998–5007. doi:10.1002/adma.201600405

Wijesiriwardana, R. (2006). Inductive fiber-meshed strain and displacement transducers for respiratory measuring systems and motion capturing systems. *IEEE Sens. J.* 6, 571–579. doi:10.1109/JSEN.2006.874488

Winslow, D. S., and Shorten, M. R. (1989). Spectral analysis of impact shock during running. *J. Appl. Biomech.* 8, 288–304. doi:10.1016/0021-9290(89)90511-3

Wu, X., Han, Y., Zhang, X., and Lu, C. (2016). Highly sensitive, stretchable, and wash-durable strain sensor based on ultrathin conductive Layer@Polyurethane yarn for tiny motion monitoring. *ACS Appl. Mater. Interfaces* 8, 9936–9945. doi:10.1021/acsami.6b01174

Yang, T., Xie, D., Li, Z., and Zhu, H. (2017). Recent advances in wearable tactile sensors: materials, sensing mechanisms, and device performance. *Mater. Sci. Eng. R Rep.* 115, 1–37. doi:10.1016/j.mser.2017.02.001

Yin, B., Wen, Y., Hong, T., Xie, Z., Yuan, G., Ji, Q., et al. (2017). Highly stretchable, ultrasensitive, and wearable strain sensors based on facilely prepared reduced graphene oxide woven fabrics in an ethanol flame. *ACS Appl. Mater. Interfaces* 9, 32054–32064. doi:10.1021/acsami.7b09652

Jia, F., Li, X., Peng, H., Li, F., Yang, K., and Yuan, W. (2019). A highly sensitive, multifunctional, and wearable mechanical sensor based on RGO/synergetic fiber bundles for monitoring human actions and physiological signals. *Sens. Actuators B* 285, 179–185. doi:10.1016/j.snb.2019.01.063

Zahid, M., Papadopoulou, E. L., Athanassiou, A., and Bayer, I. S. (2017). Strain-responsive mercerized conductive cotton fabrics based on PEDOT:PSS/graphene. *Mater. Des.* 135, 213–222. doi:10.1016/j.matdes.2017.09.026

Zhang, Z., Zheng, J., Wu, H., Wang, W., Wang, B., and Liu, H. (2012). Development of a respiratory inductive plethysmography module supporting multiple sensors for wearable systems. *Sensors* 12, 13167–13184. doi:10.3390/s121013167

Zheng, S., Wu, X., Huang, Y., Xu, Z., Yang, W., Liu, Z., et al. (2019). Highly sensitive and multifunctional piezoresistive sensor based on polyaniline foam for wearable Human-Activity monitoring. *Composites Part A* 121, 510–516. doi:10.1016/j.compositesa.2019.04.014

Conflict of Interest: The authors declare that the research was conducted in the absence of any commercial or financial relationships that could be construed as a potential conflict of interest.

frontiers in Materials

ORIGINAL RESEARCH
published: 28 May 2021
doi: 10.3389/fmats.2021.668125

Creep and Recovery Behaviors of Lithium-Based Magnetorheological Grease

*Xudan Ye and Jiong Wang**

School of Mechanical Engineering, Nanjing University of Science and Technology, Nanjing, China

This article studies the creep and recovery behavior of magnetorheological grease (MRG) under constant stress shear. The experiment is done by using a parallel plate rheometer with magnetron attachment and temperature control unit. The effects of constant stress, CI particle concentration, magnetic flux density and temperature on creep and recovery behavior are systematically studied. Experimental results show that as the constant stress increases, the response strain will also increase. The creep strain tested under zero field is higher than the value tested under a magnetic field, indicating that the creep and recovery behavior of MRG is highly dependent on the magnetic field strength. In addition, the creep and recovery behavior of MRG is greatly affected by temperature. Under the action of a magnetic flux density, the creep strain will decrease with the increase of temperature. The result is opposite at zero magnetic field.

Keywords: magnetorheological grease, rotating shear, creep and recovery behavior, magnetic field strength, creep

OPEN ACCESS

Edited by:
Xinglong Gong,
University of Science and Technology of China, China

Reviewed by:
Yangguang Xu,
China Academy of Engineering Physics, China
Song Qi,
Chongqing University, China

***Correspondence:**
Jiong Wang
wjiongz@njust.edu.cn

Specialty section:
This article was submitted to Smart Materials, a section of the journal Frontiers in Materials

Received: *15 February 2021*
Accepted: *19 April 2021*
Published: *28 May 2021*

Citation:
Ye X and Wang J (2021) Creep and Recovery Behaviors of Lithium-Based Magnetorheological Grease. Front. Mater. 8:668125. doi: 10.3389/fmats.2021.668125

INTRODUCTION

The time-dependent viscoelastic properties of polymer materials are mainly characterized by creep and recovery, which is an important standard to evaluate the dimensional stability of engineering materials (Xia et al., 2007; Iurzhenko et al., 2014; Chen et al., 2015). When the material is loaded with constant stress, the phenomenon that the strain will change with time is called creep. If the stress is removed instantaneously, the strain of materials changes with time without stress, and the phenomenon is defined as recovery. Research on creep and recovery behavior of viscoelastic materials is the main means to evaluate their properties, which provides theoretical support for its practical application.

The magnetorheological (MR) material is an intelligent material, it generally includes MR fluid (Cheng et al., 2021), MR gel (Mao et al., 2020; Zhang and Wang, 2020), MR elastomer (Yang et al., 2015; Fu et al., 2019) and MR grease (Ye et al., 2021). its rheological properties will change continuously, rapidly and reversibly under the external magnetic field. As an intelligent viscoelastic material, the creep and recovery behavior was studied by many scholars. Li et al. (2002) completed a study of the effects of magnetic field strength and temperature on creep behavior. The results indicated that MR fluids have two different viscoelastic behaviors. The behavior as linear viscoelastic bodies at small stresses. With increasing constant stresses, the MR fluids have nonlinear viscoelastic, viscoplastic and purely plastic properties at the same time. The creep and recovery behaviors of MR fluids can be explained by a typically thick column structure. Li et al. (2002), Weihua et al. (2010) studied the creep and recovery behavior of MR elastomers under constant stress. They established a four-parameter viscoelastic model to describe the creep behavior of the MR elastomer.

The comparison between the experimental results and the model prediction results shown that the model can well predict the creep behavior of the MR elastomer. Xu et al. (2012) investigated the creep and recovery behaviors of MR plastomer under constant stress and proposed a hypothesis to explain the temperature effect on the creep behaviors of the MR plastomer. The experiment showed that there are a great discrepancy in creep curves for the isotropic and anisotropic MR plastomer under an external magnetic field. Qi et al. (2016) investigated the creep and recovery behaviors of MR elastomers based on polyurethane/epoxy resin (EP) graft interpenetrating polymer networks. The experiment illustrated that the presence of interpenetrating polymer networks leads to a significant improvement of creep resistance of MR elastomers. Several theoretical models [i.e., Findley's power law model (Findley et al., 1977), Burgers model (Yao et al., 2013), and Weibull distribution equation (Fancey, 2005)] were used to simulate the creep and recovery of the specimens. The influence of EP content and magnetic field on the fitting parameters were discussed, and the corresponding physical mechanism was proposed to qualitatively explain it.

The magnetorheological grease (MRG), as a kind of MR material. It has the advantages of good anti-settling performance, less leakage, high MR effect and simple preparation. Thus, it has a good application prospect in various devices such as buffer (Ou et al., 2017; Ouyang et al., 2019), clutch (Kavlicoglu et al., 2013; Fernandez et al., 2018) and brake (Wang D. et al., 2019). At present, researchers have carried out a lot of research on the related properties (viscosity, shear stress, yield stress, storage modulus, and energy dissipation modulus, etc.) of MRG (Rankin et al., 1999; Park et al., 2011; Kim et al., 2012; Hu et al., 2015; Mohamad et al., 2016a,b, 2018; Wang H. X. et al., 2019). However, there are no published literature reports on the creep and recovery behavior of MRG.

Based on the existing research results of the creep and recovery behavior for smart materials, the creep and recovery test research for MRG is carried out, which provides theoretical guidance for the future and its applications. In this paper, The main contents of this paper are as follows. An advanced MR instrument was used to test the flow curve, creep and recovery behavior of MRG in shear mode. The effects of constant stress, magnetic field strength, CI particle content and temperature on creep and recovery behavior are systematically studied. The reasons that why the creep and recovery behavior are affected by different factors are analyzed and discussed.

EXPERIMENTAL TESTING

Materials Preparation

In this paper, MRG is made by uniformly mixing carbonyl iron powder and the grease. Among them, the carbonyl iron particles (dispersed phase) are purchased by BASF and the average particle size is 6 μm. Lithium-based grease is manufactured by Shell (china) Ltd. It is used as a carrier medium for magnetic particles. The physical properties of lithium grease are shown in **Table 1**. In this article, a MRG sample containing 70% carbonyl iron powder was prepared. The simple preparation process is shown in **Figure 1**. First, weigh 30 g of grease and pour it into a vial, then use a mechanical stirrer to stir at 800 rpm for about 10 min, and keep its temperature at 80°C. After the stirring is completed, 70 g of CI particles are poured into the stirred matrix. Finally, use a stirrer to thoroughly mix the grease and CI particles to obtain MRG. At this time, it is recorded as MRG-70. In addition, for experimental needs, a MRG with a mass fraction of carbonyl iron powder of 50% was also prepared. It is referred to as MRG-50 for short. Due to the unique characteristics of lithium-based grease in MRG, the sedimentation in the material is greatly reduced. Due to the unique characteristics of lithium-based grease in MRG, the precipitation in the material is greatly reduced.

TABLE 1 | Features of the grease used in this paper.

Product category	Gadus S2V220
NIGL grade	0
Soap base	Lithium
Kinematic viscosity @ 40°C, cSt	220
Kinematic viscosity @ 100°C, cSt	19
Base Oil	Mineral oil
ASTM worked penetration @ 25°C 0.1 mm	355–385

Creep and Recovery Behavior of Viscoelastic Materials

At a constant temperature, the creep and recovery curve of a typical viscoelastic material is shown in **Figure 2**. It can be seen from **Figure 2** that the strain of the material increases logarithmically with time in the stress section, that is, the creep stage. When the stress is removed, the strain of the material quickly decreases to a certain value, that is, the viscoelastic material is in the recovery stage. In **Figure 2**, τ_0 is a constant stress and γ is a strain.

Creep Phase

It can be seen from **Figure 2**, when a constant stress τ_0 is applied to the sample for a time period, the strain generated by the sample is composed of instantaneous strain γ_s, retardation strain $\gamma_d(t)$, and viscous flow $\gamma_v(t)$. Therefore, the relationship between the creep strain γ_C of the sample and the time t can be expressed as formula (1).

$$\gamma_C(t) = \gamma_s + \gamma_d(t) + \gamma_v(t) \quad (1)$$

For linear viscoelastic materials, the strain only has instantaneous strain, which represents the material's reversible

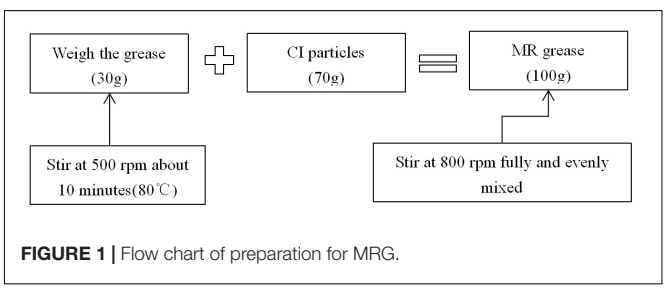

FIGURE 1 | Flow chart of preparation for MRG.

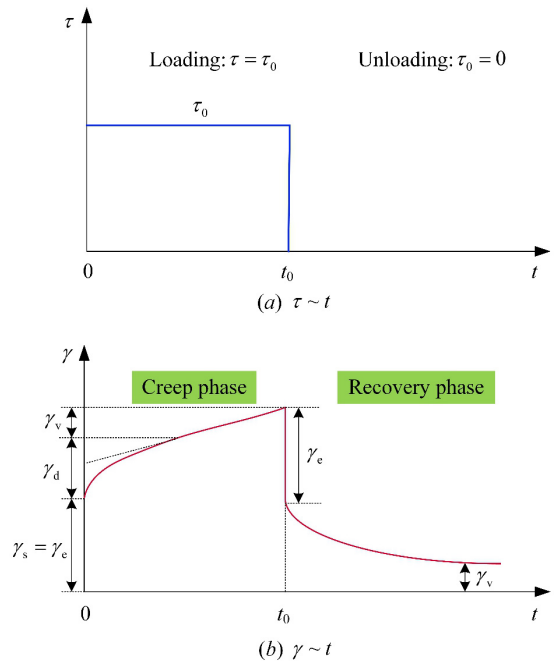

FIGURE 2 | Creep and recovery behavior to an applied constant stress for linear viscoelastic materials.

(when stress is applied and eliminated) elastic characteristics. Usually, the elastic strain of linear viscoelastic materials is expressed as $\gamma_s = \gamma_e$, The second term on the right side of the formula (1) represents the retardation strain, which decreases with the increasing trend of time, showing a yielding trend. Under the effect of the chain uncoiling of the material, it can be fully recovered within a certain period of time and has elastic properties (Qi et al., 2016). The viscous flow is the irreversible part of the creep strain. It has a linear relationship with time in a linear viscoelastic fluid (Qi et al., 2016).

Since the magnitude of the three components of creep strain is proportional to the magnitude of the input stress, a creep compliance function can be defined as:

$$J_C(t) = \frac{\gamma_C(t)}{\tau_0} = J_e + J_d(t) + J_v(t) \tag{2}$$

Substitute equation (1) into equation (2) to get

$$\gamma_C(t) = \tau_0 J_C(t) = \tau_0 \left(J_e + J_d(t) + J_v(t)\right) \tag{3}$$

Recovery Phase

It can be seen from **Figure 2** that when the sample stress ($t = t_0$) is eliminated, the instantaneous strain γ_s recovers instantly, the retardation strain $\gamma_d(t)$ gradually recovers, and the viscous flow $\gamma_v(t)$ does not change. Therefore, the relationship between recovery strain with time can be expressed by equation (4).

$$\gamma_R(t) = \gamma_e + \gamma_d(t) \tag{4}$$

Similar to the definition of $J_C(t)$, the definition of a recovery compliance function is as shown in formula (5)

$$J_R(t) = \frac{\gamma_R(t)}{\tau_0} = J_e + J_d(t) \tag{5}$$

Assuming that the viscoelasticity of the sample is linear, the total creep strain at any time can be expressed as the sum of two independent strains, as shown in eq. (6).

$$\gamma(t) = \tau_0 \left(J_C(t_0) - J_R(t - t_0)\right) \quad (t > t_0) \tag{6}$$

where, $\tau_0 J_C(t_0)$ is the creep strain at $t = t_0$ and $\tau_0 J_R(t - t_0)$ is unloading at $t = t_0$.

Creep and Recovery Behavior of Nonlinear Viscoelastic Materials

The instantaneous strain produced by linear viscoelastic materials under constant stress loading only represents its elastic coefficient($\gamma_s = \gamma_e$), which can be completely restored after stress is eliminated. However, for nonlinear viscoelastic-plastic materials, the instantaneous strain generated under constant stress loading characterizes the elastic and plastic properties of the material, as shown in **Figure 3**, and the expression is shown in eq. (7). As shown in **Figure 3**, after the stress is removed, the instantaneous recovery strain is equal to the elastic strain, and the plastic strain cannot be recovered.

$$\gamma_s = \gamma_e + \gamma_p \tag{7}$$

In the formula, γ_p represents plastic strain.

Experimental Method and Testing

Magnetorheological grease was measured by using a parallel plate rheometer (Physica MCR 302, Anton Paar, Austria) with a magnetron unit (MRD 180) and a temperature control unit (JULABO F25). In this study, a plate rotor with a diameter of 20 mm was used. During the experiment, the gap between the plate and the base was set to 1 mm. The calculated results show that the sample required for each experiment is about 0.315 mL.

This experiment mainly studies the creep and recovery characteristics of MRG. In the rotating shear test, the flow curve

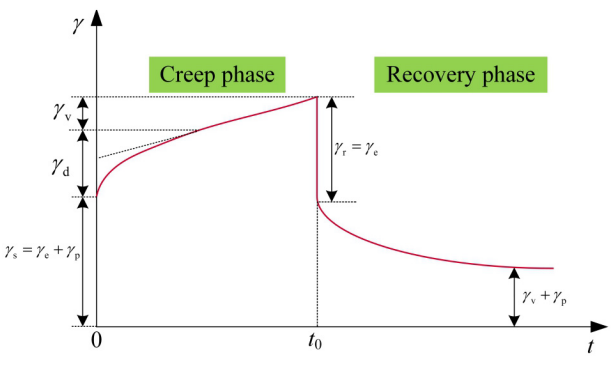

FIGURE 3 | Creep and recovery behavior of nonlinear viscoelastic materials.

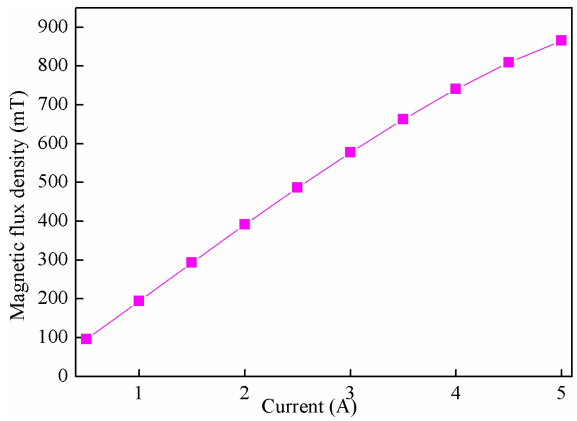

FIGURE 4 | The relationship between current and magnetic flux density.

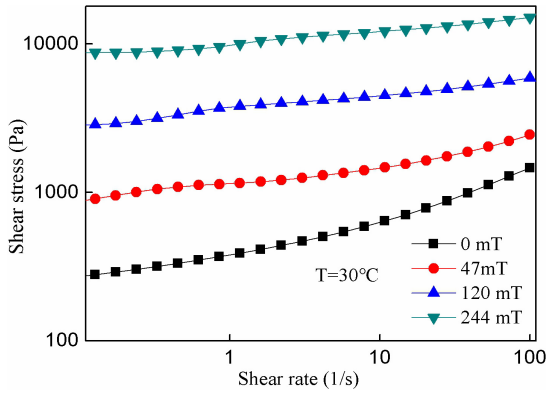

FIGURE 5 | The flow curve of MRG-70 under various magnetic flux density.

of MRG under different magnetic flux density was measured, and the shear rate was set to 0.1 s^{-1} to 100 s^{-1}. Creep and recovery characteristics are also tested under shear conditions. For the experiment on the effect of creep recovery behavior under constant stress, the constant stress is 50, 100, 165, and 200 Pa when the zero field is set, and when the magnetic flux density is 47 mT, the constant stress is 50, 100, and 200 Pa. In the magnetic field strength test, the fixed stress is set to 50 Pa and the magnetic flux density is set to 0, 24, 47, 67, 96, and 120 mT. In addition, the effect of the mass fraction of CI particles in different MRGs on the creep recovery curve is studied. And in the temperature influence experiment, set the temperature to 10, 50, and 70°C, and the fixed stress is 200 Pa; Compare the creep and recovery behavior with or without magnetic field. In the experiment, except for the temperature experiment, all other test temperatures were tested at 30°C. In addition, the entire test must be pre-sheared (the shear rate is constant at 10 s^{-1}, pre-shearing time 20 s) to ensure the consistency of each measurement and all experiments are performed three times to ensure the data obtained repeatability.

RESULTS AND DISCUSSION

Dynamic Yield Stress

When using rheometer equipment, the selected magnetic field is expressed in the form of current, and the magnetic flux density corresponding to the current is calculated by the relationship between the current and the magnetic flux density in **Figure 4**. **Figure 5** shows the relationship between the shear rate and shear stress of MRG under different magnetic field strengths. It can be seen from **Figure 4** that the shear stress increases with the increase of the shear rate. In addition, when the shear rate is constant, the value of the shear stress will increase with the increase of the magnetic flux density.

In this study, the Bingham-plastic model was used to describe the plastic flow stage of MRG in different magnetic fields. The model is defined as (Rabbani et al., 2015):

$$\begin{cases} \tau = \tau_y + \eta_p \dot{\gamma} & |\tau| \geq \tau_y \\ \dot{\gamma} = 0 & |\tau| < \tau_y \end{cases} \tag{8}$$

where τ and $\dot{\gamma}$ represent the shear stress and shear rate, respectively. τ_y is yield stress as a function of magnetic field and η_p is the plastic viscosity. Use Origin8.0 software to fit **Figure 5** to get the dynamic yield stress. **Table 2** lists the dynamic yield stress under different magnetic field conditions.

The Influence of Stress Level on Creep and Recovery Behaviors

Constant stress is an important parameter when measuring creep and recovery characteristics, and its value has an important influence on creep and recovery characteristics. In addition, MRG is a smart material that is sensitive to magnetic field. Therefore, in this section, for the purpose of comparative study, we will conduct creep recovery characteristics experiments on both the magnetic field and the non-magnetic field. The experimental results are shown in **Figure 6**. It can be seen from **Figure 6** that the MRG creep curve increases with time when it is in the retardation strain. After the stress is relieved at 150 s, the strain immediately drops to a lower level. However, there are big differences between the two cases with and without magnetic field. For example, under the same shear stress of 200 Pa, the response strain without magnetic field strength is larger than the response strain after loading the magnetic field. This is because the magnetic field makes the MRG become stiffer and the interaction of iron particles restrict the movements of chain, which leads to a reduction in strain. In addition, as the constant stress level increases, the response strain will increase accordingly, whether or not an external magnetic field is applied

TABLE 2 | The dynamic yield stress of MRG-70 under different magnetic induction intensity.

B(mT)	0	47	120	244
τ_y(Pa)	165	600	1,500	6,420

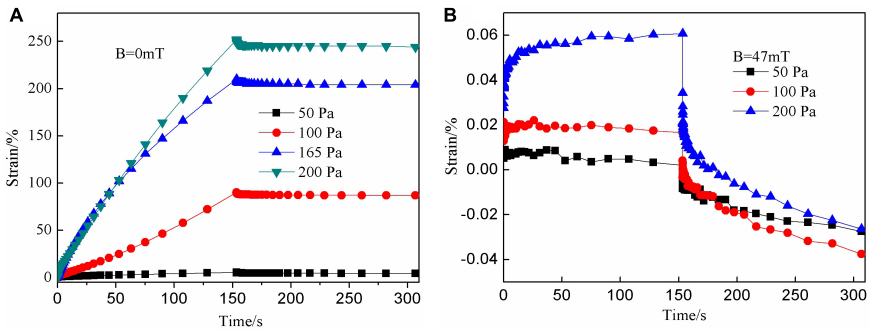

FIGURE 6 | Creep and recovery curves of MRG under different constant stress. **(A)** B = 0 mT; **(B)** B = 47 mT.

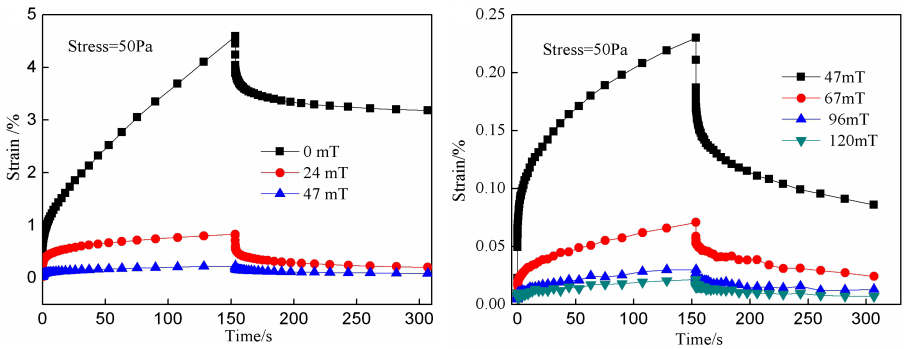

FIGURE 7 | Creep and recovery curves of MRG under the combined action of 50 Pa stress and different magnetic fields.

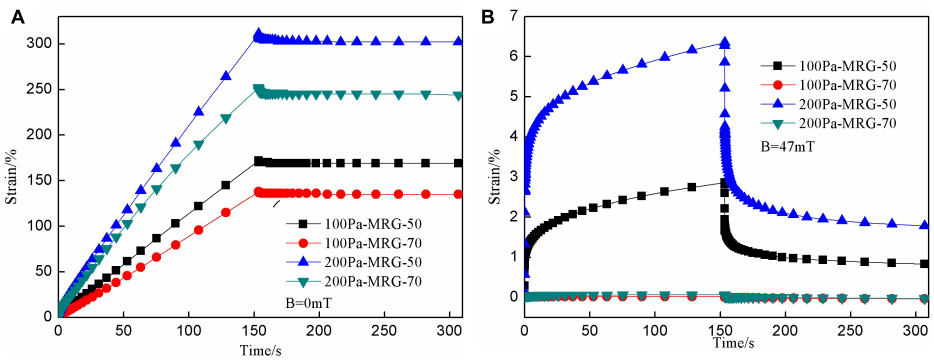

FIGURE 8 | Creep and recovery curves of MRG under different mass fractions **(A)** B = 0 mT; **(B)** B = 47 mT.

to MRG. Moreover, the response strain is proportional to creep time in the absence of magnetic field. According to **Table 2**, the dynamic yield stress of MRG under zero magnetic field is 165 Pa, so when the shear stress is set to be greater than or equal to 165 Pa, the material basically has no recovery behavior.

The Influence of Magnetic Field Strength on Creep and Recovery Behaviors

Magnetic excitation is one of the most important characteristics of MR materials. **Figures 7A,B** shows the dependence of the magnetic field on MRG creep and recovery behavior under a constant stress of 50 Pa, where the field strength is set to 0, 24, 47, 67, 96, and 120 mT; It can be seen from **Figure 7** that under the same creep time and stress, the creep strain decreases sharply with the increase of the magnetic field. The creep strain of the MRG without a magnetic field is 213 times that of the MRG with a 120 mT magnetic field, and the ratio will increase as the creep time increases. The reason is that the greater the magnetic field strength, the more stable the chain structure in the MRG will reduce the creep strain. In the absence of a magnetic field, MRG behaves as a viscous liquid, and its low viscosity makes the

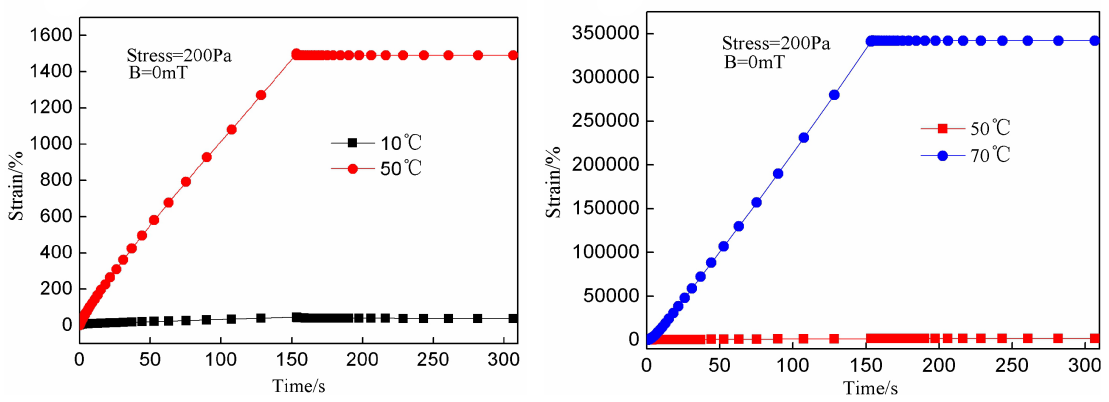

FIGURE 9 | The creep and recovery curves of MRG-70 under a 200 Pa constant stress for MRG-70 at different temperatures.

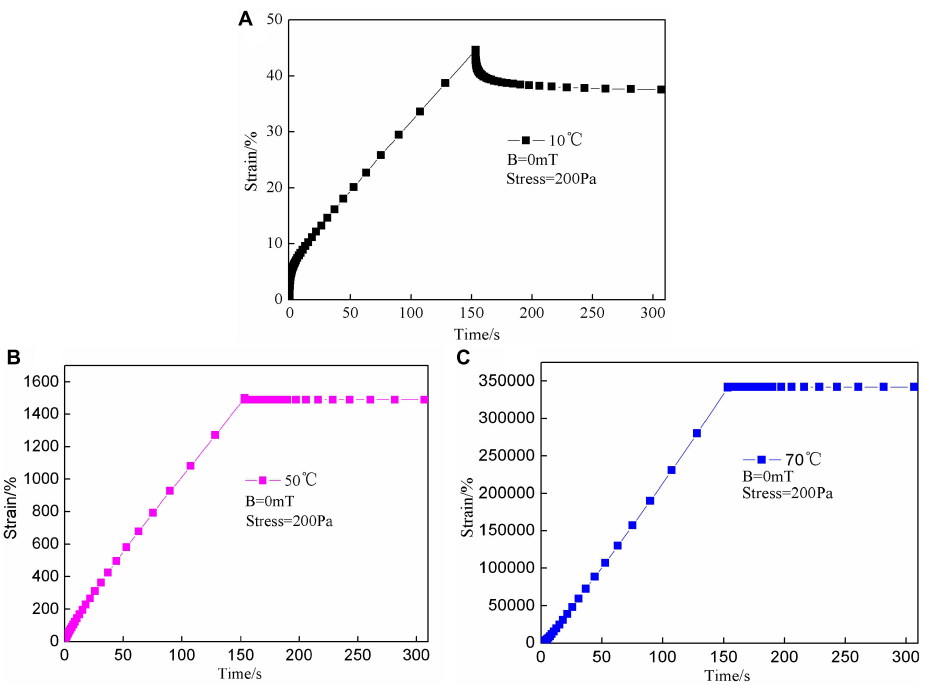

FIGURE 10 | The creep and recovery curves of MRG-70 under a 200 Pa constant stress for MRG-70 under different temperatures **(A)** T = 10°C; **(B)** T = 50°C; **(C)** T = 70°C.

shear stress of the material very low. However, after the constant shear stress is eliminated (more than 150 s), the creep strain can drop sharply, and change smoothly after reaching a certain value. It can be seen from **Figure 7** that the creep strain can be partially recovered.

The Influence of CI Particle Content the Creep and Recovery Behavior

Previous studies have shown that the content of CI particles has a great influence on the viscosity and shear stress of MR materials, so this experiment tested the effect of the content of CI particles in MRG on creep recovery characteristics. **Figure 8A** shows the creep and recovery characteristics of the tested MRG mass fractions of 50% and 70% under no magnetic field and constant stress of 100 and 200 Pa. It can be seen from **Figure 8A** that before 150 s, the response stress increases linearly with time, and after 150 s, the MRG strain almost stabilizes, which is consistent with the results in section "The Influence of Stress Level on Creep and Recovery Behaviors." In addition, under the same mass fraction (50 or 70%), the greater the response stress applied, the greater the strain of MRG, which is consistent with the results in section "The Influence of Stress Level on Creep and Recovery Behaviors." For different mass fractions, the higher the

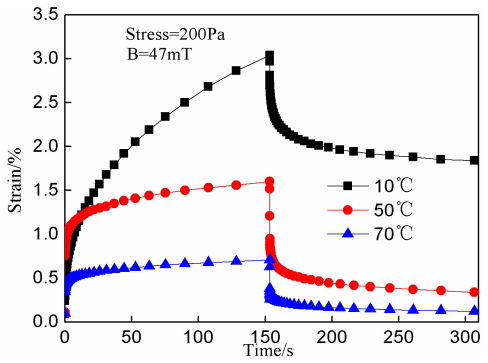

FIGURE 11 | The creep and recovery curves of MRG-70 under a 200 Pa constant stress for MRG-70 under different temperatures T = 10°C; T = 50°C; T = 70°C.

CI mass fraction in the MRG, the smaller the strain value, because the higher the CI mass fraction, the viscosity value in the MRG will increase, which will make the strain value higher than the low mass fraction MRG. In addition, **Figure 8B** shows the creep and recovery characteristics of the tested MRG mass fractions of 50 and 70% under the magnetic field of 47 mT. It can be seen from **Figure 8B** that the result after applying a magnetic field has a similar trend to the result without applying a magnetic field, but the difference is that the amount of strain of the MRG material is smaller after applying a magnetic field. This result has been obtained in section "The Influence of Magnetic Field Strength on Creep and Recovery Behaviors."

The Influence of Temperature on the Creep and Recovery Behavior of MRG

Figure 9 shows the creep recovery behavior of MRG at three temperatures of 10, 50, and 70°C under a constant stress of 200 Pa. The experiment was done under the absence of magnetic field. It can be seen from **Figure 9** that under the same creep time, the creep strain will increase with the increase of temperature. This is because the viscosity of MRG will become thinner under the action of no magnetic field with the increase of temperature (Wang H. X. et al., 2019). The softening of the material results in a smaller creep strain. This is exactly the same as the result of MR plastomer (Xu et al., 2012).

In order to clearly see the recovery behavior of MRG at various temperatures (10, 50, and 70°C), **Figure 9** is drawn separately to obtain **Figures 10A–C**. From **Figures 10A–C**, when the temperature is 10°C, the recovery behavior of MRG is the best. When the temperature increases to 70°C, it can be seen that the recovery part is basically the same, so it can be concluded that the recovery is very small. This is because when there is no magnetic field, the viscosity of the MRG will decrease with the increase of temperature (Fernandez et al., 2018), so its deformation will become larger.

Compared with **Figures 10**, **11** was tested under a magnetic flux density of 47 mT to study the creep recovery behavior of MRG at different temperatures (10, 50, and 70°C), and the shear stress was set to 200 Pa. It can be clearly seen from **Figure 11** that the creep strain will decrease with the increase of temperature under the same creep time, which indicates that the strain in MRG is not only related to the matrix but also to the strength of the magnetic field. Under the influence of the matrix, it becomes harder with increasing temperature. This is quite different from the results obtained from MR fluid (Li et al., 2002), the conclusion may be caused by a different matrix from the material of the research object.

CONCLUSION

In this paper, a commercial lubricating grease was used as a matrix to prepare MRGs with carbonyl iron powder mass fractions of 50 and 70%, respectively. Constant stress, magnetic field strength, CI particle content and temperature were studied by Anton Paar MCR302 rheometer. The main conclusions of the influence on the creep and recovery characteristics of MRG are as follows:

(a) Different constant stresses show different creep and recovery characteristics. As the constant stress level increases, the response strain will increase accordingly. In addition, the creep strain of MRG decreases with the increase of the magnetic field strength. The creep strain of MRG tested under no magnetic field is greater than that of MRG tested under magnetic field.

(b) The higher the content of CI particles in MRG at zero field, the higher its viscosity value, which will make the creep strain value smaller. In addition, when the applied magnetic flux density is 47 mT, it is found that the research results have a similar trend with the results without the applied magnetic field. However, the strain amount of the MRG material is smaller after the applied magnetic field.

(c) In the absence of a magnetic field, the creep strain of the MRG increases with the increase in temperature during the same time test. on the contrary, under the action of a magnetic field, the creep strain will decrease with the increase of temperature. Therefore, it can be inferred that the magnetic interaction between the iron particles and the coupling between the matrix and the iron particle chain are the reasons for the influence of temperature on the magnetic field creep behavior of the MRG.

DATA AVAILABILITY STATEMENT

The raw data supporting the conclusions of this article will be made available by the authors, without undue reservation.

ETHICS STATEMENT

The studies involving human participants were reviewed and approved by Nanjing University of Science and Technology. Written informed consent to participate in this study was provided by the participants' legal guardian/next of kin. The animal study was reviewed and approved by Smart materials.

Written informed consent was obtained from the owners for the participation of their animals in this study. Written informed consent was obtained from the individual(s), and minor(s)' legal guardian/next of kin, for the publication of any potentially identifiable images or data included in this article.

AUTHOR CONTRIBUTIONS

Both authors listed have made a substantial, direct and intellectual contribution to the work, and approved it for publication.

REFERENCES

Chen, L. G., Shuai, C. G., Chen, L. G., and Yang, S. L. (2015). Study on creep property of polyurethane composites. *Mater. Res. Innov.* 19, 199–201.

Cheng, J., Liu, K., Zhang, Z., Wei, Z., Ma, Y., and Lu, S. (2021). Effect of compound surfactants modified carbonyl iron on magnetorheological fluids. *J. Supercond. Nov. Magn.* 34, 1177–1183.

Fancey, K. S. (2005). A mechanical model for creep, recovery and stress relaxation in polymeric materials. *J. Mater. Sci.* 40, 4827–4831. doi: 10.1007/s10853-005-2020-x

Fernandez, M. A., Jen-Yuan, C., and Chih-Yung, H. (2018). Development of a passive magnetorheological fluid clutch with field-blocking mechanism. *IEEE Trans. Magn.* 54, 1–5. doi: 10.1109/tmag.2018.2834389

Findley, W. N., Lai, J. S., and Onaran, K. (1977). Creep and relaxation of nonlinear viscoelastic materials with an introduction to linear viscoelasticity. *J. Appl. Mech.* 44, 505–509.

Fu, J., Bai, J., Lai, J., Li, P., Yu, M. K., and Lam, H.-K. (2019). Adaptive fuzzy control of a magnetorheological elastomer vibration isolation system with time-varying sinusoidal excitations. *J. Sound Vib.* 456, 386–406. doi: 10.1016/j.jsv.2019.05.046

Hu, Z. D., Yan, H., Guo, X. C., Wang, X. M., and Wen, H. (2015). Rheological properties and stability of lithium-based magnetorheological grease with damping effect. *Acta Petrolei Sin.* 31, 166–171.

Iurzhenko, M., Mamunya, Y., Boiteux, G., and Matkovska, L. (2014). Creep/stress relaxation of novel hybrid organic-inorganic polymer systems synthesized by joint polymerization of organic and inorganic oligomers. *Macromol. Symp.* 341, 51–56. doi: 10.1002/masy.201300163

Kavlicoglu, B. M., Gordaninejad, F., and Wang, X. (2013). Study of a magnetorheological grease clutch. *Smart Mater. Struct.* 22:5030.

Kim, J. E., Ko, J. D., Liu, Y. D., Kim, I. G., and Choi, H. J. (2012). Effect of medium oil on magnetorheology of soft carbonyl iron particles. *IEEE Trans. Magn.* 48, 3442–3445. doi: 10.1109/tmag.2012.2195160

Li, W. H., Du, H., Chen, G., and Yeo, S. H. (2002). Experimental investigation of creep and recovery behaviors of magnetorheological fluids. *Mater. Sci. Eng. A* 333, 368–376. doi: 10.1016/s0921-5093(01)01865-2

Mao, R., Wang, H., Zhang, G., Yea, X., and Wang, J. (2020). Magneto-induced rheological properties of magnetorheological gel under quasi-static shear with large deformation. *RSC Adv.* 10, 31691–31704. doi: 10.1039/d0ra05843b

Mohamad, N., Mazlan, S. A., and Sabino, U. (2016a). "Effect of carbonyl iron particles composition on the physical characteristics of MR grease," in *Proceeding of the International Conference & Exhibition on Sustainable Energy & Advanced Materials*, (College Park: AIP Publishing LLC).

Mohamad, N., Mazlan, S. A., Ubaidillah, S., Choi, S.-B., and Nordin, M. F. M. (2016b). The field-dependent rheological properties of magnetorheological grease based on carbonyl-iron-particles. *Smart Mater. Struct.* 25:10.

Mohamad, N., Ubaidillah, Mazlan, S. A., Imaduddin, F., Choi, S. B., and Yazid, I. I. M. (2018). A comparative work on the magnetic field-dependent properties of plate-like and spherical iron particle-based magnetorheological grease. *PLoS One* 13:e0191795. doi: 10.1371/journal.pone.0191795

Ou, Y. Q., Li, Z. C., Zheng, J. J., and Wang, J. (2017). Controllability characteristics of magnetorheological damper with multi-stage parallel coil under impact load. *J. Zhejiang Univ.* 51, 961–968.

Ouyang, Q., Hu, H., Qian, C., Zhang, G., Wang, J., Zheng, J., et al. (2019). Investigation of the influence of magnetic field distribution on the magnetorheological absorber with individually controllable coils. *IEEE Trans. Magn.* 55, 1–13. doi: 10.1109/tmag.2019.2907515

Park, B. O., Park, B. J., Hato, M. J., and Choi, H. J. (2011). Soft magnetic carbonyl iron microsphere dispersed in grease and its rheological characteristics under magnetic field. *Colloid Polym. Sci.* 289, 381–386. doi: 10.1007/s00396-010-2363-y

Qi, S., Yu, M., Fu, J., Li, P. D., and Zhu, M. (2016). Creep and recovery behaviors of magnetorheological elastomer based on polyurethane/epoxy resin IPNs matrix. *Smart Mater. Struct.* 25:015020. doi: 10.1088/0964-1726/25/1/015020

Rabbani, Y., Ashtiani, M., and Hashemabadi, S. H. (2015). An experimental study on the effects of temperature and magnetic field strength on the magnetorheological fluid stability and MR effect. *Soft Matter* 11, 4453–4460. doi: 10.1039/c5sm00625b

Rankin, P. J., Horvath, A. T., and Klingenberg, D. J. (1999). Magnetorheology in viscoplastic media. *Rheol. Acta* 38, 471–477. doi: 10.1007/s003970050198

Wang, D., Yao, L., Shao, W., Zi, B., and Chen, W. (2019). Simulation and experimental study on temperature characteristics of magnetorheological fluid brake for vehicles. *J. Mech. Eng.* 55:100. doi: 10.3901/jme.2019.06.100

Wang, H. X., Li, Y. C., Zhang, G., and Wang, J. (2019). Effect of temperature on rheological properties of lithium-based magnetorheological grease. *Smart Mater. Struct.* 28:035002. doi: 10.1088/1361-665x/aaf32b

Weihua, L., Zhou, Y., Tian, T., and Alici, G. (2010). Creep and recovery behaviors of magnetorheological elastomers. *Front. Mech. Eng. China* 5:341–346. doi: 10.1007/s11465-010-0096-8

Xia, H., Song, M., Zhang, Z., and Richardson, M. (2007). Microphase separation, stress relaxation, and creep behavior of polyurethane nanocomposites. *J. Appl. Polym. Sci.* 103, 2992–3002. doi: 10.1002/app.25462

Xu, Y., Gong, X., Xuan, S., Li, X., Qina, L., and Jiang, W. (2012). Creep and recovery behaviors of magnetorheological plastomer and its magnetic-dependent properties. *Soft Matter* 8, 8483–8492. doi: 10.1039/c2sm25998b

Yang, C. Y., Fu, J., Yu, M., Zheng, X., and Ju, B. X. (2015). A new magnetorheological elastomer isolator in shear-compression mixed mode. *J. Intell. Mater. Syst. Struct.* 26, 1290–1300. doi: 10.1177/1045389x14541492

Yao, Z., Wu, D., Chen, C., and Zhang, M. (2013). Creep behavior of polyurethane nanocomposites with carbon nanotubes. *Compos. Part A Appl. Sci. Manuf.* 50, 65–72. doi: 10.1016/j.compositesa.2013.03.015

Ye, X., Mao, R., and Wang, J. (2021). Analysis of magnetorheological grease normal force characteristics in static and dynamic shear modes. *Mater. Res. Express* 8:015701. doi: 10.1088/2053-1591/abbf81

Zhang, G., and Wang, J. (2020). A novel phenomenological model for predicting the nonlinear hysteresis response of magnetorheological gel. *Mater. Des.* 196:109074. doi: 10.1016/j.matdes.2020.109074

Conflict of Interest: The authors declare that the research was conducted in the absence of any commercial or financial relationships that could be construed as a potential conflict of interest.

frontiers in Materials

ORIGINAL RESEARCH
published: 06 July 2021
doi: 10.3389/fmats.2021.692273

A Liquid-Metal-Based Freestanding Triboelectric Generator for Low-Frequency and Multidirectional Vibration

Huaxia Deng, Zizheng Zhao, Chong Jiao, Jingchang Ye, Shiyu Zhao, Mengchao Ma and Xiang Zhong*

School of Instrument Science and Opto-electronics Engineering, Hefei University of Technology, Hefei, China

There are a lot of vibrational energies, which are low frequency, multidirectional, and broadband, in the nature. This creates difficulties for devices that aim at harvesting vibration energy. Here, we present a liquid-metal-based freestanding triboelectric generator (LM-FTG) for vibration energy harvesting. In this device, the fluidity of liquid is used to increase sensitivity to vibration for better low-frequency response and multidirectional vibration energy harvesting capability. The freestanding power generation mode is able to increase power generation stability. Experiments show that the bandwidth of LM-FTG can almost cover the entire sweep frequency range, and a 10 μF capacitor can be charged to 6.46 V at 7.5 Hz in 60 s by LM-FTG. In particular, 100 LEDs are illuminated in the low-frequency environmental experiment successfully. The proposed LM-FTG can work in low frequency with large working bandwidth, which provides an effective method for energy harvesting of low-frequency and multidirectional vibrations.

Keywords: vibration energy harvesting, liquid-metal-based, freestanding, low-frequency, multidirectional, broadband

OPEN ACCESS

Edited by:
Miao Yu,
Chongqing University, China

Reviewed by:
Yancheng Li,
University of Technology Sydney, Australia
Junlei Wang,
Zhengzhou University, China

****Correspondence:***
Huaxia Deng
hxdeng@hfut.edu.cn

Specialty section:
This article was submitted to Smart Materials, a section of the journal Frontiers in Materials

Received: *08 April 2021*
Accepted: *07 June 2021*
Published: *06 July 2021*

Citation:
Deng H, Zhao Z, Jiao C, Ye J, Zhao S, Ma M and Zhong X (2021) A Liquid-Metal-Based Freestanding Triboelectric Generator for Low-Frequency and Multidirectional Vibration. Front. Mater. 8:692273. doi: 10.3389/fmats.2021.692273

1 INTRODUCTION

Internet of Things technology and distributed sensor networks have gradually become the development trend of society, such as wearable devices, smart home appliances, and marine monitoring buoys. They are distributed in all aspects of our lives. These devices can only be powered by distributed independent power sources, and the batteries need to be replaced one by one to ensure the reliability of the device, which will greatly increase maintenance costs (Kim et al., 2017; Yildirim et al., 2017). To convert energy from nature, such as light energy (Park et al., 2016; Kim et al., 2015; Wen et al., 2016), heat energy (Siddique et al., 2017; Sebald et al., 2009; Kim et al., 2014), vibration energy (Sang et al., 2019; Li et al., 2019; Wang et al., 2018b), and so on (Starner, 1996; Guo et al., 2016), has become an effective solution (Yu et al., 2019; Jiang et al., 2018; Pu et al., 2018). A wearable textile battery (Lee et al., 2013), charged by polymer solar cells, can effectively harvest the light energy, providing enough power to light up nine LEDs. But, this kind of energy harvester generally has a poor energy harvesting effect because of the small area of the surface and its susceptibility to the environment, such as the night and cloudy days. Although some designs that harvest heat energy to power the devices have been proposed, they are very sensitive to the temperature and humidity of the environment (Kyono et al., 2003). Vibration energy is an inherent solution to harvest the energy from nature and is not so sensitive to environmental factors such as

light intensity, temperature, and humidity (Rome et al., 2005; Dai et al., 2012). Vibration occurs widely in nature, for example, in the form of human walking, ocean waves, and vibration of mechanical systems. Typically, these vibrations are low frequency, multidirectional, and broadband, which means that traditional electromagnetic energy harvesters (EMGs) are not suitable (Yang et al., 2010; Zuo et al., 2010; Miki et al., 2012).

The reason why EMG is not suitable is that EMG is based on Faraday's law of electromagnetic induction, which means that it relates to the time derivative of the electric field (Khaligh et al., 2010; Siddique et al., 2015). So, EMG is generally suitable for high-frequency situations (above 50 Hz) (Zi et al., 2016; Zhu et al., 2019). Although many people have been working to improve the EMG's capability to operate at low frequencies over the years, it has not been effective for vibrations below 5 Hz because of its incompatibility (Fan et al., 2018; Yildirim et al., 2017a). In addition to EMG, there are some designs that harvest vibration energy with piezoelectric energy harvesters (PEHs) (Zeng et al., 2013; Wei et al., 2013; Safaei et al., 2019; Xiujian et al., 2018). However, PEHs have a common problem: considering the low rate of open-circuit voltage, and piezoelectric modules are often used in series in order to reach the right voltage, which increases the volume of the device. Due to the limited range of the bearing capacity, piezoelectric materials require frequent replacement during usage (Saadon and Sidek, 2011; Liu et al., 2011; Jung et al., 2017).

A triboelectric nanogenerator (TENG) uses the coupling of the triboelectric effect and the electrostatic induction effect, which determine the excellent performance of the TENG in the low-frequency range (Zhang et al., 2014; Qian et al., 2020; Hou et al., 2018; Wang S. et al., 2020; Gao et al., 2018; Wang Z. et al., 2020; Liu et al., 2020a, b). An optimized TENG-based insole designed by Wang (Hou et al., 2013) can harvest the energy of unidirectional vibration excited by contact separation between feet and insoles, which can provide enough power to light up 30 LEDs simultaneously. A self-powered backpack (Yang et al., 2013), which is $5cm \times 7.5cm \times 20cm$ and weighs 2 kg, has been designed to harvest vibration energy and can light up 40 LEDs. It has been proposed to add the bistable system (Deng et al., 2019a; Deng et al., 2019b; Harne and Wang, 2013), which increases the complexity of the structure and the weight of the system, on the TENG-based harvester to broaden the frequency band (Yildirim et al., 2017b). Although these designs can be used to harvest vibration energy, it is difficult to satisfy the requirements of low-frequency, multidirectional, and broadband vibration at the same time. The proposal of using liquid as the friction material provides a new method to solve the problem (Zheng et al., 2014; Chen et al., 2016). Due to the fluidity of liquid, the liquid has a better response to vibration, especially for low-frequency, multidirectional, and broadband vibration (Zhang et al., 2016; Xie et al., 2020). Water as a kind of liquid has previously been proven to be the friction material, but this type of TENG generally does not have good energy conversion capability (due to the limitations of free electrons in water) (Lin et al., 2013). A liquid-metal-based contact-sliding triboelectric principle (Tang et al., 2015) has been proposed, which proves that the liquid metal can also be used as the friction material. The output charge density of this way is 4–5 times that of the TENG, which is a solid film electrode under the same conditions. Typically, there have been some designs of triboelectric generators based on the liquid metal, but they use the liquid metal as a conductor rather than this principle (Wang et al., 2018a; Yang et al., 2018). Therefore, in order to harvest vibration energy, a triboelectric device based on the liquid metal can be designed.

Here, we present a liquid-metal-based freestanding triboelectric generator (LM-FTG) to solve the problem of vibration energy harvesting. The power generation mode of LM-FTG is freestanding in order to ensure the stability of power generation, which avoids the situation that the liquid metal cannot contact the metal electrode to generate electricity. We show the details of the specific electricity generation process. The multidirectional harvesting capability and low-frequency adaptability are proved by intuitive experiments and theoretical analysis. In the experiments, we perform an inertial frequency-sweep experiment, which proves the multidirectional and broadband vibration harvesting capability of the device. The power experiment under inertial force constant frequency excitation further proves superiority of different working modes and the low-frequency response of LM-FTG. Through the low-frequency environmental experiment, the practicality of this device is proved.

2 DESIGN AND MECHANISM

As shown in **Figure 1A**, LM-FTG, which consists of an aluminum alloy threaded cylinder, two aluminum alloy threaded caps, a 3D printed material sleeve (polylactic acid), a suitable amount (the height of the liquid level is about a quarter of the height of the container) of the liquid metal (mercury, gallium, or gallium–indium), two triboelectric components, and two silicone seals, is similar in shape to a cylindrical container. In order to prevent the liquid metal from conducting with the external metal shell, which enhances the overall impact resistance, a 3D printed material sleeve is used to isolate the liquid metal from the metal shell. The silicone sealing ring is placed between the aluminum alloy threaded cap and the triboelectric component. By screwing the threaded cap tightly, the container is sealed. When LM-FTG is subjected to external excitation, the internal liquid metal collides between the surfaces of Kapton at both sides to generate electricity. The detailed information of LM-FTG is shown in **Supplementary Figure S1**.

It is worth noting that, in the selection of the liquid metal, we put the droplets of mercury, gallium, and water on the Kapton's surface, respectively, and observed their surface morphology. As shown in **Figure 2**, the droplets of mercury and gallium on the Kapton's surface basically maintain a spherical droplet state while the water is flat on the surface. This proves not only that gallium can be easily separated from Kapton without adhesion but also that mercury has this property. However, compared to mercury, gallium is easier to oxidize in the air and forms an oxide layer that is difficult to detach on the Kapton's surface. In response to this phenomenon, we chose mercury, which is extremely difficult to oxidize, as the liquid metal in LM-FTG.

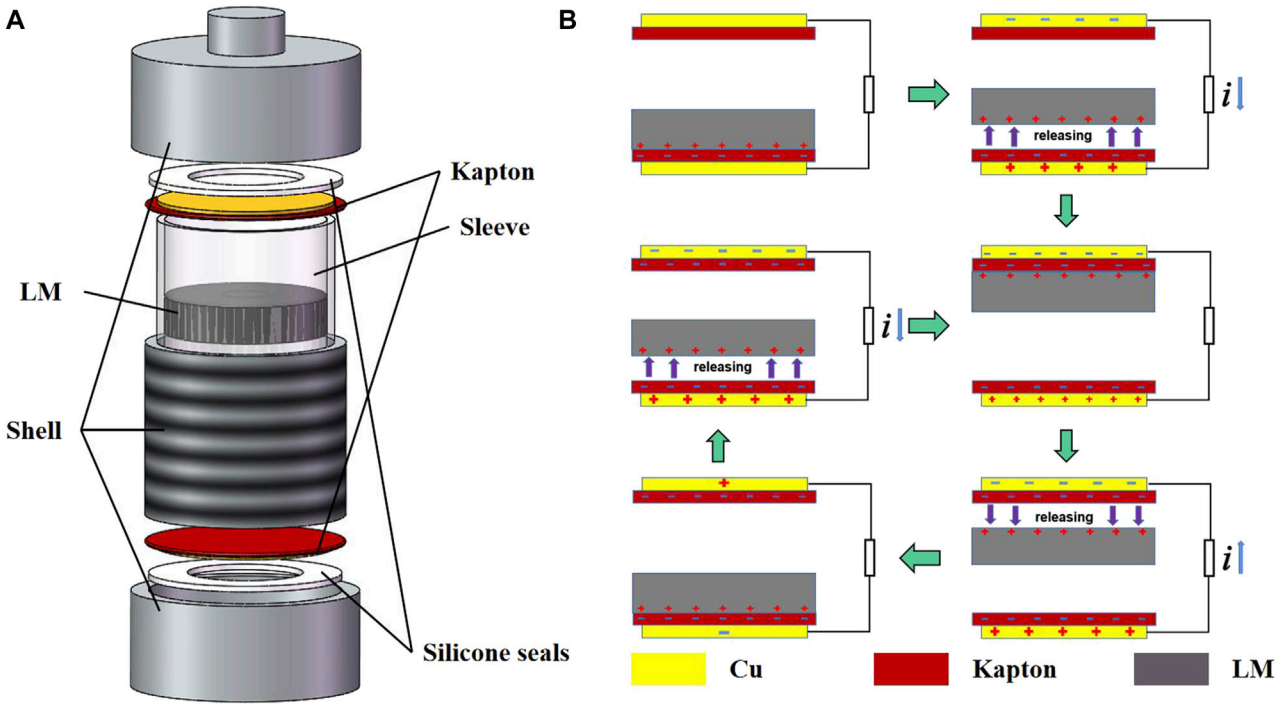

FIGURE 1 | Working principle of LM-FTG. **(A)** Schematic illustration showing the device configuration of LM-FTG; **(B)** step-by-step illustration showing the working principle of LM-FTG.

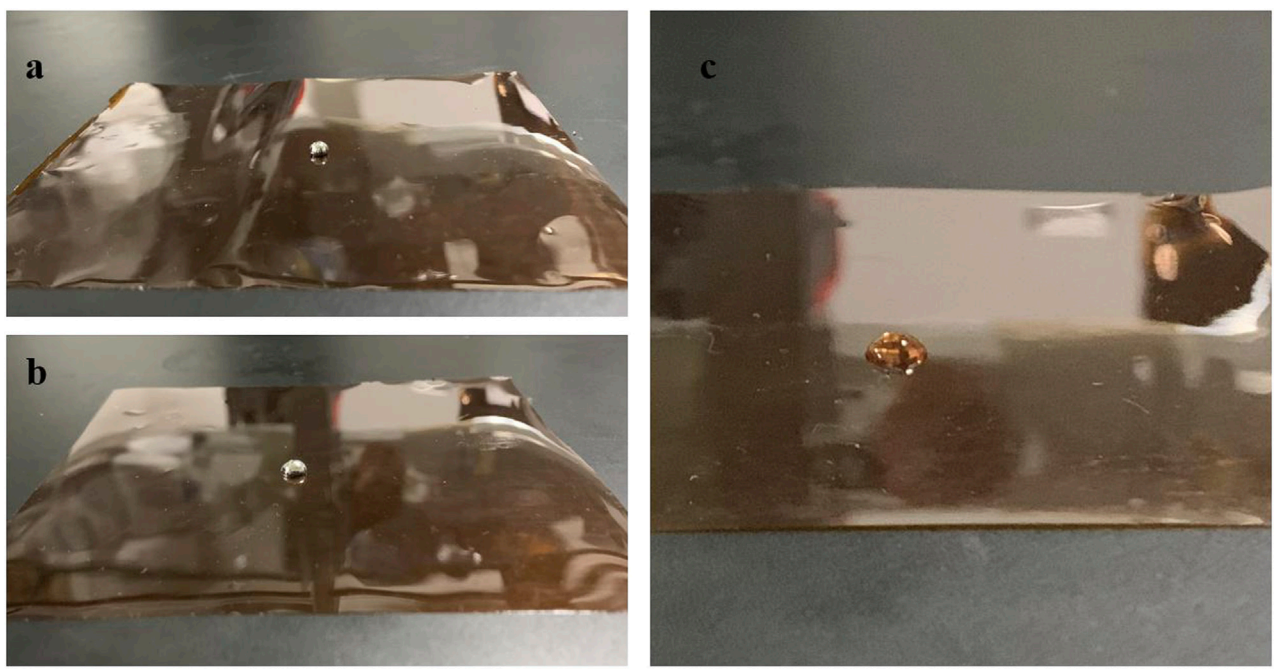

FIGURE 2 | Droplets of mercury, gallium, and water on Kapton's surface. **(A)** Mercury; **(B)** gallium; and **(C)** water.

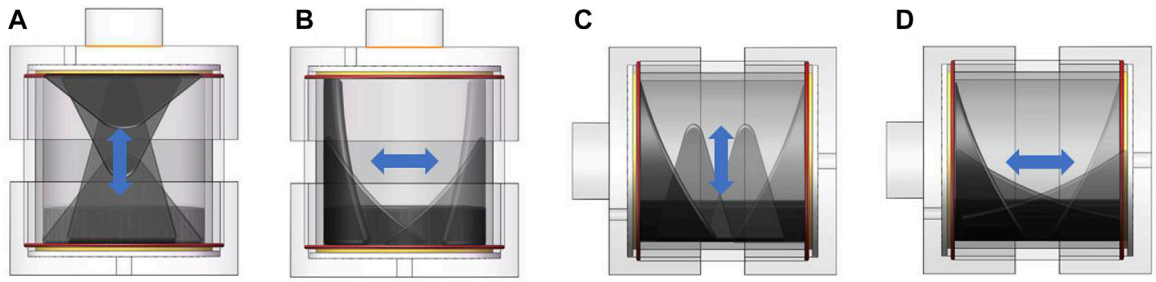

FIGURE 3 | Internal liquid flow. **(A)** Liquid flow in the VV mode; **(B)** liquid flow in the VH mode; **(C)** liquid flow in the HV mode; and **(D)** liquid flow in the HH mode.

A complete cycle of the electricity generation process is shown in **Figure 1B**. The contact-separation movement between the liquid metal and the triboelectric components is driven by the excitation of the outer casing. First, after pouring the liquid metal into the container, the liquid metal makes contact with the Kapton surface on one side. Due to the different capabilities of the liquid metal and Kapton to absorb electrons, electrons are transferred from the liquid metal onto the Kapton's surface, causing positive charges at the interface of the liquid metal and negative charges on the Kapton's surface. Then, the two materials are separated by the external excitation, and a potential difference is formed between them. In order to counteract the electric field, electrons will flow from the lower surface copper electrode to the upper surface copper electrode, which forms a reverse current. As the liquid metal continues to rise, it will collide with the upper Kapton's surface. Similar to the previous process, the liquid metal also undergoes charge transfer with the upper Kapton. Finally, during the liquid-metal drop process, due to the potential difference between the liquid metal and the upper surface, it will produce a current in the opposite direction to the previous process. Therefore, the pulse output of the entire process exhibits the characteristics of AC. In particular, this freestanding power generation mode causes the device to contact-separate the upper and lower surfaces twice in one power generation cycle, so it is equivalent to two power generations, which increases the number of power generations and improves power generation efficiency. In addition, compared with the first proposed sliding friction power generation mode, this power generation mode does not need to ensure that the internal liquid metal is always in contact with the conductor, which increases the stability of power generation.

Since the internal liquid metal can generate electricity just by impacting and shaking between Kapton at both sides, we set four working modes, which are vertical placement and vertical vibration (VV mode), vertical placement and horizontal vibration (VH mode), horizontal placement and vertical vibration (HV mode), and horizontal placement and horizontal vibration (HH mode), according to the LM-FTG's placement and vibration direction. **Figure 3** shows the liquid flow mode under different working modes. In order to prove that the vibration modes are similar to the pictures, we put the liquid metal in the transparent tube and shook the hand to simulate vibration (see **Supplementary Movies S1–S4**). It can be seen from the video that the liquid metal can impact surfaces of both sides regardless of the working mode under external excitation. So, the multidirectional vibration harvesting capability of LM-FTG can also be demonstrated.

In order to prove that the liquid metal can better respond to external low-frequency vibration, we develop the fluid field equations for one of the working modes and estimate the relationship between the liquid free surface wave height and the frequency of external excitation. As shown in **Figure 4A**, we assume that LM-FTG works in the VH mode and set up an inertial frame and a moving coordinate system. The height of the liquid surface is represented by h, and the radius of the circular surface of the cylindrical container is represented by R.

Assuming the container is laterally excited in the x-axis direction,

$$X(t) = A\sin\omega t, \tag{1}$$

where A and ω are the excitation amplitude and frequency, respectively. Since the analysis can be simplified if the fluid equations are linearized for small displacements, the linearized fluid field equations take the form

$$\nabla^2\tilde{\Phi} = 0, \tag{2}$$

$$\left.\frac{\partial\tilde{\Phi}}{\partial r}\right|_{r=R} = 0, \left.\frac{\partial\tilde{\Phi}}{\partial z}\right|_{z=-h} = 0, \tag{3}$$

$$g\eta - \frac{\partial\tilde{\Phi}}{\partial t} + \ddot{X}r\cos\theta = 0,\ at\ z = \eta(r,\theta,t), \tag{4}$$

$$-\frac{\partial\tilde{\Phi}}{\partial z} = \frac{\partial\eta}{\partial t}\ \text{at}\ z = \eta(r,\theta,t). \tag{5}$$

The dynamic and kinematic free surface conditions in **Eq. 4** and **Eq. 5** can be combined into

$$g\frac{\partial\tilde{\Phi}}{\partial z} + \frac{\partial^2\tilde{\Phi}}{\partial t^2} = \dddot{X}r\cos\theta. \tag{6}$$

A typical solution of **Eq. 2** subject to conditions in **Eq. 3** is

$$\tilde{\Phi} = \sum_{n=1}^{\infty}[A_n(t)\cos\theta + B_n(t)\sin\theta]J(\xi_n r/R)\frac{\cosh[\xi_n(z+h)/R]}{\cosh\xi_n h/R}, \tag{7}$$

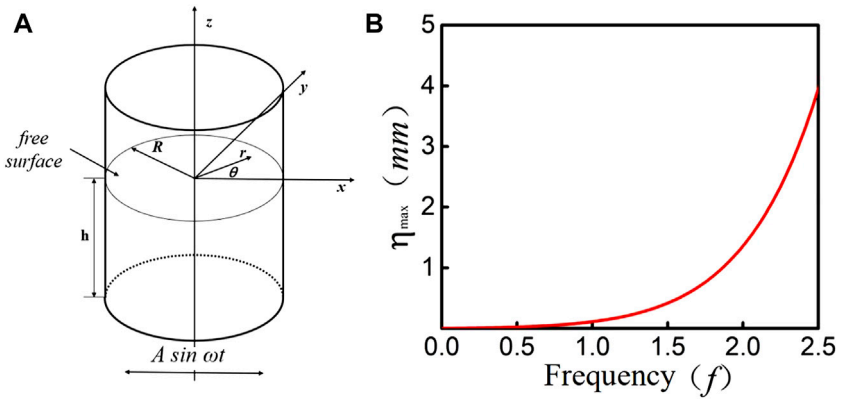

FIGURE 4 | (A) Cylindrical tank under sinusoidal lateral excitation. **(B)** Relationship between maximum wave height η_{max} and external excitation frequency ω.

where $\xi_n = (2n-1)\pi/2$. J (.) is the Bessel function of the first kind. A_n and B_n are time dependent to be determined from the free-surface initial conditions. Under the constraints of the free-surface condition in **Eq. 6**, we can get

$$A_n(t) = -\frac{A\omega^3 F_n}{(\omega_n^2 - \omega^2)\cosh(\xi_n h/R)}\cos\omega t, B_n(t) = 0, \quad (8)$$

where ω_n is the multiorder natural frequency of the liquid and $\omega_n^2 = (g\xi_n\pi)/R\tanh(\xi_n h/R)$.

Substituting **Eq. 8** into **Eq. 7**, **Eq. 7** can be rewritten as

$$\tilde{\Phi} = -A\omega\cos\theta\cos\omega t \times \sum_{n=1}^{\infty}\left[\frac{2R}{(\xi_n^2-1)}\frac{\omega^2}{(\omega_n^2-\omega^2)}\frac{J(\xi_n r/R)}{J(\xi_n)}\frac{\cosh[\xi_n(z+h)/R]}{\cosh(\xi_n h/R)}\right]. \quad (9)$$

The total potential function is the sum of the fluid perturbed function $\tilde{\Phi}$ and the tank potential function $\Phi = -A\omega\cos\theta\cos\omega t$, that is,

$$\Phi = -A\omega\cos\theta\cos\omega t \times\left\{r + \sum_{n=1}^{\infty}\left[\frac{2R}{(\xi_n^2-1)}\frac{\omega^2}{(\omega_n^2-\omega^2)}\frac{J(\xi_n r/R)}{J(\xi_n)}\frac{\cosh[\xi_n(z+h)/R]}{\cosh(\xi_n h/R)}\right]\right\}. \quad (10)$$

Substituting **Eq. 10** into condition **Eq. 4** gives the surface wave height

$$\eta = \frac{A\omega^2}{g}\cos\theta\cos\omega t\left[r + \sum_{n=1}^{\infty}\frac{2R}{(\xi_n^2-1)}\frac{\omega^3}{(\omega_n^2-\omega^2)}\frac{J(\xi_n r/R)}{J(\xi_n)}\right]. \quad (11)$$

The maximum wave height occurs at $r = R$, $\theta = 0$, and $\omega t = \pi/2$ and is given by the following expression:

$$\eta_{max} = \frac{A\omega^2}{g}\left[R + \sum_{n=1}^{\infty}\frac{2R}{(\xi_n^2-1)}\frac{\omega^3}{(\omega_n^2-\omega^2)}\right]. \quad (12)$$

We set the amplitude A = 0.001 m and substitute the relevant parameters of LM-FTG into the expression (R = 0.015 m and h = 0.015 m) to obtain the maximum wave height of the liquid surface η_{max} as a function of the external excitation frequency ω. As shown in **Figure 4B**, although the external amplitude is only 0.001 m, the maximum wave height can reach 1.3 mm under the external vibration frequency of 2 Hz. Typically, η_{max} shows a nonlinear growth with the increase of the ω. This proves that the liquid in the tank has a remarkable response to the low-frequency vibration in the VH mode. In addition, although we only conduct a specific analysis for the VH mode, since the liquid metal is in the same tank, no matter which working mode is used, the form of ω_n and the free-surface condition of the liquid metal are not changed. It also means the liquid metal can have great response in each working mode, which reflects the device's capability to harvest multidirectional vibrations.

3 EXPERIMENT

In order to explore the performance and characteristics of LM-FTG, we conducted two major experiments based on the experimental environment. The first part is an experiment conducted on a vibrating table, mainly to explore the material properties and multidirectional vibration harvesting capability of LM-FTG. The experimental results also play a guiding role in the subsequent experiments. This part of the experimental system mainly consists of a vibration table (Sushi DC-1000–15) and its controller (RC-3000), a digital multimeter (ZLG DMM6001), a computer, and a resistance box (see **Supplementary Figure S2**).

The second part of the experiment is a low-frequency environmental experiment, which proves the practicality of this device.

3.1 Vibrating Table Experiment

For the experiment on the vibration table, it is mainly divided into three parts, namely, basic output experiment, frequency-sweep experiment, and power experiment. Firstly, the basic output experiment is used to measure the internal resistance of the material, and then, a frequency-sweep test is used to not only investigate the influence of the working modes on the test data

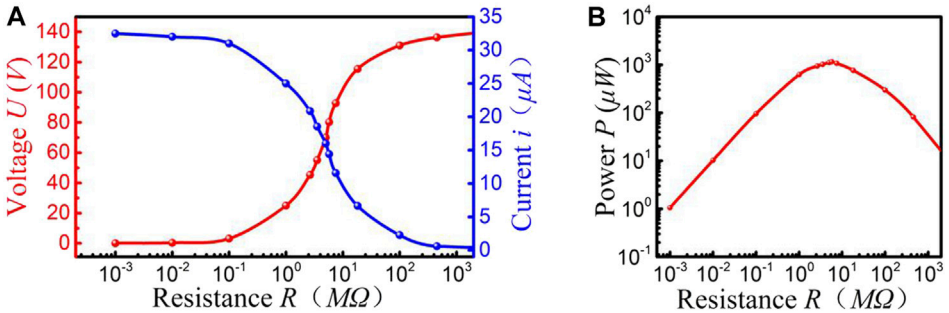

FIGURE 5 | Basic output of the material. **(A)** Output voltage and output current of Kapton under different resistance values. **(B)** The power of Kapton at different resistance values.

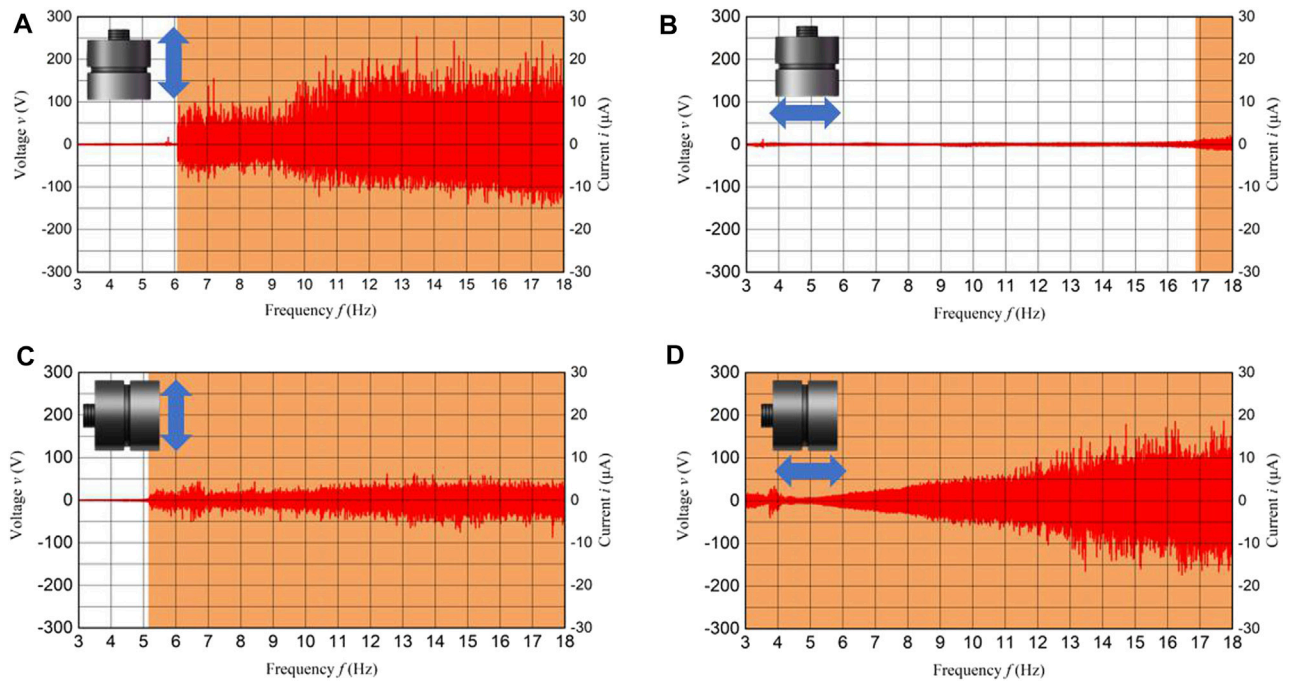

FIGURE 6 | Results of the inertial-force frequency-sweep test under 13 mm peak-to-peak excitation at 3–18 Hz sweep frequency: **(A)** Output voltage and current of LM-FTG in the VV mode. **(B)** Output voltage and current of LM-FTG in the VH mode. **(C)** Output voltage and current of LM-FTG in the HV mode. **(D)** Output voltage and current of LM-FTG in the HH mode.

but also verify broadband output. The final power experiment explores the continuous discharge capability of LM-FTG at low frequencies and further verifies the effects of different working modes, which plays a guiding role in the low-frequency environmental experiment.

3.1.1 Basic Output

In order to measure the maximum output power and power density of LM-FTG in the frequency-sweep experiment, the basic output of LM-FTG needs to be determined to infer the internal resistance. The output voltage, output current (**Figure 5A**), and power of LM-FTG (**Figure 5B**) is measured at constant frequency (10 Hz) and peak-to-peak value (15 mm) excitation. We sequentially change the resistance of the resistance box to measure the output voltage and current of LM-FTG. Then, the optimum resistance of the generator is determined by obtaining the maximum output power. Through the experimental results and drawing, it can be found that the maximum output power is obtained when the resistance is 8 MΩ.

3.1.2 Frequency Sweep

According to the analysis of the theoretical part, the working modes of LM-FTG have an impact on its power generation capability. Two fixed LM-FTG's bases are fixed on the vibration table, and the vertical and horizontal vibration tables are used to test LM-FTG. In order to explore the power generation capability and working bandwidth of each mode, we perform an inertial-force frequency-

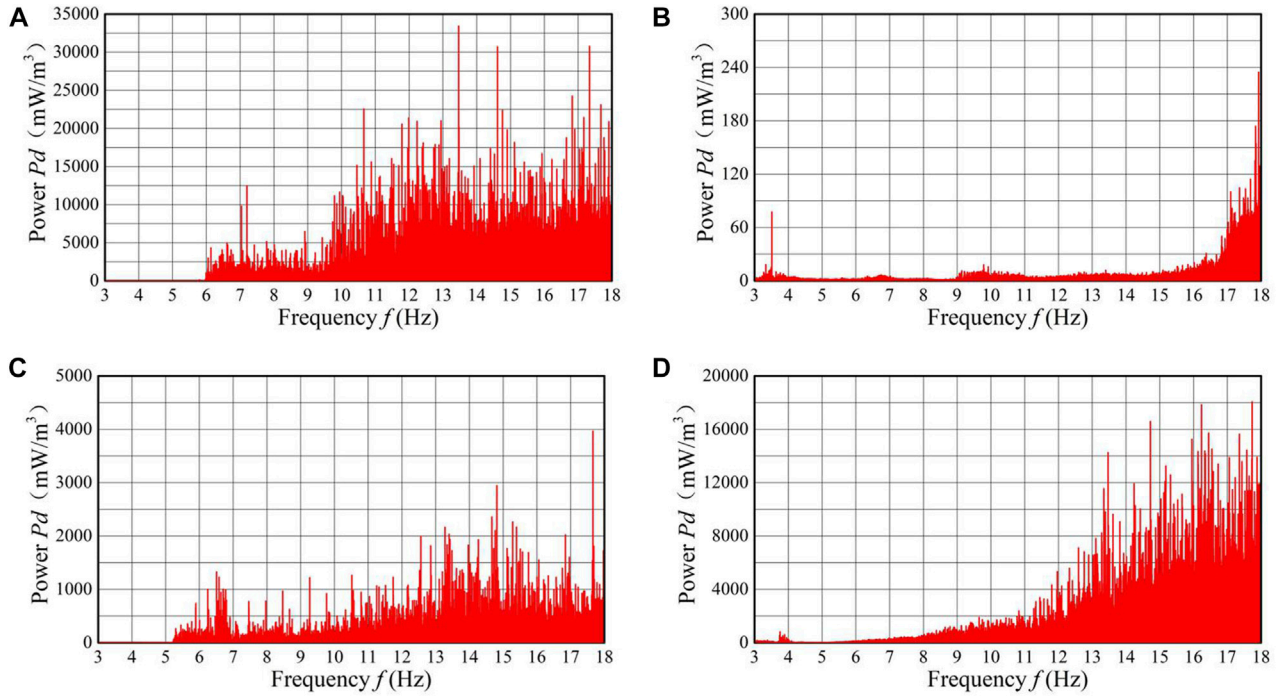

FIGURE 7 | Power density of the frequency-sweep test under 13 mm peak-to-peak excitation at 3–18 Hz sweep frequency. **(A)** Power density of LM-FTG in the VV mode. **(B)** Power density of LM-FTG in the VH mode. **(C)** Power density of LM-FTG in the HV mode. **(D)** Power density of LM-FTG in the HH mode.

sweep experiment in four working modes (see **Supplementary Figure S3**). **Figure 6** shows the frequency-domain performance results of LM-FTG under an excitation in which the peak-to-peak value is 13 mm and the frequency f sweep is from 3 to 18 Hz at a frequency rise rate of 0.05 Hz/s.

It can be seen from **Figure 6A** that when LM-FTG is in the VV mode, the output of LM-FTG always shows an upward trend after 6.2 Hz (the effective frequency bands, which are the colored areas, are defined as the frequency bands, where the output voltage exceeds 10 V), and the peak output voltage and current can reach 252 V and 25.2 μA, respectively. However, in the case of the VH mode (**Figure 6B**), LM-FTG has a small output after 16.2 Hz, and the peak output can only reach 15 V and 0.2 μA, which is not ideal. **Figures 6C**,D show the situation of horizontal placement. It can be seen from **Figure 6C** that, for the vertical vibration, LM-FTG starts to show an obvious output after 5.2 Hz. Although the peak output can only reach 58 V and 5.8 μA, the output is relatively stable, which covers the entire frequency band after 5.2 Hz. In particular, in the case of horizontal vibration, the output, which is shown in **Figure 6D**, achieves a full-band coverage of 3–18 Hz, and the peak output can reach 181 V and 1.8 μA. Based on the abovementioned data, it can be seen that, in the case of vertical placement, although the maximum peak output in the four modes can be achieved in vertical vibration and the frequency band width is great, the response to the horizontal vibration is poor, which hardly has output and is difficult to meet the energy harvesting of multidirectional vibrations. When placed horizontally, although the peak output does not shine in the two vibration directions, it has a wide frequency band and even achieves full-band coverage under horizontal vibration, which is more in line with the requirements of vibration energy harvesting. It is worth noting that LM-FTG has a good effect in both VV and HH modes. The reason is that the vibration direction in these two modes is kept parallel to the tank body, which can ensure that the liquid metal is better contacted and separated from the Kapton on both sides.

The power density of LM-FTG can be calculated according to the formula $Pd = U^2/(RV)$ (U, R, and V are the output voltage, the load resistance, and the effective volume, respectively). According to the internal resistance of the device in the first part of the experiment, we chose a 8 MΩ load resistor to get the best power density. The optimal power density in the four modes is shown in **Figure 7**. It is worth noting that the power density in the case of vertical placement and vertical vibration can reach 33000 mW/ m^3. The use of the liquid metal to generate electricity can get the ultra-high power density, so that this device can output high energy in a small volume and is suitable for different environments.

In order to explore the impact of different amplitudes on LM-FTG, we performed sweep experiments on LM-FTG with the peak-to-peak values of 9 and 16 mm (see **Supplementary Figure S6**). Although the output voltage and current are proportional to the amplitude in some working modes, there is not much difference in the working frequency band and output of LM-FTG under these three amplitude conditions.

3.1.3 Power Experiment

In order to verify LM-FTGs ability of vibration harvesting at low frequency and further prove the conclusion about the influence of

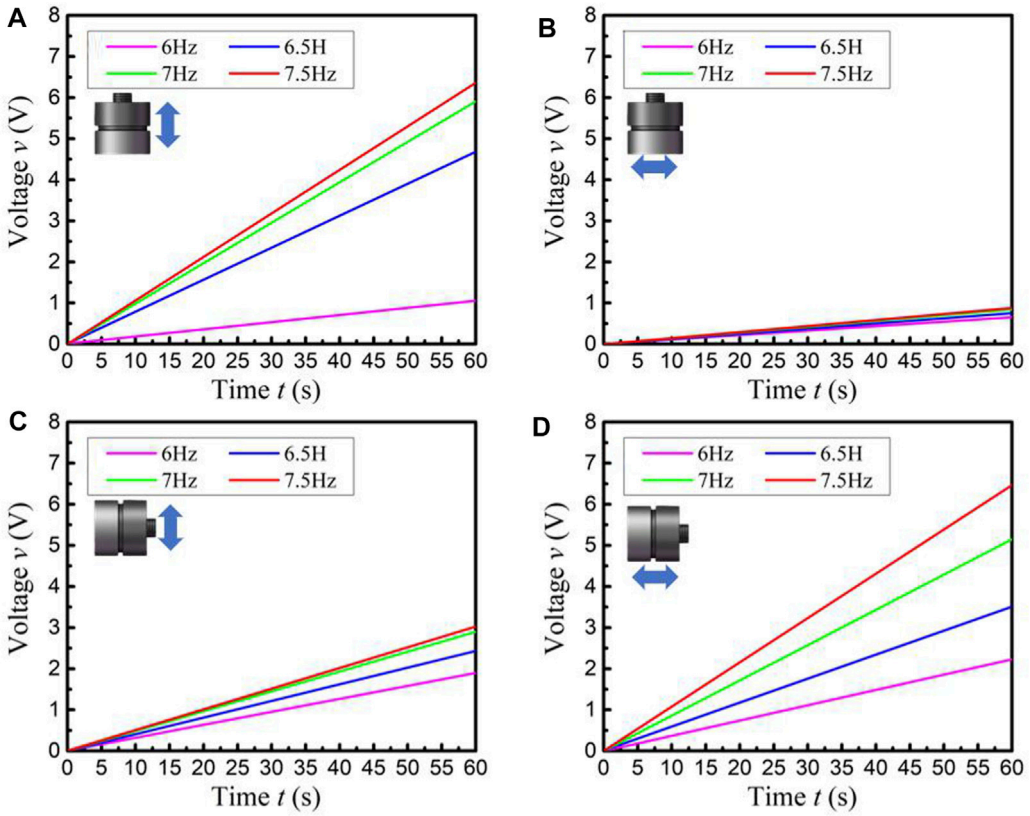

FIGURE 8 | Voltage of the 10 μF capacitor charged by LM-FTG. **(A)** Low-frequency response of LM-FTG in the VV mode. **(B)** Low-frequency response of LM-FTG in the VH mode. **(C)** Low-frequency response of LM-FTG in the HV mode. **(D)** Low-frequency response of LM-FTG in the HH mode.

working modes on harvesting capability, we performed the power experiment using the capacitor to charge in four modes like the frequency-sweep experiment. The vibration amplitude of the vibration table is set to 13 mm and the excitation frequencies applied are 6, 6.5, 7, and 7.5 Hz. The output of LM-FTG is connected to a 10 μF electrolytic capacitor to charge it, and the capacitor voltage is measured by a digital multimeter.

It can be seen from **Figure 8B** that, in the vertical placement, the output power of LM-FTG is very low when excited by the horizontal direction. Within 60 s, the voltage of the capacitor is below 0.4 V. **Figure 8A** shows the results when the vibration direction is vertical. The output power of LM-FTG is not ideal at 6 Hz, and the capacitor is only charged to 1.05 V. As the frequency gradually increases to 6.5, 7, and 7.5 Hz, the voltage of the capacitor suddenly increases to 4.68, 5.90, and 6.36 V. In the horizontal placement, the voltage of the capacitor reaches 1.89, 2.43, 2.89, and 3.02 V within 60 s at the excitation frequencies of 6, 6.5, 7, and 7.5 Hz when excited in the vertical direction. When excited by the vertical direction, the output voltage increases to 2.22, 3.50, 5.14, and 6.46 V. At horizontal placement, not only the device shows great harvesting capability for both directions of vibration but also the harvesting of low-frequency vibration energy is better than the vertical placement. In general, similar to the conclusion of the sweep-frequency experiment, LM-FTG has a good effect when the vibration direction is parallel to the tank body.

3.2 Low-Frequency Environmental Experiment

Since the walking vibration not only has the characteristics of low frequency, multidirection, and broadband but also is very common, we use the walking experiment to prove the practicality of LM-FTG. In the frequency-sweep experiment, the influence of the placement on the harvesting capability is verified. Here, in order to verify the impact of the placement in practice, we tied two identical LM-FTGs to the two calves in two ways (**Figure 9**) and conducted the walking experiment. In particular, for verifying the effect of walking speed on the LM-FTG's harvesting capability, we measure the output voltage of LM-FTG and the acceleration of walking (see **Supplementary Figure S4**) at speeds of 0.8, 1.2, 2 ,and 4 m/s.

Figure 9C shows the output voltage of LM-FTG under horizontal placement. It can be seen intuitively that the output voltage of LM-FTG increases with the increase in walking speed, which is an obvious proportional relationship. As shown in **Figure 7C**, the peak output voltage of LM-FTG is only 48 V at a walking speed of 0.8 m/s, while the peak output voltages of 1.2, 2, and 4 m/s reach 71, 82, and 169 V, respectively. The huge impact of walking speed on the open circuit

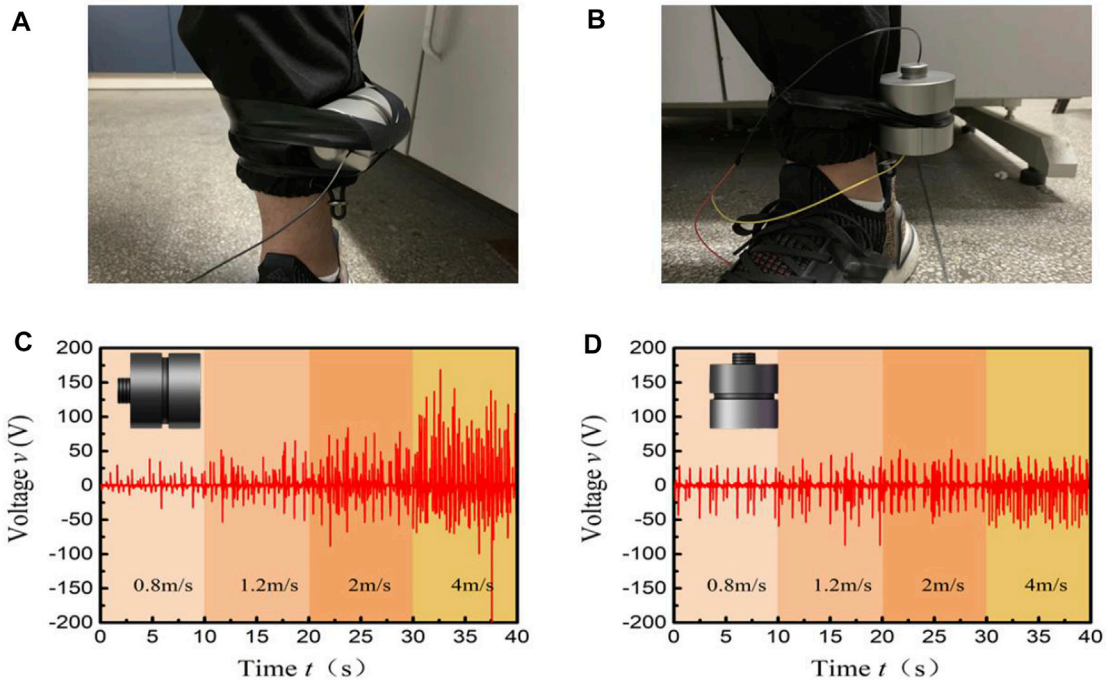

FIGURE 9 | (A) LM-FTG in horizontal placement.**(B)** LM-FTG in vertical placement. **(C)** Output voltage of LM-FTG in horizontal placement. **(D)** Output voltage of LM-FTG in vertical placement.

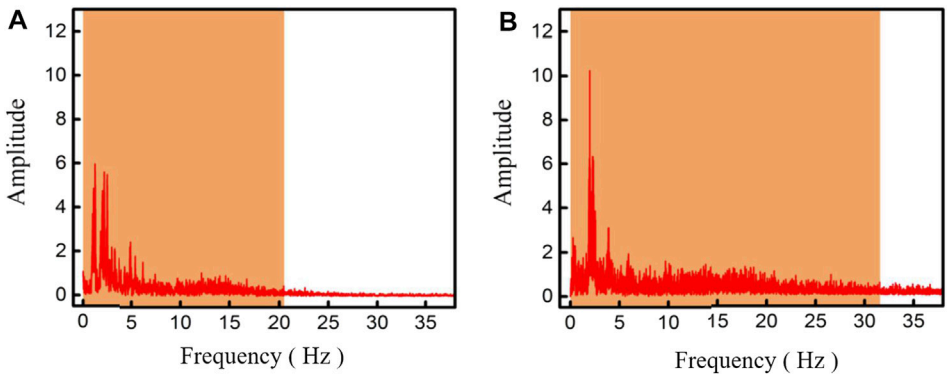

FIGURE 10 | (A) Spectrogram of walking.**(B)** Spectrogram of running.

voltage was verified. However, compared with the output voltage of LM-FTG in the vertical mode shown in **Figure 9D**, it can be seen that the difference of the output voltages is not obvious at the four walking speeds, and the peak output voltages do not exceed 50 V at most. The conclusions drawn in the frequency-sweep experiment are verified in practice.

In order to investigate the vibration frequency of walking, we measure the acceleration (see **Supplementary Figure S3**) of walking at the speed of 0.8 and 4 m/s. **Figure 10A** shows the spectrograms obtained by Fourier transform of the measured acceleration data at walking speeds of 0.8 and 4 m/s. As can be seen from **Figure 10A**, at a walking speed of 0.8 m/s, most of the frequency components are concentrated around 2.4 and 5 Hz. In this case where the effective band is defined as a band having an amplitude of 0.4 or more, the vibration frequency ranges from 0 to 20.82 Hz. This proves that the general walking vibration frequency band is wide and mainly concentrated in the low-frequency range. **Figure 10B** shows the spectrum at a walking speed of 4 m/s. Most of the frequency components are also concentrated below 5 Hz, but the frequency range can range from 0 to 32.03 Hz. By comparison, it can be seen that most of the frequency components are concentrated below

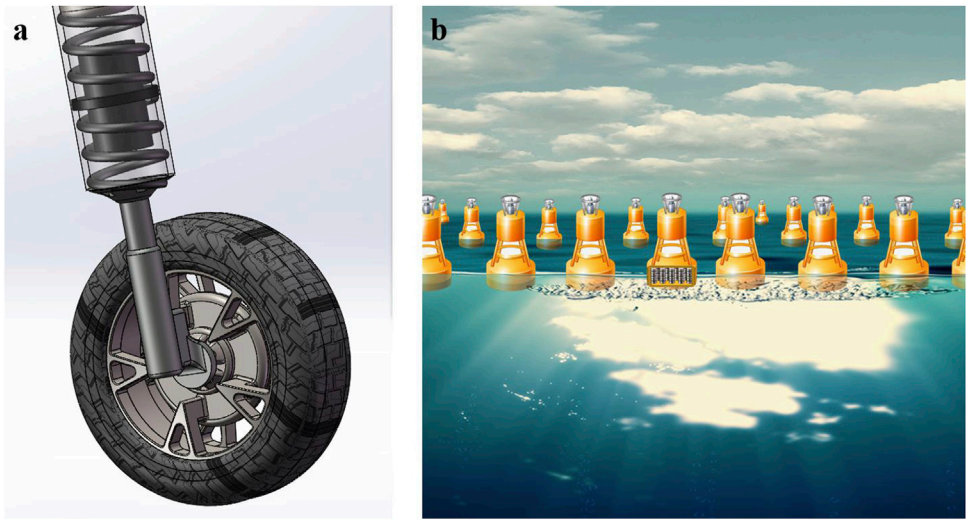

FIGURE 11 | (A) LM-FTG in car suspension.**(B)** LM-FTG in the ocean buoy.

5 Hz, but the increase in speed increases the bandwidth. In summary, it can be shown that the vibration frequency of walking is mostly concentrated in 0–3 Hz, and the power generation experiment under actual walking can prove the LM-FTG's harvesting capability in this frequency band.

In order to more intuitively demonstrate the power generation capability of LM-FTG, we wanted to light up LEDs with LM-FTG in actual walking. According to the previous experiments, we attached LM-FTG to the calf under the horizontal mode and it successfully lit up 100 series-connected LEDs (see **Supplementary Movie S5**).

4 CONCLUSION

In order to harvest vibration energy which is low frequency, multidirectional, and broadband, a triboelectric generator, which bases on the liquid metal and freestanding power generation mode, has been proposed. The device utilizes the fluidity of the liquid to more efficiently harvest low-frequency and multidirectional vibrations. Also, the freestanding power generation mode is used to decrease the structural complexity and ensure the stability of power generation. The frequency-sweep experiment shows that the difference of the working modes has a great influence on the power generation capability. The multidirectional vibration can be harvested and the working frequency band of LM-FTG is wide. In addition, the peak output can reach up to 252 V and 25.2 μA, and a 10 μF capacitor can be charged to 6.46 V at 7.5 Hz in 60 s by LM-FTG. In the low-frequency environmental experiment, the peak output voltage of LM-FTG under the horizontal mode with 4 m/s of the walking speed can reach 169 V and it can light up 100 LEDs in walking.

In addition, although the experiment was only carried out under the condition of wearing, the device can also be used in more fields. As shown in **Figure 11**, LM-FTG can be placed in the marine buoy to harvest wave energy from ocean waves or placed in the car suspension to harvest the vibrational energy of the car. So, we believe that LM-FTG not only provides a welcome boost for the development of a vibration energy harvester but also has a broader application prospect.

DATA AVAILABILITY STATEMENT

The raw data supporting the conclusions of this article will be made available by the authors, without undue reservation.

AUTHOR CONTRIBUTIONS

HD, ZZ, and CJ conceived and designed the manuscript. JY, SZ, MM, and XZ revised it. All authors contributed to the article and approved the submitted version.

FUNDING

The authors appreciate the support of the National Natural Science Foundation of China (Grant Nos. 11872167, 51675156, 51775164, and 51705122) and Natural Science Foundation of Anhui 281 Province (No. 1908085J15).

SUPPLEMENTARY MATERIAL

The Supplementary Material for this article can be found online at: https://www.frontiersin.org/articles/10.3389/fmats.2021.692273/full#supplementary-material

REFERENCES

Chen, J., Guo, H., Zheng, J., Huang, Y., Liu, G., Hu, C., et al. (2016). Self-Powered Triboelectric Micro Liquid/Gas Flow Sensor for Microfluidics. *ACS Nano* 10, 8104–8112. doi:10.1021/acsnano.6b04440

Dai, D., Liu, J., and Zhou, Y. (2012). Harvesting Biomechanical Energy in the Walking by Shoe Based on Liquid Metal Magnetohydrodynamics. *Front. Energ.* 6, 112–121. doi:10.1007/s11708-012-0186-x

Deng, H., Du, Y., Wang, Z., Ye, J., Zhang, J., Ma, M., et al. (2019a). Poly-stable Energy Harvesting Based on Synergetic Multistable Vibration. *Commun. Phys.* 2, 10. doi:10.1038/s42005-019-0117-9

Deng, H., Ye, J., Du, Y., Zhang, J., Ma, M., and Zhong, X. (2019b). Bistable Broadband Hybrid Generator for Ultralow-Frequency Rectilinear Motion. *Nano Energy* 65, 103973. doi:10.1016/j.nanoen.2019.103973

Fan, K., Liu, S., Liu, H., Zhu, Y., Wang, W., and Zhang, D. (2018). Scavenging Energy from Ultra-low Frequency Mechanical Excitations through a Bi-directional Hybrid Energy Harvester. *Appl. Energ.* 216, 8–20. doi:10.1016/j.apenergy.2018.02.086

Gao, H., Minh, P. T., Wang, H., Minko, S., Locklin, J., Nguyen, T., et al. (2018). High-performance Flexible Yarn for Wearable Piezoelectric Nanogenerators. *Smart Mater. Struct.* 27, 095018. doi:10.1088/1361-665X/aad718

Guo, H., Yeh, M.-H., Lai, Y.-C., Zi, Y., Wu, C., Wen, Z., et al. (2016). All-in-one Shape-Adaptive Self-Charging Power Package for Wearable Electronics. *ACS Nano* 10, 10580–10588. doi:10.1021/acsnano.6b06621

Harne, R. L., and Wang, K. W. (2013). A Review of the Recent Research on Vibration Energy Harvesting via Bistable Systems. *Smart Mater. Struct.* 22, 023001. doi:10.1088/0964-1726/22/2/023001

Hou, T.-C., Yang, Y., Zhang, H., Chen, J., Chen, L.-J., and Lin Wang, Z. (2013). Triboelectric Nanogenerator Built inside Shoe Insole for Harvesting Walking Energy. *Nano Energy* 2, 856–862. doi:10.1016/j.nanoen.2013.03.001

Hou, X., Zhu, J., Qian, J., Niu, X., He, J., Mu, J., et al. (2018). Stretchable Triboelectric Textile Composed of Wavy Conductive-Cloth PET and Patterned Stretchable Electrode for Harvesting Multivariant Human Motion Energy. *ACS Appl. Mater. Inter.* 10, 43661–43668. doi:10.1021/acsami.8b16267

Jiang, Q., Wu, C., Wang, Z., Wang, A. C., He, J.-H., Wang, Z. L., et al. (2018). MXene Electrochemical Microsupercapacitor Integrated with Triboelectric Nanogenerator as a Wearable Self-Charging Power Unit. *Nano Energy* 45, 266–272. doi:10.1016/j.nanoen.2018.01.004

Jung, I., Shin, Y.-H., Kim, S., Choi, J.-y., and Kang, C.-Y. (2017). Flexible Piezoelectric Polymer-Based Energy Harvesting System for Roadway Applications. *Appl. Energ.* 197, 222–229. doi:10.1016/j.apenergy.2017.04.020

Khaligh, A., Peng Zeng, P., and Cong Zheng, C. (2010). Kinetic Energy Harvesting Using Piezoelectric and Electromagnetic Technologies-State of the Art. *IEEE Trans. Ind. Electron.* 57, 850–860. doi:10.1109/TIE.2009.2024652

Kim, B. J., Kim, D. H., Lee, Y.-Y., Shin, H.-W., Han, G. S., Hong, J. S., et al. (2015). Highly Efficient and Bending Durable Perovskite Solar Cells: toward a Wearable Power Source. *Energy Environ. Sci.* 8, 916–921. doi:10.1039/c4ee02441a

Kim, J., Kumar, R., Bandodkar, A. J., and Wang, J. (2017). Advanced Materials for Printed Wearable Electrochemical Devices: a Review. *Adv. Electron. Mater.* 3, 1600260. doi:10.1002/aelm.201600260

Kim, S. J., We, J. H., and Cho, B. J. (2014). A Wearable Thermoelectric Generator Fabricated on a Glass Fabric. *Energ. Environ. Sci.* 7, 1959–1965. doi:10.1039/c4ee00242c

Kyono, T., Suzuki, R. O., and Ono, K. (2003). Conversion of Unused Heat Energy to Electricity by Means of Thermoelectric Generation in Condenser. *IEEE Trans. Energ. Convers.* 18, 330–334. doi:10.1109/TEC.2003.811721

Lee, Y.-H., Kim, J.-S., Noh, J., Lee, I., Kim, H. J., Choi, S., et al. (2013). Wearable Textile Battery Rechargeable by Solar Energy. *Nano Lett.* 13, 5753–5761. doi:10.1021/nl403860k

Li, Y., Shen, W., and Zhu, H. (2019). Vibration Mitigation of Stay Cables Using Electromagnetic Inertial Mass Dampers: Full-Scale experiment and Analysis. *Eng. Structures* 200, 109693. doi:10.1016/j.engstruct.2019.109693

Lin, Z.-H., Cheng, G., Lin, L., Lee, S., and Wang, Z. L. (2013). Water-solid Surface Contact Electrification and its Use for Harvesting Liquid-Wave Energy. *Angew. Chem.* 125, 12777–12781. doi:10.1002/ange.201307249

Liu, H., Tay, C. J., Quan, C., Kobayashi, T., and Lee, C. (2011). Piezoelectric MEMS Energy Harvester for Low-Frequency Vibrations with Wideband Operation Range and Steadily Increased Output Power. *J. Microelectromech. Syst.* 20, 1131–1142. doi:10.1109/JMEMS.2011.2162488

Liu, W., Wang, Z., Wang, G., Zeng, Q., He, W., Liu, L., et al. (2020a). Switched-capacitor-convertors Based on Fractal Design for Output Power Management of Triboelectric Nanogenerator. *Nat. Commun.* 11, 1883. doi:10.1038/s41467-020-15373-y

Liu, Y., Liu, W., Wang, Z., He, W., Tang, Q., Xi, Y., et al. (2020b). Quantifying Contact Status and the Air-Breakdown Model of Charge-Excitation Triboelectric Nanogenerators to Maximize Charge Density. *Nat. Commun.* 11, 1599. doi:10.1038/s41467-020-15368-9

Miki, S., Fujita, T., Kotoge, T., Jiang, Y. G., Uehara, M., Kanda, K., Higuchi, K., and Maenaka, K. (2012). "Electromagnetic Energy Harvester by Using Buried NdFeB," in 2012 IEEE 25th International Conference on Micro Electro Mechanical Systems (MEMS), 1221–1224. doi:10.1109/memsys.2012.6170409

Park, M., Kim, J.-Y., Son, H. J., Lee, C.-H., Jang, S. S., and Ko, M. J. (2016). Low-temperature Solution-Processed Li-Doped SnO2 as an Effective Electron Transporting Layer for High-Performance Flexible and Wearable Perovskite Solar Cells. *Nano Energy* 26, 208–215. doi:10.1016/j.nanoen.2016.04.060

Pu, X., Hu, W., and Wang, Z. L. (2018). Toward Wearable Self-Charging Power Systems: the Integration of Energy-Harvesting and Storage Devices. *Small* 14, 1702817. doi:10.1002/smll.201702817

Qian, J., He, J., Qian, S., Zhang, J., Niu, X., Fan, X., et al. (2020). A Nonmetallic Stretchable Nylon-Modified High Performance Triboelectric Nanogenerator for Energy Harvesting. *Adv. Funct. Mater.* 30, 1907414. doi:10.1002/adfm.201907414

Rome, L. C., Flynn, L., Goldman, E. M., and Yoo, T. D. (2005). Generating Electricity while Walking with Loads. *Science* 309, 1725–1728. doi:10.1126/science.1111063

Saadon, S., and Sidek, O. (2011). A Review of Vibration-Based MEMS Piezoelectric Energy Harvesters. *Energ. Convers. Manage.* 52, 500–504. doi:10.1016/j.enconman.2010.07.024

Safaei, M., Sodano, H. A., and Anton, S. R. (2019). A Review of Energy Harvesting Using Piezoelectric Materials: State-Of-The-Art a Decade Later (2008-2018). *Smart Mater. Struct.* 28, 113001. doi:10.1088/1361-665X/ab36e4

Sang, M., Wang, S., Liu, S., Liu, M., Bai, L., Jiang, W., et al. (2019). A Hydrophobic, Self-Powered, Electromagnetic Shielding PVDF-Based Wearable Device for Human Body Monitoring and protection. *ACS Appl. Mater. Inter.* 11, 47340–47349. doi:10.1021/acsami.9b16120

Sebald, G., Guyomar, D., and Agbossou, A. (2009). On Thermoelectric and Pyroelectric Energy Harvesting. *Smart Mater. Struct.* 18, 125006. doi:10.1088/0964-1726/18/12/125006

Siddique, A. R. M., Mahmud, S., and Heyst, B. V. (2015). A Comprehensive Review on Vibration Based Micro Power Generators Using Electromagnetic and Piezoelectric Transducer Mechanisms. *Energ. Convers. Manage.* 106, 728–747. doi:10.1016/j.enconman.2015.09.071

Siddique, A. R. M., Mahmud, S., and Heyst, B. V. (2017). A Review of the State of the Science on Wearable Thermoelectric Power Generators (TEGs) and Their Existing Challenges. *Renew. Sustain. Energ. Rev.* 73, 730–744. doi:10.1016/j.rser.2017.01.177

Starner, T. (1996). Human-powered Wearable Computing. *IBM Syst. J.* 35, 618–629. doi:10.1147/sj.353.0618

Tang, W., Jiang, T., Fan, F. R., Yu, A. F., Zhang, C., Cao, X., et al. (2015). Liquid-metal Electrode for High-Performance Triboelectric Nanogenerator at an Instantaneous Energy Conversion Efficiency of 70.6%. *Adv. Funct. Mater.* 25, 3718–3725. doi:10.1002/adfm.201501331

Wang, S., Ding, L., Fan, X., Jiang, W., and Gong, X. (2018a). A Liquid Metal-Based Triboelectric Nanogenerator as Stretchable Electronics for Safeguarding and Self-Powered Mechanosensing. *Nano Energy* 53, 863–870. doi:10.1016/j.nanoen.2018.09.035

Wang, S., Gong, L., Shang, Z., Ding, L., Yin, G., Jiang, W., et al. (2018b). Novel Safeguarding Tactile E-Skins for Monitoring Human Motion Based on SST/PDMS-AgNW-PET Hybrid Structures. *Adv. Funct. Mater.* 28, 1707538. doi:10.1002/adfm.201707538

Wang, S., Yuan, F., Liu, S., Zhou, J., Xuan, S., Wang, Y., et al. (2020). A Smart Triboelectric Nanogenerator with Tunable Rheological and Electrical Performance for Self-Powered Multi-Sensors. *J. Mater. Chem. C* 8, 3715–3723. doi:10.1039/C9TC05969E

Wang, Z., Liu, W., Hu, J., He, W., Yang, H., Ling, C., et al. (2020). Two Voltages in Contact-Separation Triboelectric Nanogenerator: From Asymmetry to Symmetry for Maximum Output. *NANO ENERGY* 69, 104452. doi:10.1016/j.nanoen.2020.104452

Wei, S., Hu, H., and He, S. (2013). Modeling and Experimental Investigation of an Impact-Driven Piezoelectric Energy Harvester from Human Motion. *Smart Mater. Struct.* 22, 105020. doi:10.1088/0964-1726/22/10/105020

Wen, Z., Yeh, M.-H., Guo, H., Wang, J., Zi, Y., Xu, W., et al. (2016). Self-powered Textile for Wearable Electronics by Hybridizing Fiber-Shaped Nanogenerators, Solar Cells, and Supercapacitors. *Sci. Adv.* 2, e1600097. doi:10.1126/sciadv.1600097

Xie, J., Li, F., Kuang, S., Yang, H., Li, X., Tang, S., et al. (2020). Modeling and Motion Control of a Liquid Metal Droplet in a Fluidic Channel. *Ieee/asme Trans. Mechatron.* 25, 942–950. doi:10.1109/TMECH.2020.2964387

Xiujian, C., Jie, Z., Shuo, Q., Xushi, N., Jichao, Q., Xiaojuan, H., et al. (2018). All-in-one Filler-Elastomer-Based High-Performance Stretchable Piezoelectric Nanogenerator for Kinetic Energy Harvesting and Self-Powered Motion Monitoring. *Nano Energy* 53, 550. doi:10.1016/j.nanoen.2018.09.006

Yang, B., Lee, C., Wei, L. K., and Lim, S.-P. (2010). Hybrid Energy Harvester Based on Piezoelectric and Electromagnetic Mechanisms. *J. Micro/nanolith. MEMS MOEMS* 9, 023002. doi:10.1117/1.3373516

Yang, W., Chen, J., Zhu, G., Yang, J., Bai, P., Su, Y., et al. (2013). Harvesting Energy from the Natural Vibration of Human Walking. *ACS Nano* 7, 11317–11324. doi:10.1021/nn405175z

Yang, Y., Sun, N., Wen, Z., Cheng, P., Zheng, H., Shao, H., et al. (2018). Liquid-Metal-Based Super-stretchable and Structure-Designable Triboelectric Nanogenerator for Wearable Electronics. *ACS Nano* 12, 2027–2034. doi:10.1021/acsnano.8b00147

Yildirim, T., Ghayesh, M. H., Li, W., and Alici, G. (2017a). A Nonlinearly Broadband Tuneable Energy Harvester. *J. Dynamic Syst. Meas. Control.* 139, 011008. doi:10.1115/1.4034321

Yildirim, T., Ghayesh, M. H., Li, W., and Alici, G. (2017). A Review on Performance Enhancement Techniques for Ambient Vibration Energy Harvesters. *Renew. Sustain. Energ. Rev.* 71, 435–449. doi:10.1016/j.rser.2016.12.073

Yildirim, T., Ghayesh, M. H., Searle, T., Li, W., and Alici, G. (2017b). A Parametrically Broadband Nonlinear Energy Harvester. *J. Energ. Resour. Tech.* 139, 011008. doi:10.1115/1.4034514

Yu, L., Yi, Y., Yao, T., Song, Y., Chen, Y., Li, Q., et al. (2019). All VN-Graphene Architecture Derived Self-Powered Wearable Sensors for Ultrasensitive Health Monitoring. *Nano Res.* 12, 331–338. doi:10.1007/s12274-018-2219-1

Zeng, W., Tao, X.-M., Chen, S., Shang, S., Chan, H. L. W., and Choy, S. H. (2013). Highly Durable All-Fiber Nanogenerator for Mechanical Energy Harvesting. *Energ. Environ. Sci.* 6, 2631–2638. doi:10.1039/c3ee41063c

Zhang, C., Tang, W., Han, C., Fan, F., and Wang, Z. L. (2014). Theoretical Comparison, Equivalent Transformation, and Conjunction Operations of Electromagnetic Induction Generator and Triboelectric Nanogenerator for Harvesting Mechanical Energy. *Adv. Mater.* 26, 3580–3591. doi:10.1002/adma.201400207

Zhang, J., Yan, S., Yuan, D., Alici, G., Nguyen, N.-T., Ebrahimi Warkiani, M., et al. (2016). Fundamentals and Applications of Inertial Microfluidics: a Review. *Lab. Chip* 16, 10–34. doi:10.1039/C5LC01159K

Zheng, L., Lin, Z.-H., Cheng, G., Wu, W., Wen, X., Lee, S., et al. (2014). Silicon-based Hybrid Cell for Harvesting Solar Energy and Raindrop Electrostatic Energy. *Nano Energy* 9, 291–300. doi:10.1016/j.nanoen.2014.07.024

Zhu, H., Li, Y., Shen, W., and Zhu, S. (2019). Mechanical and Energy-Harvesting Model for Electromagnetic Inertial Mass Dampers. *Mech. Syst. Signal Process.* 120, 203–220. doi:10.1016/j.ymssp.2018.10.023

Zi, Y., Guo, H., Wen, Z., Yeh, M.-H., Hu, C., and Wang, Z. L. (2016). Harvesting Low-Frequency (. *ACS Nano* 10, 4797–4805. doi:10.1021/acsnano.6b01569

Zuo, L., Scully, B., Shestani, J., and Zhou, Y. (2010). Design and Characterization of an Electromagnetic Energy Harvester for Vehicle Suspensions. *Smart Mater. Struct.* 19, 045003. doi:10.1088/0964-1726/19/4/045003

Conflict of Interest: The authors declare that the research was conducted in the absence of any commercial or financial relationships that could be construed as a potential conflict of interest.

frontiers in Materials

REVIEW
published: 28 July 2021
doi: 10.3389/fmats.2021.681960

This Review Recent Advances in Chitosan and Alginate-Based Hydrogels for Wound Healing Application

*Cuthbert Kibungu, Pierre P. D. Kondiah, Pradeep Kumar and Yahya E. Choonara**

Wits Advanced Drug Delivery Platform Research Unit, Department of Pharmacy and Pharmacology, School of Therapeutic Sciences, Faculty of Health Sciences, University of the Witwatersrand, Johannesburg, South Africa

Wound healing is a complicated yet necessary event that takes place in both animals and human beings for the body to repair itself due to injury. Wound healing involves various stages that ensure the restoration of the injured tissue at the end of the process. Wound dressing material acts as a protective extracellular barrier against potential damage to the injury and microbial invasion. Naturally, polysaccharides (chitosan and alginate) have inherent properties that have made them attractive for their usage in wound healing therapy. Alginate and chitosan have been used to develop novel wound healing and smart biomaterials due to various functionalities such as reducing swelling, non-toxic nature, biocompatibility, antimicrobial potential, and maintenance moist environment, ability to absorb wound fluid, and skin regeneration promotion. Functionalization of polysaccharides is one of the many approaches that have been used to modify and enhance the wound healing properties of these biomaterials. Many studies have been done to modify the polysaccharide hydrogels. Some of these are highlighted in this paper. The designing and development of smart hydrogels that react to their environment have recently sparked a significant scientific and pharmaceutical interest. Smart hydrogel development has been the primary focal area for developing highly advanced and sophisticated wound healing therapeutic technologies. This paper seeks to comprehensively shed light on the advancements of functionalized chitosan and alginate-based hydrogels and their applicability in wound healing therapeutics. In addition to this, thus identifying critical drawbacks faced in existing hydrogel systems and how prospective technologies enable digitally controlled bio-platforms coupled with biomaterials to improve wound care. This review hopes to stimulate and encourage researchers to identify future avenues worth investigation.

Keywords: smart, wound management, wound healing, functionalization, polysaccharide, biomaterial

OPEN ACCESS

Edited by:
Yanju Liu,
Harbin Institute of Technology, China

Reviewed by:
Haibao Lu,
Harbin Institute of Technology, China
Yilong Cheng,
Xi'an Jiaotong University, China

****Correspondence:***
Yahya E. Choonara
Yahya.Choonara@wits.ac.za

Specialty section:
This article was submitted to Smart Materials, a section of the journal Frontiers in Materials

Received: *17 March 2021*
Accepted: *15 July 2021*
Published: *28 July 2021*

Citation:
Kibungu C, Kondiah PPD, Kumar P and Choonara YE (2021) This Review Recent Advances in Chitosan and Alginate-Based Hydrogels for Wound Healing Application. Front. Mater. 8:681960. doi: 10.3389/fmats.2021.681960

INTRODUCTION

Today wound management remains a serious problem regardless of the recent advancements made regarding wound healing materials development. Wounds are classified based on their depth, appearance, location, etiology, and the nature of the injury (Baranoski and Ayello, 2008). In addition to this, wounds can be further categorized as partial, full, and superficial thickness (Boateng et al.,

2008). Worldwide, a wide variety of wounds are generated annually for various reasons such as surgical procedures, non-healing ulcers, gunshots car accidents and burns (Aderibigbe and Buyana, 2018). The cost to manage wounds increases as the population size increases. The urban lifestyle is an indicator for the greater need to develop novel hydrogel-based wound dressings materials that are relevant, effective, and affordable (Cullum et al., 2016). Wound dressings are produced from various biopolymers and synthetic polymers. Alginate has been extensively researched to develop pharmaceutically relevant biomaterials. Alginate is toxic-free, antimicrobial, abundant in nature, offers excellent biodegradability, hydrophilic, biocompatible, and does not elicit immune responses (Noh et al., 2006). Wound dressings developed as hydrogels have become very important for successful wound healing and wound management over the years, more especially when modified chemically, physically or combined with technological devices. Different polymers have been used to produce wound dressings which are available in retail markets (Wild et al., 2009). Hydrogels are defined as water-soluble cross-linked polymeric networks developed by either physical or chemical cross-linking of soluble polymers.

Their unique properties, such as hydrophilic nature, soft tissue-like water content, high-sensitivity to physiological environments, and adequate flexibility, have made them the preferred and excellent choice for wound healing-related therapeutics. Polysaccharide-based hydrogels can swell in water, showing specific stimuli-responsiveness to their environment due to changes in environmental conditions such as temperature, light, and pH. Thus, hydrogels' intelligence to respond to changes in physiological variables change suggests their meaningful use in several biomedical applications, one of them being wound healing (Sood et al., 2014). Therefore, the importance of this manuscript is to review the recent work done by researchers in the field of wound healing and to look at the main achievements as result of functionalising polysaccharides (alginate and chitosan).

The application of alginate and chitosan for wound healing is due to these polymers having favourable and distinctive attributes. These include having a high absorption capacity, biocompatible, non-toxic, non-immunogenicity, and low cost (Sudarsan et al., 2015). However, these natural polymers can usually be limited by their unfavourable mechanical attributes. As a result, they are combined with other synthetic platforms or are derivatized to enhance their mechanical characteristics (Noh et al., 2006).

This manuscript seeks shed light on the progress made regarding wound healing therapy using functionalised alginate/chitosan as well as the drawbacks which still exist in the development of sophisticated and smart wound healing systems. The importance of developing a wound dressing material which has ideal wound healing properties that create an environment that allows the wound to heal quickly under pathological conditions while achieving an acceptable skin appearance at an affordable price (Sweeney et al., 2012) is also covered to assist researchers in understanding the importance of designing or developing wound healing systems based on the factors that promote successful wound healing therapy and improve patient compliance. A major development in wound healing therapy is the emergence of smart hydrogels which have been developed by combining technological platforms or devices such as chips, wearable bands, and sensors with polymers. These have shown significant advancement in the control of drug release, swelling, or absorption in response to pH, temperature, oxygen levels, or light as developed by Mostafalu et al. [95]. Microneedles are also another type of platform advancing over the years. The development of the first solid microneedle (MNs) was developed in 1971 [97]. More promising technologies have been produced since 2012, resulting in the first hydrogel-based microchip microneedles, which were developed by Donnelly et al. [102]. Therefore, incorporating bioactive components in wound dressings has been found to improve these novel systems' overall effectiveness.

Therefore, novel and technologically advanced polysaccharide-based-hydrogel dressings may encourage more efficient wound healing over a short period, provide pain relief and reduce scarring, thus improving overall patient compliance. Polysaccharides have diverse structures, which make them differ in their chemical composition and attributes and this should always be taken into consideration when designing and producing modified biomaterials. Different design strategies by functionalization have been highlighted in this manuscript to provide information on the properties and benefits of functionalising different molecules such as peptides (RDG), acyl containing compounds, amine containing compounds and methyl containing compounds These properties provide a range of structural properties and chemical attributes that can be manipulated for the synthesis and combined with various technological systems for the development of novel wound dressing hydrogels specific to the wound etiology, thus providing endless avenues for investigation. This review aims to provide recent information and data regarding the advancement and progress of modified chitosan and alginate wound healing systems and the benefits of combining such systems with technological devices to produce smart and intelligent wound healing products.

WOUND HEALING PROCESS

Several growth factors like cytokines, chemokines, and other biomolecules facilitate the wound healing process (Thomas, 1990). Wound healing occurs in 4 phases, as seen in **Figure 1**. The first stage is the exudative phase, 2. Inflammatory phase, 3. Proliferative phase and 4. Regenerative phase (Yadav et al., 2015). Several growth factors are required for wound healing to take place. These mainly include chemokines and cytokines (Coger et al., 2019; Gupta et al., 2019; Stern and Cui, 2019).

Exudative Stage

The exudative stage also referred to as coagulation and hemostasis, involves preventing blood loss. It is the act of stopping excessive bleeding by hemostatic reflex vasoconstriction and forming an insoluble plug fibrin, and excessive blood loss is prevented. Blood flows and interacts with collagen exposed together with other extracellular matrix components. This phase is followed by

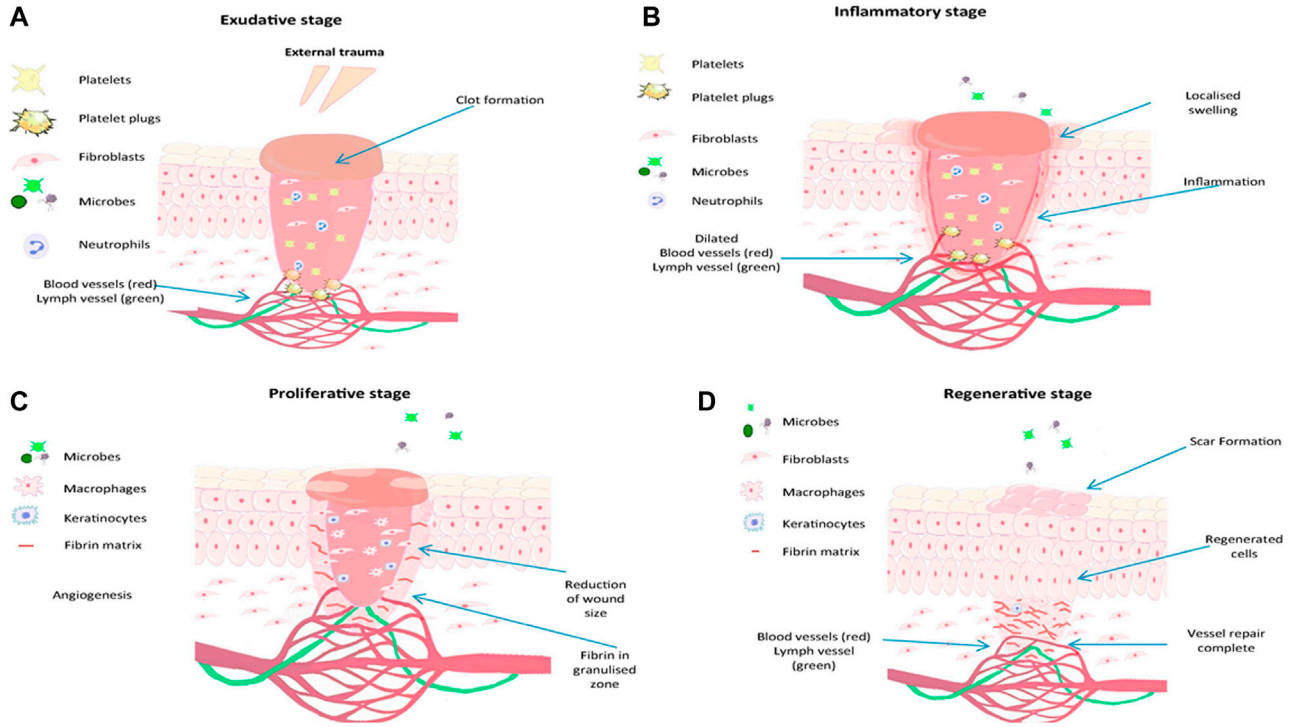

FIGURE 1 | Representation of steps involved in wound the healing process, reproduced with permission from Gupta et al. (2019), **(A)** exudative stage with the formation of blood clot, **(B)** inflammatory stage, marked with oedema, pain and inflammation, **(C)** proliferation stage with granulation tissue formation and **(D)** regenerative stage, characterised by scar tissue formation.

platelet activation to release clotting factors before their aggregation forms a plug mash network, thus regulating and preventing blood loss (Ding et al., 2018).

Inflammation Stage

For wound healing to continue effectively, neutrophils must be cleared from the wound through phagocytosis by macrophages, followed by removing the wound utilizing shredding, autolytic debridement, and apoptosis. Mononucleated macrophages make their way to the wound site about 48–72 h post-injury and become changed into reparative macrophages (Yang et al., 2017) that enable and mediate inflammation together with the removal of dead cells by phagocytosis (Vishwakarma et al., 2014; Kuivaniemi and Tromp, 2019).

Proliferation Stage

Upon successful autolytic debridement and the immune response has concluded. The wound healing process then continues to the proliferation stage; at this stage, tissue formation occurs due to the tissue's repairing and closure of the being started. The area which is damaged is then covered by granulation tissue; this is then followed by the damaged tissue's epithelialization occurring. The epithelial cells around the wound parameters grow by mitosis and move resulting in a long and wide layer of cells forms. The protein known as collagen is produced by fibroblasts, mimics a temporary matrix, and supports the newly developed granulation tissue, which is crucial in determining scars' appearance (Wild et al., 2009; Vishwakarma et al., 2014). To distribute nutrients and oxygen to freshly deposited tissue, it is at this phase when angiogenesis can occur. Therefore, allowing a network of microvascular blood capillaries to be formed from existing normal blood vessels (Coger et al., 2019; Kuivaniemi and Tromp, 2019).

Regeneration Stage

The final phase of wound healing is the regeneration phase. During this final step, the typical dermal structure is reproduced, and the mechanical strength of the tissue is improved. All cells responsible for inflammation are cleared from the fixed area while remodeling collagen occurs to improve the tissue's tensile strength (Simões et al., 2018).

TYPES OF WOUND HEALING MATERIALS

Materials used as wound healing material can be categorized into traditional, artificial, biomaterial-based, and bioactive dressings (Yu et al., 2018). Passive wound dressings protect wounds from the external environment and stop bleeding (Harding et al., 2000). Classic wound dressing examples include gauze-cotton and gauze composites that typically can absorb high amounts of wound fluid. However, classic dressings can cause the wound to bleed, display low vapor transmission properties, and destroy recently formed tissue (epithelium) when removed. Exudates leaking from such dressings can lead to bacterial invasion (Moura et al., 2013).

TABLE 1 | Wound dressing classifications.

Category	Benefit of use	Examples	References
Passive wound dressings	It does not have apart from covering and protecting the wound. It needs frequent changing and does not provide a moist environment	Gauze, gauze composites, bandages, and plasters	Qu et al. (2018)
Skin substitutes	Improve wound closure and replace the skin function, thereby promoting wound healing	Allografts, amnion, autografts, tissue-engineered derivatives	Bradford et al. (2009)
Artificial materials	Promote wound healing and protect wounds from bacterial infections	Gels, sprays, hydrocolloids, hydrofibres, foams, and films	Liang et al. (2019)
Bioactive natural dressings	These polymers have natural properties such as antimicrobial, bio-adhesive, biodegradable, and proliferative properties. Growth factors may be incorporated to enhance wound healing	Collagen. Elastin, alginate, and chitosan	Almeida et al. (2011)

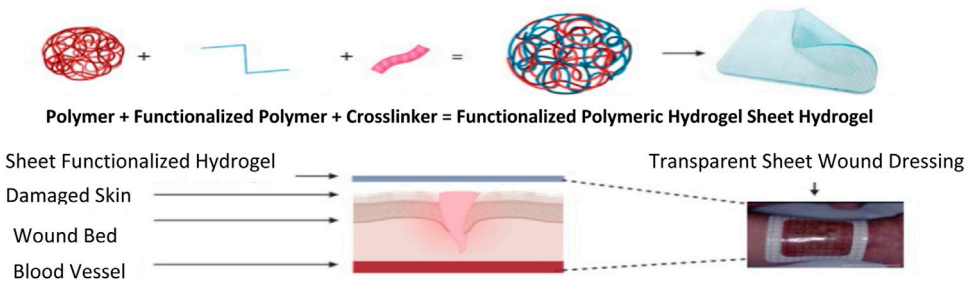

FIGURE 2 | Synthesis and application of sheet functionalized hydrogels for wound healing purposes.

Wound dressings that are biomaterial-based are further characterized as allografts, tissue derivatives, or xenografts. Skin fragments, also known as allografts, are available as either freeze-dried or newly received tissue from donors. Their usage is often restricted by immunological responses leading to the rejection recipient's body. In addition to this, the transmission of diseases and infection risk is great (Line et al., 1995). Allografts costs are high and have a low shelf life (Greenwood and Dearman, 2012). Artificial dressings are categorized as composites, films, gels, films, foams, and sprays (Morgan, 2002), [110]. These are synthesized from natural and synthetic polymers. Commonly used biopolymers include alginate, chitosan, cellulose, and xanthan due to their intrinsic and beneficial properties. Such wound dressings are further grouped and characterized as bioactive wound dressing. Alginates, chitosan, xanthan, collagens, hydrofibres, and hydrocolloids are examples of bioactive wound dressings. An improved wound healing process can be achieved by adding growth factors, nanoparticles, functional groups, and antimicrobials (Parenteau et al., 1996). Wound dressing classifications are summarised in **Table 1**.

APPLICATION OF ALGINATE AND CHIOTSAN AS WOUND DRESSINGS

Sheet Hydrogel Dressings and Amorphous Hydrogels

Hydrogel dressings can exist in two main forms, amorphous dressing, and sheet dressing (Qu et al., 2018). Amorphous hydrogel dressings exhibit low exudate absorptive capabilities because of their high-water content. However, they provide a moist environment for dry wounds; functionalizing these hydrogels improves the absorbent capabilities, swelling profile, moisture retention ability, stretchability, and hydrogels' mechanical strength (Bradford et al., 2009). Hydrogel dressings classified as sheet dressings are mainly applied during the final phases during the recovery of wounds. Such steps include the epithelial phase and phlebitis. Clear and transparent sheet hydrogels can also be used to monitor wound healing progress in real-time, as seen in **Figure 2**. Hydrogel dressings are classified as amorphous hydrogels' primary use is to support autolysis debridement and scab softening. Such amorphous biomaterial is frequently used by doctors and nurses in clinics (**Figure 3**) (Liang et al., 2019).

DEVELOPMENT APPROACHES OF NOVEL CHITOSAN AND ALGINATE-BASED HYDROGELS

The treatment of chronic wounds and acute wounds is a serious challenge. Wound dressings derived from natural polymers offer numerous advantages in comparison to traditional wound dressings (Almeida et al., 2011). Alginate and chitosan-based wound dressings can be made to take up several forms, such as sponges, foams, nanofibers, films, and hydrogels (Huang and Fu, 2010; Mndlovu et al., 2019). Alginate application as a wound-healing material is because

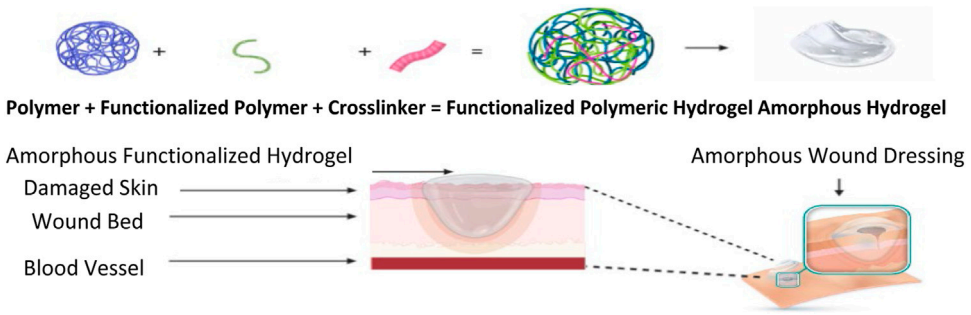

FIGURE 3 | Synthesis and application of functionalized amorphous hydrogels.

of its inherent features (non-toxicity, biocompatible nature, non-immunogenic, cheap to buy, and high absorption profile) (Huang and Fu, 2010). However, natural polymers are usually limited by their unfavorable mechanical attributes. The combination of natural and synthetic polymers is done to enhance their physical properties, degradation patterns, and overall antimicrobial properties (Almeida et al., 2011).

Alginate Based Formulations

Thiol Functionalized Alginate Hydrogels

Alginate, derived from algae, has widely been researched for its suitability as a wound care therapeutic product, and the delivery of drugs to wounds because of its non-toxic and biocompatible attributes (Mansoor et al., 2019) by derivatization led to several favourable properties being imparted onto Alginate. Meidong et al. (Lee and Mooney, 2012) investigated an *in situ* formed thiolated alginate hydrogel, which was synthesized using disulfide bonds being formed due to oxygen, a water-containing solution with available thiol groups. Therefore, to illustrate the hydrogel's cytocompatibility properties, human hepatocytes were fabricated in the hydrogel, resulting in 85% cell viability after five days. This meant that the interaction of the thiol groups with hepatocytes cellular environment resulted in the reduction of Reactive Oxygen Species (ROS) resulting in improved cellular viability. In terms of the potential of the functionalized hydrogel to lower the homeostatic time, animal-based experiments were carried out using a rat's tail. The duration of hemostasis decreased from 8.26 to 3.24 min in comparison with a calcium alginate hydrogel The reason for this is because disulfide bonds have been found to play a role as redox switches. Disulfide bonds are present in the β subunit of the platelet integrin αIIbβ3 and in other integrins involved in thrombus formation. Redox agents such as gluthione, nitric oxide and enzymatic thiol isomerase are responsible for the regulation of the integrins because of thiol or disulfide exchange or disulfide bond reduction thus controlling the rate of thrombus formation. Therefore, thiolated platform could absorb a significant amount of blood compared to calcium alginate hydrogel (Xu et al., 2016). Yin and co-worker's (Li et al., 2017) investigated another cross-linked disulfide hydrogel of thiolated alginate as a biomaterial for tissue engineering (Lynch et al., 2020). The platform was stable for 14 days in an aqueous solution, and stability was influenced by the degree of thiolation and the degree of cross-linking. This hydrogel further showed homeostatic potential and significant biocompatibility. This was made possible due to the abundant free thiol groups as these groups are easily oxidized when they are in aqueous solutions. The degree of crosslinking on the other hand further provides reinforcement by improving the mechanical stability to the biomaterial. Hydrogel-based wound dressings have been intensively studied as promising materials for wound healing and care. Popescu et al. (Lynch et al., 2020) reported the mixed-mode thiol-acrylate photopolymerization is used in their work for alginate/poloxamer hydrogels formation. First, the alginate was modified with thiol groups using the esterification reaction with cysteamine, and second, the terminal hydroxyl groups of poloxamer were esterified with acryloyl chloride to introduce polymerizable acrylate groups. Finally, the cross-linking reaction between the two macromers was performed to produce degradable alginate/poloxamer hydrogels. The biological assays show that the alginate/poloxamer hydrogels induce proliferation of human keratinocyte and have an anti-inflammatory effect on lipopolysaccharides (LPS)-activated keratinocytes by inhibiting the extracellular signal-regulated kinases (ERK)/nuclear factor (NF)-kB/tumor necrosis factor (TNF)-α signalling pathway. Their results showed that the chemical cross-linked alginate/poloxamer hydrogels may function as a dressing/patch applied directly on the skin lesion to heal the wound by reducing the exacerbated inflammation which causes wounds not to heal or increases their healing time.

Alginate Functionalization With Furan Compounds

Since alginate can be modified by both its carboxyl groups and hydroxyl present in its backbone structure, it enables several interesting features to be achieved which will enhance the wound healing capabilities of the polysaccharide. Oxidation or light-curable cross-linking strategies have been used to prepare hydrogels in drug delivery. Li et al. (2017) synthesized chemically cross-linked alginate hydrogels by reacting alginate modified using furfuryl amine and stimuli-responsive crosslinkers. The ensuing hydrogels' investigation toward pH stimuli revealed an apparent pH-dependent swelling. The system can be designed to absorb wound fluid and release drugs at low pH. It is at a pH of 5 whereby fibroblasts are

activated and proliferate the most in contrast to neutral or alkali pH. This design strategy would result in a faster wound healing process and ensure that the wound is kept moist and does not contain excess wound fluid as opposed to ionic cross-linked alginate hydrogels. The synthesized cross-linked alginate hydrogels had stable polymeric networks, and their properties can be adjusted according to the cross-linking degree. However, this can be limiting as certain properties are not imparted onto the pristine polymer when crosslinking is done. The introduction of functional groups to the pristine biopolymer will result new physical, chemical and biomedical properties being obtained which are beneficial to the success and efficiency of the wound healing process. Heo and coworkers (Heo et al., 2020) developed a light curable Furfuryl alginate hydrogel responsive to light stimulus. The release studies demonstrated that the prepared furan alginate hydrogels showed different gelation, swelling, and degradation abilities in response to light exposure. Therefore, they appeared to be good candidates for a dermal drug delivery system (Heo et al., 2020). In addition to this the introduction of bioactive drugs and nanocarriers into the furan alginate-based biomaterials could accelerate and enhance the wound healing process due to the adjustable release, gelling, and degradation properties of bioinspired smart hydrogels. This type of hydrogel could be designed in the form of microneedles perhaps this would improve the mechanical strength of the biomaterial, release kinetics of the system, drug bioavailability, interaction between the modified biomaterial and the wound tissue due to the large surface area.

Aldehyde Functionalized Alginate Hydrogels

Lu et al. (Deng et al., 2020) synthesized a multifunctional alginate hydrogel for healing complex skin injuries. Their study developed a sodium alginate aldehyde hydrogel and cross-linked it with divalent Strontium ions ($Sr\ 2^{+}$). The rationale behind their study incorporating an aldehyde group to their alginate was to achieve excellent biocompatibility, biodegradability, non-toxic, and improved swelling properties and could adhere closely to tissues. They also observed self-healing abilities due to the slow release of strontium ions. In addition to this, the hydrogel promoted immediate and fast angiogenesis of the skin tissue. This occurred due to the slow release of the strontium ions which have been found to play an important role in promoting angiogenesis of skin tissue. The repair of the defects was accelerated at the same time. Such properties imparted to alginate are suitable for allowing rapid skin defects in complex wound injuries (Mondal et al., 2020).

This type of study was significant in shedding light on other focal areas in which alginate can be modified to advance wound healing. Such areas of study should be further evaluated as most studies only focus on the healing of wounds using composite biomaterials or synthetic polymers with biopolymers. In contrast, few studies have considered evaluating the skin tone restoration and architecture using functionalized polysaccharides. In addition to this it would be interesting to conduct research on the hemostatic potentials of these aldehyde-based alginate hydrogels.

Arginine-Glycine-Aspartic Acid Derivatized Alginate Hydrogel

Even though alginate has excellent biocompatibility properties, it is made of inert monomers that naturally lack the bioactive ligands necessary for cell anchoring. This cell-crosslinking method introduces ligands, such as the arginine-glycine-aspartic acid (RGD) sequence, onto alginate for cells to adhere to the Alginate-RDG modified hydrogel by chemically coupling, which uses water-soluble carbodiimide synthesis has been extensively used (Ansari et al., 2021). Upon the addition of mammalian cells to the RGD-modified alginate, a uniform dispersion is formed within the solution, and receptors follow this on the cell surface, binding to the RDG-Alginate ligands. The RGD-modified alginate solution is subsequently cross-linked to form network structures through specific receptor-ligand interactions between the cells and RGD sequences. The combination of RGD-alginate-with stem cells can further accelerate and improve soft tissue regeneration. Ansari et al. (2021) reported the use of Gingival mesenchymal stem cells (GMSCs) in RGD modified alginate hydrogels. The regenerative potential of mesenchymal stem cells (MSCs) encapsulated in hydrogels is well documented, however for polysaccharide-based polymers little work has been reported for wound healing therapy. Here, an RGD-alginate–gelatin-methacrylate (GelMA) hydrogel formulation was developed encapsulating GMSCs within the developed hydrogel. From their results it was observed that the encapsulated MSCs remain viable within the hydrogel with enhanced collagen deposition. An excisional wound model in mice was utilized in their study to evaluate the *in vivo* functionality of the RGD-Alginate GMSC–hydrogel construct for wound healing and soft tissue regeneration. The histology and immunofluorescence analyses confirmed the effectiveness of the GMSC–hydrogel in expediting wound healing was through enhancing angiogenesis and suppressing local proinflammatory cytokines. Based on these findings, it can be seen that GMSCs encapsulated in an functionalized polysaccharide (alginate) based sheet hydrogel can be used to expedite wound healing and soft tissue regeneration, with potential applications in not just wound healing therapy but also plastic and reconstructive surgery as well as dentistry (Ansari et al., 2021).

Krause et al. (Krause et al., 2012) concluded that RGD-pentapeptide functionalized hydrogel exhibit a biomimetic microenvironment on wounds. Their study further displayed enhanced biocompatibility, cell proliferation, cell adhesion, and good biodegradation (Yu et al., 2010). Although the cell-crosslinked hydrogel shows excellent bioactivities, the major drawbacks that the network exhibited were low mechanical strength and toughness, limiting the practical applications of their advanced biomaterial. Such types of hydrogels could be made as a 3D printed scaffold in combination with an additional polymer such as chitosan, to maximize the systems interaction with the wound. This approach could further enhance the mechanical strength of the scaffold and improve the absorptive (due to a controllable pore

size), cell adhesion (presence of RDG) cell proliferative capabilities (chitosan) and hemostatic (chitosan properties) properties of the system. Studies should not look at the functionalization of one specific polymer but rather a combination of polymers which can be combined to produce or develop a product with novel properties. Very few of these types of studies involving RDG and two types of polysaccharide-based polymers have been reported in literature.

Chitosan-Based Formulations

Heparin Functionalized Chitosan Hydrogels

Peptide-based polysaccharide formations have attracted significant attention over the years. This an attractive strategy for wound healing biomaterials, except for using the delivery of blood factors as an approach, is to derivatize the natural polysaccharide materials with amino acid sequences that would interact with surface receptors of dermal cells. Such receptors are those of skin cells, thus enabling cell differentiation, proliferation, and cell migration, thus enabling a more rapid and complete healing process. Heparin functionalized with chitosan has favorable outcomes in the last phases of wound healing stages. Kratz et al. (Kampf et al., 2018) formulated heparin complexed chitosan bio-platform. Their study discovered heparin-chitosan platforms to have wound healing potential, which was depended on the concentration of heparin. Furthermore, 1.9% (w/w) heparin could not induce re-epithelialization, but 7.7% of heparin (w/w) generated almost complete re-epithelialization. From this, it can be concluded that the time-controlled delivery of heparin at the correct dose is required to reach therapeutic efficacy. It was further observed that heparin-chitosan hydrogels exhibited no tissue ingrowth, resulting in the formation of a highly vascularized granulation layer (Krajewska, 2004). Thus, implying that heparin functionalized chitosan's ability to initiate an angiogenic response. Jin et al. (Mi et al., 2002) compared chitosan's effect when used as a powder, without and with the presence of heparin on deep partial burns. The wounds were created on the dorsum of rats. Following 72 h, their study's histology results revealed that chitosan in its powdered form stopped an early extension of burns, while the peptide under study, whether by itself or embedded inside the polysaccharide, was not effective (Kampf et al., 2018). Based on most of literature the contrary, heparin functionalized with chitosan exhibited positive effects on the last stages of healing.

Arginine-Glycine-Aspartic Acid (RGD) Functionalized Chitosan Hydrogels

Arginine-glycine-aspartic acid (RGD) sequence has been found to induce cell adhesion by binding and activating integrin, allowing cell to cell and cell to extracellular matrix adhesion (Kratz et al., 1997). Arginine-glycine-aspartic acid (RGD) functionalized with chitosan were tested for cell adhesive properties to the extracellular matrix (ECM) (Chai et al., 2017). It was shown that RGD functionalization onto chitosan biomaterials imparts improved properties. Such properties are cell adhesive and biocompatibility properties. This process occurs because the adhesion cell receptors recognize RGD. Therefore, the functionalized chitosan takes up an artificial ECM role, allowing cellular adhesion to occur (Jin et al., 2007), these finding further show the potential which chitosan has in wound healing therapy. Furthermore, the combination of peptides with natural polymers yields numerous properties in the product which is much more suitable for wound care application as compared to the pristine polymers. Karakecili et al. (Chai et al., 2017) studied cell interactions with peptides using chitosan membranes functionalized with RGD sequences. Results from the *in vitro* study suggested that L929 mouse fibroblasts exhibited an increased cell attachment with time. They concluded that RGD was crucial for cell attachment, cell migration, and cell proliferation. Their findings further show the importance of attaching key peptides with known wound healing properties to natural biomaterials like alginate to impart favorable properties to the biomaterials. The relevance of their study further highlights the role cell attachment, cell migration and cell proliferation in the wound healing therapy.

Ammonium Functionalized Chitosan Hydrogels

One of the many factors that limit the application of native chitosan is its non-solubility in neutral and alkaline aqueous solutions (Jia et al., 2001). N-trimethyl chitosan chloride and found that it interacts with negatively charged cell membranes thus, inhibiting the growth of microorganisms (Abueva et al., 2021). They also observed that their synthesized N-trimethyl chitosan was water-soluble, and therefore an important new property was obtained compared to the pristine polymer. They further observed that the chitosan's heterogeneous chemical modification could tune the hydrogel's surface properties. Their observations noted that when a stearoyl group was attached to N-Trimethyl chitosan hydrogels, the hydrogels became more hydrophobic and promoted protein adsorption. Antimicrobial resistance has been a problem for public health professionals. Therefore, wound healing patches with broad spectrum bioactivity against Hospital-Associated Multi-Drug resistance (MDR) strains of bacterial and fungal pathogens is important. Abueva et al. (Jia et al., 2001) N,N,N-trimethyl chitosan chloride (TMC) with inherent bactericidal property was synthesized and complexed with povidone-iodine (PVP-I) to create a potentially more potent antibacterial properties that could also significantly enhance the wound healing process. TMC, a positively charged, water-soluble derivative of chitosan, formed stable solutions with PVP-I at 5% w/v TMC concentration. TMC5/PVP-I was significantly effective against multidrug-resistant bacteria *S. aureus* compared with PVP-I alone. TMC/PVP-I solutions also showed fungicidal property against *C. albicans*. This further illustrates that although derivatization may impart new and useful properties to alginate, further modification or analogs of quaternary ammonium alginates can introduce novel properties beneficial for wound healing application. Chitosan's insolubility in water makes it difficult for the biomaterial to dissolve into wound fluid over time as it degrades. However, by functionalizing the biomaterial with a trimethyl group chitosan then become more wound friendly. This is a major achievement as one of the ideal properties of any wound healing system is its ability to solubilize in aqueous solutions.

TABLE 2 | Functionalized types of chitosan and their respective properties.

Derivatization approach	Outcome
Carboxymethyl chitosan	Enhances water solubility, solubility is dependent on pH when pH is greater than seven, results in water-solubility
Chitosan derivatives by alkylation	It is an amphiphilic polysaccharide-based polymer. Enhances the interfacial film stability profile, surfactant cationic, can be adsorbed on the alkyl chain grafted onto chitosan, enabling solubilization
Trimethylated chitosan	Cationic derivative, water-soluble across all pH ranges, obtained by the quaternization of chitosan. Exhibits good flocculating and antistatic properties
Carbohydrate chitosan (branched)	These are soluble in water. Reductive alkylation allows different types of carbohydrates to be grafted onto chitosan. Specific lectins easily recognize these grafted chains, thus equipping them with drug targeting potentials
Chitosan-grafted copolymers	One of the extensively studied derivatives is polyethylene glycol-grafted chitosan; it has the advantage of being water-soluble
Thiolated urea derivatives	Thiourea chitosan enhances the bactericidal properties of chitosan

N-Succinyl Chitosan

Succinyl chitosan (NSC) is synthesized through acyl group introduction. These groups' introduction imparts chitosan with excellent biological, chemical, and physical attributes (Nam et al., 2004). NSC has excellent water retention attributes, which can be exploited for the development of wound healing matrices. Straccia et al. (Zhai et al., 2002) developed a hydrogel consisting of NSC with alginate, and this wound healing material exhibited antimicrobial activity, showed good stability, a significant degree of swelling, and a regulated rate at which water vapor is transmitted, most modified polysaccharide biomaterials exhibit poor absorption especially pristine chitosan.

Furthermore, chitosan-based hydrogel was effective in maintaining a moist wound environment resulting in the enhancement of tissue regeneration and epithelialization (Kamoun and Menzel, 2012). Also, NSC bio-platforms were evaluated *in vivo*, and their result suggested that the NCS system successfully prevented microbial infection and improved wound healing. In a different approach Qing et al. (2021) reported that polyvinyl alcohol (PVA)/*N*–succinyl chitosan (NSCS)/lincomycin hydrogels were effective in their wound healing properties. From their results it can be observed that the introduction of NSCS remarkably enhanced the swelling capacity, leading to the maximum swelling ratio of 19.68 g/g in deionized water. The optimal compression strength of 0.75 MPa was achieved with 30% NSCS. Additionally, the incorporation of lincomycin brought a remarkable antibacterial activity against both *Escherichia coli* and *Staphylococcus aureus*. Their hydrogel showed not toxicity properties. Therefore,/NSCS/ lincomycin hydrogel shows promising potential for wound dressing due to its non-toxic, excellent absorption and significant compression strength which makes this functionalized composite suitable for wound healing. Such findings further show that the combination of functuionalized polymers with other polymers can further improve the properties of the pristine and functionalized polymer. Modified types of Chitosan hydrogels are shown in **Table 2**. These findings show that NSC or NSC-Alginate possess most of the properties required for an accelerated and successful wound healing process. The combination of NSC with alginate further shows the importance of combining a modified polymer with a pristine polymer to achieve a variety of new properties which will be beneficial for wound healing.

DRAWBACKS OF ALGINATE AND CHITOSAN-BASED HYDROGELS

Natural polysaccharides have generally demonstrated favourable properties which allow them to be used as a therapeutic option for chronic wounds. Despite this, a natural polysaccharide may elicit the immune system to react adversely and cause irritation. Hence, the natural polysaccharide's molecular weight control may be used to overcome such limitations. In addition to this, in dry wounds, these properties could affect the wound healing process (Saarai et al., 2012). This may result in dehydration, thus reducing blood flow and the ability of epithelial cell migration within the wound site, interrupting new tissue creation. As evidence, re-epithelialization of the wound site is more rapid under moist conditions than under dry ones with natural polysaccharide wound dressing treatment (Kamoun et al., 2017), with a controllable molecular weight, probably, the capabilities of natural polysaccharides in speeding up the wound healing process can be exploited to treat various types of wound injury. The advantages and disadvantages of hydrogel wound dressing materials are shown in **Table 3**, as reported by Kamoun et al. (Price et al., 2007).

Natural polysaccharides are the human dermal Extracellular matrix ECM (Suzuki et al., 1998). Polysaccharides are abundant in nature, and they have been shown to have great potential for pharmaceutical, medical and biomedical applications. Wound healing dressings used for tissue regeneration have been developed from polysaccharides because of their economic, low toxic nature, and favourable compatibility profile. However, possessing a lack of protein structure, natural polysaccharide exhibits a very poor bio-stability and difficulty assembling a "matrix" to cover the damaged tissue during the wound healing, thus facilitating contraction of the wound resulting in scar formation (Chansiripornchai et al., 2003). In addition to this, the synthesis of temperature or pH-responsive and functionalized biomaterials requires toxic chemicals that are expensive and hazardous.

PROPERTIES OF AN IDEAL POLYSACCHARIDE-BASED HYDROGEL FOR WOUND HEALING

Polysaccharide hydrogels are considered effective candidates for wound healing therapy. This because of their high water-

TABLE 3 | Advantages and disadvantages of Hydrogels used as dressing materials.

Types	Characteristics	Indications	Advantage	Disadvantages
Hydrogels	Amorphous or sheet hydrogel is used for auxiliary and autolysis debridement	Full-thickness injury or partial-thickness injury. Necrotic or desquamate wounds small to medium exudation. Hydration promotes self-dissolving debridement	It positively providing water to dry wounds and keeping the wound moist. No wound adherence. They promote autolysis debridement for scab debridement Conducive to epithelial migration and granulation growth non-sticking wound. Pain relief protecting germ infection	The poor absorptive capacity of exudates. Not for severe exudative wounds and infectious wounds. No bacterial barrier. Easy to cause skin immersion around The second layer of dressing is needed. The dressing color will turn green

TABLE 4 | Properties of an ideal wound healing hydrogel.

Property	Description
Maintain a moist environment	Prevents wound from drying because of vapor loss
Excellent gas transmission	Allow the movement of oxygen through the hydrogel and into the wound bed
Superabsorbent capabilities	Remove excess exudates without reaching saturation on the wound's outer surface
Protection against microbial infections or contaminations	Should possess antimicrobial properties against a broad spectrum of microorganisms and contaminants
Environmentally friendly	A readily biodegradable platform that is not an environmental threat due to the components used in the hydrogel synthesis
Excellent wound healing regulator	Reduce inflammation, stimulate growth factors release, tissue regeneration, and prevents scarring
Provide mechanical protection	Acts as a protective physical bearer that prevents further damage to the site of injury
Stops bleeding	Possess excellent homeostatic properties to prevent further blood loss
Adhesiveness	Possess easy and comfortable removal properties
Non-immunogenic and biocompatible	It is non-allergic and non-toxic to the body
Clear hydrogel membrane	Transparent, thus allowing wounding healing to be monitored
Affordable and commercially available	Accessible and affordable to buy and improves patient compliance

retaining capacity, non-toxicity, biodegradability, and biocompatibility (Winter, 1962; Silva et al., 2018; Zhu et al., 2019). Over the years, different approaches in designing or developing efficient and effective wound dressing materials have been considered; it has been demonstrated that healing of wounds with wet dressings is faster than dried dressings. This is ultimately ascribed to the healing and formation of renewed skin without eschars or inflammation, taking place only in a wet environment (Lee and Mooney, 2012).

Thus, wet or moisten dressings were the suitable dressing candidate for skin repair, hence the successful applicability of hydrogel dressings in wound care therapy due to their high-water content and inherent permeability (Becker et al., 2016). An ideal wound dressing material should fulfil the following characteristics, as shown in **Table 4** (Winter, 1962). If most of these properties can be contained in a developed hydrogel system, this would result in wound healing taking place efficiently and faster in a wet environment, as provided by hydrogel in contrast to the dried environment. Given the growing demand, developments and manufactures of novel wound dressings with high performance have become a research focus in the field of medical materials, among which hydrogel is found to satisfy most of the criteria for treating and managing wounds. A hydrogel is a 3D network composed of hydrophilic polymers, which can absorb and swell in water because of the highly mimic natural extracellular matrix (ECM) properties, hydrogel has been extensively utilized in pharmaceutical and biomedical applications. In terms of wound dressings, hydrogel do not only form a physical barrier and remove excess exudate but also encapsulate bioactive molecules and provide a moisture environment that promotes the wound healing process (Silva et al., 2018).

In addition, the injectable hydrogel would also be able to completely fulfill the irregular shaped wound and deal with deep bleeding wound more efficiently. Due to the numerous merits of hydrogels, a series of commercial hydrogels as wound dressings have been emerged, such as Algisite M, Tegaderm TM hydrocolloid dressing, Evicel VR, and Coseal VR. Despite their good wound healing performance, there exist some deficiencies, including high cost, harsh storage conditions, inability to provide adequate mechanical protection, and poor permeability of gases. Since the demand for higher performance dressings, novel hydrogel dressings with multifunctional properties (antibacterial ability, biodegradability, responsiveness, and injectability) received increasing attention in the field of wound dressings in recent years (Lee and Mooney, 2012; Zhu et al., 2019). Interestingly, hydrogels can control scab formation and allow a swift and well-coordinated cell proliferation and epithelialization process to take place. Furthermore, smart hydrogels' development using modern technology and software has used some of these ideal properties to develop the most sophisticated biomaterial dressings that are beneficial for wound healing therapeutics.

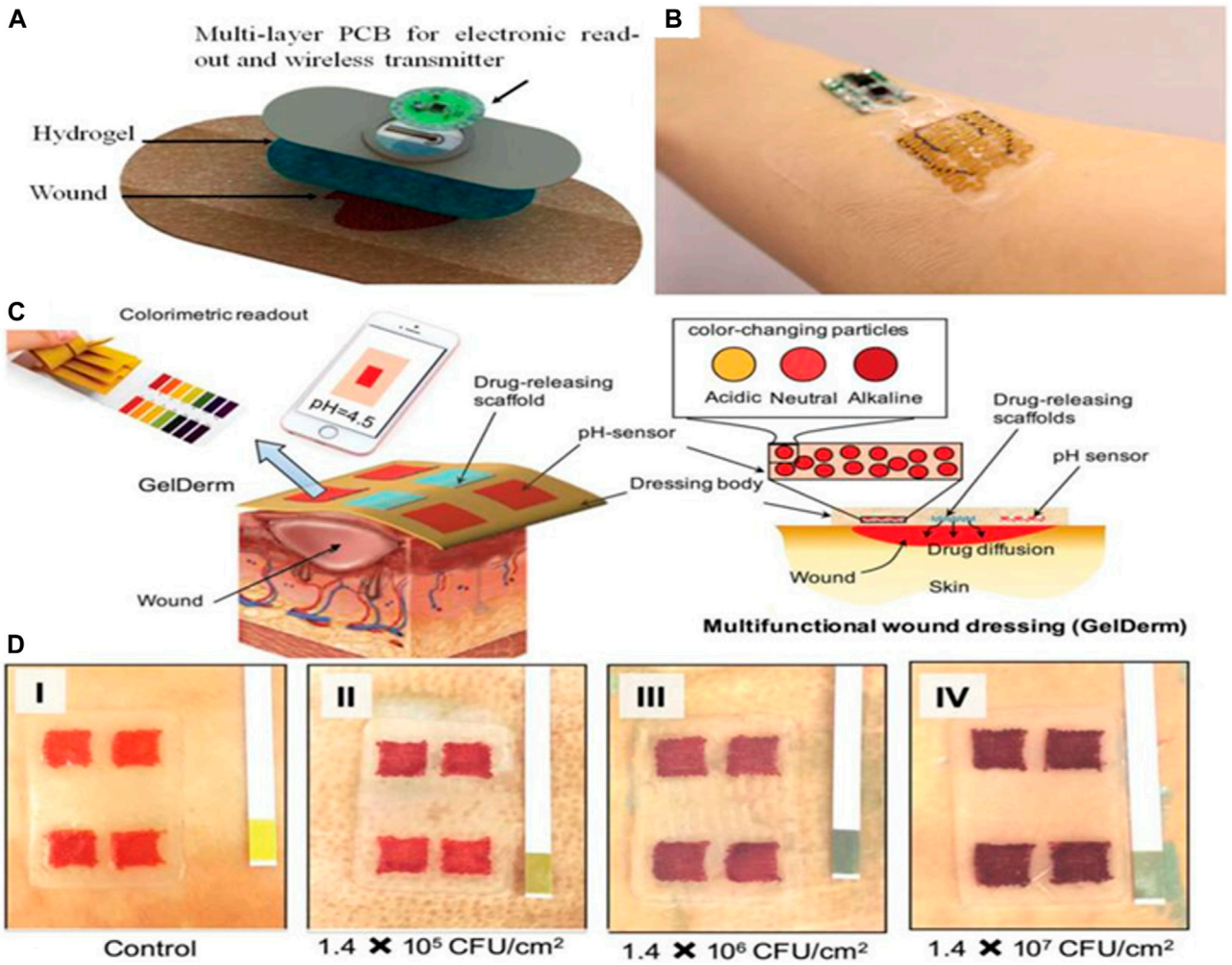

FIGURE 4 | Smart and automated bandages for treatment of chronic wounds. **(A)** Schematic of multi-layer dressing with both sensing and drug delivery. The onboard electronics can process the data and trigger the drug delivery if needed. **(B)** A photograph of the wearable bandage with both sensing and drug delivery capabilities. **(C)** Schematic of a 3D printed bandage with colorimetric pH sensor and drug delivery capability. **(D)** Effect of bacterial culture on the color of the engineered bandage.

SMART AND INTELIGENT HYDROGELS USED IN WOUND HEALING THERAPY

Smart drug delivery devices were designed to control the level of drug, cytokines, pH, and temperature in patients at desirable levels (Stewart, 2002). Existing medical instruments can either monitor or deliver bioactive agents. Such individuals must interpret information and recommend the appropriate therapy course. Electronic devices' advancements have led to the development of devices with fast data interpreting abilities in wearable and portable forms, which have been attached to the biopolymer (**Figures 4–6**). Other devices include the development of microneedles, which penetrate through the wound to all direct delivery of active drugs or growth factors and provide direct interaction of the biomaterial with the wound. Such devices also have a feature that allows them to be paired to wireless devices through Bluetooth communication, Infrared, or internet connectivity (Kasagana and Karumuri, 2011).

Thus, allowing the data to be quickly processed onboard or online, and the decisions can be made automatically for proper treatment of the wounds. Chronic wounds affect many populations and the continuous need for hospital visit by patients to be assessed on their wound healing progress place substantial pressure on medical professionals and patients. The development of such technologies will assist in the simplification of wound management and assist in the reduction or eradication of the transmission of wound related infections. These intelligent systems or devices also provide medical stuff and patients with confidence and certainty of the wound healing progress of the injury(s) being treated in real-time.

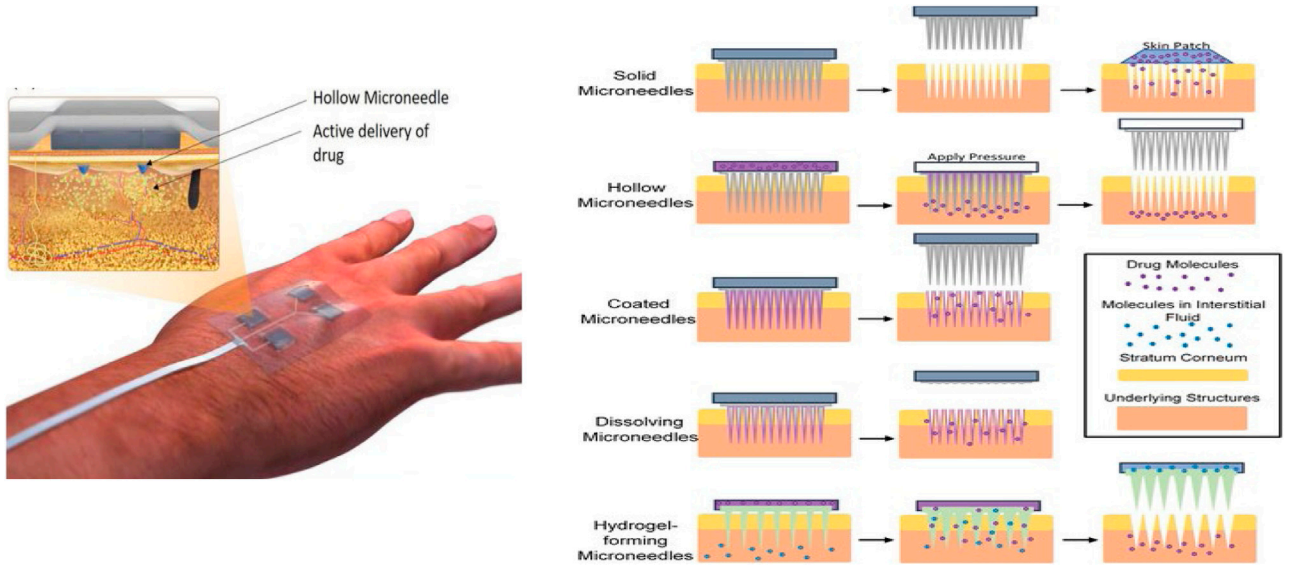

FIGURE 5 | Application of smart microneedle hydrogel used in wound healing.

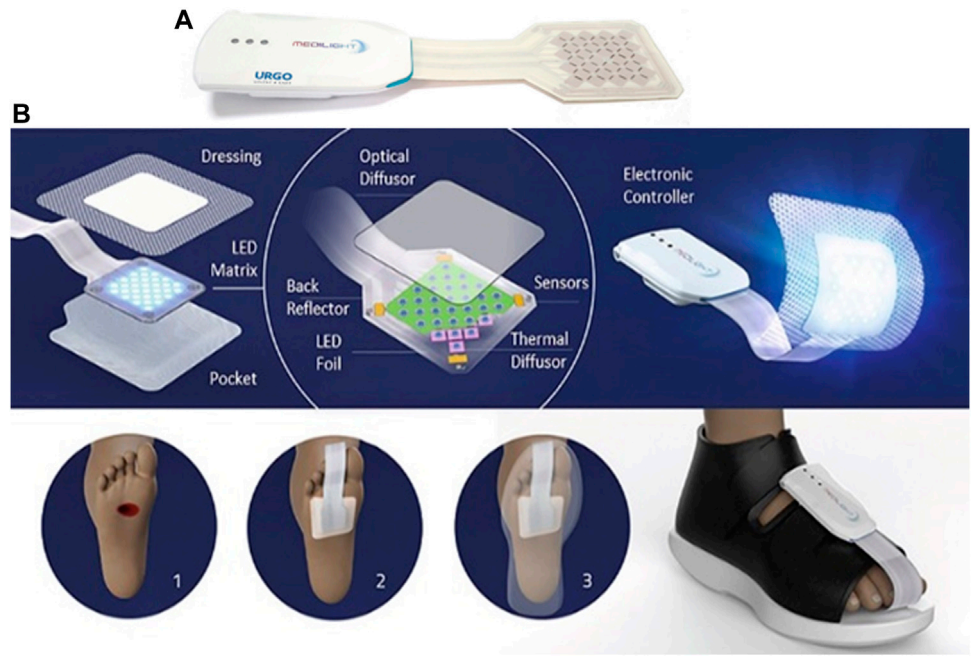

FIGURE 6 | (A) Developed smart foot patch used in the treatment of chronic wounds, with the permission from MEDILIGHT © Group AMIRES-EU Projects, **(B1)** Illustration of the components and application of the MEDILIGHT © foot patch used in wound healing therapy. Depiction of bare chronic wound, **(B2)** depiction of the MEDILIGHT © foot patch being applied on a patient's foot, and **(B3)** MEDILIGHT © foot patch appearance when the shoes are fitted on.

Smart Bandages

Two separate studies looked at the development of automated bandages equipped with either pH sensors, drug delivery modules, or temperature sensors (**Figure 4**) (Botsis and Hartvigsen, 2008; Mirani et al., 2017). Critical pH values can be set on the controller, and once the pH reaches outside the acceptable range, the heater is triggered to release antibiotics. Overall, this area is still developing, and it is expected that more

advanced automated devices are to be engineered. A pain-free and easy-to-use automated system would revolutionize the way hydrogels are used and how they respond to different types of wounds. Such systems' effectiveness can be enhanced by incorporating nanosystems that can offer dual insulin delivery (De la Harpe et al., 2020), a drug containing nanoparticles (Chivere et al., 2020), to chronic wounds. Mostafalu et al. (2015) were the first to design and develop an integrated multilayer bandage. An array of electrochemical pH sensors was embedded within a hydrogel layer carrying thermo-responsive drug carriers cast on a flexible heater (Mirani et al., 2017). The sensors and heater were connected to a microcontroller that could communicate with smartphones. The nanosystem proposed by Essa et al. (De la Harpe et al., 2020) makes use of a hydrophobic core, a cationic component, and surface density of Polyethylene glycol (PEG) chains, which created favorable-sized particles and drug entrapment efficiencies suitable for drug delivery. Their hydrophobic poly (lactide-co-glycolide) (PLGA) core further encouraged a high degree of carrier-drug interactions. Simultaneously, chitosan and PEG coatings provided cationic and hydrophilic properties to enable enhanced biocompatibility and solubility.

Microneedle Based-Smart Wound Patches

In 2012, the first hydrogel-forming microneedle (HFMs) were the newest form of MNs (**Figure 5**) (Cheung and Das, 2016). They were made of polymers with swelling properties (cross-linked); these HFMs exhibited different operation mechanisms compared to other microneedles. Hollow microneedles are solid needles and have a hollow center that enables the delivery of desired drugs upon applying pressure or response to the pH or temperature of the wound. HFMs swell when inserted into the skin and release drugs, and uptake wound fluid (Cheung and Das, 2016; Chai et al., 2017). The development of Injectable smart thermo-responsive hydrogel systems for biomedical applications has sparked great attention over the years (Essa et al., 2020; Popescu et al., 2021). Injectable smart hydrogel can be introduced into solid biodegradable microneedles. Since microneedles interact directly with damaged tissue, they can be directly applied in the same way injectable hydrogel would have been directly injected into the wound. This method would be less painful and long-lasting. A casted microneedle casing could be made using RGD peptide-functionalized chitosan or alginate hydrogel as the starting polymer. The smart thermoresponsive hydrogel would then be pumped into the microneedle. Therefore, the biopolymer acts as the second layer within the microneedle upon degradation of the functionalized starting polymer. The second hydrogel, which may contain growth factors, drugs, stem cells, or nanoparticles, is released. These agents would interact with the wound in a sustained manner following the starting polymers degradation as its role would be to attach the microneedles to cells following the end of the first stages of wound healing. After this, the release of growth factors and drugs will encourage sustainable wound healing. Thus, allowing complete tissue regeneration.

LED-Based System for Treating Foot-Based Chronic Wounds

Based on what is reported in the literature, light therapy could be used for various medical conditions, especially skin-related abnormalities or even tissue regeneration. Non-healing of acute or chronic wounds occurs because of impaired cell function, unregulated and frequent inflammatory processes, and molecular deficiencies inside the wound (Chi et al., 2020). The antimicrobial and anti-proliferative effects of blue light are well known and explicitly described in the literature (Frykberg and Banks, 2015; Mamalis et al., 2015). MEDILIGHT suggested that blue light could be used in the early wound healing stages to enhance wound healing and inhibit bacterial growth. It is also essential to prevent excess epimerization by keratinocytes at the wound surface as this can lead to premature closure of the trauma. Contrary, red light is supposed to stimulate cell proliferation, migration, and differentiation (Dai et al., 2012), which is vital in later stages of healing, leading to a wound's closure. This process would start right from the wound bed. **Figures 6A,B** shows the smart patch prototype, which can be controlled via Bluetooth and modern mobile software.

Future Prospects

It is therefore essential to gain insight into the benefit of using other derivatization approaches together with the combination of sophisticated electronic devices as this will provide new information and data as to how existing systems can be further enhanced and controlled electronically to best suit the intended biomedical application. The new properties gained can therefore be practically understood before being translated to human wound healing application(s). It is for this reason why there are a few smart hydrogels are being commercialized, in addition to this the rate at which these technologies are being commercialized is very slow. New and promising applications of polysaccharide-based hydrogels like stable or semisolid-state microneedle hydrogels, bioinspired smart, flexible LED foot patches for robust electrolyte and flexible electronic devices, controlled growth factors release, and medications, pH, and temperature response should be further studied as these advanced technological bio-platforms are the future of biomedical therapeutics.

Although these technologies have been developing for some time now, only a few of these smart devices have reached the commercialization stage; secondly, these smart devices have been studied using the combination of biopolymers and synthetic polymers. None of them looked at the applicability of functionalized hydrogels with smart systems for example RGD-Alginate microneedle system which is linked to a electrical smart biosensor device. More defined biomarkers and wearable sensors should be identified for rapid diagnosis and treatment as this allows accurate diagnostics and provide advanced wound care therapy using a combination of multi-drug delivery systems. These include the measurement of oxygen levels, moisture content of the wound and pH of the wound, collagen and hydroxylysine levels, reactive oxygen species (ROS) concentrations. The advantage of smart bandages is

that they are automated and can efficiently respond to the recorded data.

Thus, initiating a therapeutic response usually does not require a single drug or initiator molecule to induce healing or alleviate patients' symptoms. Continuous research is necessary to develop cheaper, unique, versatile, and smart wound healing hydrogels that will significantly improve patient compliance, accessibility, and a greener environment. Challenges such as controllable drug release, hydrogel interaction with human wound fluid and tissue, and the biodegradation of polysaccharide-based hydrogels *in vivo* is another a big problem which still needs to be solved in the future, this requires more extensive to be done. Lastly since it is very difficult to translate *in vitro* based studies to *in vivo* studies as the two study approaches offer varying environmental conditions and these parameters influence the overall applicability of the developed biomaterial system novel testing approaches need to be developed to ensure that the data obtained at levels of production is accurate and ensures that the developed biomaterial can work on human beings.

CONCLUSION

Alginate and chitosan-modified hydrogels possess unique properties such as excellent water retention abilities, biocompatibility with human beings and animals, biodegradable properties, and non-toxic nature. Such properties can be very useful in the research and development of smart wound healing biomaterials. In addition to this, such polysaccharide-based platforms are advantageous in specific medical applications due to their structure, which can be manipulated to have desired physical or chemical properties.

Such gels would help facilitate several functions such as controlling the rate of diffusion, response to environmental stimulus, growth factor, drug release, and gas exchange between the wound and external environment. Even though polysaccharide-based hydrogels have become popular and possess numerous superiorities.

Significant obstacles that need to be circumvented for polysaccharide hydrogels' to be used as commercial products still exist even today. The major issues include introducing hazardous solvents or reagents during the synthesis process, modification, and cross-linking of the hydrogels. Therefore, there is an urgent need to explore advanced ways of chemically developing smart polysaccharide platforms with broad biomedical application properties not just for general wound healing but also skin cancer, pressure sores, and ulcer-related wounds. The use of green chemistry and advanced technological devices can be used as a smart approach in achieving this. In addition to this, it remains a significant challenge not just for wound healing but also for drug management and patient compliance as products are not environmentally friendly and affordable for purchase by people, especially the poor. Research should also be streamlined towards achieving biopolymers with unique properties, such as excellent stability, ability to maintain suitable pH required for wound healing, wound fluid enzyme tolerance, sound absorption, improve bioavailability of loaded drug, self-healing properties, provide mechanical support and protection to the wound, superior elasticity and can be integrated to electronic devices with ease.

AUTHOR CONTRIBUTIONS

The manuscript was completed through contributions of all authors. CK, PPDK, PK and YEC conceived, designed the framework and main content of the manuscript, as well as wrote and revised the manuscript. All authors finally approved the submission.

FUNDING

This work was financially supported by the National Research Foundation (NRF) of South Africa.

ACKNOWLEDGMENTS

Professor Viness Pillay, who passed away on July 24, 2020, is hereby kindly acknowledged and remembered for his contributions to the conceptualization of this work.

REFERENCES

Abueva, C., Ryu, H. S., Min, J. W., Chung, P. S., Sook, Y. H., Suk, Y. M., et al. (2021). Quaternary Ammonium N, N, N-Trimethyl Chitosan Derivative and Povidone-Iodine Complex as a Potent Antiseptic with Enhanced Wound Healing Property. *Int. J. Biol. Macromol* 182, 1713. doi:10.1016/j.ijbiomac.2021.05.153

Aderibigbe, B. A., and Buyana, B. (2018). Alginate in Wound Dressings. *Pharmaceutics* 10 (2), 42. doi:10.3390/pharmaceutics10020042

Almeida, J. F., Ferreira, P., Lopes, A., and Gil, M. H. (2011). Photocrosslinkable Biodegradable Responsive Hydrogels as Drug Delivery Systems. *Int. J. Biol. macromolecules* 49 (5), 948–954. doi:10.1016/j.ijbiomac.2011.08.010

Ansari, S., Pouraghaei Sevari, S., Chen, C., Sarrion, P., and Moshaverinia, A. (2021). RGD-modified Alginate–GelMA Hydrogel Sheet Containing Gingival Mesenchymal Stem Cells: A Unique Platform for Wound Healing and Soft Tissue Regeneration. *ACS Biomater. Sci. Eng.* doi:10.1021/acsbiomaterials.0c01571

A. Vishwakarma, P. Sharpe, S. Shi, and M. Ramalingam (Editors) (2014). *Stem Cell Biology and Tissue Engineering in Dental Sciences* (Cambridge: Academic Press).

Baranoski, S., and Ayello, E. A. (2008). *Wound Care Essentials: Practice Principles*. Philadelphia: Lippincott Williams & Wilkins.

Becker, A., Klapczynski, A., Kuch, N., Arpino, F., Simon-Keller, K., De la Torre, C., et al. (2016). Gene Expression Profiling Reveals Aryl Hydrocarbon Receptor as a Possible Target for Photobiomodulation when Using Blue Light. *Sci. Rep.* 6 (1), 1–11. doi:10.1038/srep33847

Boateng, J. S., Matthews, K. H., Stevens, H. N. E., and Eccleston, G. M. (2008). Wound Healing Dressings and Drug Delivery Systems: a Review. *J. Pharm. Sci.* 97 (8), 2892–2923. doi:10.1002/jps.21210

Botsis, T., and Hartvigsen, G. (2008). Current Status and Future Perspectives in Telecare for Elderly People Suffering from Chronic Diseases. *J. Telemed. Telecare* 14 (4), 195–203. doi:10.1258/jtt.2008.070905

Bradford, C., Freeman, R., and Percival, S. L. (2009). *In Vitro* study of Sustained Antimicrobial Activity of a New Silver Alginate Dressing. *The J. Am. Coll. Certified Wound Specialists* 1 (4), 117–120. doi:10.1016/j.jcws.2009.09.001

Chai, Q., Jiao, Y., and Yu, X. (2017). Hydrogels for Biomedical Applications: Their Characteristics and the Mechanisms behind Them. *Gels* 3 (1), 6. doi:10.3390/gels3010006

Chansiripornchai, P., Pramatwinai, C., Rungsipipat, A., Ponsamart, S., and Nakchat, O. (2003). "February. The Efficiency of Polysaccharide Gel Extracted from Fruit-Hulls of Durian (Durio Zibethinus L.) for Wound Healing in Pigskin," in III WOCMAP Congress on Medicinal and Aromatic Plants, Chiang Mai, February 1, 2005, 37–43.

Cheung, K., and Das, D. B. (2016). Microneedles for Drug Delivery: Trends and Progress. *Drug Deliv.* 23 (7), 2338–2354. doi:10.3109/10717544.2014.986309

Chi, J., Zhang, X., Chen, C., Shao, C., Zhao, Y., and Wang, Y. (2020). Antibacterial and Angiogenic Chitosan Microneedle Array Patch for Promoting Wound Healing. *Bioactive Mater.* 5 (2), 253–259. doi:10.1016/j.bioactmat.2020.02.004

Chivere, V. T., Kondiah, P. P. D., Choonara, Y. E., and Pillay, V. (2020). Nanotechnology-based Biopolymeric Oral Delivery Platforms for Advanced Cancer Treatment. *Cancers* 12 (2), 522. doi:10.3390/cancers12020522

Coger, V., Million, N., Rehbock, C., Sures, B., Nachev, M., Barcikowski, S., et al. (2019). Tissue Concentrations of Zinc, Iron, Copper, and Magnesium during the Phases of Full Thickness Wound Healing in a Rodent Model. *Biol. Trace Elem. Res.* 191 (1), 167–176. doi:10.1007/s12011-018-1600-y

Cullum, N., Buckley, H., Dumville, J., Hall, J., Lamb, K., Madden, M., et al. (2016). "Data Extraction Tables: Silver Dressings for Venous Leg Ulcers," in *Wounds Research for Patient Benefit: A 5-year Program of Research* (Southampton United Kingdom: The National Institute for Health Research (NIHR)).

Dai, T., Gupta, A., Murray, C. K., Vrahas, M. S., Tegos, G. P., and Hamblin, M. R. (2012). Blue Light for Infectious Diseases: Propionibacterium Acnes, *Helicobacter pylori*, and beyond?. *Drug Resist. Updates* 15 (4), 223–236. doi:10.1016/j.drup.2012.07.001

De la Harpe, K. M., Kondiah, P. P., Marimuthu, T., Du Toit, L. C., Kumar, P., Choonara, Y. E., et al. (2020). An Advanced 3D Monofilament Biosuture. *South Afr. Pharm. J.* 87 (1), 45–48.

Deng, Z., Wang, H., Ma, P. X., and Guo, B. (2020). Self-healing Conductive Hydrogels: Preparation, Properties and Applications. *Nanoscale* 12 (3), 1224–1246. doi:10.1039/c9nr09283h

Ding, X., Duan, S., Ding, X., Liu, R., and Xu, F.-J. (2018). Versatile Antibacterial Materials: an Emerging Arsenal for Combatting Bacterial Pathogens. *Adv. Funct. Mater.* 28 (40), 1802140. doi:10.1002/adfm.201802140

Essa, D., Choonara, Y. E., Kondiah, P. P. D., and Pillay, V. (2020). Comparative Nanofabrication of PLGA-Chitosan-PEG Systems Employing Microfluidics and Emulsification Solvent Evaporation Techniques. *Polymers* 12 (9), 1882. doi:10.3390/polym12091882

Frykberg, R. G., and Banks, J. (2015). Challenges in the Treatment of Chronic Wounds. *Adv. Wound Care* 4 (9), 560–582. doi:10.1089/wound.2015.0635

Greenwood, J. E., and Dearman, B. L. (2012). Split Skin Graft Application over an Integrating, Biodegradable Temporizing Polymer Matrix. *J. Burn Care Res.* 33 (1), 7–19. doi:10.1097/bcr.0b013e3182372be9

Gupta, A., Kowalczuk, M., Heaselgrave, W., Britland, S. T., Martin, C., and Radecka, I. (2019). The Production and Application of Hydrogels for Wound Management: A Review. *Eur. Polym. J.* 111, 134–151. doi:10.1016/j.eurpolymj.2018.12.019

Harding, K. G., Jones, V., and Price, P. (2000). Topical Treatment: Which Dressing to Choose. *Diabetes Metab. Res. Rev.* 16 (S1), S47–S50. doi:10.1002/1520-7560(200009/10)16:1+<::aid-dmrr133>3.0.co;2-q

Heo, Y., Akimoto, J., Kobatake, E., and Ito, Y. (2020). Gelation and Release Behavior of Visible Light-Curable Alginate. *Polym. J.* 52 (3), 323–332. doi:10.1038/s41428-019-0280-6

Huang, S., and Fu, X. (2010). Naturally Derived Materials-Based Cell and Drug Delivery Systems in Skin Regeneration. *J. Controlled Release* 142 (2), 149–159. doi:10.1016/j.jconrel.2009.10.018

Jia, Z., shen, D., and Xu, W. (2001). Synthesis and Antibacterial Activities of Quaternary Ammonium Salt of Chitosan. *Carbohydr. Res.* 333 (1), 1–6. doi:10.1016/s0008-6215(01)00112-4

Jin, Y., Ling, P.-X., He, Y.-L., and Zhang, T.-M. (2007). Effects of Chitosan and Heparin on Early Extension of burns. *Burns* 33 (8), 1027–1031. doi:10.1016/j.burns.2006.12.002

Kamoun, E. A., Kenawy, E.-R. S., and Chen, X. (2017). A Review on Polymeric Hydrogel Membranes for Wound Dressing Applications: PVA-Based Hydrogel Dressings. *J. Adv. Res.* 8 (3), 217–233. doi:10.1016/j.jare.2017.01.005

Kamoun, E. A., and Menzel, H. (2012). HES-HEMA Nanocomposite Polymer Hydrogels: Swelling Behavior and Characterization. *J. Polym. Res.* 19 (4), 9851. doi:10.1007/s10965-012-9851-3

Kampf, N., Wachtel, E. J., Zilman, A., Ben-Shalom, N., and Klein, J. (2018). Anomalous Viscosity-Time Behavior of Polysaccharide Dispersions. *J. Chem. Phys.* 149 (16), 163320. doi:10.1063/1.5027720

Kasagana, V., and Karumuri, S. S. (2011). Recent Advances in Smart Drug Delivery Systems. *Int. J. Novel Drug Deliv.* 1 (3), 201–207.

Krajewska, B. (2004). Application of Chitin-And Chitosan-Based Materials for Enzyme Immobilizations: a Review. *Enzyme Microb. Technol.* 35 (2-3), 126–139. doi:10.1016/j.enzmictec.2003.12.013

Kratz, G., Arnander, C., Swedenborg, J., Back, M., Falk, C., Gouda, I., et al. (1997). Heparin-chitosan Complexes Stimulate Wound Healing in Human Skin. *Scand. J. Plast. Reconstr. Surg. Hand Surg.* 31 (2), 119–123. doi:10.3109/02844319709085478

Krause, A., Kirschning, A., and Dräger, G. (2012). Bioorthogonal Metal-free Click-Ligation of cRGD-Pentapeptide to Alginate. *Org. Biomol. Chem.* 10 (29), 5547–5553. doi:10.1039/c2ob25604e

Kuivaniemi, H., and Tromp, G. (2019). Type III Collagen (COL3A1): Gene and Protein Structure, Tissue Distribution, and Associated Diseases. *Gene* 707, 151. doi:10.1016/j.gene.2019.05.003

Lee, K. Y., and Mooney, D. J. (2012). Alginate: Properties and Biomedical Applications. *Prog. Polym. Sci.* 37 (1), 106–126. doi:10.1016/j.progpolymsci.2011.06.003

Lee, K. Y., and Mooney, D. J. (2012). Alginate: Properties and Biomedical Applications. *Prog. Polym. Sci.* 37 (1), 106–126. doi:10.1016/j.progpolymsci.2011.06.003

Li, M., Li, H., Li, X., Zhu, H., Xu, Z., Liu, L., et al. (2017). A Bioinspired Alginate-Gum Arabic Hydrogel with Micro-/nanoscale Structures for Controlled Drug Release in Chronic Wound Healing. *ACS Appl. Mater. Inter.* 9 (27), 22160–22175. doi:10.1021/acsami.7b04428

Liang, M., Chen, Z., Wang, F., Liu, L., Wei, R., and Zhang, M. (2019). Preparation of Self-regulating/anti-adhesive Hydrogels and Their Ability to Promote Healing in Burn Wounds. *J. Biomed. Mater. Res.* 107 (5), 1471–1482. doi:10.1002/jbm.b.34239

Line, A. S., Morykwas, M. J., and Line, S. W. (1995). Use of Cultured Human Epidermal Xenografts for Wound Treatment in Nonhuman Primates. *J. Zoo Wildl. Med.*, 517–524.

Lynch, C. R., Kondiah, P. P. D., Choonara, Y. E., Du Toit, L. C., Ally, N., and Pillay, V. (2020). Hydrogel Biomaterials for Application in Ocular Drug Delivery. *Front. Bioeng. Biotechnol.* 8, 228. doi:10.3389/fbioe.2020.00228

Mamalis, A., Garcha, M., and Jagdeo, J. (2015). Light Emitting Diode-Generated Blue Light Modulates Fibrosis Characteristics: Fibroblast Proliferation, Migration Speed, and Reactive Oxygen Species Generation. *Lasers Surg. Med.* 47 (2), 210–215. doi:10.1002/lsm.22293

Mansoor, S., Kondiah, P. P. D., Choonara, Y. E., and Pillay, V. (2019). Polymer-based Nanoparticle Strategies for Insulin Delivery. *Polymers* 11 (9), 1380. doi:10.3390/polym11091380

Mi, F.-L., Wu, Y.-B., Shyu, S.-S., Schoung, J.-Y., Huang, Y.-B., Tsai, Y.-H., et al. (2002). Control of Wound Infections Using a Bilayer Chitosan Wound Dressing with Sustainable Antibiotic Delivery. *J. Biomed. Mater. Res.* 59 (3), 438–449. doi:10.1002/jbm.1260

Mirani, B., Pagan, E., Currie, B., Siddiqui, M. A., Hosseinzadeh, R., Mostafalu, P., et al. (2017). An Advanced Multifunctional Hydrogel-Based Dressing for Wound Monitoring and Drug Delivery. *Adv. Healthc. Mater.* 6 (19), 1700718. doi:10.1002/adhm.201700718

Mndlovu, H., du Toit, L. C., Kumar, P., Marimuthu, T., Kondiah, P. P. D., Choonara, Y. E., et al. (2019). Development of a Fluid-Absorptive Alginate-

Chitosan Bioplatform for Potential Application as a Wound Dressing. *Carbohydr. Polym.* 222, 114988. doi:10.1016/j.carbpol.2019.114988

Mondal, S., Das, S., and Nandi, A. K. (2020). A Review on Recent Advances in Polymer and Peptide Hydrogels. *Soft Matter* 16 (6), 1404–1454. doi:10.1039/c9sm02127b

Morgan, D. (2002). Wounds—what Should a Dressing Formulary Include. *Hosp. Pharmacist* 9, 261–266.

Mostafalu, P., Amugothu, S., Tamayol, A., Bagherifard, S., Akbari, M., Dokmeci, M. R., Khademhosseini, A., and Sonkusale, S. (2015). "October. Smart Flexible Wound Dressing with Wireless Drug Delivery," in 2015 IEEE biomedical circuits and systems conference (BioCAS) (Piscataway: IEEE), 1–4.

Moura, L. I. F., Dias, A. M. A., Carvalho, E., and de Sousa, H. C. (2013). Recent Advances on the Development of Wound Dressings for Diabetic Foot Ulcer Treatment-A Review. *Acta Biomater.* 9 (7), 7093–7114. doi:10.1016/j.actbio.2013.03.033

Nam, S. Y., Nho, Y. C., Hong, S. H., Chae, G. T., Jang, H. S., Suh, T. S., et al. (2004). Evaluations of Poly(vinyl Alcohol)/alginate Hydrogels Cross-Linked by γ-ray Irradiation Technique. *Macromol. Res.* 12 (2), 219–224. doi:10.1007/bf03218391

Noh, H. K., Lee, S. W., Kim, J.-M., Oh, J.-E., Kim, K.-H., Chung, C.-P., et al. (2006). Electrospinning of Chitin Nanofibers: Degradation Behavior and Cellular Response to normal Human Keratinocytes and Fibroblasts. *Biomaterials* 27 (21), 3934–3944. doi:10.1016/j.biomaterials.2006.03.016

Parenteau, N., Sabolinski, M., Prosky, S., Nolte, C., Oleson, M., Kriwet, K., et al. (1996). Biological and Physical Factors Influencing the Successful Engraftment of a Cultured Human Skin Substitute. *Biotechnol. Bioeng.* 52 (1), 3–14. doi:10.1002/(sici)1097-0290(19961005)52:1<3::aid-bit1>3.0.co;2-p

Popescu, I., Turtoi, M., Suflet, D. M., Dinu, M. V., Darie-Nita, R. N., Anghelache, M., et al. (2021). Alginate/poloxamer Hydrogel Obtained by Thiol-Acrylate Photopolymerization for the Alleviation of the Inflammatory Response of Human Keratinocytes. *Int. J. Biol. Macromolecules* 180, 418–431. doi:10.1016/j.ijbiomac.2021.03.082

Price, R. D., Berry, M. G., and Navsaria, H. A. (2007). Hyaluronic Acid: the Scientific and Clinical Evidence. *J. Plast. Reconstr. Aesthet. Surg.* 60 (10), 1110–1119. doi:10.1016/j.bjps.2007.03.005

Qing, X., He, G., Liu, Z., Yin, Y., Cai, W., Fan, L., et al. (2021). Preparation and Properties of Polyvinyl alcohol/N-Succinyl Chitosan/lincomycin Composite Antibacterial Hydrogels for Wound Dressing. *Carbohydr. Polym.* 261, 117875. doi:10.1016/j.carbpol.2021.117875

Qu, J., Zhao, X., Liang, Y., Zhang, T., Ma, P. X., and Guo, B. (2018). Antibacterial Adhesive Injectable Hydrogels with Rapid Self-Healing, Extensibility and Compressibility as Wound Dressing for Joints Skin Wound Healing. *Biomaterials* 183, 185–199. doi:10.1016/j.biomaterials.2018.08.044

Saarai, A., Sedlacek, T., Kasparkova, V., Kitano, T., and Saha, P. (2012). On the Characterization of Sodium Alginate/gelatine-Based Hydrogels for Wound Dressing. *J. Appl. Polym. Sci.* 126 (S1), E79–E88. doi:10.1002/app.36590

Silva, R., Singh, R., Sarker, B., Papageorgiou, D. G., Juhasz-Bortuzzo, J. A., Roether, J. A., et al. (2018). Hydrogel Matrices Based on Elastin and Alginate for Tissue Engineering Applications. *Int. J. Biol. macromolecules* 114, 614–625. doi:10.1016/j.ijbiomac.2018.03.091

Simões, D., Miguel, S. P., and Correia, I. J. (2018). Biofunctionalization of Electrospun Poly(caprolactone) Fibers with Maillard Reaction Products for Wound Dressing Applications. *Reactive Funct. Polym.* 131, 191–202. doi:10.1016/j.reactfunctpolym.2018.07.021

Sood, A., Granick, M. S., and Tomaselli, N. L. (2014). Wound Dressings and Comparative Effectiveness Data. *Adv. Wound Care* 3 (8), 511–529. doi:10.1089/wound.2012.0401

Stern, D., and Cui, H. (2019). Crafting Polymeric and Peptidic Hydrogels for Improved Wound Healing. *Adv. Healthc. Mater.* 8 (9), 1900104. doi:10.1002/adhm.201900104

Stewart, J. (2002). *Next-generation Products for Wound Management. Surgical Materials Testing Laboratory*. Wales, UK: Worldwide wounds.

Sudarsan, S., Franklin, D. S., and Guhanathan, S. (2015). Imbibed Salts and pH-Responsive Behaviors of Sodium-Alginate-Based Eco-Friendly Biopolymeric Hydrogels-A Solventless Approach. *MMAIJ* 11, 24–29.

Suzuki, Y., Nishimura, Y., Tanihara, M., Suzuki, K., Nakamura, T., Shimizu, Y., et al. (1998). Evaluation of a Novel Alginate Gel Dressing: Cytotoxicity to Fibroblastsin Vitro and Foreign-Body Reaction in Pig Skinin Vivo. *J. Biomed. Mater. Res.* 39 (2), 317–322. doi:10.1002/(sici)1097-4636(199802)39:2<317::aid-jbm20>3.0.co;2-8

Sweeney, I. R., Miraftab, M., and Collyer, G. (2012). A Critical Review of Modern and Emerging Absorbent Dressings Used to Treat Exuding Wounds. *Int. Wound J.* 9 (6), 601–612. doi:10.1111/j.1742-481x.2011.00923.x

Thomas, S. (1990). *Functions of a Wound Dressing. Wound Management and Dressings*, 9–19.

Turner, J. G., White, L. R., Estrela, P., and Leese, H. S. (2020). Hydrogel-Forming Microneedles: Current Advancements and Future Trends. *Macromol. Biosci.* 21, 2000307. doi:10.1002/mabi.202000307

Wild, D., Eremenco, S., Mear, I., Martin, M., Houchin, C., Gawlicki, M., et al. (2009). Multinational Trials-Recommendations on the Translations Required, Approaches to Using the Same Language in Different Countries, and the Approaches to Support Pooling the Data: The ISPOR Patient-Reported Outcomes Translation and Linguistic Validation Good Research Practices Task Force Report. *Value in health* 12 (4), 430–440. doi:10.1111/j.1524-4733.2008.00471.x

Winter, G. D. (1962). Formation of the Scab and the Rate of Epithelization of Superficial Wounds in the Skin of the Young Domestic Pig. *Nature* 193 (4812), 293–294. doi:10.1038/193293a0

Winter, G. D. (1962). Formation of the Scab and the Rate of Epithelization of Superficial Wounds in the Skin of the Young Domestic Pig. *Nature* 193 (4812), 293–294. doi:10.1038/193293a0

Xu, G., Cheng, L., Zhang, Q., Sun, Y., Chen, C., Xu, H., et al. (2016). *In Situ* thiolated Alginate Hydrogel: Instant Formation and its Application in Hemostasis. *J. Biomater. Appl.* 31 (5), 721–729. doi:10.1177/0885328216661557

Yadav, P., Yadav, H., Shah, V. G., Shah, G., and Dhaka, G. (2015). Biomedical Biopolymers, Their Origin and Evolution in Biomedical Sciences: A Systematic Review. *J. Clin. Diagn. Res.* 9 (9), ZE21–5. doi:10.7860/JCDR/2015/13907.6565

Yang, X., Liu, W., Li, N., Wang, M., Liang, B., Ullah, I., et al. (2017). Design and Development of Polysaccharide Hemostatic Materials and Their Hemostatic Mechanism. *Biomater. Sci.* 5 (12), 2357–2368. doi:10.1039/c7bm00554g

Yu, H. C., Zhang, H., Ren, K., Ying, Z., Zhu, F., Qian, J., et al. (2018). Ultrathin κ-Carrageenan/Chitosan Hydrogel Films with High Toughness and Antiadhesion Property. *ACS Appl. Mater. Inter.* 10 (10), 9002–9009. doi:10.1021/acsami.7b18343

Yu, J., Du, K. T., Fang, Q., Gu, Y., Mihardja, S. S., Sievers, R. E., et al. (2010). The Use of Human Mesenchymal Stem Cells Encapsulated in RGD Modified Alginate Microspheres in the Repair of Myocardial Infarction in the Rat. *Biomaterials* 31 (27), 7012–7020. doi:10.1016/j.biomaterials.2010.05.078

Zhai, M., Yoshii, F., Kume, T., and Hashim, K. (2002). Syntheses of PVA/starch Grafted Hydrogels by Irradiation. *Carbohydr. Polym.* 50 (3), 295–303. doi:10.1016/s0144-8617(02)00031-0

Zhu, T., Mao, J., Cheng, Y., Liu, H., Lv, L., Ge, M., et al. (2019). Recent Progress of Polysaccharide-Based Hydrogel Interfaces for Wound Healing and Tissue Engineering. *Adv. Mater. Inter.* 6 (17), 1900761. doi:10.1002/admi.201900761

Conflict of Interest: The authors declare that the research was conducted in the absence of any commercial or financial relationships that could be construed as a potential conflict of interest.

Publisher's Note: All claims expressed in this article are solely those of the authors and do not necessarily represent those of their affiliated organizations, or those of the publisher, the editors and the reviewers. Any product that may be evaluated in this article, or claim that may be made by its manufacturer, is not guaranteed or endorsed by the publisher.

frontiers | Frontiers in Materials

ORIGINAL RESEARCH
published: 08 April 2022
doi: 10.3389/fmats.2022.844469

Modeling, Simulation and Testing of Atomization Temperature Change Point of Thermochromic Glass for Building Energy Saving

Zeng Kai[1], Liang YuDai[1], Zhang BaoRong[2], Shi Quan[1], Wu JinBo[1] and Wen WeiJia[1,3]**

[1]Materials Genome Institute, Shanghai University, Shanghai, China, [2]China Automotive Engineering Research Institute Co., Ltd, Chongqing, China, [3]Department of Physics, Hong Kong University of Science and Technology, Hong Kong, Hong Kong SAR, China

Thermochromic glass possesses great potential for reducing the energy demand and providing indoor comfort in buildings. Suitable atomization temperature change points have a great influence on the application of thermochromic glass. Based on energy consumption simulations and theoretical calculations by introducing solar radiation in a transparent envelope, this paper investigates the atomization temperature change point of thermochromic glass in hot summer and cold winter zones in Chongqing, showing that the suitable temperature change point of the thermochromic glass is 39°C with air conditioning and 42.9°C without air conditioning. Furthermore, the results of simulations and theoretical calculations are applied to a test model, revealing that thermochromic glass with the temperature change point of 42.9°C compared with Low-E glass can reduce the temperature of a sunlight room by up to 5°C in the summer and displays a certain thermal insulation effect in winter.

Keywords: energy consumption simulation, thermochromic glass, temperature change point, smart window, low-e glass

OPEN ACCESS

Edited by:
Weihua Li,
University of Wollongong, Australia

Reviewed by:
Tongfei Tian,
University of the Sunshine Coast, Australia
Shuaishuai Sun,
University of Science and Technology of China, China

****Correspondence:***
Shi Quan
quanshi@t.shu.edu.cn
Wen WeiJia
phwen@ust.hk

Specialty section:
This article was submitted to Smart Materials, a section of the journal Frontiers in Materials

Received: *28 December 2021*
Accepted: *21 February 2022*
Published: *08 April 2022*

Citation:
Kai Z, YuDai L, BaoRong Z, Quan S, JinBo W and WeiJia W (2022) Modeling, Simulation and Testing of Atomization Temperature Change Point of Thermochromic Glass for Building Energy Saving. Front. Mater. 9:844469. doi: 10.3389/fmats.2022.844469

INTRODUCTION

Urban building energy consumption is the total energy consumption of buildings in the city, including Heating, Ventilation, and Air Conditioning energy consumption (Sadineni et al., 2011; Nguyen et al., 2014) lighting energy consumption, the electrical energy consumption of sockets, etc., which can account for the total energy consumption 30–40% of the whole society (Li et al., 2011; Nguyen et al., 2014; Zhu et al., 2020) (that is, the sum of all energy consumption of industry, agriculture, and residents, etc.). The energy performance of a building depends on the building envelopes, especially windows, which frequently let in or let out energy and are responsible for 20–40% of wasted energy in a building (Hee et al., 2015; Konis et al., 2016). The energy saving potentials of windows are important determinants in building energy saving, and window glazing selection is one of the crucial issues in designing windows. Low-emissivity (Low-E) glass has been widely used in new buildings in western developed countries and regions and has been promoted in China. Low-E coatings are spectrum selective films designed to allow visible light to pass through and block infrared and ultraviolet wavelengths that normally generate heat. Due to its high infrared reflectance, this kind of glass has been greatly developed. Over the past 2 decades, great progress has been made to explore their different attributes (Cai et al., 2013). There are two kinds of typical low radiation coatings (Ruffolo and

FIGURE 1 | Atomization process of thermochromic glass at change temperature 35°C.

La Russa, 2019): tin oxide based hard coatings and silver based soft coatings, which have high infrared reflectance and low transmittance. However, the visible light transmittance of the hard coating can be improved by using the antireflection properties of silica.

Existing Low-E glass still has some limitations (Pierucci et al., 2018; Abundiz-Cisneros et al., 2020), including that its optical properties cannot be changed with people's wishes or environmental conditions, and that it is difficult to achieve the best energy-saving effect in hot summer and cold winter areas. The comfort and energy-saving effects also have certain limitations. People hope to develop a kind of glass with intelligent adjustment ability (Cai et al., 2018), which can automatically adjust the optical properties according to the environmental temperature, sunlight intensity, and other conditions: when the indoor temperature is low, it could let the sunlight enter the room to heighten the indoor temperature; when the room temperature is high, it can block all or part of the sunlight and play a heat-resistant role (Gao et al., 2012). The glass with this adjustment ability is called "intelligent or smart glass". Smart windows were first proposed by Lambert of the United States. It has the advantages of energy saving, heat insulation, heat preservation, and decoration (Jin et al., 2019; Zhang et al., 2019). It has important application values in automobiles, building doors and windows, display equipment, and other fields. Specifically, smart window is an intelligent device composed of transparent substrate (such as glass and a dimming material layer) (Javad and Navid, 2019). Under certain conditions (Calas et al., 2006) (such as temperature, electric field, gas, and light), the dimming material will undergo chemical or physical changes, change the transmission and reflection characteristics of sunlight in a specific band (Charaya et al., 2019; Kim and Yang, 2020), then adjust the intensity of light entering the room, reduce the energy consumption of cooling and heating, and achieve the purpose of energy saving. This kind of intelligent glass overcomes the shortcoming that traditional solar control glass and Low-E glass cannot adjust dynamically according to need. It is a more promising energy-saving window material (Allen et al., 2017).

Thermochromic glass (Wang and Narayan, 2021; Mlyuka et al., 2009) is a curtain wall shading integrated glass formed by the tight combination of nanogel thermochromic film, VO_2-based coating film, and tempered glass (Gong et al., 2009; Yang et al., 2020; Muramoto et al., 2020). The nanogel thermochromic film is a three-dimensional network polymer, which is colorless, odorless, and non-toxic (Zhou et al., 2016). When the ambient temperature is higher than the temperature change point, the thermochromic film changes to dimming and plays the role of shading and heat insulation. When the temperature is lower, transparency is restored (**Figure 1**), thereby achieving penetration of natural light and solar radiations. According to the characteristics of thermochromic glass, the temperature change point can be set between 16 and 50°C (**Supplementary Figure S1**, **Supplementary Figure S2**). If the temperature change point is set too high, there may be a situation where the glass cannot be atomized under any working conditions, then the thermochromic glass completely loses its characteristics of reducing the solar heat gain of the building and cannot reduce the cooling load from air conditioning. If the temperature change point is set too low, there may be frequent dimming of the glass, when the outdoor temperature is low, meaning the glass will be fogged by the Sun, which is not conducive to introducing more sunlight into the room in winter. Based on this, choosing an appropriate temperature change point has great influence on the application of thermochromic glass. The temperature change point of glass fogging needs to be determined according to the application environment (Cannavale et al., 2010).

Based on an energy consumption simulation and theoretical calculations, this paper aimed to obtain the most suitable temperature change point of this kind of thermotropic glass and combines the theoretical calculation results with results from a test house in Chongqing. The test results are in good agreement with the theoretical calculations. This result is of great significance for the wide application of thermotropic glass.

METHODOLOGY

We used Ladybug (Kharvari, 2020) and energy plus (Iqbal et al., 2018; Kim et al., 2019) to build the model. Solar radiation is an important factor affecting the indoor thermal environment and

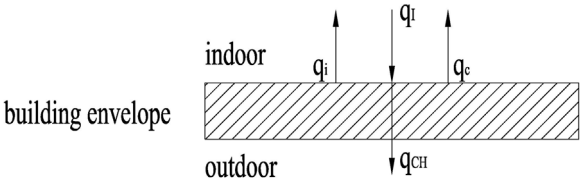

FIGURE 2 | Heat balance relationship of the building envelope.

energy consumption (Hasan et al., 2008; Negendahl and Nielsen, 2015). At the same time, the absorption of solar radiation by the building envelope will also increase the exterior surface temperature of the building envelope (Li et al., 2022). The external surface temperature of the glass is expressed by the temperature value, which indicates the thermal effect of outdoor air temperature, solar radiation, and atmospheric long wave radiation on the outer surface of the glass (Wu et al., 2019).

According to the heat balance relation of the building surface (**Figure 2**), we can deduce the calculation formula of the temperature of the glass outer surface. The expression is expressed as follows:

$$q_I = q_{ch} + q_i + q_c \tag{1}$$

where q_I is the heat flux intensity of glass absorbing solar radiation; q_{ch} is the heat flux intensity of glass to interior heat transfer; q_i is the radiation heat flux intensity of the outer surface; q_c is the intensity of convective heat transfer on the outer surface. Further q_I, q_{ch}, q_i, q_c can be expressed as:

$$q_I = \rho I \tag{2}$$

$$q_{ch} = k(T_o - T_i) \tag{3}$$

$$q_i = \alpha_d\left(T_o - T_{sky}\right) \tag{4}$$

$$q_c = \alpha_c(T_o - T_\varepsilon) \tag{5}$$

where I is the solar radiation intensity, k is the heat transfer coefficient of glass, T_o is the temperature of the outer surface of the glass, T_i is the indoor temperature, α_d is the radiation heat transfer coefficient T_{sky} is the sky temperature, α_c is the convection heat transfer coefficient, T_ε is the outdoor temperature. According to the above formula, we can sort the expression of the outer surface temperature of the glass as:

$$T_o = \frac{\alpha_\varepsilon}{k + \alpha_\varepsilon}T_\varepsilon + AI - \frac{k}{k + \alpha_\varepsilon}T_i + K \tag{6}$$

Among the equation, K is a constant, A is the solar radiation absorption rate of glass, which is a constant. Since in the calculation, the commonly taken value is 23 W/m^2K, and the heat transfer coefficient k of the glass is generally 1.5 W/m^2K, therefore, the above formula can be further simplified as:

$$T_o = T_\varepsilon + AI + K \tag{7}$$

From this simple expression, we can see that there is a simple linear relationship between the glass outdoor surface temperature, the outdoor air temperature, and the amount of solar radiation.

According to the characteristics of the thermochromic glass, the temperature change point can be approximately regarded as the outer surface temperature of the glass, which is determined by the outdoor temperature and solar radiation intensity. To fully realize the energy-saving effect of the product, two conditions should be met at the same time: higher outdoor temperature and larger solar radiation. Because when the outdoor temperature is high, but the solar radiation is very low, the energy saving effect of glass atomization is not obvious, and reduces the permeability; when the outdoor temperature is low and the solar radiation is large, it is most likely to be in winter, and the glass should not be atomized at this time. Transform the formula appropriately:

$$T_o - T_\varepsilon = AI + K \tag{8}$$

When the difference between the temperature of the glass outer surface and the temperature of the outdoor air is larger, the energy-saving effect brought by the glass atomization is better, and it can block more solar radiation (McCormick and Suehrcke, 2018) from entering the room. Therefore, we can conclude that the appropriate temperature change point should meet the high outdoor temperature, sufficient solar radiation, and large temperature difference between the outer surface of the glass and the air temperature (Xu et al., 2012).

The thermotropic glass used in this article was fabricated by Chongqing Hewei Technology Co., Ltd. The thermochromic properties of thermotropic glass were monitored on a Lambda 1,050 spectrophotometer equipped with a heating unit in the wavelength range of 300–2,500 nm. The temperature of the sunlit room was measured by an online temperature tester.

RESULTS AND DISCUSSION

Building Performance Evaluation and Simulation Analysis

As mentioned above, when the temperature difference between the outside surface of the thermochromic glass and outdoor temperature is larger, the glass is atomized at this time, which can effectively reduce the increase in heat caused by solar radiation, and the effect of atomization is better. When the outer surface temperature of the glass is lower than that of outdoor temperature, the temperature rise caused by solar radiation is smaller. Currently, the effect of glass atomization is poor and even has an adverse effect in winter. Therefore, we calculated the outside surface and outdoor temperature of the glass in distinctive climatic regions of the city with typical climatic characteristics of hot summer and cold winter, and determine the temperature change points suitable for different regions by searching for their internal change rules.

In this study, the energy consumption simulation software EnergyPlus was used to simulate the 8,760 h energy consumption of the standard model, and the 8,760 h glass surface temperature was obtained. At the same time, the annual climate parameters of Chongqing used in the calculation were read to know the out-of-

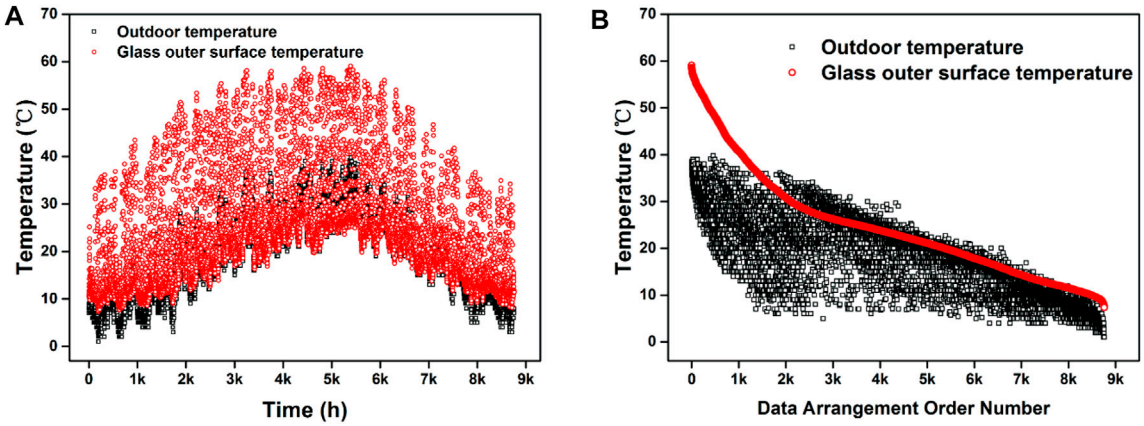

FIGURE 3 | The raw data of the outdoor air temperature and the outer surface temperature of the glass for 8,760 h **(A)** and the data sorted by the descending order of the glass surface temperature **(B)**.

doors air temperature at the corresponding time. The calculated value of 8,760 h glass surface temperature and the outdoor air temperature value of the whole year can be obtained (**Figure 3A**). According to the data of 8,760 h of glass outer surface temperature and outdoor air temperature obtained by energy consumption simulation software, it is impossible to find relevant laws to determine the temperature change point before processing the data.

After sorting the temperature of the glass outer surface from high to low, the temperature distribution shows a certain rule, as shown in **Figure 3B**. In the front part of the graph, there is a large gap between the temperature of the outer surface of the glass and the air temperature. This section meets the three conditions for selecting the temperature change point, that is, the temperature is high enough, the solar radiation is strong, and the temperature of the outer surface of the glass is higher than the air temperature. When the glass is in this time period, the atomization can exert the greatest energy saving effect. In the middle and later part of the graph, the difference between the outdoor air temperature and the outer surface temperature of the glass gradually decreases, and the change trend of the outdoor air temperature and the outer surface temperature of the glass tends to be the same. This time period is not suitable for atomization during this time period because of lower solar radiation. By performing regression processing on the temperature curve of the outer surface of the glass, an obvious boundary area between the front section and the middle and rear sections can be found. The temperature of the outer surface of the glass corresponding to this area should be the selected suitable temperature change point.

Considering that during the use of glass, the orientation of the glass and whether the indoor air conditioner is used may also affect the selection of its reasonable temperature change point, we designed two simulation conditions in an air-conditioned environment and a natural ventilation environment. Among them, the influence of glass orientation is also studied under air-conditioning environment.

In the simulation, to unify the building calculation model of each climate zone and minimize the impact of building form, we select the standard calibration building model in ASHRAE 140–2014 classic method of test for the evaluation of building energy analysis computer programs as the standard model of simulation. The model is a square box with a size of 6 m × 8 m × 2.7 m. In the air-conditioning environment, we designed four location conditions of east, west, south, and skylight. In addition, the location conditions of skylights are designed in a naturally ventilated environment. The method of setting the exterior windows in the model involved the exterior walls of the study orientation being set as exterior windows. That is, if the east exterior windows are studied, all exterior walls in the east orientation are set as exterior windows, and other orientations are set as walls, and the roof has no skylights. The principles of other orientations are the same.

According to the data processing method and temperature change point determination method mentioned above. The linear regression formula of the outer surface temperature of the skylight in **Figure 4A** is: $T_0 = -0.0039x + 39$, $R^2 = 0.9806$. As a result, the temperature change point is selected as 39°C. In the same way, we get the linear regression equations of the outer surface temperature of the skylights facing east, west, and south, which are $T_0 = -0.003x + 31.95$, $R^2 = 0.9916$, $T_0 = -0.0031x + 32.834$, $R^2 = 0.948$, and $T_0 = -0.003x + 31.466$, $R^2 = 0.948$, respectively. The temperature change points in the east, west, and south directions are selected as 31.95°C, 32.83°C, and 31.47°C, respectively.

The temperature distribution of skylight with large space outer surface and outdoor air temperature in Chongqing area is shown in **Figure 5**. The outer surface temperature of the skylight with large space is linearly regressed, and the regression formula is $T_0 = -0.0052x + 42.9$, $R^2 = 0.932$. So, the temperature change point is selected as 42.9°C.

Sunlight Room Performance Test

To further verify the practicability and reliability of our simulation results, we tested the temperature changes in the test house in a natural ventilation environment. As shown in **Figure 6**, we designed two Sun rooms with a size of 3 m × 3 m×2.7 m for testing. The Sun room-1 on the left in **Figure 6** is

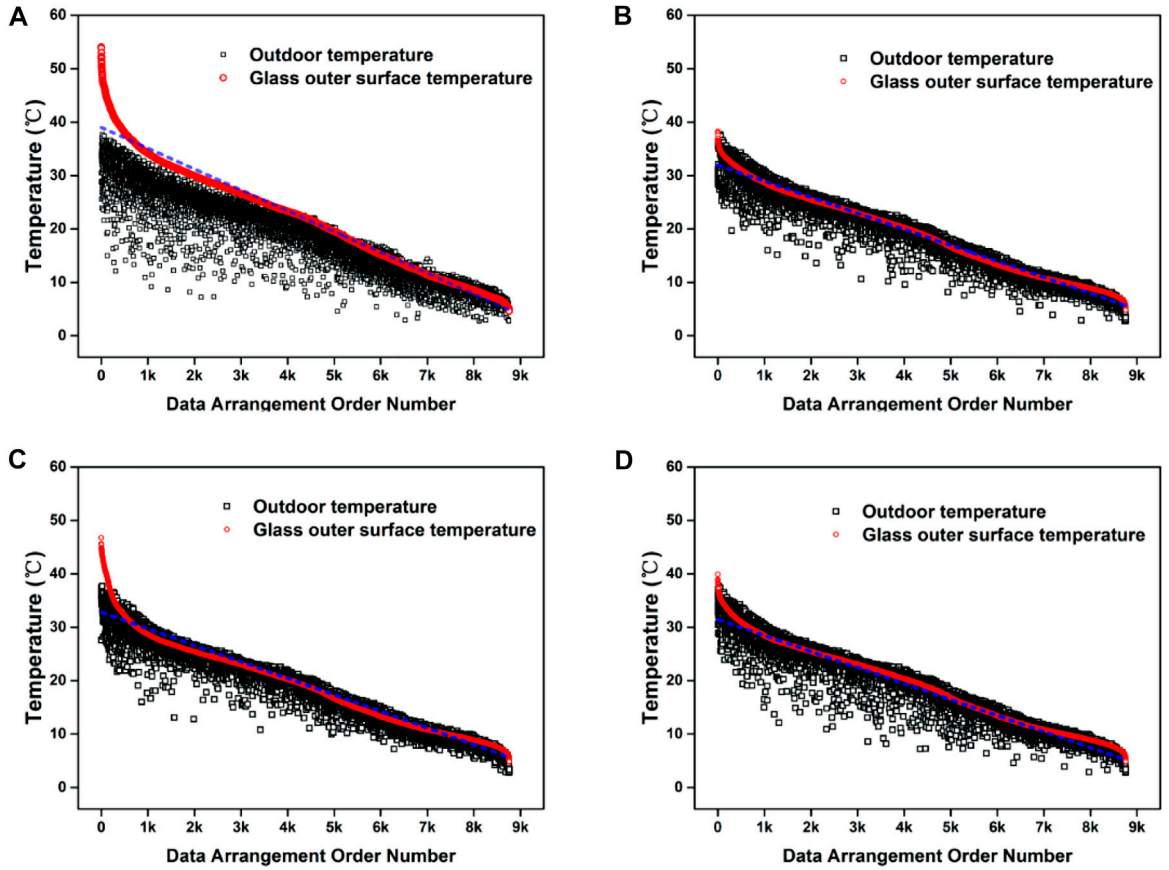

FIGURE 4 | Temperature distribution of skylight **(A)**, east **(B)**, west **(C)**, and south windows **(D)** outer surface and outdoor air temperature in Chongqing area. The blue dotted line is the linear regression curve of the outer surface temperature of the skylight.

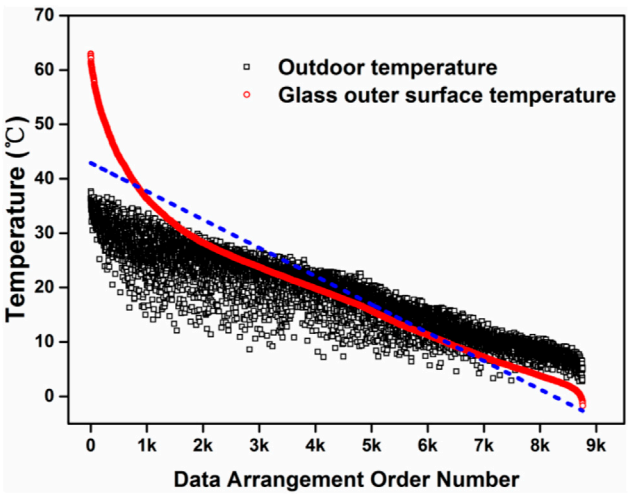

FIGURE 5 | Temperature distribution of skylight outer surface and outdoor air temperature in Chongqing area in natural ventilation condition.

installed with ordinary Low-E glass, and the thermochromic glass is installed in the Sun room-2 on the right. Based on theoretical calculation, the thermochromic glass with a temperature change point of 42.9°C is tested without air conditioning.

We collected data on temperature changes in the two rooms over 3 days of summer and winter, as shown in **Figure 7**. Due to the high intensity of solar radiation in summer, the thermochromic glass on the roof of room-2 sunlight house began to atomize from 11:00 a.m. and gradually reached the full atomization state, thereby isolating solar radiation and slowing the increase in indoor temperature. According to the data analysis and as shown in **Figure 7A**, compared with room-1, the indoor temperature of room-2 drops by up to 5.07°C. Moreover, over a 72-h period, the thermochromic glass can reduce the indoor temperature of room-2 by an average of 1.35°C, and over the period from 8 o'clock to 17 o'clock, the thermochromic glass can reduce the indoor temperature by an average of 3.06°C. In winter, as shown in **Figure 7B**, the solar radiance intensity is weak, the thermochromic glass on the roof of room-2 sunlight room does not reach

FIGURE 6 | Comparison of thermochromic glass and ordinary Low-E glass sunlight room.

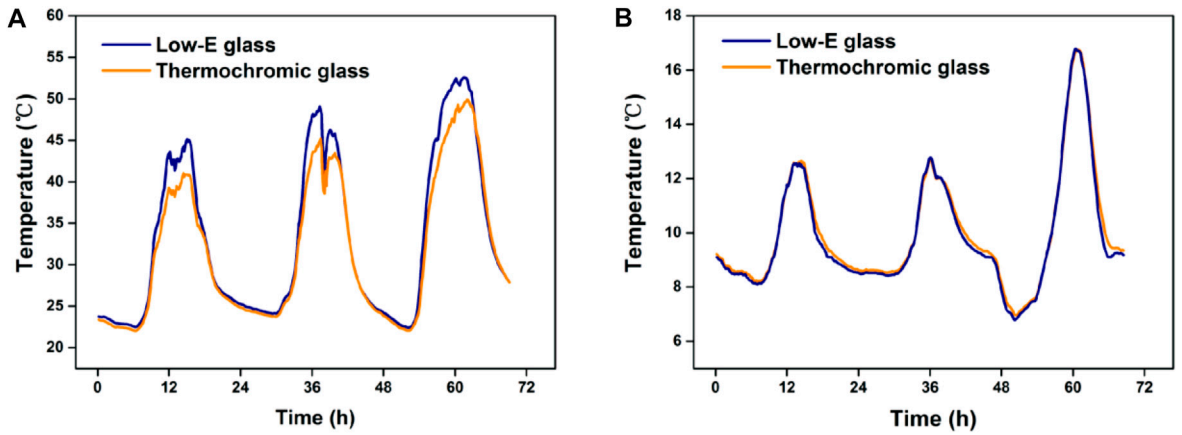

FIGURE 7 | Comparison of temperature between thermal dimming glass and Low-E glass sunlight room in summer **(A)** and winter **(B)**.

the temperature change point, and the indoor air temperature of the two sunlight rooms is the same. However, after the Sun sets, the indoor air temperature of the sunlight room with the thermochromic glass is higher than that of the ordinary glass. This test proves that the temperature change point obtained by the method in this study is suitable for various conditions in the actual use of thermochromic glass. Furthermore, it was proven that the thermochromic glass with a suitable temperature change point, especially in summer, has a significant effect of hindering solar radiation.

CONCLUSION

This paper investigates the atomization temperature change point of thermochromic glass in hot summer and cold winter zones based on energy consumption simulations and theoretical calculations. Under the climatic conditions of the summer hot and winter cold areas in Chongqing, with the premise of landscape permeability, based on the heat balance relationship of the transparent building envelope and the temperature atomization point of the thermochromic glass were simulated in the presence or absence of air conditioning. The thermal effects of outdoor air temperature, solar radiation, and atmospheric long-wave radiation on the external surface of the glass were considered in the energy simulation and theoretical calculation. Systematic investigations demonstrate that the suitable temperature change point of thermochromic glass under air-conditioned conditions is 39°C, while the value is 42.9°C under non-air-conditioned conditions. This simulation result is exactly consistent with the application environment. In comparison to Low-E glass, thermochromic glass with a temperature change point of 42.9°C can reduce the temperature

of the sunlit room by up to 5.07°C, showing a significant contribution to energy consumption.

DATA AVAILABILITY STATEMENT

The raw data supporting the conclusion of this article will be made available by the authors, without undue reservation.

AUTHOR CONTRIBUTIONS

ZK and LY have contributed equally to this work and share first authorship.

FUNDING

This work was supported in part by the Project of Hetao Shenzhen-Hong Kong Science and Technology Innovation Cooperation Zone (HZQB-KCZYB-2020083).

SUPPLEMENTARY MATERIAL

The Supplementary Material for this article can be found online at: https://www.frontiersin.org/articles/10.3389/fmats.2022.844469/full#supplementary-material

REFERENCES

Abundiz-Cisneros, N., Sanginés, R., Rodríguez-López, R., Peralta-Arriola, M., Cruz, J., and Machorro, R. (2020). Novel Low-E Filter for Architectural Glass Pane. *Energ. Buildings.* 206, 109558. doi:10.1016/j.enbuild.2019.109558

Allen, K., Connelly, K., Rutherford, P., and Wu, Y. (2017). Smart Windows-Dynamic Control of Building Energy Performance. *Energ. Buildings.* 139, 535–546. doi:10.1016/j.enbuild.2016.12.093

Cai, B., Yang, M., Liu, J., Li, J., and Liu, B. (2018). Atomistic Simulation Study of Favored Compositions of Ni-Nb-Al Metallic Glasses. *Sci. China Technol. Sc.* 61, 1829–1838. doi:10.1007/s11431-018-9342-3

Cai, M., Guo, R., Zhou, F., and Liu, W. (2013). Lubricating a Bright Future: Lubrication Contribution to Energy Saving and Low Carbon Emission. *Sci. China Technol. Sc.* 56, 2888–2913. doi:10.1007/s11431-013-5403-2

Calas, G., Majérus, O., Galoisy, L., and Cormier, L. (2006). Determination of the thermal Expansion of Cr^{3+} Sites in Glasses. *Appl. Phys. Lett.* 88, 121918. doi:10.1063/1.2189111

Cannavale, A., Fiorito, F., Manca, M., Tortorici, G., Cingolani, R., and Gigli, G. (2010). Multifunctional Bioinspired Sol-Gel Coatings for Architectural Glasses. *Build Environ.* 45, 1233–1243. doi:10.1016/j.buildenv.2009.11.010

Charaya, H., La, T. G., Rieger, J., and Chung, H. J. (2019). Thermochromic and Piezocapacitive Flexible Sensor Array by Combining Composite Elastomer Dielectrics and Transparent Ionic Hydrogel Electrodes. *Adv. Mater. Technol.* 4, 1900327. doi:10.1002/admt.201900327

Gao, Y., Luo, H., Zhang, Z., Kang, L., Chen, Z., Du, J., et al. (2012). Nanoceramic VO_2 Thermochromic Smart Glass: A Review on Progress in Solution Processing. *Nano Energy* 1, 221–246. doi:10.1016/j.nanoen.2011.12.002

Gong, X., Li, J., Chen, S., and Wen, W. (2009). Copolymer Solution-Based "Smart Window". *Appl. Phys. Lett.* 95, 251907. doi:10.1063/1.3276289

Hasan, A., Vuolle, M., and Sirén, K. (2008). Minimisation of Life Cycle Cost of a Detached House Using Combined Simulation and Optimisation. *Build Environ.* 43, 2022–2034. doi:10.1016/j.buildenv.2007.12.003

Hee, W. J., Alghoul, M. A., Bakhtyar, B., Elayeb, O., Shameri, M. A., and Alrubaih, M. S. (2015). The Role of Window Glazing on Daylighting and Energy Saving in Buildings. *Renew. Sust. Energ. Rev.* 42, 323–343. doi:10.1016/j.rser.2014.09.020

Iqbal, M. I., Himmler, R., and Gheewala, S. H. (2018). Environmental Impacts Reduction Potential through a PV Based Transition from Typical to Energy Plus Houses in Thailand: A Life Cycle Perspective. *Sci. China Technol. Sc.* 37, 307–322. doi:10.1016/j.scs.2017.11.028

Javad, K., and Navid, G. (2019). Thermal comfort Investigation of Stratified Indoor Environment in Displacement Ventilation: Climate-Adaptive Building with Smart Windows. *Sustain. Cities Soc.* 46, 101354. doi:10.1016/j.scs.2018.11.029

Jin, J., Zhang, D., Qin, X., Imran, H. I. A., Yang, Y., Huang, Y., et al. (2019). Remarkable Improved Solar Transmission of VO_2 Smart Windows by Partial Controlled Oxygen Plasma Bombarding. *Energ. Buildings.* 202, 109345. doi:10.1016/j.enbuild.2019.109345

Kharvari, F. (2020). An Empirical Validation of Daylighting Tools: Assessing Radiance Parameters and Simulation Settings in Ladybug and Honeybee against Field Measurements. *Sol. Energ.* 207, 1021–1036. doi:10.1016/j.solener.2020.07.054

Kim, H.-N., and Yang, S. (2020). Responsive Smart Windows from Nanoparticle-Polymer Composites. *Adv. Funct. Mater.* 30, 1902597. doi:10.1002/adfm.201902597

Kim, M. H., Kim, J. K., Lee, K. H., Baek, N. C., Park, D. Y., and Jeong, J. W. (2019). Performance Investigation of an Independent Dedicated Outdoor Air System for Energy-Plus Houses. *Appl. Therm. Eng.* 146, 306–317. doi:10.1016/j.applthermaleng.2018.09.131

Konis, K., Gamas, A., and Kensek, K. (2016). Passive Performance and Building Form: An Optimization Framework for Early-Stage Design Support. *Sol. Energ.* 125, 161–179. doi:10.1016/j.solener.2015.12.020

Li, W., Luo, X., Yang, P., Wang, Q., Zeng, M., and Markides, C. N. (2022). Solar-thermal Energy Conversion Prediction of Building Envelope Using Thermochemical Sorbent Based on Established Reaction Kinetics. *Energ. Convers. Manage.* 252, 115117. doi:10.1016/j.enconman.2021.115117

Li, Z., Luo, D., Shi, W., Li, Z., and Liang, X. (2011). Field Measurement of Wind-Induced Stress on Glass Facade of a Coastal High-Rise Building. *Sci. China Technol. Sci.* 54, 2587–2596. doi:10.1007/s11431-011-4512-z

McCormick, P. G., and Suehrcke, H. (2018). The Effect of Intermittent Solar Radiation on the Performance of PV Systems. *Sol. Energ.* 171, 667–674. doi:10.1016/j.solener.2018.06.043

Mlyuka, N. R., Niklasson, G. A., and Granqvist, C. G. (2009). Mg Doping of Thermochromic VO_2 Films Enhances the Optical Transmittance and Decreases the Metal-Insulator Transition Temperature. *Appl. Phys. Lett.* 95, 171909. doi:10.1063/1.3229949

Muramoto, K., Takahashi, Y., Terakado, N., Yamazaki, Y., Suzuki, S., and Fujiwara, T. (2020). Fabrication of VO_2-Dispersed Glass in B_2O_3-P_2o_5-V_2o_5 System and its Thermal Property. *Front. Mater.* 7, 00005. doi:10.3389/fmats.2020.00005

Negendahl, K., and Nielsen, T. R. (2015). Building Energy Optimization in the Early Design Stages: A Simplified Method. *Energ. Buildings.* 105, 88–99. doi:10.1016/j.enbuild.2015.06.087

Nguyen, A.-T., Reiter, S., and Rigo, P. (2014). A Review on Simulation-Based Optimization Methods Applied to Building Performance Analysis. *Appl. Energ.* 113, 1043–1058. doi:10.1016/j.apenergy.2013.08.061

Pierucci, A., Cannavale, A., Martellotta, F., and Fiorito, F. (2018). Smart Windows for Carbon Neutral Buildings: A Life Cycle Approach. *Energ. Buildings.* 165, 160–171. doi:10.1016/j.enbuild.2018.01.021

Ruffolo, S. A., and La Russa, M. F. (2019). Nanostructured Coatings for Stone Protection: An Overview. *Front. Mater.* 6, 00147. doi:10.3389/fmats.2019.00147

Sadineni, S. B., Madala, S., and Boehm, R. F. (2011). Passive Building Energy Savings: A Review of Building Envelope Components. *Renew. Sustain. Energ. Rev.* 15, 3617–3631. doi:10.1016/j.rser.2011.07.014

Wang, X., and Narayan, S. (2021). Thermochromic Materials for Smart Windows: A State-Of-Art Review. *Front. Energ. Res.* 9, 800382. doi:10.3389/fenrg.2021.800382

Wu, Y., Liu, H., Li, B., Kosonen, R., Deyu, K., Zhou, S., et al. (2019). Thermal Adaptation of the Elderly during Summer in a Hot Humid Area: Psychological, Behavioral, and Physiological Responses. *Energ. Buildings.* 203, 109450. doi:10.1016/j.enbuild.2019.109450

Xu, X., Wu, X., Zhao, C., Wang, J., and Ge, X. (2012). Simulation and Improvement of Energy Consumption on Intelligent Glasses in Typical Cities of China. *Sci. China Technol. Sc.* 55, 1999–2005. doi:10.1007/s11431-012-4854-1

Yang, Z., Yang, Q., Yang, L., Dai, B., Xia, F., Wang, P., et al. (2020). Effect of Thickness on Infrared Optical Property of VO_2 Film Deposited by Magnetron Sputtering. *Sci. China Technol. Sc.* 63, 1591–1598. doi:10.1007/s11431-020-1656-5

Zhang, Y., Tso, C. Y., Iñigo, J. S., Liu, S., Miyazaki, H., Chao, C. Y. H., et al. (2019). Perovskite Thermochromic Smart Window: Advanced Optical Properties and Low Transition Temperature. *Appl. Energ.* 254, 113690. doi:10.1016/j.apenergy.2019.113690

Zhou, Y., Layani, M., Boey, F. Y. C., Sokolov, I., Magdassi, S., and Long, Y. (2016). Electro-Thermochromic Devices Composed of Self-Assembled Transparent Electrodes and Hydrogels. *Adv. Mater. Technol.* 1, 1600069. doi:10.1002/admt.201600069

Zhu, H., Chen, F., Zhang, H., and Cui, Z. (2020). Review on Modeling and Simulation of Microstructure Evolution during Dynamic Recrystallization Using Cellular Automaton Method. *Sci. China Technol. Sci.* 63, 357–396. doi:10.1007/s11431-019-9548-x

Conflict of Interest: ZB was employed by the company China Automotive Engineering Research Institute Co., Ltd.

The remaining authors declare that the research was conducted in the absence of any commercial or financial relationships that could be construed as a potential conflict of interest.

Publisher's Note: All claims expressed in this article are solely those of the authors and do not necessarily represent those of their affiliated organizations, or those of the publisher, the editors, and the reviewers. Any product that may be evaluated in this article, or claim that may be made by its manufacturer, is not guaranteed or endorsed by the publisher.

frontiers | Frontiers in Materials

PERSPECTIVE
published: 01 July 2022
doi: 10.3389/fmats.2022.850115

Synthesis and Characterisation of Mg^{2+} and Al^{3+} Co-Doped $CoCr_2O_4$ Inorganic Pigments With High Near-Infrared Reflectance

Xueling Wei[1], Xiangyu Zou[1], Zhifeng Deng[1], Weiwei Bao[1], Taotao Ai[1] and Qi Zhang[2]**

[1]School of Materials Science and Engineering, Shaanxi University of Technology (SNUT), Hanzhong, China, [2]School of Environmental and Chemistry Engineering, Kunming Metallurgy College, Kunming, China

A new class of near-infrared (NIR) reflectance pigments based on $Co_{1-x}Mg_xCr_{2-y}Al_yO_4$ (x = 0–1 and y = 0–2) was synthesised using the Pechini-type sol-gel process. The developed powders were characterised by thermogravimetry and differential scanning calorimetry, X-ray diffraction (XRD), ultraviolet–visible near-infrared diffuse reflectance spectroscopy, and colour Commission Internationale del'Eclairage (CIE) 1976 (L*a*b*) colour scales. The XRD patterns revealed characteristic peaks of the spinel structure with good crystallinity. Substituting Mg^{2+} for Co^{2+} ions in the tetrahedral positions and Al^{3+} for Cr^{3+} ions in the octahedral positions of $CoCr_2O_4$ reduces the cost and changes the colour of the pigment (green to yellow and then blue). Moreover, the synthesised pigments exhibited high NIR solar reflectance in the 780–2,500 nm wavelength range. The thermal and chemical stability of the pigments was also studied. Our findings demonstrate the potential for applying these pigments in cool colourants.

Keywords: near-infrared reflectance, sol-gel method, Mg^{2+} and Al $^{3+}$ co-doped, cool pigments, solar reflectance

OPEN ACCESS

Edited by:
Weihua Li,
University of Wollongong, Australia

Reviewed by:
Ayman Awad Ali,
Benha University, Egypt

****Correspondence:***
Weiwei Bao
baowei1834@163.com
Qi Zhang
480807767@qq.com

Specialty section:
This article was submitted to Smart Materials, a section of the journal Frontiers in Materials

Received: *07 January 2022*
Accepted: *24 May 2022*
Published: *01 July 2022*

Citation:
Wei X, Zou X, Deng Z, Bao W, Ai T and Zhang Q (2022) Synthesis and Characterisation of Mg^{2+} and Al^{3+} Co-Doped $CoCr_2O_4$ Inorganic Pigments With High Near-Infrared Reflectance. Front. Mater. 9:850115. doi: 10.3389/fmats.2022.850115

HIGHLIGHTS

(1) A new class of near-infrared reflectance pigments based on $Co_{1-x}Mg_xCr_{2-y}Al_yO_4$ (x=0-1 and y=0-2) were synthesised via Pechini-type sol-gel method.
(2) The colours of the pigment samples can be tuned from green to yellow and then blue.
(3) Decreasing the Co and Cr contents reduces the cost and environmental damages.
(4) Pigment properties make it a potential candidate for use as cool pigments.

INTRODUCTION

In recent years, near-infrared (NIR) reflective pigments have received considerable attention in construction, plastic, ink, and military industries. NIR reflective pigments are complex metal oxides with high reflectance for NIR radiation (Song et al., 2019; Ali et al., 2018; Rossi et al., 2020; Jing et al., 2018; Zhou et al., 2020). The everyday use of solar reflective roofing materials has been proven to save energy, alleviate urban heat islands, and curb global warming (Ferrari et al., 2015; Zou and Zhang, 2020; Yang et al., 2017). Most of the literature on NIR reflective pigments are available as patents (Swiler et al., 2003; Blonski et al., 2001), demonstrating their vast applications. Many of these inorganic pigments consist of hazardous heavy metals such as cobalt (Co), lead (Pb), cadmium (Cd),

and chromium (Cr), which are restricted under present environmental regulations. Several of these methods are expensive (Hedayati et al., 2015; Schildhammer et al., 2017; Yuan et al., 2018). Recently, many rare-earth-based NIR reflective pigments have been suggested as substitutes for traditional pigments, owing to their low toxicity (Raj et al., 2019; Han et al., 2014). Aju Thara et al. (2017); Zhao et al. (2015) prepared a series of NIR pigments based on yttrium molybdate ($Y_2Mo_3O_{12}$) and yttrium cerate, and illustrated the NIR reflectance and colouring mechanism. However, rare-earth compounds are expensive because they are difficult to mine.

Numerous methods have been employed to synthesise simple oxide or oxide-based systems. Most conventional methods involve solid-state reactions (Zhang et al., 2018), co-precipitation (Frolova et al., 2017), hydrothermal (McMahon et al., 2019; Elakkiya and Sumathi, 2020), evaporative drying (Droguet et al., 2021), and sol-gel (polymeric precursor method) (Lima et al., 2020). The sol-gel method should be emphasised as it has numerous desirable characteristics, such as using affordable reagents and reducing costs, and requiring low temperature for oxide synthesis. In addition, the method has excellent chemical homogeneity at the molecular level of all components and has easy stoichiometric control in complex systems (Gonzaga et al., 2020).

Spinel pigments, which are represented chemically as AB_2O_4, have generated an increasing interest. These pigments exhibit a myriad of colours and tonalities owing to their ability to accommodate different cations (Bao et al., 2016). For example, cobalt chromite ($CoCr_2O_4$) is an essential commercial material and is extensively used as a catalyst, magnetic compound, and pigment owing to its superior properties. Because cobalt and chromium are generally rare and harmful, incorporating less toxic and expensive metals into the $CoCr_2O_4$ minimises the cost of production and impact on the environment. Therefore, in this study, Mg^{2+} substitution for Co^{2+} and Al^{3+} substitution for Cr^{3+} in $CoCr_2O_4$ was facilitated using the Pechini-type sol-gel process. The effects of these enrichments on the crystal structures, optical properties, and thermal and chemical stabilities of as-synthesised pigments were thoroughly investigated.

EXPERIMENTAL

Materials and Methods

Magnesium nitrate ($Mg(NO_3)_2{\cdot}6H_2O$), cobalt nitrate ($Co(NO_3)_2{\cdot}6H_2O$), citric acid (CA, $C_6H_8O_7$), chromium nitrate ($Cr(NO_3)_3{\cdot}9H_2O$), aluminium nitrate ($Al(NO_3)_3{\cdot}9H_2O$), and ethylene glycol (EG, $C_2H_6O_2$) were the starting materials. All chemicals utilised were analytical grade, acquired from Beijing Chemical Reagent Corporation, and used as received without further purification. All pigment samples of $Co_{1-x}Mg_xCr_{2-y}Al_yO_4$ (x = 0–1 and y = 0–2) were synthesised using the Pechini-type sol-gel method.

First, CA was dissolved in distilled water and stirred continuously at 80°C. Subsequently, nitrates of cobalt, chromium, magnesium, and aluminium were added stoichiometrically into the acid solution. The molar ratio of the CA/metal was 3:1. After dissolution, EG was added at a CA/EG ratio of 3:2. All solutions were mixed using a magnetic stirrer. The resultant solution was then heated on a hot plate at approximately 80°C for approximately 1 h to produce polymerisation gel through a polymerisation reaction. Subsequently, the beaker was kept in a thermostat drier at 120°C for 12 h. The preliminary heat treatment (350°C) of the gel was performed in air for 2 h. Gas liberation by combustion during heat treatment partially degraded the organic structure and its expansion, forming a brittle black powder precursor. Finally, the obtained powder of the precursor was ground into a fine powder and then calcined at 900°C at a heating rate of 10°C/min for 6 h to remove residual organic materials, and powder samples were synthesised.

Characterisation Techniques

Thermogravimetry and differential scanning calorimetry (TG-DSC) were performed using a STAR E TGA/DSC1 instrument to analyse the powder precursor and synthesised pigments. The powdered samples were heated under nitrogen in the temperature range 50–900°C at a rate of 20°C/min. Approximately 10 mg of the sample was loaded into aluminium crucibles for testing. Tabular α-Al_2O_3 was used as the reference for weight loss.

A Rigaku Ultima IV X-ray diffractometer equipped with Ni-filtered Cu Kα radiation (λ = 0.15406 nm, 40 kV, and 40 mA) was used to examine the crystal structures of the synthesised samples at 25°C. Step scanning over an angular range of 2θ (10°–80°) with a step size of 0.02°and a counting time of 5 s at each step were used for data collection.

The diffuse reflectance of the samples was measured with a 5-nm step size in the range 380–2,500 nm using a Lambda 950 UV–vis NIR spectrophotometer with an integrating sphere attachment, calibrated by a white standard (D65 illumination such as daylight).

The colour Commission Internationale del'Eclairage chromaticity analysis software (Perkin Elmer) was used to estimate the pigment colour parameters from the reflection data of visible light. The CIE 1976 L*a*b*colourimetry method was employed following the recommendations of the CIE. In this system, the L* value signifies the lightness or darkness of the colour (L* is equal to 0 and 100 for black and white, respectively). The values of a* (green (−) → red (+) axis) and b* (blue (−) → yellow (+) axis) indicate the colour hue. The parameter C* (chroma) represents the colour saturation and is defined in **Eq. (1)** (Sukmarani et al., 2020; Gong et al., 2021).

$$C^* = \left(a^{*2} + b^{*2}\right)^{1/2}, \tag{1}$$

The measurement standard JG/T 235-2014 was used to guide the calculations for the NIR solar reflectance (R^*) in the wavelength range 780–2,500 nm. The function R^* was determined using **Eq. (2)**, as follows:

$$R^* = \frac{\int_{780}^{2500} r(\lambda) i(\lambda) d(\lambda)}{\int_{780}^{2500} i(\lambda) d(\lambda)}, \tag{2}$$

where $i(\lambda)$ is the solar special irradiance (W m^{-2} nm^{-1}), and $r(\lambda)$ corresponds to the spectral reflectance achieved experimentally

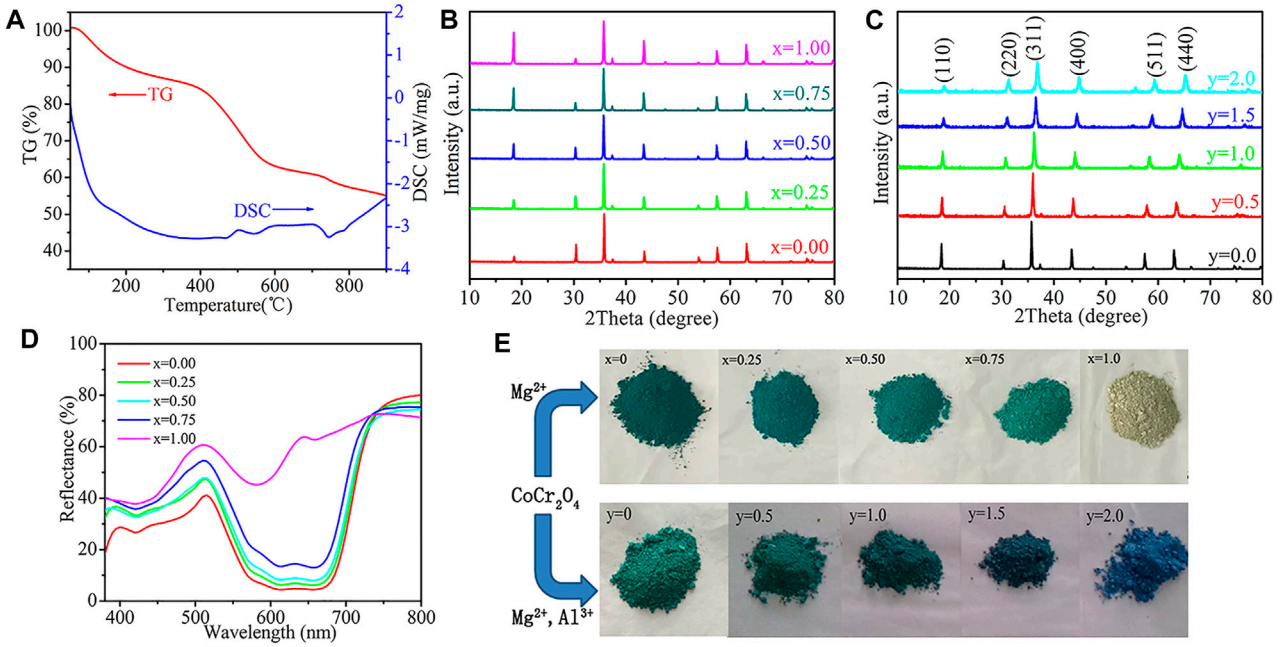

FIGURE 1 | (A) TG-DSC curves of $CoCr_2O_4$ pigment precursor **(B)** XRD diffraction patterns of $Co_{1-x}Mg_xCr_2O_4$ (x = 0.00, 0.25, 0.50, 0.75, 1.00) pigments **(C)** XRD diffraction patterns of $Co_{0.25}Mg_{0.75}Cr_{2-y}Al_yO_4$ (y = 0.0, 0.5, 1.0, 1.5, 2.0) pigments **(D)** UV–vis absorption spectra of $Co_{1-x}Mg_xCr_2O_4$ (x = 0.00, 0.25, 0.50, 0.75, 1.00) powdered pigments **(E)**photographs of $Co_{1-x}Mg_xCr_2O_4$ (x = 0.00–1.00) and $Co_{0.25}Mg_{0.75}Cr_{2-y}Al_yO_4$ (y = 0.0–2.0) pigments.

(W m^{-2}). The NIR solar reflectance value quantifies the unabsorbed solar radiation on the surface of a substance and signifies the build-up of heat in structures upon exposure to the Sun (Hedayati et al., 2015).

RESULTS AND DISCUSSION

Thermal Analysis

Figure 1A shows the thermal analysis (TG-DSC) results for the synthesised pigment. The TG curve depicts three different stages with a total weight loss of 43%, which can be observed from the TG curve. For instance, increasing the temperature (50°C–300°C), decreased the weight of the $CoCr_2O_4$ precursor by 13%. Weight loss is associated with the removal of residual water, unpolymerised CA, and EG from the precursor. The weight loss increased by more than 25% at 300°C–600°C.

An exothermic peak in the DSC curve was observed at approximately 500°C–600°C, indicating the evolution of H_2O, CO_x, and NO_x via the combustion of the nitrates and organic impurities (Liu et al., 2015). Furthermore, a highly exothermic peak in the DSC curve was observed at 700°C–800°C, which was attributed to the precursor decomposition into $CoCr_2O_4$ particles. The mass loss was less than 5% at temperatures higher than 600°C, implying the realisation of final $CoCr_2O_4$ pigments.

Powder X-Ray Diffraction Analysis

Figure 1B shows the XRD patterns of the as-synthesised $Co_{1-x}Mg_xCr_2O_4$ (x = 0.00, 0.25, 0.50, 0.75, and 1.00) precursors after grinding and calcining at 900°C for 6 h. The analysis revealed peaks of the cubic spinel structure, which were observed for all samples. The space groups, Fd3m, of $CoCr_2O_4$ and $MgCr_2O_4$ were distinguished based on JCPDS 22-1084 and 65-3106, respectively. In addition, the XRD patterns did not exhibit non-spinel impurity phases.

Figure 1C illustrates the XRD patterns of $Co_{0.25}Mg_{0.75}Cr_{2-y}Al_yO_4$ (y = 0.0, 0.5, 1.0, 1.5, and 2.0). All the diffraction peaks were associated with the cubic spinel crystal structure of $CoCr_2O_4$, and the structure was not altered by co-doping with Mg^{2+} and Al^{3+}. The addition of Al^{3+} ions slightly shifted the XRD peaks towards higher diffraction angles than the parent oxide. A variation in the cell volume may have caused the observed 2θ shift. Typically, an increase in the Al^{3+} concentration decreases the cell volume because a smaller Al^{3+} (0.051 nm) displaces the larger Cr^{3+} (0.061 nm) ions (Liu et al., 2015; Wu et al., 2018). **Supplementary Tables S1, S2** show that there is no obvious change in cell volume with the increase in Mg concentration in $CoCr_2O_4$, which is mainly due to the similar ionic radii of Mg^{2+} and Co^{2+}. With the increase in Al concentration, the cell volume decreases regularly, indicating that the replacement of Cr by Al is successful. The pigment morphology was characterised by SEM (**Supplementary Figure S1**), and the average grain size was less than 5 μm. Elemental mapping analysis (**Supplementary Figure S2**) further revealed that Cr, Co, O, Mg, and Al elements exhibited a uniform distribution.

Optical Properties of Magnesium Doping

Figure 1D demonstrates the UV–vis absorption spectra of the powdered $Co_{1-x}Mg_xCr_2O_4$ (x = 0.00, 0.25, 0.50, 0.75, and 1.00)

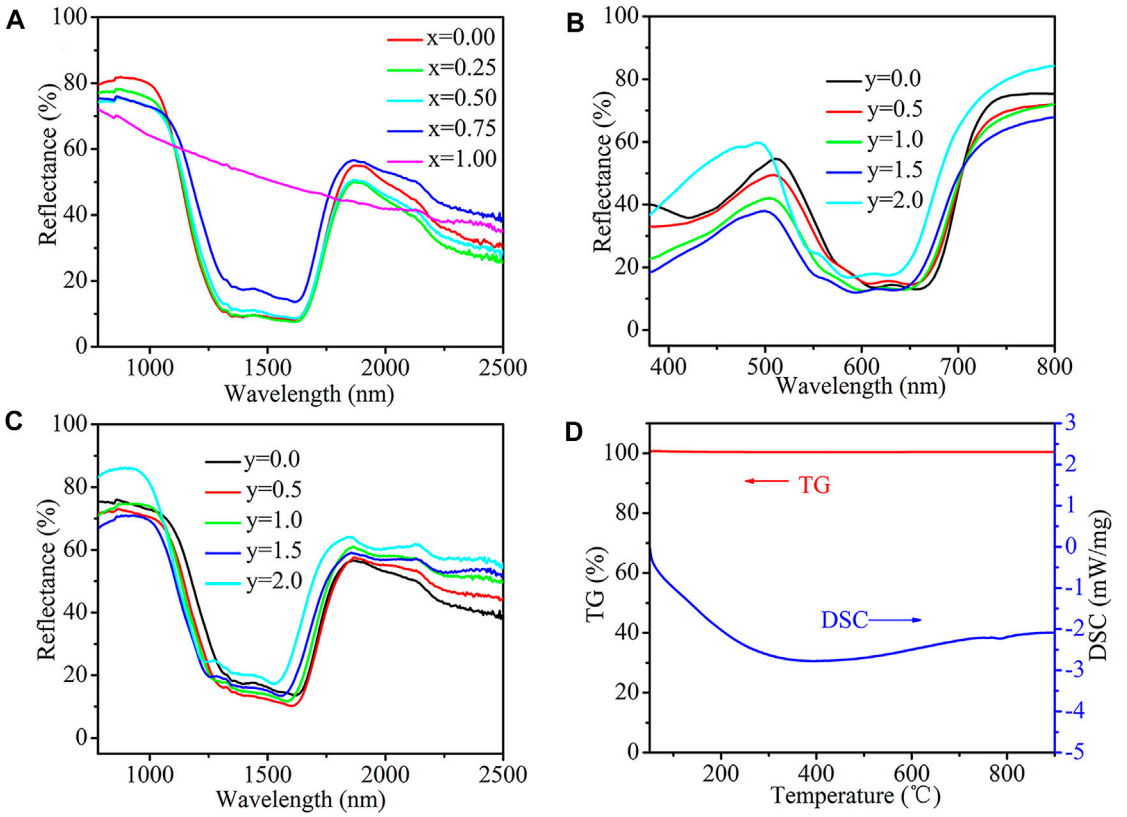

FIGURE 2 | (A) NIR reflectance of $Co_{1-x}Mg_xCr_2O_4$ (x = 0.00, 0.25, 0.50, 0.75, 1.00) powdered samples **(B)** UV–vis absorption spectra of $Co_{0.25}Mg_{0.75}Cr_{2-y}Al_yO_4$ (y = 0.0, 0.5, 1.0, 1.5, 2.0) powdered pigments **(C)** NIR reflectance of $Co_{0.25}Mg_{0.75}Cr_{2-y}Al_yO_4$ (y = 0.0, 0.5, 1.0, 1.5, 2.0) powdered samples **(D)**TG-DSC analysis of powdered $Co_{0.25}Mg_{0.75}Al_2O_4$ pigment sample.

samples. An intense triple band at approximately 570, 610, and 660 nm was observed for the $CoCr_2O_4$ sample spectrum. The absorption peaks steadily weakened with increasing and decreasing concentrations of Mg and Co, respectively. According to the Tanabe–Sugano energy level diagrams, the ^4F ground-state term separates into three terms, $^4A_2$, $^4T_2$, and $^4T_1(F)$ in the tetrahedral coordination of Co^{2+} ions with the d^7 configuration, while the ^4P excited-state term transforms into $^4T_1(P)$. Thus, the three possible spin transitions are ν_1: $^4A_2(F) \rightarrow {}^4T_2(F)$, ν_2: $^4A_2(F) \rightarrow {}^4T_1(F)$, and ν_3: $^4A_2(F) \rightarrow {}^4T_1(P)$. The first and second bands lie within the IR region, whereas the third band lies in the visible region. The broadband can be ascribed to the ν_3 transition ($^4A_2(F) \rightarrow {}^4T_1(P)$ transition) of Co^{2+} ions, which decomposes into three bands because of L-S Russell–Saunders coupling (Hedayati et al., 2015; Lourenco et al., 2016). Therefore, this broad triple band within 500 and 700 nm results in blue pigmentation of compounds containing Co^{2+}.

The chromatic properties of the synthesised $Co_{1-x}Mg_xCr_2O_4$ pigments were assessed using their CIE 1976 L*a*b*colour coordinates (**Supplementary Table S3**). The addition of Mg^{2+} lightened the colour of the samples, as evidenced by the increasing L* from 52.92 to 77.56. In contrast, increasing Mg^{2+} substitution results in the loss of the green pigment hue, as is apparent from the change in the colour coordinate a* from −38.80 to −7.32. Moreover, the b* values increased from −15.43 to 9.14, indicating intensification of the yellow colour in the pigments. The C* values, representing the richness of the colour hue, decreased significantly from 41.76 to 11.71. The observed hue angles of the pigments are found to be in the green region of the cylindrical colour space. **Figure 1E** shows the photographs of the synthesised powdered pigment samples.

Figure 2A shows the NIR reflectance spectra of the $Co_{1-x}Mg_xCr_2O_4$ pigments. The base compound, $CoCr_2O_4$, has an NIR solar reflectance (R*) of 55.1%. Simultaneously, substituting Co^{2+} ions with Mg^{2+} ions decreased the NIR reflectance of the pigments from 55.1 (x = 0.00) to 52.8% (x = 0.50). Further doping of Mg^{2+} with Co^{2+} increased the NIR reflectance to 60.3% (x = 1.00). **Supplementary Table S3** presents detailed information on the NIR solar reflectance of the powdered pigments. The NIR reflectance of a typical pigment sample $Co_{0.25}Mg_{0.75}Cr_2O_4$ (R* = 56.3%) was significantly higher than that of the Y_2BaCuO_5 green pigment reported elsewhere (R* = 50%) (Shankland et al., 1974; Jose et al., 2014). The designed class of pigments displayed high reflectance in the NIR region, suggesting that these formulations could be considered cooling pigments. In addition, with the increase in Mg doping amount, the as-prepared pigments showed a red shift in the band gap transition.

Optical Properties of Aluminium Doping

Figure 2B illustrates the UV–vis absorption spectra of the developed $Co_{0.25}Mg_{0.75}Cr_{2-y}Al_yO_4$ (y = 0.0, 0.5, 1.0, 1.5, and 2.0) samples. A prominent blue shift of the triple band occurred when the Al^{3+} content was increased from 0 to 2. The energy level of the excitation state for Co^{2+} and the position of the absorption band are dependent on the Co^{2+} ion surroundings. The gradual substitution of Al^{3+} for Cr^{3+} indicates a substantial change in the volume of the octahedral site. Subsequently, oxygen ligands experience less attraction from octahedrally coordinated ions because of the lower atomic mass of aluminium than that of chromium. Therefore, the exposure of the oxygen ligands is more to $Mg^{2+}$and Co^{2+}, enhancing the splitting of the d-orbital energy levels and the blue shift of the absorption band (**Figure 2B**) (Hedayati et al., 2015; Shankland et al., 1974).

The chromatic properties of the synthesised $Co_{0.25}Mg_{0.75}Cr_{2-y}Al_yO_4$ pigments were obtained from their CIE 1976 L*a*b* colour coordinates (**Supplementary Table S4**). Substituting Al^{3+} for Cr^{3+} in $Co_{0.25}Mg_{0.75}Cr_2O_4$ spinel increased a* and decreased b*, weakening the intensity of the green colour in the pigments while enhancing the blue pigmentation. Substituting Al^{3+} with Cr^{3+} ions in the spinel structure decreased L* from 64.82 to 53.87, darkening the samples. Consequently, C*, which represents the richness of the colour hue, decreased from 34.93 to 24.33. However, the L* and C* values changed slightly when Al^{3+} was completely substituted with Cr^{3+} ions in the spinel structure. With the increasement of Al doping, the hue angles of pigment move from green to blue region of the cylindrical colour space. **Figure 1E** shows photographs of the synthesised powdered pigment samples.

Figure 2C shows the NIR reflectance spectra of the powdered samples. The NIR solar reflectance of the samples decreased from 56.3 (y = 0.0) to 51.9 (y = 1.5) with the substitution of Al^{3+} for Cr^{3+}. **Supplementary Table S4** lists the NIR solar reflectance of the powdered pigments. The reflectance reached a maximum (R* = 61.7%) for y = 2.0, which was higher than that of aluminium-doped cobalt chromite pigments of similar colour, as reported elsewhere (R* = 52%) (Hedayati et al., 2015). Furthermore, with the increase in Al doping amount, the as-obtained pigments also exhibit a red shift in the band gap transition. These observations demonstrate that Mg^{2+} and Al^{3+} co-doped $CoCr_2O_4$ systems are appropriate cooling pigments.

Studies on Thermal and Chemical Stabilities of the Pigments

The $Co_{0.25}Mg_{0.75}Al_2O_4$ pigments were investigated from 50 to 900 °C for their thermal stability. The results indicated that there was a negligible weight loss and phase transition of the pigment (**Figure 2D**). The chemical resistance of the pigment was investigated using 5% $HCl/H_2SO_4/HNO_3$ and NaOH (Bao et al., 2016; Jose and Reddy, 2013). A pre-weighed pigment powder was soaked in an acid/alkali solution for 30 min and stirred using a magnetic stirrer. The pigment powder slurry was filtered, washed with water, dried, and weighed again. Negligible weight loss of the pigment was observed for all the tested acids and alkalis. The colour coordinates of the pigments were measured and had negligible total colour difference (△E*) (**Supplementary Table S5**). These results demonstrate that the pigments were chemically and thermally stable.

CONCLUSION

In this study, a series of NIR reflective pigments with the general formula $Co_{1-x}Mg_xCr_{2-y}Al_yO_4$ (x = 0–1 and y = 0–2) were synthesised using the Pechini-type sol-gel method. The effect of Mg^{2+} and Al^{3+} enrichment on the structure and optical and chromatic properties of the products was investigated. XRD analyses revealed that the pigments were well crystallised in spinel cubic structures. The pigments exhibited a wide range of colours from green to yellow and blue and showed clear NIR reflective performance (greater than 51%). The pigments also showed good thermal and chemical stability.

DATA AVAILABILITY STATEMENT

The original contributions presented in the study are included in the article/**Supplementary Material**, and further inquiries can be directed to the corresponding authors.

AUTHOR CONTRIBUTIONS

XW and XZ: Synthesis of pigments and corresponding characterisations and analysis; writing of original drafts. DZ and TA: helped in data analysis; WB revised the manuscript.

FUNDING

This research was supported by the National Natural Science Foundation of China (Grant Nos. 51504147) and the National & Local Joint Engineering Laboratory for Slag Comprehensive Utilization and Environmental Technology Open Fund (Grant Nos. SLGPT2019KF01-03).

SUPPLEMENTARY MATERIAL

The Supplementary Material for this article can be found online at: https://www.frontiersin.org/articles/10.3389/fmats.2022.850115/full#supplementary-material

REFERENCES

Aju Thara, T. R., Rao, P. P., Divya, S., Raj, A. K. V., and Sreena, T. S. (2017). Enhanced Near Infrared Reflectance with Brilliant Yellow Hues in Scheelite Type Solid Solutions, $(LiLaZn)_{1/3}MoO_4$-$BiVO_4$ for Energy Saving Products. *ACS Sustain. Chem. Eng.* 5, 5118–5126. doi:10.1021/acssuschemeng.7b00485

Ali, A. A., El Fadaly, E., and Ahmed, I. S. (2018). Near-infrared Reflecting Blue Inorganic Nano-Pigment Based on Cobalt Aluminate Spinel *via* Combustion Synthesis Method. *Dyes Pigments* 158, 451–462. doi:10.1016/j.dyepig.2018.05.058

Bao, W., Ma, F., Zhang, Y., Hao, X., Deng, Z., Zou, X., et al. (2016). Synthesis and Characterization of Fe^{3+} Doped $Co_{0.5}Mg_{0.5}Al_2O_4$ Inorganic Pigments with High Near-Infrared Reflectance. *Powder Technol.* 292, 7–13. doi:10.1016/j.powtec.2016.01.013

Blonski, R. P., Pipoly, R. A., and Sliwinski, T. R. (2001). *Infrared Reflective Color Pigment*. EP1141105 A1.

Droguet, B., Liang, H., Frka-Petesic, B., Parker, R., De Volder, M., Baumberg, J., et al. (2021). Large-scale Fabrication of Structurally Coloured Cellulose Nanocrystal Films and Effect Pigments. *Nat. Mater.* 21, 352–358.doi:10.1038/s41563-021-01135-8

Elakkiya, V., and Sumathi, S. (2020). Low-temperature Synthesis of Environment-Friendly Cool Yellow Pigment: Ce Substituted $SrMoO_4$. *Mater. Lett.* 263, 127246. doi:10.1016/j.matlet.2019.1272460167

Ferrari, C., Muscio, A., Siligardi, C., and Manfredini, T. (2015). Design of a Cool Color Glaze for Solar Reflective Tile Application. *Ceram. Int.* 41, 11106–11116. doi:10.1016/j.ceramint.2015.05.058

Frolova, L., Pivovarov, A., and Butyrina, T. (2017). Synthesis of Pigments in Fe_2O_3-Al_2O_3-CoO by Co-precipitation Method. *Prt* 46, 356–361. doi:10.1108/PRT-07-2016-0073

Gong, L., Liang, J., Kong, L., Chen, B., Li, Y., and Tian, G. (2021). Synthesis of High-Performance Copper Barium Silicate Composite Pigment from Waste Iron Ore Tailings. *Ceram. Int.* 47, 27987–27997. doi:10.1016/j.ceramint.2021.06.230

Gonzaga, L. A., Santana, V. T., Bernardi, M. I. B., Hrubý, J., Neugebauer, P., and Mesquita, A. (2020). CeO_2 and CeO_2 :Pr Nanocrystalline Powders Prepared by the Polymeric Precursor Method: Yellow and Red Pigments with Tunable Color. *J. Am. Ceram. Soc.* 103, 6280–6288. doi:10.1111/jace.17339

Han, A., Ye, M., Liu, L., Feng, W., and Zhao, M. (2014). Estimating Thermal Performance of Cool Coatings Colored with High Near-Infrared Reflective Inorganic Pigments: Iron Doped $La_2Mo_2O_7$ Compounds. *Energy Build.* 84, 698–703. doi:10.1016/j.enbuild.2014.08.024

Hedayati, H. R., Sabbagh Alvani, A. A., Sameie, H., Salimi, R., Moosakhani, S., Tabatabaee, F., et al. (2015). Synthesis and Characterization of $Co_{1-x}Zn_xCr_{2-y}Al_yO_4$ as a Near-Infrared Reflective Color Tunable Nano-Pigment. *Dyes Pigments* 113, 588–595. doi:10.1016/j.dyepig.2014.09.030

Jing, J., Zhang, Y., Sun, J., Zhao, X., Gao, D., and Zhang, Y. (2018). A Comparative Study on Different RE-doped (RE=Pr, Nd, Sm) $SrCuSi_4O_{10}$ Blue Pigments with High Near-Infrared Reflectance. *Dyes Pigments* 150, 9–15. doi:10.1016/j.dyepig.2017.10.045

Jose, S., Prakash, A., Laha, S., and Natarajan, S. (2014). Green Colored Nano-Pigments Derived from Y_2BaCuO_5: NIR Reflective Coatings. *Dyes Pigments* 107, 118–126. doi:10.1016/j.dyepig.2014.03.025

Jose, S., and Reddy, M. L. (2013). Lanthanum-strontium Copper Silicates as Intense Blue Inorganic Pigments with High Near-Infrared Reflectance. *Dyes Pigments* 98, 540–546. doi:10.1016/j.dyepig.2013.04.013

Lima, N. A., Alencar, L. D. S., Siu-Li, M., Feitosa, C. A. C., Mesquita, A., M'peko, J.-C., et al. (2020). $NiWO_4$ Powders Prepared via Polymeric Precursor Method for Application as Ceramic Luminescent Pigments. *J. Adv. Ceram.* 9, 55–63. doi:10.1007/s40145-019-0347-z

Liu, L., Han, A., Ye, M., and Zhao, M. (2015). Synthesis and Characterization of Al^{3+} Doped $LaFeO_3$ Compounds: A Novel Inorganic Pigments with High Near-Infrared Reflectance. *Sol. Energy Mater. Sol. Cells* 132, 377–384. doi:10.1016/j.solmat.2014.08.048

Lourenço, S. A., Silva, R. S., and Dantas, N. O. (2016). Tunable Dual Emission in Visible and Near-Infrared Spectra Using Co^{2+}-Doped PbSe Nanocrystals Embedded in a Chalcogenide Glass Matrix. *Phys. Chem. Chem. Phys.* 18, 23036–23043. doi:10.1039/c6cp04419k

McMahon, M. E., Santucci, R. J., Glover, C. F., Kannan, B., Walsh, Z. R., and Scully, J. R. (2019). A Review of Modern Assessment Methods for Metal and Metal-Oxide Based Primers for Substrate Corrosion Protection. *Front. Mat.* 6, 190–213. doi:10.3389/fmats.2019.00190

Raj, A. K. V., Rao, P. P., Sreena, T. S., and Thara, T. R. A. (2019). Pigmentary Colors from Yellow to Red in $Bi_2Ce_2O_7$ by Rare Earth Ion Substitutions as Possible High NIR Reflecting Pigments. *Dyes Pigments* 160, 177–187. doi:10.1016/j.dyepig.2018.08.010

Rossi, S., Lindmark, H., and Fedel, M. (2020). Colored Paints Containing NIR-Reflective Pigments Exposed to Accelerated Ultraviolet Radiation Aging with Possible Application as Roof Coatings. *Coatings* 10, 1135–1152. doi:10.3390/coatings10111135

Schildhammer, D., Fuhrmann, G., Petschnig, L., Schottenberger, H., and Huppertz, H. (2017). Synthesis and Optical Properties of New Highly NIR Reflective Inorganic Pigments $RE_6Mo_2O_{15}$ (RE = Tb, Dy, Ho, Er). *Dyes Pigments* 140, 22–28. doi:10.1016/j.dyepig.2017.01.021

Shankland, T. J., Duba, A. G., and Woronow, A. (1974). Pressure Shifts of Optical Absorption Bands in Iron-Bearing Garnet, Spinel, Olivine, Pyroxene, and Periclase. *J. Geophys. Res.* 79, 3273–3282. doi:10.1029/jb079i023p03273

Song, Y., Chen, W., Lim, X. M., Hu, X., Liu, M., and Zhang, Q. (2019). Electronic Configuration in Outset Orbitals of Doping Elements Plays as a Key Factor in Tuning Near Infrared Reflection of $YMn_{0.9}M_{0.1}O_3$ (M = Cr, Mn, Fe, Co, Al, Ga and In). *J. Solid State Chem.* 273, 81–84. doi:10.1016/j.jssc.2019.02.040

Sukmarani, G., Kusumaningrum, R., Noviyanto, A., Fauzi, F., Habieb, A. M., Amal, M. I., et al. (2020). Synthesis of Manganese Ferrite from Manganese Ore Prepared by Mechanical Milling and its Application as an Inorganic Heat-Resistant Pigment. *J. Mater. Res. Technol.* 9, 8497–8506. doi:10.1016/j.jmrt.2020.05.122

Swiler, D. R., Detrie, T. J., and Axtell, E. A. (2003). *Rare Earth Transition Metal Oxide Pigments*. US, US6582814 B2.

Wu, Y., Qiu, K., Tang, Q., Zhang, W., and Wang, J. (2018). Luminescence Enhancement of Al^{3+} Co-doped $Ca_3Sr_3(VO_4)_4$:Eu^{3+} Red-Emitting Phosphors for White LEDs. *Ceram. Int.* 44, 8190–8195. doi:10.1016/j.ceramint.2018.01.267

Yang, R., Han, A., Ye, M., Chen, X., and Yuan, L. (2017). Synthesis, Characterization and Thermal Performance of Fe/N Co-doped $MgTiO_3$ as a Novel High Near-Infrared Reflective Pigment. *Sol. Energy Mater. Sol. Cells* 160, 307–318. doi:10.1016/j.solmat.2016.10.045

Yuan, L., Han, A., Ye, M., Chen, X., Yao, L., and Ding, C. (2018). Synthesis and Characterization of Environmentally Benign Inorganic Pigments with High NIR Reflectance: Lanthanum-Doped $BiFeO_3$. *Dyes Pigments* 148, 137–146. doi:10.1016/j.dyepig.2017.09.008

Zhang, S., Pan, Z., and Wang, Y. (2018). Synthesis and Characterization of (Ni, Sb)-Co-Doped Rutile Ceramic Pigment via Mechanical Activation-Assisted Solid-State Reaction. *Particuology* 41, 20–29. doi:10.1016/j.partic.2017.12.016

Zhao, X., Zhang, Y., Huang, Y., Gong, H., and Zhao, J. (2015). Synthesis and Characterization of Neodymium Doped Yttrium Molybdate High NIR Reflective Nano Pigments. *Dyes Pigments* 116, 119–123. doi:10.1016/j.dyepig.2015.01.018

Zhou, N., Sha, S., Zhang, Y., Li, S., Xu, S., and Luan, J. (2020). Coprecipitation Synthesis of a Green Co-doped Wurtzite Structure High Near-Infrared Reflective Pigments Using Ammonia as Precipitant. *J. Alloys Compd.* 820, 153183–483191. doi:10.1016/j.jallcom.2019.153183

Zou, J., and Zhang, P. (2020). Ni-doped BaTi5O11: New Brilliant Yellow Pigment with High NIR Reflectance as Solar Reflective Fillers. *Ceram. Int.* 46, 3490–3497. doi:10.1016/j.ceramint.2019.10.063

Conflict of Interest: The authors declare that the research was conducted in the absence of any commercial or financial relationships that could be construed as a potential conflict of interest.

Publisher's Note: All claims expressed in this article are solely those of the authors and do not necessarily represent those of their affiliated organizations, or those of the publisher, the editors and the reviewers. Any product that may be evaluated in this article, or claim that may be made by its manufacturer, is not guaranteed or endorsed by the publisher.

frontiers | Frontiers in Materials

ORIGINAL RESEARCH
published: 20 July 2022
doi: 10.3389/fmats.2022.930885

Flow-State Identification of Oil-Based Magnetic Fluid Seal Based on Acoustic Emission Technology

Jinyu Xue[1], *Yancai Xiao*[1]* *and Decai Li*[1,2]

[1]School of Mechanical, Electronic and Control Engineering, Beijing Jiaotong University, Beijing, China, [2]State Key Laboratory of Tribology, Tsinghua University, Beijing, China

At present, most research studies on the changing process of the magnetic fluid seal are analyzed with the pressure signal of each chamber or the magnetic fluid flow photos taken by a camera, which need to change the seal structure. Based on nondestructive acoustic emission technology, a flow-state identification model of the oil-based magnetic fluid seal using the grey wolf optimizer and random forest is proposed in this study. The acoustic emission signal and pressure signal are collected at the same time under static conditions in the two-stage pole shoes oil-based magnetic fluid seal experiment. Through power spectrum analysis of the acoustic emission signal with the aid of pressure signal, the changing process before seal failure is divided into three states: no magnetic fluid flow, the first pole shoe magnetic fluid flow, and two pole shoes magnetic fluid flow together. Then, the time- and frequency-domain features of acoustic emission signal samples are extracted to form feature vectors as inputs, and the flow-state identification model is established based on the grey wolf optimizer and random forest. The experimental results show that the testing accuracy and F1 scores (the index representing the precision and recall at the same weight) of three states are close to or higher than 90%. The effectiveness of oil-based magnetic fluid seal flow-state identification model based on non-destructive acoustic emission technology is proved.

Keywords: acoustic emission, oil-based magnetic fluid seal, flow-state identification, random forest, grey wolf optimizer

OPEN ACCESS

Edited by:
Weihua Li,
University of Wollongong, Australia

Reviewed by:
Xufeng Dong,
Dalian University of Technology, China
Song Qi,
Chongqing University, China

***Correspondence:**
Yancai Xiao
ycxiao@bjtu.edu.cn

Specialty section:
This article was submitted to Smart Materials, a section of the journal Frontiers in Materials

Received: *28 April 2022*
Accepted: *17 May 2022*
Published: *20 July 2022*

Citation:
Xue J, Xiao Y and Li D (2022) Flow-State Identification of Oil-Based Magnetic Fluid Seal Based on Acoustic Emission Technology. Front. Mater. 9:930885. doi: 10.3389/fmats.2022.930885

INTRODUCTION

The magnetic fluid seal is a new seal technology controlled by a magnetic field. Magnetic fluid is injected in the gap of a magnetic circuit comprising a permanent magnet, pole shoes, and rotating shaft to form several magnetic fluid "O" rings. It has the advantages of zero leakage, long service life, and high reliability compared with other seal technologies. So, it has an important application value in aerospace, military, and other fields (Li and Hao, 2018). Its good seal performance is the premise for these fields' normal functioning.

The pressure signal has often been used to characterize magnetic fluid seal performance at present. Chen (2019) judged each magnetic fluid "O" ring' seal performance by the pressure signal of the cavity between the two pole shoes. Wang (2019) designed a new seal structure with two seal units. The pressure detection devices distributed between them can monitor magnetic fluid sealing liquid medium's performance online and realize seal failure warning. The holes must be drilled on the seal element to connect the pressure detection devices. The more holes are drilled, the more leakage

points exist, which is more unfavorable to the seal effect. According to the flow simulation model established by Chen (2019) when studying the mechanism of magnetic fluid seal, its seal performance is closely related to the flow state of magnetic fluid. When conducting experiments under static conditions, he unfolded the rotating structure along the circumference, pressed the front and rear end faces with transparent materials to achieve seal, and photographed magnetic fluid flow with a macro camera. Wang (2019) used a transparent shell, changed pole teeth's location and shape to achieve seal, and captured the magnetic fluid's interface changes with a camera. Kurfess and Müller (1990) transformed the rotating shaft into a hollow glass rod. The plane mirror extended into it and reflected the magnetic fluid's flow change, which can be observed by a microscope. The way of camera shooting or microscope observation needs to change the seal structure and replace it with transparent materials, which is not universal.

The abovementioned research studies are all carried out on the experimental platform. In practical applications, magnetic fluids are mostly wrapped by opaque devices. They are not allowed to be disassembled at will after assembly. Therefore, new nondestructive testing technology is needed to monitor the flow state of magnetic fluid in the seal gap.

Liquid film seal is a non-contact mechanical seal based on the hydrodynamic lubrication theory. A micron groove with certain geometry is set on the end face of the seal ring. A full-liquid film is formed based on the dynamic pressure effect between end faces during the seal operation. Maintaining the liquid film's stable existence is the key to ensuring good liquid film seal performance (Li, 2017). Sun et al. (2018) pointed out that acoustic emission technology applied to liquid film seal monitoring is a new development direction in the seal field. The friction between the moving and stationary ring as a secondary sound source can be detected by an acoustic emission sensor. Relevant studies include the monitoring of the seal opening process and liquid film thickness (Li et al., 2014; Jiang, 2015; Zhang, 2015; Ge et al., 2016; Li, 2016; Zhang, 2016). Jiang (2015) distinguished the three friction states (dry friction, mixed friction, and fluid friction) in the seal opening process, then collected the acoustic emission signal and performed wavelet packet analysis, extracted time-frequency domain eigenvalues, and took them as input to train the Elman network model to identify the different friction states. Li (2016) pointed out that different film thicknesses will lead to different degrees of friction between dynamic and static rings, so the acoustic emission signal can be connected with the film thickness. Li et al. (2014) divided the film thickness into three states (thin, medium, and thick), found the corresponding acoustic emission signals and performed empirical mode decomposition (EMD), and then proposed a dual back propagation (BP) neural network to identify the different states. In a word, most of the current research studies collect the acoustic emission signals as samples and use machine learning methods to identify different states of the liquid film seal.

In the process of magnetic fluid flow, there is viscous friction of fluid and friction between the fluid and solid walls such as rotating shaft and pole shoes. Therefore, acoustic emission technology is used to monitor the flow state of the oil-based magnetic fluid in the seal gap in this study based on the similarity between the magnetic fluid seal and liquid film seal. The time- and frequency-domain features are extracted from the acoustic emission signal samples, and the random forest model based on the grey wolf optimizer is trained to identify the different states before seal failure. The effectiveness of this monitoring method is verified by the results.

COLLECTION OF ACOUSTIC EMISSION SIGNAL SAMPLES

In order to explore the information of the oil-based magnetic fluid flow for rotating shaft seals, an experiment of sealing gas with oil-based magnetic fluid under static conditions is designed. The acoustic emission and pressure signals are collected at the same time in this experiment. With the aid of pressure signals, the acoustic emission signal samples of different states are collected.

Introduction of the Experiment Devices

The experimental devices include an acoustic emission sensor, 2/4/6 preamplifier, pressure transmitter, data acquisition instrument, 24 V DC power supply, air compressor, pressure relief valve, and so on. The connection diagram of these devices is shown in **Figure 1**.

The rotating shaft seal element has two-stage pole shoes. The oil-based magnetic fluid's theoretical maximum pressure is 323.08 kPa under static conditions. The propagation distance is an important factor affecting the attenuation degree of the acoustic emission signal. The distance from the magnetic fluid to shell is about 25 mm in this structure. The cylindrical magnets are arranged closely along the circumference to provide a magnetic field, and there is a gap between the two adjacent cylindrical magnets. Therefore, the pressure transmitter 2 can detect the gas leaked after the first-stage pole shoe (close to the seal cavity) seal failure, and the pressure measured reflects the first-stage seal state. The oil-based magnetic fluid seal state of the two-stage pole shoe is reflected by pressure transmitter 1. The cycle of pressure data acquisition is 0.04 s. The PICO acoustic emission sensor produced by the American Physical Acoustics Company (PAC) is used for acoustic emission signal acquisition. A coupling agent is coated on the contact between the sensor and shell to reduce signal loss and fix the acoustic emission sensor between the two pole shoes with transparent glue. Acoustic emission signals are collected and stored by AE-win software after being amplified by a 2/4/6 preamplifier. The software can record a short-time acoustic emission wave at regular cycles with a specified sampling rate and a specified number of sampling points. The data contained in each short-time wave can be saved as a text document, and each text document will be regarded as a sample for subsequent state recognition research. As shown in **Figure 2**, the recording cycle of the short-time wave is set as T_w = 1.3ms, the sampling rate is f_s = 2MHz, and sampling points N = 1024.

Process of the Experiment

1) Clean the disassembled parts with kerosene and then make them dry. Inject 1mL oil-based magnetic fluid into the pole shoes. Reassemble the seal devices and rotate the rotating

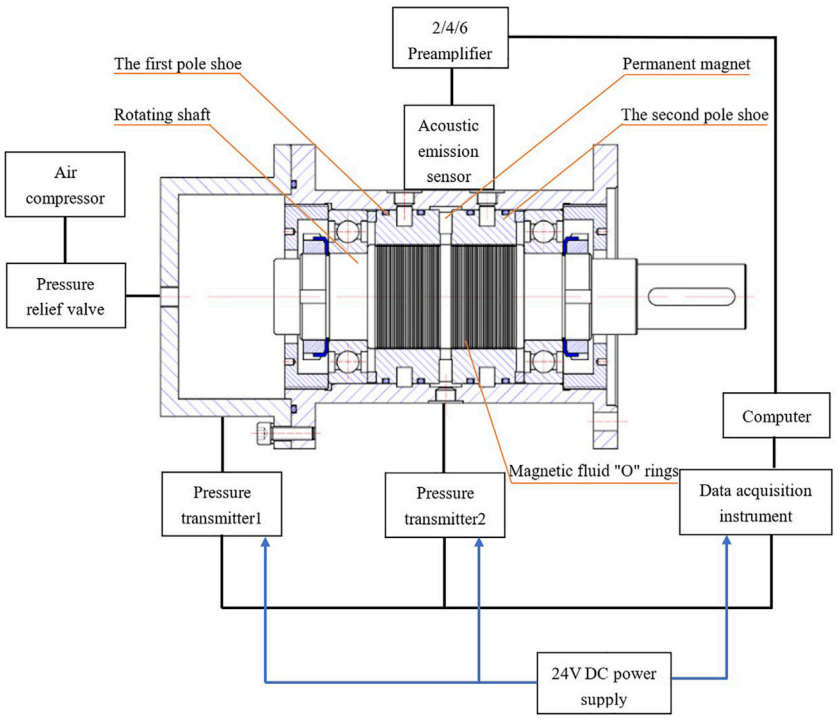

FIGURE 1 | Connection diagram of the experimental devices.

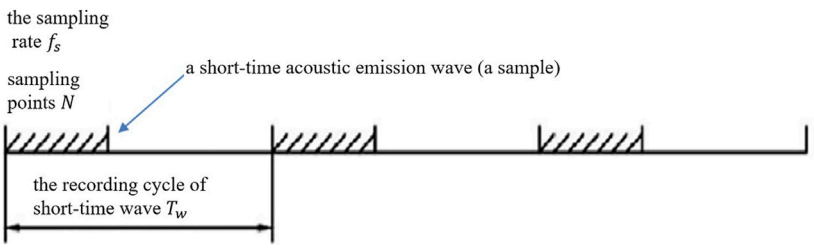

FIGURE 2 | Schematic diagram of the acoustic emission signal acquisition mode.

shaft to make oil-based magnetic fluid distribution more uniform.

2) Connect the pipeline and paste the sensor as shown in **Figure 1**.
3) Turn on the power supply and inflate the air pump of the air compressor to 700 kPa (greater than the theoretical maximum pressure of the seal element).
4) Click the acoustic emission and pressure signal acquisition software at the same time to start data acquisition. Start the air pump. Adjust the pressure relief valve knob clockwise manually and pressurize slowly until the seal fails.
5) Adjust the knob counterclockwise to close the pressure relief valve and stop inflation. Stop collecting the signals and save the data.
6) Turn off the power and disassemble devices. Adjust the pressure relief valve knob clockwise to discharge the remaining gas in the air pump.
7) Disassemble the seal element and clean it for the next experiment.

Analysis of Experiment Results

The pressure variation is shown in **Figure 3**. Phase I does not supply air to the seal cavity, and there is no magnetic fluid flow in this time period. Therefore, there is only noise signal. Phase II begins to pressurize the seal cavity. When the pressure of the seal cavity is greater than the first pole tooth magnetic fluid's maximum pressure, the magnetic fluid begins to flow. Therefore, there is only noise signal in the front part of this phase, and the latter part is the mixture of noise and the first pole shoe magnetic fluid flow signals. But, the exact time of magnetic fluid beginning to flow cannot be judged only by the pressure curve. The stepped pressure rise in phase III represents the first pole shoe seal failure. Then, it basically remains horizontal, indicating the first pole shoe magnetic fluid has a

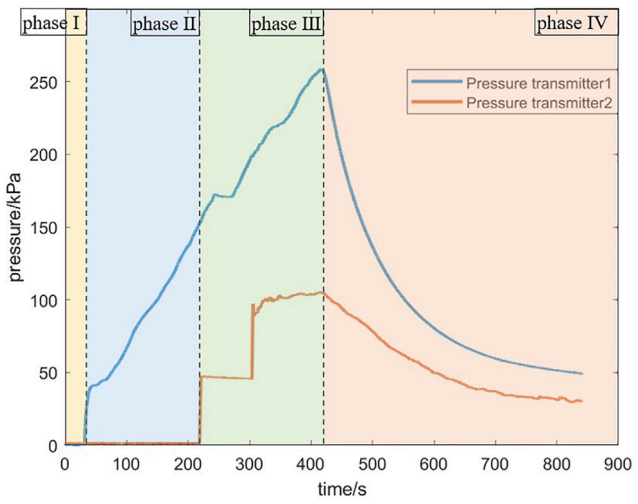

FIGURE 3 | Pressure variation in the oil-based magnetic fluid seal experiment.

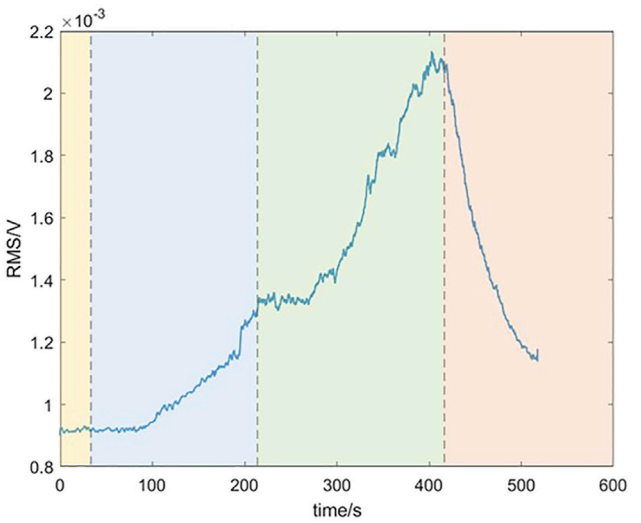

FIGURE 5 | Smoothed acoustic emission signal segmentation in the experiment.

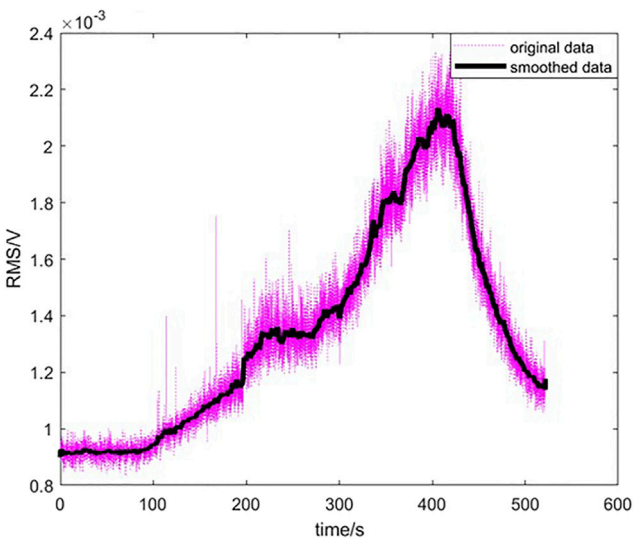

FIGURE 4 | Time-domain curve of the acoustic emission signal in the experiment.

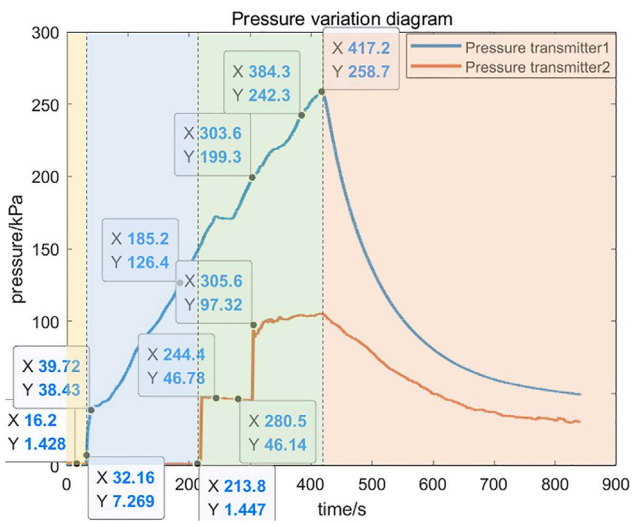

FIGURE 6 | Selection of points for power spectrum analysis.

self-healing phenomenon and plays a seal role again. The horizontal section has a slightly inclined downward trend and fluctuation phenomenon, which indicates the second pole shoe magnetic fluid flows. The pressure of both transmitters drops in phase IV, which represents two-stage pole shoe seal failure.

Next, the acoustic emission signal is analyzed. The directly collected acoustic emission data often has a lot of noise interference, which is reflected in the curve by some "burrs and spikes". If the noise is too large, the useful information will be covered up. So, we use the "moving average of $(2n + 1)$ points" in MATLAB to smooth and preprocess original data. The principle is to take out $2n + 1$ data $(y_{i-n}, \ldots, y_{i-1}, y_i, y_{i+1}, \ldots, y_{i+n})$ that centered on y_i. Also, their average is calculated to replace y_i. Namely,

$$y_i^{'} = \frac{1}{2n+1} \sum_{k=-n}^{n} y_{i+k}, \tag{1}$$

where y_{i+k} is the original data and $y_i^{'}$ is the smoothed data. In this study, $n = 25$. The time-domain diagram of the acoustic emission signal is shown in **Figure 4**. The smoothed curve can reflect the overall trend of continuous signal change.

Segment the smoothed acoustic emission signal with the aid of the pressure signal at the same time point. As shown in

TABLE 1 | Power spectrum analysis of the acoustic emission signal.

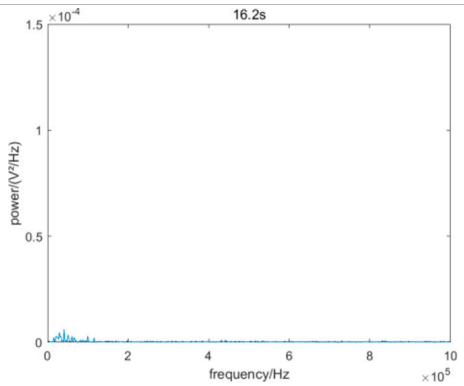

There is no magnetic fluid flow in 16.2 s.
All the measured signals are noise, and its frequency is concentrated in the frequency band lower than 200 kHz.

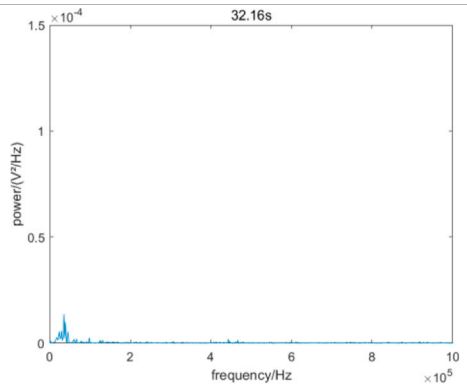

32.16 s is the same as 16.2 s.

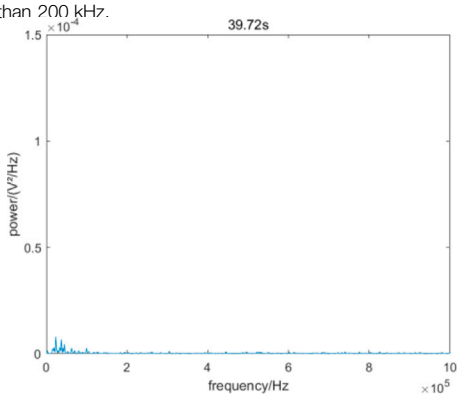

39.72 s is the same as 16.2 s.

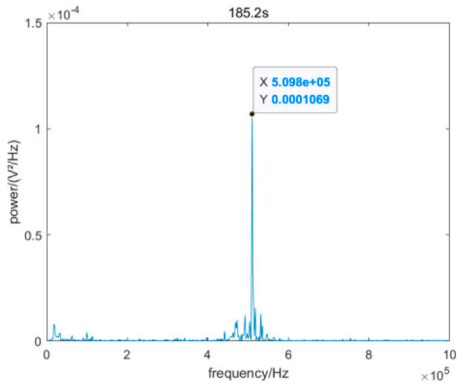

185.2 s is located at the later stage of the first pole shoe magnetic fluid flow in phase II. The peak frequency of 509.8 kHz in power spectrum reflects the information of the first pole shoe magnetic fluid flow.

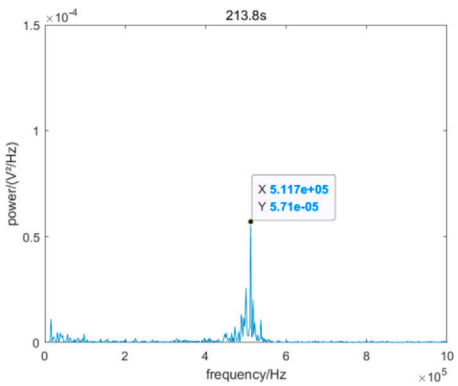

The indication of pressure transmitter 2 rises steeply for the first time, which represents the first pole shoe seal failure. The peak frequency changes.

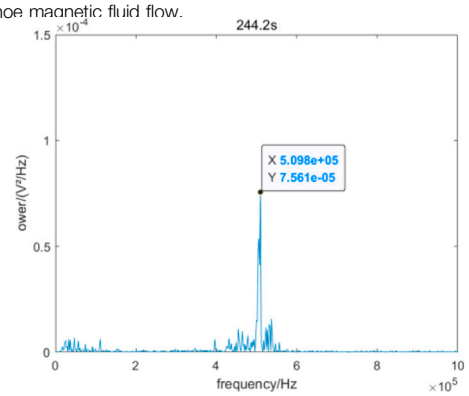

244.2 s is located in the first approximate horizontal section of the indication of pressure transmitter 2.

(Continued on following page)

TABLE 1 | (*Continued*) Power spectrum analysis of the acoustic emission signal.

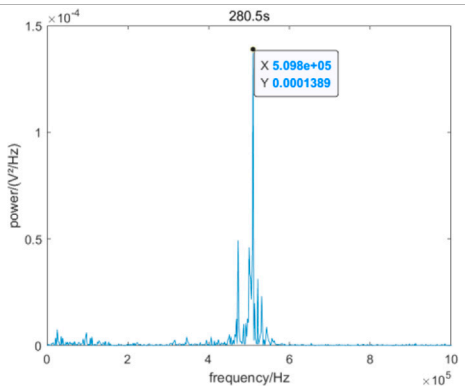

280.5 s is also located in the first approximate horizontal section of the indication of pressure transmitter 2. Compared with 244.2 s, the power value of 509.8 kHz acoustic emission signal increases, which can reflect the intensity of the first pole shoe magnetic fluid flow.

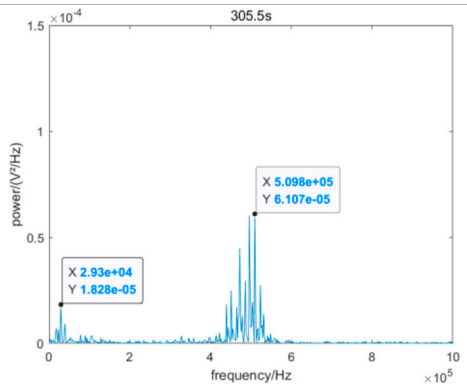

The indication of pressure transmitter 2 rises steeply for the second time. At 305.5 s, the low-frequency components have obvious protrusions compared with previous ones, containing the flow information of the second pole shoe magnetic fluid flow.

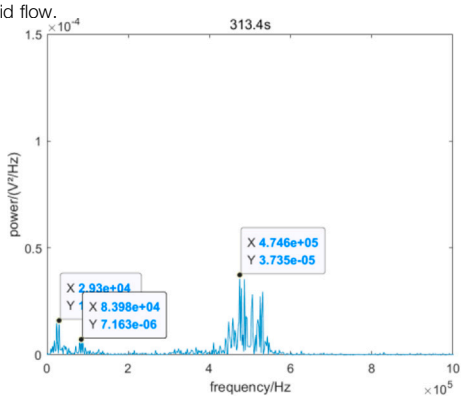

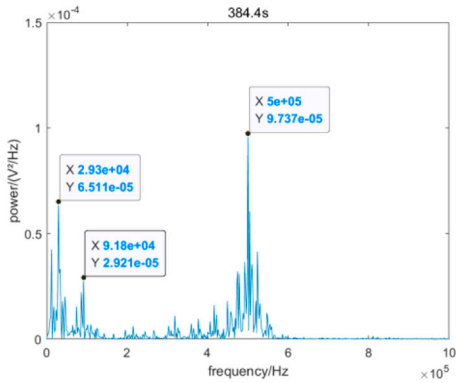

313.4 and 384.4 s are located in the second horizontal fluctuation section of pressure transmitter 2. Compared the power spectrum at 384.4 s with that at 313.4 s, the frequency peaks in low- and middle-frequency band are larger, indicating that two pole shoes magnetic fluid flow is more and more intense.

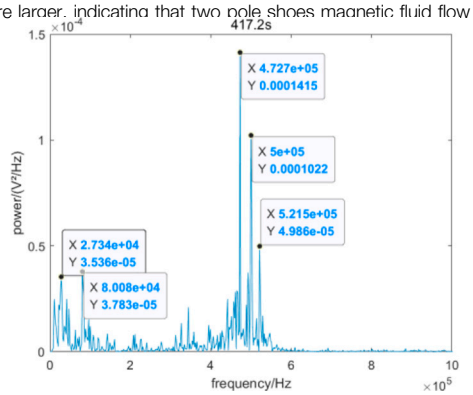

At 417.2 s, the seal fails completely

Figure 5, the acoustic emission signal in phase I is constant, indicating stable noise interference in this experiment. The rising acoustic emission signal in phases II and III contains the information on oil-based magnetic fluid flow. In phase IV, the acoustic emission signal decreases after complete leakage, which means the magnetic fluid flow becomes weaker and weaker.

Select different pressure points at each phase, as shown in **Figure 6**, and analyze the power spectrum of the acoustic emission signal at that time.

The DC component does not carry useful information with time. The frequency of the DC component is 0, and its power amplitude is generally large. It is inconducive to observe the dynamic changes of other frequency signals with small power amplitude. So, in **Table 1**,

TABLE 2 | Designed Butterworth digital filter.

Design index	Bandpass filter	Lowpass filter
Passband cut-off frequencies	460 kHz; 540 kHz	100 kHz
Stopband cut-off frequencies	400 kHz; 600 kHz	200 kHz
Maximum attenuation of passband	3dB	3dB
Minimum attenuation of stopband	40dB	40dB

the power spectrum analysis of the acoustic emission signal after removing the DC component is recorded.

To sum up, the medium-frequency band contains information about the first pole shoe magnetic fluid flow, and the low-frequency band contains the information about the second pole shoe magnetic fluid flow. The key frequency points include 509.8, 500, and 472.7 kHz in the medium-frequency band and 29.3 kHz in the low-frequency band.

According to the abovementioned key frequency points, bandpass and lowpass Butterworth digital filters are designed to filter acoustic emission signals. The specific parameters are shown in **Table 2**. The amplitude and phase frequency responses of the filters are shown in **Figure 7**. The time-domain original and smoothed curves before and after filter processing are shown in **Figure 8**.

The signal of the first pole shoe magnetic fluid flow is retained after bandpass filtering (**Figure 8D**), whose overall trend is consistent with the original (**Figure 8B**), indicating that it accounts for a large proportion of this experiment. The curve after bandpass filtering shows an upward trend from about 70 s, which means the first pole shoe magnetic fluid begins to flow. The signal's root mean square (RMS) is not 0 before that because of existing noises. The signal of the second pole shoe magnetic fluid flow and main noises are retained after lowpass filtering (**Figure 8F**). The curve shows obvious protrusion in 298–416 s, which indicates the second pole shoe magnetic fluid flow at this time. At other times, the curve is approximately horizontal, and the RMS is not 0 because of the stable noises. This curve is quite different from the original one. It means that the proportion of the second pole shoe magnetic fluid flow signal is small in this experiment. Furthermore, the initial distribution of magnetic fluid is uneven.

Therefore, the specific time of two pole shoes magnetic fluid flow can be obtained after power spectral analysis and filtering. The filtered acoustic emission signal's RMS can reflect the intensity of the magnetic fluid flow. The initial distribution of magnetic fluid under two pole shoes can be inferred from the above mentioned two pole shoes. So, the oil-based magnetic fluid flow information reflected by the acoustic emission signal is richer than the pressure signal.

According to the abovementioned analysis, the process before oil-based magnetic fluid seal failure can be divided into three stages: 0–70.16 s is the first stage, and there is no magnetic fluid flow; 70.16–298.2 s is the second stage, the first pole shoe magnetic fluid flow; and 298.2–416 s is the third stage, two pole shoes magnetic fluid flow together. In order to avoid the inaccuracy of acoustic emission signal sample classification by artificially selecting time points, take 8s before and after the abovementioned time points as the transition period. Therefore, the acoustic emission signal samples collected in 0–62.16 s correspond to the first stage, 78.16–290.2 s correspond to the second stage, and 306.2–408s correspond to the third stage. It will take a long time and low efficiency if all of the acoustic emission data are read and processed. So, we read a sample every 0.04 s using MATLAB in order to correspond well with the pressure data. A total of 9,330 samples are obtained. Among them, there are 1,543 samples in the first stage, 5,261 samples in the second stage, and 2,526 samples in the third stage. The training set and testing set are divided according to the ratio of 2:1, so there are 6,220 training set samples and 3,110 testing set samples.

FLOW-STATE IDENTIFICATION OF OIL-BASED MAGNETIC FLUID SEAL BASED ON RANDOM FOREST

Feature Extraction

An acoustic emission signal sample $\boldsymbol{X} = [x_1, x_2, \ldots, x_N]$ is a discrete time series with finite length, and $P(f_i)$ is the signal's

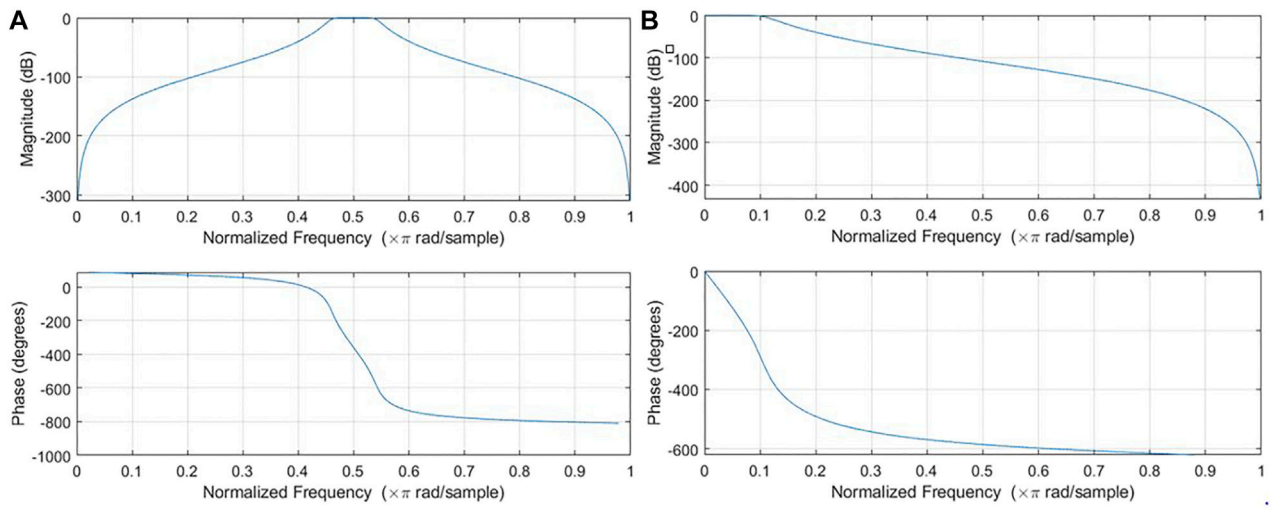

FIGURE 7 | Amplitude and phase-frequency response of filters. **(A)** Bandpass filter.**(B)** Lowpass filter.

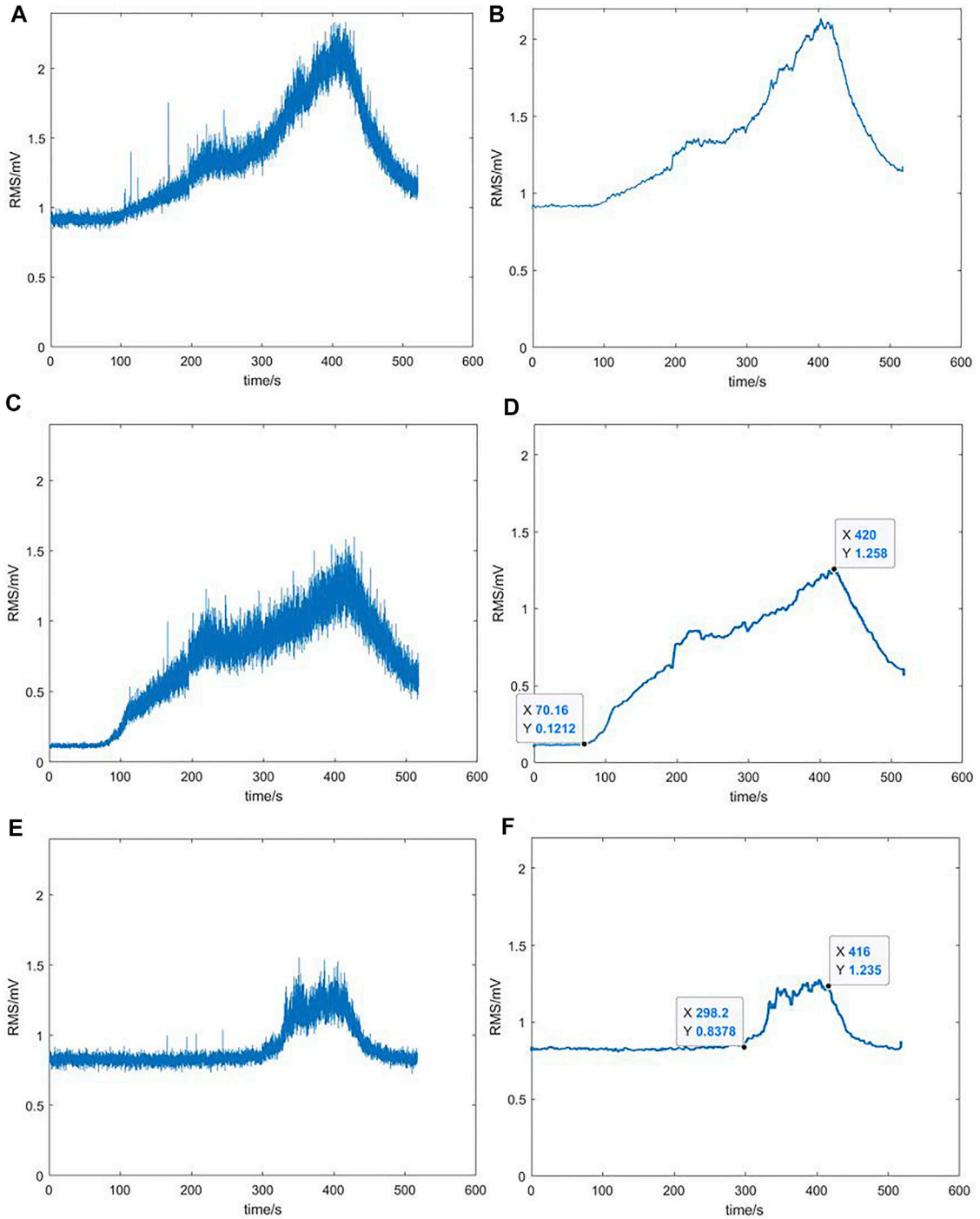

FIGURE 8 | Comparison of original and smoothed acoustic emission signal before and after filtering. **(A)** Original signal. **(B)** Smoothed signal. **(C)** Original signal after bandpass filtering. **(D)** Smoothed signal after bandpass filtering. **(E)** Original signal after lowpass filtering. **(F)** Smoothed signal after lowpass filtering.

power value at frequency f_i. The common time- and frequency-domain eigenvalues are shown in **Tables 3**, **4**. Those eigenvalues obtained from acoustic emission signal samples form a 21-dimensional eigenvector as input of the subsequent identification model.

Random Forest Identification Model Based on Grey Wolf Optimizer

Random forest is a supervised learning algorithm that integrates the results of multiple classification and regression trees (CART), as shown in **Figure 9**. Its specific process is as follows.

TABLE 3 | Calculation formulas of common time-domain eigenvalues.

Dimensional index	Maximum	$x_{max} = \max(x_1, x_2, \ldots, x_N)$	Minimum	$x_{min} = \min(x_1, x_2, \ldots, x_N)$
	Mean	$\mu = \frac{1}{N}\sum_{n=1}^{N} x_n$	Peak to peak	$x_{pp} = x_{max} - x_{min}$
	Peak	$x_{pk} = \max\lvert x_n \rvert$	Variance	$V = \frac{1}{N-1}\sum_{n=1}^{N} \lvert x_n - \mu \rvert^2$
	Standard deviation	$\sigma = \sqrt{\frac{1}{N-1}\sum_{n=1}^{N} \lvert x_n - \mu \rvert^2}$	Root mean square	$x_{RMS} = \sqrt{\frac{1}{N}\sum_{n=1}^{N} \lvert x_n \rvert^2}$
	Average amplitude	$x_{avg} = \frac{1}{N}\sum_{n=1}^{N} \lvert x_n \rvert$		
Dimensionless index	Kurtosis	$x_{kurt} = \frac{E(x-\mu)^4}{\sigma^4}$	Skewness	$x_{skew} = \frac{E(x-\mu)^3}{\sigma^3}$
	Peak factor	$x_{CF} = \frac{x_{pk}}{x_{RMS}}$	Waveform factor	$x_{SF} = \frac{x_{RMS}}{x_{avg}}$
	Pulse factor	$x_{IF} = \frac{x_{pk}}{x_{avg}}$	Clearance factor	$x_{MF} = \frac{x_{pk}}{(\frac{1}{N}\sum_{n=1}^{N} \sqrt{\lvert x_n \rvert})^2}$

TABLE 4 | Calculation formulas of common frequency-domain eigenvalues.

Dimensional index	Center of gravity frequency	$f_c = \frac{\sum_{i=0}^{N/2} [f_i \cdot P(f_i)]}{\sum_{i=0}^{N/2} P(f_i)}$
	Mean square frequency	$f_{MS} = \frac{\sum_{i=0}^{N/2} [f_i^2 \cdot P(f_i)]}{\sum_{i=0}^{N/2} P(f_i)}$
	Root mean square frequency	$f_{RMS} = \sqrt{\frac{\sum_{i=0}^{N/2} [f_i^2 \cdot P(f_i)]}{\sum_{i=0}^{N/2} P(f_i)}}$
	Frequency variance	$f_V = \frac{\sum_{i=0}^{N/2} [(f_i - f_c)^2 \cdot P(f_i)]}{\sum_{i=0}^{N/2} P(f_i)}$
	Frequency standard deviation	$f_S = \sqrt{\frac{\sum_{i=0}^{N/2} [(f_i - f_c)^2 \cdot P(f_i)]}{\sum_{i=0}^{N/2} P(f_i)}}$
Dimensionless index	Spectral peak stability index	$S = \sqrt{\frac{\sum_{i=0}^{N/2} [f_i^2 \cdot P(f_i)]}{\sum_{i=0}^{N/2} P(f_i)}} \Big/ \sqrt{\frac{\sum_{i=0}^{N/2} [f_i^4 \cdot P(f_i)]}{\sum_{i=0}^{N/2} [f_i^2 \cdot P(f_i)]}}$

1) Construct sub-training samples. Repeat random sampling with putting back (bootstrap sampling) from the original samples to construct sub-training samples.
2) Construct the sub-input eigenvalues set. Randomly sample $mtry$ eigenvalues without putting back from $m(mtry < m)$ originals to construct the sub eigenvalues set as the input of the base classifier.
3) Train CART base classifier. CART is a binary tree as shown in **Figure 9**. Select the classification eigenvalue at the parent node and classify the samples according to set rules. The leaf node represents the classification result. Since the input eigenvalues in this study are continuous, it is necessary to discretize them by dichotomy. The specific process is shown in **Figure 10**. $t_i(i \in [1,\ l \cdot (n-1)])$ is the selected classification point according to the Gini coefficient, which can reflect the purity of samples in child nodes. The smaller the Gini coefficient, the higher the purity of samples. The Gini coefficient of t_i is defined as

$$Gini_{index(D_i,t_i)} = p_L\left[1 - \sum_{j=1}^{J} p(k)^2\right] + p_R\left[1 - \sum_{j=1}^{J} p(k)^2\right], \quad (2)$$

where p_L and p_R represent the proportion of samples in the left and right child nodes, respectively. $p(k)$ represents the proportion of samples belonging to category j in child nodes. The total number of categories is J. Select the corresponding eigenvalue M of t_i with the smallest Gini coefficient as the classification eigenvalue of the parent node. The left and right child nodes, respectively, contain samples with $M \le t_i$ and $M > t_i$. In this way, the samples are classified. The training is completed until the sample purity in the child node reaches the maximum or all eigenvalues have been used.

4) Construct a random forest model. Repeat steps (1) (2) (3) and *ntree* CARTs are generated in parallel to construct a random forest.
5) Output final classification results. In a CART, each path from the root node to a leaf node represents a rule. When testing, the input eigenvalues of the testing sample uniquely determine a path. The category of most samples in this leaf node is the prediction result of the testing sample. The final classification result is determined by the output of *ntree* CARTs according to the maximum number of votes.

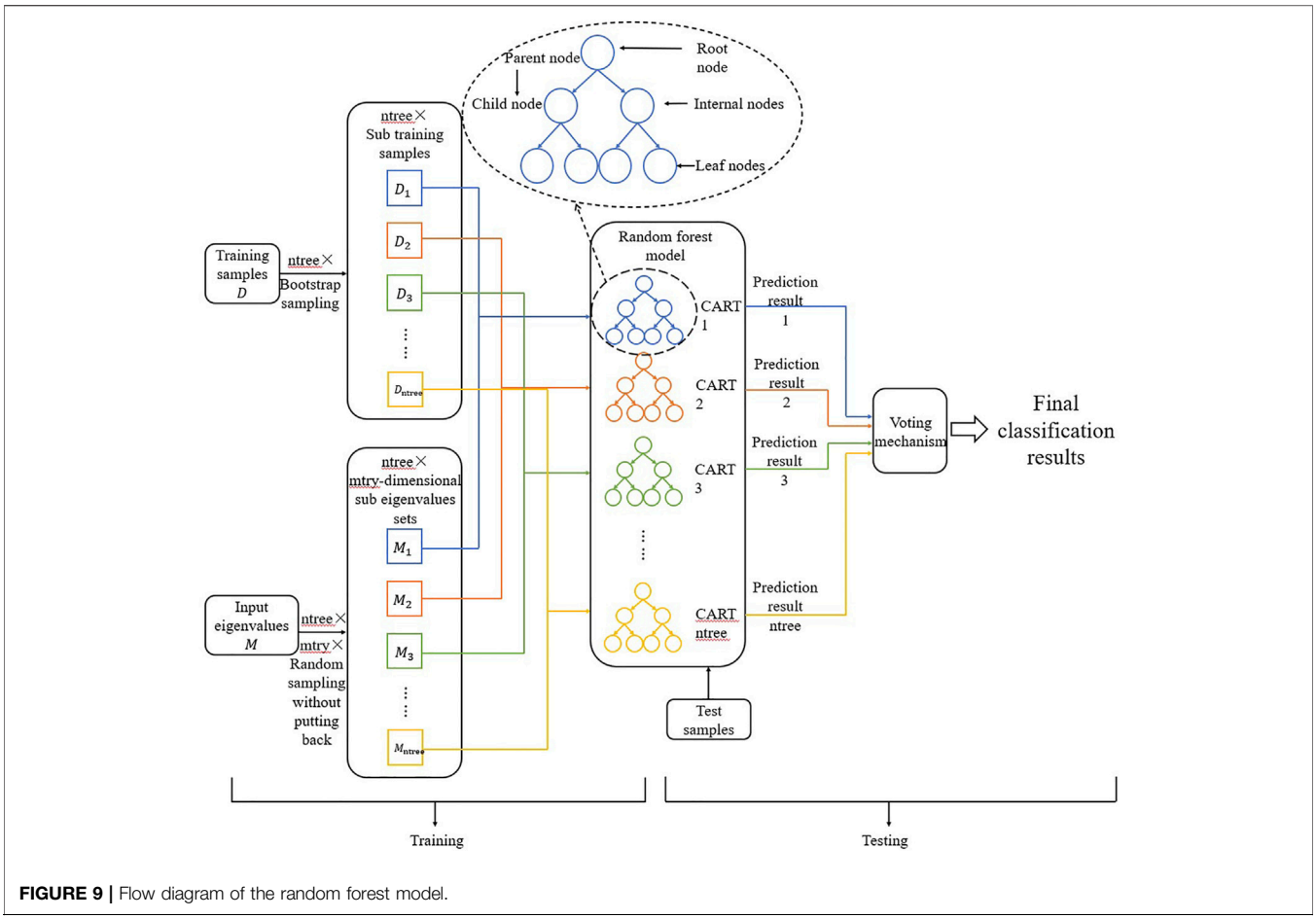

FIGURE 9 | Flow diagram of the random forest model.

Suppose that one input eigenvalue M has n different values in sub training samples to be classified, which are recorded as $M_i\ (i = 1,2,\ldots,n)$.

$$\underbrace{M_1 \le M_2}_{} \le \cdots\cdots \le \underbrace{M_{n-1} \le M_n}_{}$$

$$\underbrace{t_1 = \frac{M_1 + M_2}{2} \quad \cdots\cdots \quad t_{n-1} = \frac{M_{n-1} + M_n}{2}}_{}$$

One input eigenvalue M has $n-1$ candidate partition points, which are recorded as $t_i (i = 1,2,\ldots,n-1)$.

There are l sub input eigenvalues for selection($l \le mtry$).

Compare the Gini coefficients of $(l \times (n-1))$ candidate partition points.

FIGURE 10 | Flow diagram of discretized continuous eigenvalues by dichotomy.

ntree and *mtry* are important to the random forest model's final classification results (Tan et al., 2022). A grey wolf optimizer (GWO) is used to find the superparameter combination in this study.

GWO is a new swarm intelligence optimization algorithm, which simulates the strict social hierarchy and collective hunting behavior of the grey wolf group. $\alpha, \beta, \delta, \omega$ are four different levels of grey wolves who are distinguished by the fitness values of individuals. The optimal solution is taken as α, the second and third are β and δ, and the remaining are ω.

The formulas imitating the behavior of wolves surrounding prey are as follows.

$$\boldsymbol{D} = \left|\boldsymbol{C} \cdot \boldsymbol{X}_p(t) - \boldsymbol{X}(t)\right|, \tag{3}$$

$$\boldsymbol{X}(t+1) = \boldsymbol{X}_p(t) - \boldsymbol{A} \cdot \boldsymbol{D}, \tag{4}$$

where $\boldsymbol{A}$ and $\boldsymbol{C}$ are coefficient vectors; $\boldsymbol{X}_p$ and $\boldsymbol{X}$ are the position vector of prey and grey wolf, respectively; t is the current number of iterations; $\boldsymbol{D}$ is the distance between the wolves and prey. $\boldsymbol{A}$ and $\boldsymbol{C}$ are calculated as follows:

$$\boldsymbol{A} = 2\boldsymbol{a} \cdot \boldsymbol{r}_1 - \boldsymbol{a}, \tag{5}$$

$$\boldsymbol{C} = 2 \cdot \boldsymbol{r}_2, \tag{6}$$

where $\boldsymbol{a}$ decreases linearly from 2 to 0 with iteration and $\boldsymbol{r}_1$ and $\boldsymbol{r}_2$ are random numbers distributed in the interval [0,1] so that grey wolves can move to any position within a certain range around the prey. The encirclement is realized as $\boldsymbol{a}$

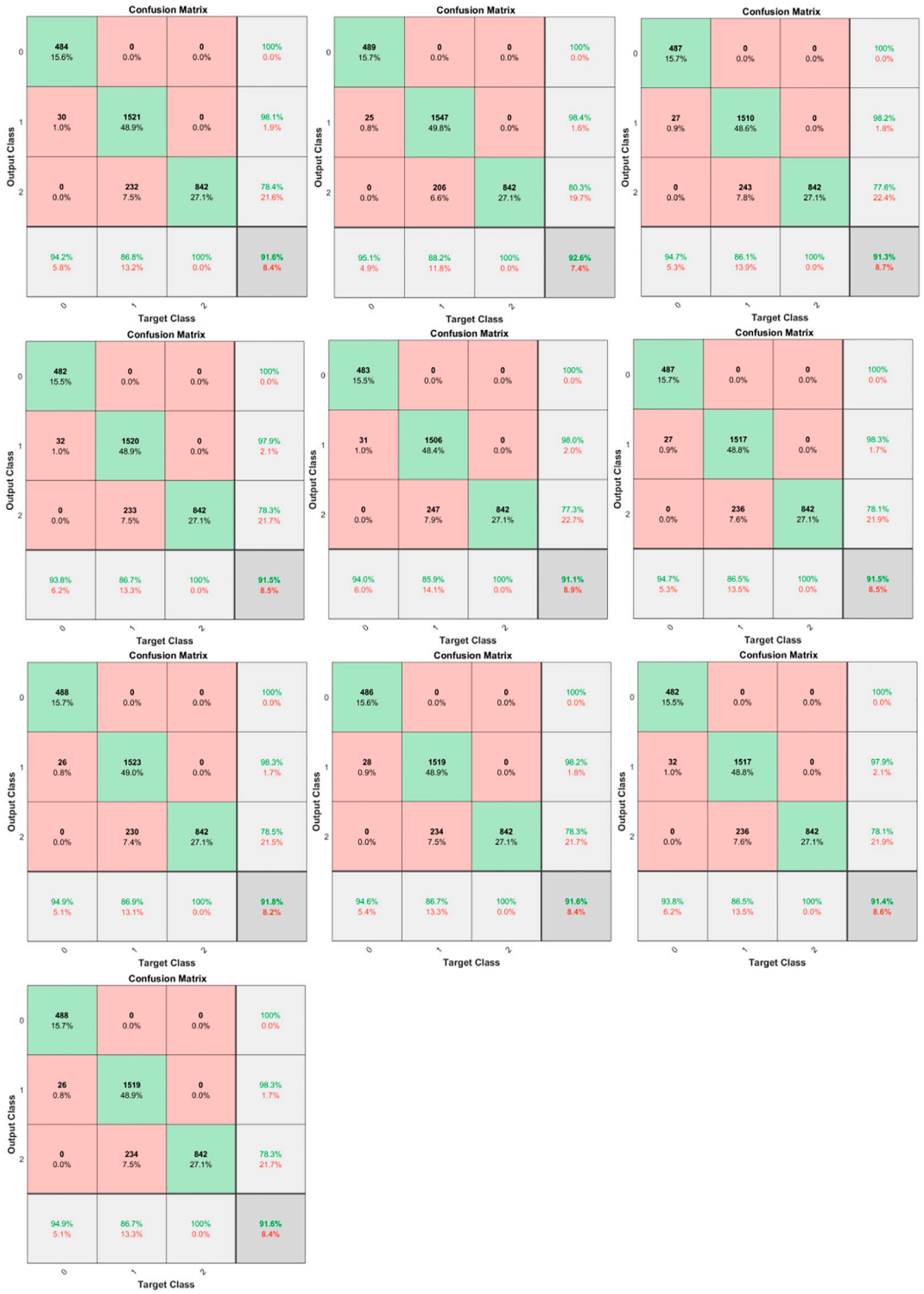

FIGURE 11 | Confusion matrixes of 10 times' training results.

decreases to 0. So the value range of $\boldsymbol{A}$ is [-a, a]. When $|\boldsymbol{A}| < 1$, the wolf will be close to attacking the prey. When $|\boldsymbol{A}| > 1$, the wolf will be far away to explore. $\boldsymbol{C}$ is the random location weight representing the wolves' influence on the prey. Its value range is [0,2]. $\boldsymbol{A}$ and $\mathbf{C}$ can avoid the algorithm falling into local optimization.

In GWO, α, β, and δ guide ω to hunt. The location update formula of wolves is as follows:

TABLE 5 | Information statistics of GWO_ RF model.

F1 Scores testing set			Training duration/s		Optimal hyperparameter		Optimal fitness
No of magnetic fluid flow (%)	The first pole shoe magnetic fluid flow (%)	Two pole shoes magnetic fluid flow (%)	Parameter optimization process	Model training process	*Ntree*	*Mtry*	Testing accuracy (%)
97.01	92.10	87.89	33.58	0.50	40	14	92.47
97.49	93.02	89.07	35.07	0.47	1	20	92.18
97.28	91.75	87.39	29.60	0.42	50	11	92.47
96.80	91.96	87.83	29.56	0.41	100	20	92.34
96.91	91.55	87.20	29.61	0.41	79	6	92.31
97.28	92.02	87.70	30.19	0.42	97	11	92.47
97.38	92.25	87.96	29.56	0.43	35	11	92.28
97.23	92.09	87.83	29.61	0.42	39	11	92.31
96.80	91.85	87.70	29.57	0.42	100	2	92.12
97.38	92.14	87.83	29.58	0.41	54	6	92.28
97.16	92.07	87.84	30.59	0.43	\	\	92.32

$$\begin{cases} \boldsymbol{D}_\alpha = |\boldsymbol{C}_1 \cdot \boldsymbol{X}_\alpha - \boldsymbol{X}(t)| \\ \boldsymbol{D}_\beta = \left|\boldsymbol{C}_2 \cdot \boldsymbol{X}_\beta - \boldsymbol{X}(t)\right| \\ \boldsymbol{D}_\delta = |\boldsymbol{C}_3 \cdot \boldsymbol{X}_\delta - \boldsymbol{X}(t)| \end{cases}, \tag{7}$$

$$\begin{cases} \boldsymbol{X}_1 = \boldsymbol{X}_\alpha - \boldsymbol{A}_1 \cdot \boldsymbol{D}_\alpha \\ \boldsymbol{X}_2 = \boldsymbol{X}_\beta - \boldsymbol{A}_2 \cdot \boldsymbol{D}_\beta \\ \boldsymbol{X}_3 = \boldsymbol{X}_\delta - \boldsymbol{A}_3 \cdot \boldsymbol{D}_\delta \end{cases}, \tag{8}$$

$$\boldsymbol{X}(t+1) = \frac{\boldsymbol{X}_1 + \boldsymbol{X}_2 + \boldsymbol{X}_3}{3}, \tag{9}$$

where $\boldsymbol{D}_\alpha$, $\boldsymbol{D}_\beta, \boldsymbol{D}_\delta$, respectively, represent the distances from α, β, δ to other individuals; $\boldsymbol{X}_\alpha, \boldsymbol{X}_\beta, \boldsymbol{X}_\delta$, respectively, represent the current location of α, β, δ; $X(t)$ is the current location of the grey wolf. **Formula (8)** defines step and direction for ω move on to α, β, δ. **Formula (9)** defines ω's final position.

In this study, the acoustic emission signal sample's time- and frequency-domain eigenvalues are extracted as the input to train GWO_RF model identifying the oil-based magnetic fluid flow state before seal failure.

Identification Result

Train the random forest model by the function classRF_train () in MATLAB R2018b. Apply GWO to optimize two super parameters of *ntree* and $mtry$. The number of grey wolf population and iterations are both 10. Optimize *ntree* in [1,100] and $mtry$ in [1,21]. Take the classification accuracy of the testing set as the fitness. The confusion matrixes of 10 times training results are shown in **Figure 11**.

In the confusion matrix, the row corresponds to the prediction class, the column corresponds to the real class, the diagonal unit corresponds to correct classification, and the non-diagonal unit corresponds to wrong classification. The number and the percentage are displayed in each cell. The rightmost column of the chart shows the correct and wrong classification in the prediction results, which are called precision and error detection rates, respectively. The row at the bottom of the chart shows the ones in the real category, which are called recall rate and false-negative rate. The cell at the bottom right of the chart shows overall accuracy. The confusion between "the first pole shoe magnetic fluid flow" and "two-pole shoes magnetic fluid flow" is serious.

Only the accuracy value is not suitable for evaluating the models with large quantity deviation in different categories of samples. In theory, the higher the precision and recall rate, the better. But they are often inconsistent. The F score is often used to consider them comprehensively. Its calculation formula is as follows:

$$F = \frac{(a^2+1)*P*R}{a^2*(P+R)}, \tag{10}$$

where P: precision, R: recall, a: weight factor. When $a = 1$, it changes to the most common evaluation index F1 score, representing the weight of precision and recall are the same. Its calculation formula is

$$F1 = \frac{2*P*R}{P+R}. \tag{11}$$

Table 5 summarizes the GWO_RF model's 10 training results. The last line is the average of them. It can be found that F1 scores of three oil-based magnetic fluid flow states before seal failure are close to or greater than 90%, among which, the F1 score of "two pole shoe magnetic fluid flow" is relatively low. The F1 scores obtained from each training are

similar although the optimization results have great randomness. Of course, GWO takes a long time to optimize the parameters.

CONCLUSION

In this study, nondestructive acoustic emission testing technology is proposed to monitor the oil-based magnetic fluid flow state before the seal failure so as to speculate the seal performance. The experiment is designed to collect the acoustic emission and pressure signals at the same time. The acoustic emission signal is analyzed and filtered assisted by the pressure signal. The process before the oil-based magnetic fluid seal failure is divided into three stages: no magnetic fluid flow, the first pole shoe magnetic fluid flow, and two pole shoe magnetic fluid flow together, and the acoustic emission signal samples are classified. Extract the time- and frequency-domain eigenvalues forming a 21-dimensional eigenvector as the input and train the random forest model based on grey wolf optimizer to optimize the $ntree$ and $mtry$. The testing accuracy and F1 scores of the three states are close to or higher than 90%, indicating the feasibility of acoustic emission technology and the effectiveness of spectrum analysis and filtering for the acoustic emission signal to distinguish three flow states. In future studies, we can redesign the structure of the seal element, which can measure the pressure change between each two pole teeth. So we can analyze the acoustic emission signal more accurately with the help of more detailed pressure signals. Also, we can compare acoustic emission signals with the changing of parameters such as shaft rotation speed and temperature under dynamic conditions.

DATA AVAILABILITY STATEMENT

The original contributions presented in the study are included in the article/**Supplementary Material**; further inquiries can be directed to the corresponding author.

ETHICS STATEMENT

Ethical review and approval was not required for the study on human participants in accordance with the local legislation and institutional requirements. The patients/participants provided their written informed consent to participate in this study.

AUTHOR CONTRIBUTIONS

Conceptualization: JX, YX, and DL; methodology: JX and YX; software: JX; validation: JX and YX; resources: DL; data curation: JX; writing—original draft preparation, JX; writing—review and editing: YX and DL; supervision: DL; project administration: DL. All authors have read and agreed to the published version of the manuscript.

FUNDING

This work was supported by the National Natural Science Foundation of China (grant numbers: 51735006, U1837206, 51927810) and the Beijing Municipal Natural Science Foundation (grant number: 3182013).

ACKNOWLEDGMENTS

We acknowledge the resources provided by the laboratory and the guidance of all teachers.

SUPPLEMENTARY MATERIAL

The Supplementary Material for this article can be found online at: https://www.frontiersin.org/articles/10.3389/fmats.2022.930885/full#supplementary-material

REFERENCES

Chen, Y. B. (2019). *Study on Magnetic Fluid Seals under High Speed Condition. Doctoral Dissertation*. Beijing: University of Science and Technology Beijing. Available at: https://kns.cnki.net/KCMS/detail/detail.aspx?dbname=CDFDLAST2019&filename=1019157279.nh.

Ge, Z. D., Fu, P., and Zhang, E. Q. (2016). Monitoring Technique of Film Seal Face Friction Condition Based on Kalman Filtering. *Lubr. Eng.* 41 (04), 106–110. Available at: https://kns.cnki.net/kcms/detail/detail.aspx?FileName=RHMF201604027&DbName=CJFQ2016.

Jiang, Y. (2015). *The Monitoring Research on the Open Process of Hydrodynamic Mechanical Seals Based on Acoustic Emission Characteristics. Master Degree Dissertation*. Chengdu, Sichuan: Southwest Jiaotong University. Available at: https://kns.cnki.net/KCMS/detail/detail.aspx?dbname=CMFD201601&filename=1015338185.nh.

Kurfess, J., and Müller, H. K. (1990). Sealing Liquids with Magnetic Liquids. *North-Holland* 85 (1-3). doi:10.1016/0304-8853(90)90059-y

Li, D. C., and Hao, D. (2018). Major Problems and Solutions in Applications of Magnetic Fluid Rotation Seal. *Chin. J. Vac. Sci. Technol.* 38 (07), 564–574. doi:10.13922/j.cnki.cjovst.2018.07.04

Li, X. H., Fu, P., and Zhang, Z. (2014). Measurement of Film Thickness in Mechanical Seals Based on AE Technology. *Adv. Eng. Sci.* 46 (06), 198–204. doi:10.15961/j.jsuese.2014.06.031

Li, X. H. (2016). *Hydrodynamic Mechanical Seal End Faces Condition Monitoring and Health Assessment. Doctor Degree Dissertation*. Chengdu, Sichuan: Southwest Jiaotong University. Available at: https://kns.cnki.net/KCMS/detail/detail.aspx?dbname=CDFDLAST2018&filename=1017298548.nh.

Li, Y. F. (2017). "Study on Condition Monitoring and Performance Evaluating System of Liquid Film Seals," in *Degree Thesis of Engineering Master*. China University of Petroleum (East China). Available at: https://kns.cnki.net/KCMS/detail/detail.aspx?dbname=CMFD201902&filename=1019838884.nh.

Sun, X. H., Dong, X. W., Zhang, T. F., Hao, M. M., Cao, H. C., Wang, Y. L., et al. (2018). Research Progress of Acoustic Emission in Seal Monitoring. *Lubr. Eng.* 43 (06), 136–140. Available at: https://kns.cnki.net/kcms/detail/detail.aspx?FileName=RHMF201806025&DbName=CJFQ2018. 10.2478/pomr-2018-0122.

Tan, C. Y., Zhang, Z. S., Zhou, X. Q., Guo, J. H., Xiao, H., Chen, T., et al. (2022). Pattern Recognition Model of Coalbed Methane Productivity Based on Random Forest Algorithm. *Saf. Coal Mines* 53 (02), 170–178+186. doi:10.13347/j.cnki.mkaq.2022.02.027

Wang, Z. Z. (2019). *The Study of Sealing Liquid with Magnetic Fluid. Doctoral Dissertation*. Beijing: Beijing Jiaotong University. Available at: https://kns.cnki.net/KCMS/detail/detail.aspx?dbname=CDFDLAST2020&filename=1019210031.nh.

Zhang, E. Q. (2015). *Research of Key Technologies on Mechanical Seal End Face Condition Monitoring and Life Prediction. Doctor Degree Dissertation*. Chengdu, Sichuan: Southwest Jiaotong University. Available at: https://kns.cnki.net/kcms/detail/detail.aspx?FileName=1016177215.nh&DbName=CDFD2016

Zhang, F. (2016). *Research on Fault Diagnosis Method for Rotating Machine Based on LMD and HSMM. Master Degree Thesis*. Chengdu, Sichuan: Southwest Jiaotong University. Available at: https://kns.cnki.net/kcms/detail/detail.aspx?FileName=1016155076.nh&DbName=CMFD2016.

Conflict of Interest: The authors declare that the research was conducted in the absence of any commercial or financial relationships that could be construed as a potential conflict of interest.

Publisher's Note: All claims expressed in this article are solely those of the authors and do not necessarily represent those of their affiliated organizations, or those of the publisher, the editors, and the reviewers. Any product that may be evaluated in this article, or claim that may be made by its manufacturer, is not guaranteed or endorsed by the publisher.

Advantages of publishing in Frontiers

OPEN ACCESS
Articles are free to read for greatest visibility and readership

FAST PUBLICATION
Around 90 days from submission to decision

HIGH QUALITY PEER-REVIEW
Rigorous, collaborative, and constructive peer-review

TRANSPARENT PEER-REVIEW
Editors and reviewers acknowledged by name on published articles

Frontiers
Avenue du Tribunal-Fédéral 34
1005 Lausanne | Switzerland

Visit us: www.frontiersin.org
Contact us: frontiersin.org/about/contact

REPRODUCIBILITY OF RESEARCH
Support open data and methods to enhance research reproducibility

DIGITAL PUBLISHING
Articles designed for optimal readership across devices

FOLLOW US
@frontiersin

IMPACT METRICS
Advanced article metrics track visibility across digital media

EXTENSIVE PROMOTION
Marketing and promotion of impactful research

LOOP RESEARCH NETWORK
Our network increases your article's readership